The Miocene-Recent evolution of the Antalya Basin, eastern Mediterranean Sea

by

A Thesis submitted to the School of Graduate Studies in partial fulfillment of the requirements for the degree of

Master of Science

Department of Earth Sciences

Memorial University of Newfoundland

Sept. 2014

St. John's Newfoundland

Abstract

Detailed interpretation of high-resolution and industry multichannel seismic reflection profiles and lithostratigraphy from onshore wells reveals that the Miocene to Recent tectonic evolution of the western Antalya Basin occurred in three distinct intervals: the pre-Messinian Miocene, the Messinian, and the Pliocene-Quaternary. During the pre-Messinian Miocene, a prominent east-west striking fold-thrust belt developed across the region. Today, this belt is characterized by NW-SE striking, SW-verging thrust panels in the east and broadly N-S striking, W-verging thrust panels in the west. The belt became buckled during the late Miocene assuming its current configuration as an inverted V-shaped structure within the marine western Antalya Basin. The Miocene fold-thrust belt mapped in the marine areas is readily correlated with the onland Isparta Angle. The Messinian interval was tectonically quiet and marked by the deposition of a thick evaporite succession within the deep Antalya Basin. The Pliocene-Quaternary interval marked a major change in tectonic style, where strain is partitioned into discrete regional morpho-tectonic domains. In the east, the Miocene fold-thrust belt remained largely inactive; however, several prominent thrusts became re-activated during this time. Mapping showed that these three thrusts can be traced toward the southeast in the deep Antalya Basin and readily correlated with the Ovgos, Kythrea and Orga thrusts mapped onland Cyprus. The shallower slope and shelf in this area are characterized by broadly actuate and NW-

SE striking and SE- and NW-dipping extensional faults with strike slip components. In the west portion of the Antalya Basin, the structural framework was dominated by a series of broadly N-S striking, invariably steeply E-dipping extensional faults which form a 20-30 km wide zone of deformation. This zone occurs over the very steep continental slope in western Antalya Basin, and extends westward into the Kemer Peninsula and the Beydağları region. Correlations with the similarly striking Pliocene-Quaternary transtensional faults mapped onland suggest that these faults must also have notable strike slip components.

Dedication

This is for you, Dad.

"Do the best you can, and can the rest."

Acknowledgements

Without the guidance, support, and *occasional* forceful push from my two supervisors, Dr. Jeremy Hall and Dr. Ali Aksu, this thesis may never have come to fruition. Thank you both for teaching me and advising me how to grow as a geoscientist, both academically and professionally. I will carry your lessons with me throughout my career. Thank you, especially, for all your efforts in the past few weeks to help me bring this chapter of my life to a close.

Thank you to my examiners, Dr. John Waldron and Dr. Rick Hiscott, for being thorough and fair in your comments and suggestions. Thank you Tom Koleszar, Jim Stewart, and Geoff Fraser at BP for your support and encouragement throughout the editing process. Thank you to all the students, staff, and professors in the Earth Sciences Department who have helped me along the way, especially those affiliated with the Eastern Mediterranean Research Group. A special thank you goes out to Peter Bruce and Sharon Deemer for all your help on the technical side of things. Also, a big thank you goes to Michelle Miskell for being on the ball with all the things.

Data for this thesis was acquired through collaboration with Dokuz Eylül University in Izmir, Turkey. Thank-you to all the staff, ship crew, scientific crew and students for their help with the data acquisition; the times we had aboard the *RV Koca Piri Reis* are unforgettable. Funding for this project has been made possible

through NSERC Discovery Grants to A. Aksu and J. Hall and the processing software was kindly provided by Landmark Graphics.

Thank you to my family, friends, and colleagues for putting up with me and being my unwavering support system throughout this process, especially: Brenda King, Derm King (always in my heart), Alyson King, Father Jim, Maria Beehan, Dan Ansley, Bahar Kurtboğan, Caroline McIlroy, Susan Kennedy, and Julie Halliday. Finally, thank you to my very best buddy and love of my life, Brad Squire, for always having my back.

******* Thank you for everything! *******

Table of Contents

Abstract **ii**

Dedication **iv**

Acknowledgments **v**

Table of Contents **xi**

List of Figures **xvi**

List of Plates **xvii**

1 Introduction **1**

1.1 Present-day tectonic framework of the eastern Mediterranean 2

1.2 Bathymetry of the eastern Mediterranean Sea 4

1.3 Marine Miocene basins in the eastern Mediterranean and the Isparta Angle 7

1.4 Thesis objectives 11

2 Methods: Acquisition, Processing and Interpretation of 2D Marine Seismic Data **13**

2.1 Acquisition of 2D marine seismic data 14

2.1.1 Basic theory of reflection seismology 14
2.1.1.1 Reflection seismology in the field 17
2.1.2 2D marine seismic surveys 17
2.1.2.1 CDPs, CMPs, and seismic data fold 19
2.1.2.2 Some issues associated with 2D marine surveys . . . 20
2.1.3 Survey parameters and geometry of the 2008 eastern Mediterranean cruise 23
2.2 Processing 2D marine seismic data 24
2.2.1 Raw shot record analysis 26
2.2.1.1 Static corrections 26
2.2.1.2 Spectral analysis and frequency filtering 28
2.2.1.3 Near-trace gather 30
2.2.2 Amplitude control: Spherical divergence and AGC 30
2.2.3 Geometry and CMP sorting 31
2.2.4 Velocity analysis and normal moveout (NMO) correction . . . 32
2.2.5 Stacking 37
2.2.6 Migration 38
2.2.7 Deconvolution 44
2.2.7.1 Spiking deconvolution 44
2.2.7.2 Predictive deconvolution 45
2.2.8 Multiple supression 47
2.3 Geological interpretation of 2D marine seismic data 47
2.3.1 Stratigraphy and chronology 48
2.3.2 Structural geology 51

3 Data processing: 2008 eastern Mediterranean Sea survey, western Antalya Basin 56

3.1 Raw shot record analysis . . . 57
3.1.1 Spectral analysis and frequency filtering . . . 57
3.1.2 Near-trace gather . . . 60
3.2 Primary processing: Hand statics and spherical divergence corrections 61
3.2.1 Static corrections . . . 61
3.2.2 Spherical divergence and AGC . . . 62
3.2.3 Results of primary processing . . . 65
3.3 Geometry and CDP sorting . . . 66
3.4 Velocity analysis and NMO correction . . . 67
3.5 Stacking . . . 67
3.6 Migration . . . 71
3.7 Deconvolution . . . 74
3.8 Multiple removal . . . 76
3.9 Processing difficulties . . . 76
3.10 Depth conversion . . . 77
3.11 Final display . . . 78
3.12 Summary . . . 78

4 Stratigraphy and chronology for the western Antalya Basin 80

4.1 Unconformities and seismic units in western Antalya Basin . . . 81
4.1.1 The M- and N- reflectors . . . 81
4.1.2 Seismic units of the western Antalya Basin . . . 83
4.2 Establishing a chrono- and lithostratigraphic framework for the western Antalya Basin . . . 85
4.2.1 Manavgat-2 Well . . . 85
4.2.2 Correlation with seismic data . . . 87
4.2.3 Correlation with surrounding areas . . . 88

4.3 Chronostratigraphic units of the western Antalya Basin 91
4.3.1 Unit 1: Pliocene-Quaternary siliciclastics 91
4.3.2 Unit 2: late-Miocene, Messinian evaporites 92
4.3.3 Unit 3: pre-Messinian Miocene siliciclastics and carbonates . . 94

5 Structural geology of the western Antalya Basin 97

5.1 Interval 1: pre-Messinian Miocene 99
5.1.1 Domain 1A: Arcuate contractional structures 99
5.1.2 Domain 1B: Poorly-imaged contractional zone 105
5.1.3 Domain 1C: Transitional zone 113
5.2 Interval 2: late-Messinian, Miocene 115
5.3 Interval 3: Pliocene-Quaternary 116
5.3.1 Domain 3A: Arcuate superficial extensional fault zone with re-activated (?) Miocene thrusts 116
5.3.2 Domain 3B: Deep-rooted extensional fault zone 123
5.3.3 Domain 3C: Halokinetic and transitional zone 130

6 Discussion 136

6.1 Morphotectonic elements of the Miocene fold-thrust belt 140
6.2 Morpho-tectonic elements of the Pliocene-Quaternary 146
6.2.1 Extensional/transtensional zone in the western Antalya Basin (Domain 3B) 146
6.2.2 Reactivated contractional structures (Domain 3C) 149
6.2.3 Pliocene-Quaternary extensional fault zone (Domain 3A) . . . 152
6.3 Regional synthesis 153

7 Conclusions 162

References **165**

List of Figures

1.1 Simplified tectonic map of the eastern Mediterranean 3

1.2 Simplified map of seismicity in eastern Mediterranean 5

1.3 Physiography of the eastern Mediterranean 6

1.4 Tectonic elements of the eastern Mediterranean Sea 8

1.5 Tectonic elements of the Isparta Angle 10

2.1 Reflection and transmission at a simple two-layer interface 15

2.2 Reflection and transmission in multilayered media 16

2.3 General marine 2D survey setup 18

2.4 Oscillation in source signature asssociated with air guns 19

2.5 Illustration of CMP and CDP non-equivalency 20

2.6 Short and long period multiples 22

2.7 Effect of short- and long- period multiples on seismic record 22

2.8 Typical processing flow for 2D seismic data. 25

2.9 Illustration of 2D marine shot records 27

2.10 Improper sampling rate leads to signal aliasing 29

2.11 Velocity analysis cartoon 34

2.12 Illustration of NMO stretching 35

2.13 Illustration of the stacking process 37

2.14 CMPs and dipping reflectors 39
2.15 Anticlines in stacked section 39
2.16 Synclines in stacked section 40
2.17 Faults in stacked section 40
2.18 Illustration of migration principles 41
2.19 Ilustration of Kirchhoff migration principles 43
2.20 Autocorrelation function and choice of prediction lag and operator length. 46
2.21 Schematic demonstration of reflector terminations used for interpretations 49
2.22 Seismic example of reflector terminations 50
2.23 Minor structures associated with faults 52
2.24 Seismic example from Antalya Basin showing reflector terminations and minor structures 54
2.25 Seismic example from Antalya Basin showing reflector terminations and minor structures 55

3.1 Survey grid for the 2008 seismic reflection survey, western Antalya Basin 58
3.2 Processing flow for the 2008 western Antalya Basin data 59
3.3 Screenshot manipulation for thesis display 60
3.4 Raw shot records from shallow and deep water 61
3.5 Spectral analysis and frequency filtering 62
3.6 Near-trace gather for Line A 63
3.7 Actual arrival time of the direct wave 64
3.8 Shallow and deep water shot gathers with AGC, frequency filtering and primary corrections applied 65
3.9 CDP gathers from shallow and deep water 66
3.10 Velocity analysis in shallow water 68

3.11 Velocity analysis in deep water 69
3.12 NMO-corrected CDP gathers 70
3.13 Stacked CDP gathers 72
3.14 Effects of migration on a stacked section 73
3.15 Deconvolution results 75
3.16 Final display for Line A 79

4.1 Map of the western Antalya Basin 82
4.2 Seismic units of the western Antalya Basin 84
4.3 Lithologies recovered from the Manavgat-2 Exploration Well 86
4.4 Onshore to offshore correlation of Manavgat-2 exploration well with seismic data 89
4.5 Chrono-stratigraphic chart of the greater Antalya Basin area 90
4.6 Thickness of Unit 1 across the western Antalya Basin 93
4.7 Weakly reflective Unit 3 95

5.1 Detailed pre-Messinian Miocene tectonic map of the western Antalya Basin 100
5.2 Index map for Miocene 101
5.3 Industry multi-channel seismic reflection profile showing structural architecture of Domain 1A 103
5.4 Industry multi-channel seismic reflection profile showing structural architecture of Domain 1A 104
5.5 High resolution multichannel seismic reflection profile showing structural architecture of Domain 1A 106
5.6 High resolution multichannel seismic reflection profile showing structural architecture of Domain 1A 107

5.7 High resolution multichannel seismic reflection profile showing the structural architecture of Domains 1B and 1C 109
5.8 High resolution multichannel seismic reflection profile showing the structural architecture of Domains 1B and 1C 110
5.9 High resolution multichannel seismic reflection profile showing the structural architecture of Domain 1B 111
5.10 High resolution multichannel seismic reflection profile showing the structural architecture of Domains 1B and 1C 112
5.11 Detailed Pliocene-Quaternary tectonic map of the western Antalya basin 117
5.12 Index map for the Pliocene-Quaternary 118
5.13 High-resolution multichannel seismic reflection profile showing the structural architecture of Domain 3A 120
5.14 High-resolution multichannel seismic reflection profile showing the structural architecture of Domain 3A 121
5.15 High-resolution multichannel seismic reflection profile showing the structural architecture of Domain 3A 122
5.16 High-resolution multichannel seismic reflection profile showing the structural architecture of Domain 3A 124
5.17 High-resolution multichannel seismic reflection profile showing the structural architecture of Domain 3A 125
5.18 High-resolution multichannel seismic reflection profile showing the structural architecture of Domain 3B 127
5.19 High-resolution multichannel seismic reflection profile showing the structural architecture of Domains 3B and 3C 128
5.20 High-resolution multichannel seismic reflection profile showing the structural architecture of Domains 3B and 3C 129

5.21 High-resolution multichannel seismic reflection profile showing the detailed structural architecture of Domain 3C 131
5.22 High-resolution multichannel seismic reflection profile showing the detailed structural architecture of Domain 3C 132
5.23 High-resolution multichannel seismic reflection profile showing the detailed structural architecture of Domain 3C 134

6.1 Structural map of the western Antalya Basin showing the imbricate crustal-scale fold-thrust belt that characterizes the structural architecture of the region during the Miocene 138
6.2 Structural map of the western Antalya Basin showing the spatial partitioning of strain that characterizes the structural architecture of the region during the Pliocene-Quaternary 139
6.3 Tectonostratigraphic chart summarizing the evolution of the greater Isparta Angle 141
6.4 Tectonic elements of the Isparta Angle 148
6.5 Physiography of the eastern Mediterranean Sea with major structural lineaments 157
6.6 Line diagram illustrating the evolution of the Antalya microblock . . 158

List of Plates

Plate A	Fix map for 2008 MUN-IMST EMED survey, western Antalya Basin
Plate 1	Uninterpreted seismic profile, fixes 1-60, 2008 MUN-IMST survey
Plate 2	Uninterpreted seismic profile, fixes 61-67, 2008 MUN-IMST survey
Plate 3	Uninterpreted seismic profile, fixes 84-106, 2008 MUN-IMST survey
Plate 4	Uninterpreted seismic profile, fixes 107-114, 2008 MUN-IMST survey
Plate 5	Uninterpreted seismic profile, fixes 115-142, 2008 MUN-IMST survey
Plate 6	Uninterpreted seismic profile, fixes 143-149, 2008 MUN-IMST survey
Plate 7	Uninterpreted seismic profile, fixes 150-177, 2008 MUN-IMST survey
Plate 8	Uninterpreted seismic profile, fixes 178-184, 2008 MUN-IMST survey
Plate 9	Uninterpreted seismic profile, fixes 185-211, 2008 MUN-IMST survey
Plate 10	Uninterpreted seismic profile, fixes 212-219, 2008 MUN-IMST survey
Plate 11	Uninterpreted seismic profile, fixes 220-245, 2008 MUN-IMST survey
Plate 12	Uninterpreted seismic profile, fixes 247-253, 2008 MUN-IMST survey
Plate 13	Uninterpreted seismic profile, fixes 254-285, 2008 MUN-IMST survey
Plate 14	Uninterpreted seismic profile, fixes 286-292, 2008 MUN-IMST survey
Plate 15	Uninterpreted seismic profile, fixes 293-320, 2008 MUN-IMST survey

Chapter 1

Introduction

Orogenesis, from the Greek *oros* for mountain and *genesis* for creation, is a fundamental Earth process responsible for creating much of the relief we see on the planet today. Majestic young mountains, such as the Alps and the Rockies, as well as ancient mountains, such as the Appalachians, are products of orogenesis: forming when two plates collide and the continental lithosphere of one plate is thrust over continental lithosphere of the other plate (Moores and Twiss, 1995). Similarly, deep arcuate oceanic trenches observed today adjacent to island arcs and continents are by-products of orogenesis: one oceanic lithospheric plate is forced to plunge beneath the continental or oceanic lithosphere of another plate, depressing the overriding plate edge. This study focusses on the geologically recent evolution of an embyonic orogen: the collision between the African and the Eurasian plates and the squeezing and shuffling of the smaller microplates and fragments. Specifically, this study focuses on the Miocene to Recent tectonic and sedimentary evolution of the the western Antalya basin. In the larger plate tectonic context, this is a forearc basin, north of the boundary between the African plate and the Aegean-Anatolian microplate

where subduction has ceased and continental collision is incipient (Şengör et al., 1985; Dewey et al., 1986). As such, the study area is an excellent modern laboratory for understanding the processes that govern deformation during the early stages of continent-continent collision as this is largely hidden in ancient orogenic belts. During the last 20-25 million years, the forearc experienced profound tectonic changes when former marine basins were uplifted to become nestled in the foothills of the evolving Tauride Mountains, while deep Antalya Basin experienced complementary subsidence and marine sedimentation.

1.1 Present-day tectonic framework of the eastern Mediterranean

The present-day tectonic framework of the eastern Mediterranean is controlled by the continuing collision between the African and Eurasian Plates and the subsequent displacements of the smaller Arabian and Aegean-Anatolian microplates (Şengör et al., 1985; Dewey et al., 1986; Fig. 1.1). The Aegean-Anatolian microplate is escaping westward, accommodated along a number of major crustal-scale transform faults, including the North and East Anatolian Transform Faults. the Ecemiş and Kozan Faults, the Tuzgölü Faults, and the prominent Misis-Kyrenia-Aksu Fault Zone (Işler et al., 2005; Aksu et al., 2005).

In the eastern Mediterranean Sea the convergence zone between the African Plate and the Aegean-Anatolian Microplate is bounded in the west by the Hellenic Arc and the Pliny-Strabo trenches and in the east by the Florence Rise, Cyprus Arc and Tartus Ridge (Şengör and Yılmaz, 1985; Robertson, 1998; Vidal et al., 2000; Hall et al., 2005a,b). The Hellenic Arc includes a series of internally parallel crustal-scale structures such as the Hellenic Trench, a prominent forethrust and an equally

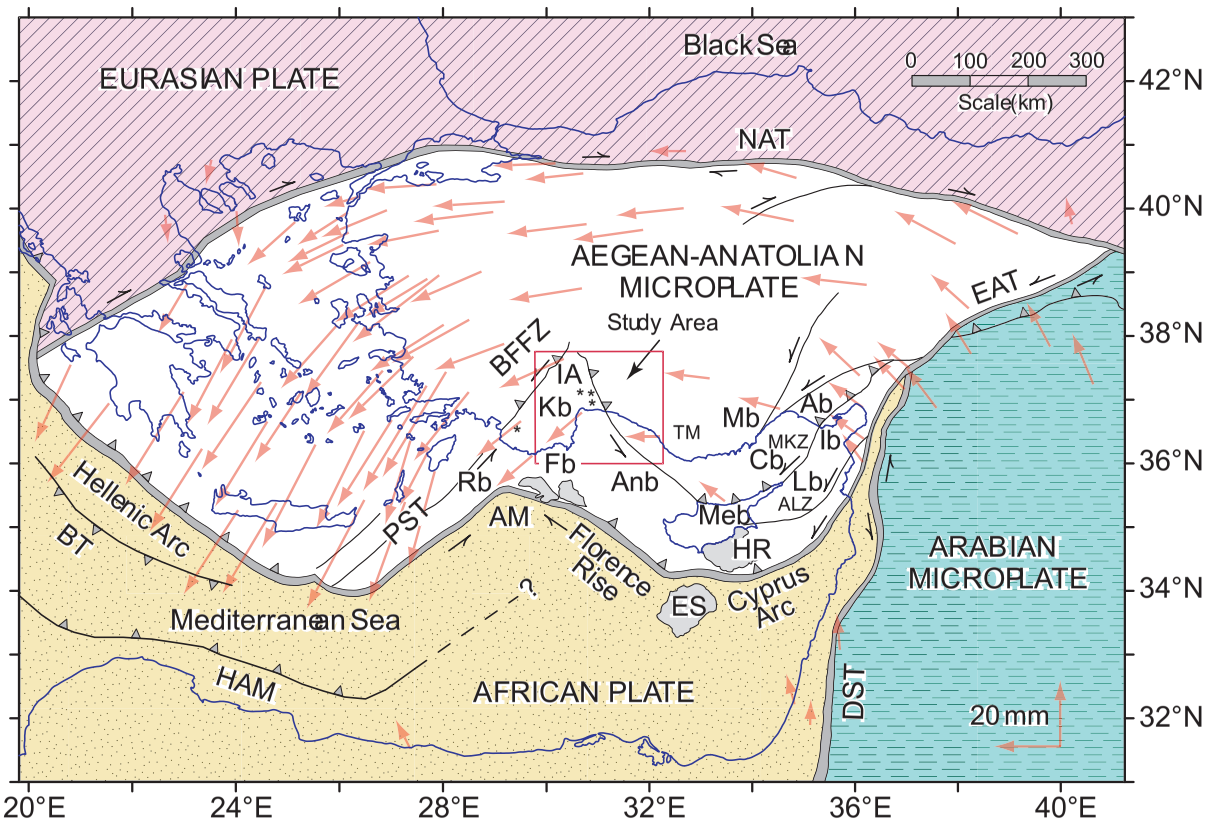

Figure 1.1: Simplified tectonic map of the eastern Mediterranean showing major structural elements; complied from Şengór and Yılmaz (1981), Dewey et al. (1986) and ten Veen et al. (2004) (map is modified from Aksu et al., 2009). Ab= Adana Basin, ALK = Amanos-Lamaka Zone, AM= Anaximander Mountains, Anb = Antalya Basin, BFFZ= Burdur-Fethiye Fault Zone, BT= backthrust, Cb= Cilicia Basin, DST = Dead Sea Transform Fault, EAT = East Anatolian Transform Fault, EF = Ecemiş Fault, ES= Eratosthenes Seamount, Fb= Finike Basin, HAM= Hellenic Arc Margin, forethrust, HR= Hecateus Ridge, IA= Isparta Angle, Ib= Iskenderun Basin, Kb= Kasaba Basin, KF = Kozan Fault, Lb= Latakia Basin, Meb= Mesaoria Basin, Mb= Mut Basin, MKZ = Misis-Kyrenia Zone, NAT = North Anatolian Transform Fault, PST= Pliny-Strabo trenches, Rb= Rhodes Basin, TM = Taurus Mountains, YF = Yumurtalık Fault. Sense of motion is indicated on major faults. GPS vectors from McClusky et al., 2000. * indicates Pliocene-Quaternary volcanism.

important backthrust (Fig. 1.1). Intense earthquake activity, the spatial and depth distribution of the earthquake foci, seismic tomography and the pronounced volcanic arc which developed north of the subduction zone (i.e. the Cyclades) collectively show that the Hellenic Arc is an active subduction zone (Fig. 1.2). While subduction is continuing along the Hellenic Arc, it is generally accepted that subduction has ceased along the Cyprus Arc (e.g. Woodside et al., 2002; Govers and Wortel, 2005). This has resulted in slab roll-back and the subsequent formation of a Subduction-Transform-Edge-Propagator fault zone (or STEP) along the present-day Pliny-Strabo trenches, laterally decoupling the actively subducting and non-subducting lithosphere (Fig. 1.1, Govers and Wortel, 2005).

The deformational zone associated with the convergence of the African Plate and Aegean-Anatolian Microplate extends approximately 300 km northward from the Florence Rise-Cyprus Arc-Tartus Ridge (e.g. Işler et al., 2005; Hall et al., 2005 a,b; Aksu et al., 2005 a,b; Calon et al., 2005 a,b) and contains three prominent south-convex arcuate deformation fronts, from south to north: (i) the Amanos-Lamaka zone, (ii) the Misis-Kyrenia zone, and (iii) the central Taurus Mountains (Fig. 1.1). Hence, the Antalya Basin emerges as an arcuate forearc basin that appears to link with the onland Isparta Angle in the north. Recent work in onland southwest Turkey further demonstrated the morpho-tectonic linkage between this region and the Isparta Angle and the westernmost Antalya Basin (van Hinsbergen et al., 2007).

1.2 Bathymetry of the eastern Mediterranean Sea

The bathymetry and topography of the eastern Mediterranean region (Fig. 1.3) are controlled by large-scale tectonic features: offshore, these include the Anaximander Mountains, the Florence Rise, the Misis-Kyrenia-Aksu zone, and the Cyprus

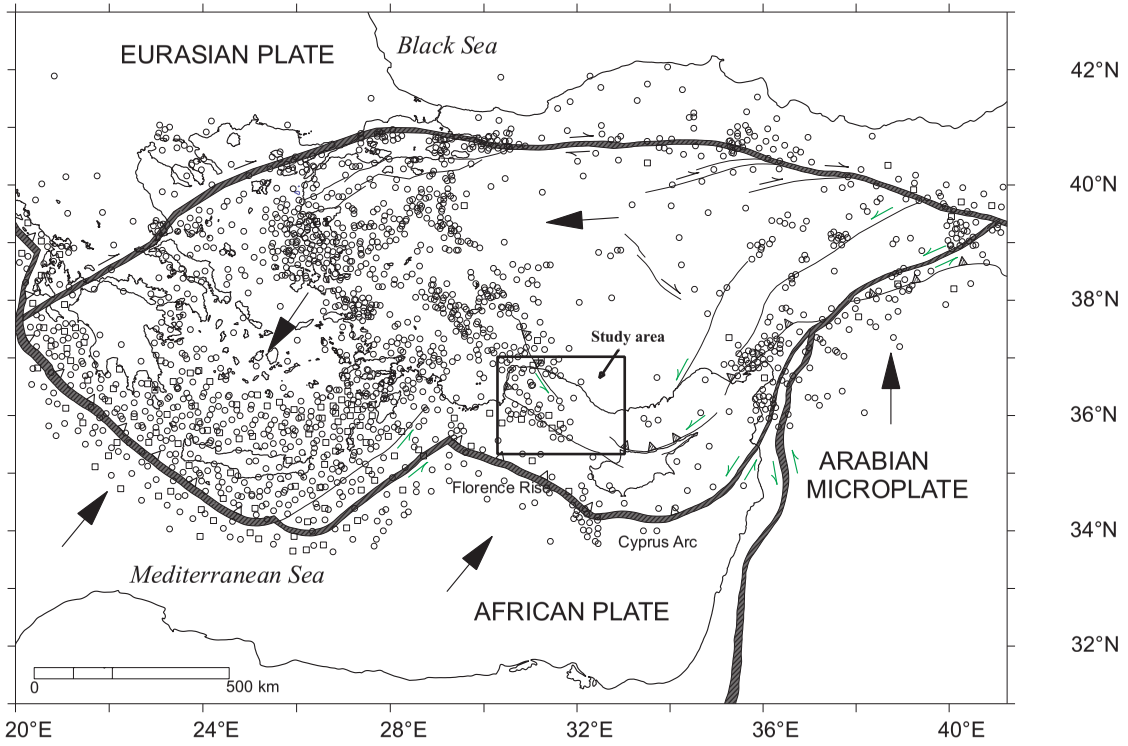

Figure 1.2: Seismicity map of the eastern Mediterranean region showing the distribution of earthquake epicentres with magnitude >4, compiled using data from Kandilli Observatory Earthquake Research Institute, and International Bathymetric Chart of the Mediterranean- Seismicity-IBCM-S. Focal depths <50 km and >50 km are represented by unfilled circles and unfilled squares, respectively. Large arrows show plate motion relative to fixed Eurasian Plate. Subduction zones are shown by double lines with filled triangles positioned on the overriding plate. Major thrust faults are shown by single lines with hatched triangles on the hanging wall. Strike-slip faults are displayed by half arrows showing the directions of relative displacement.

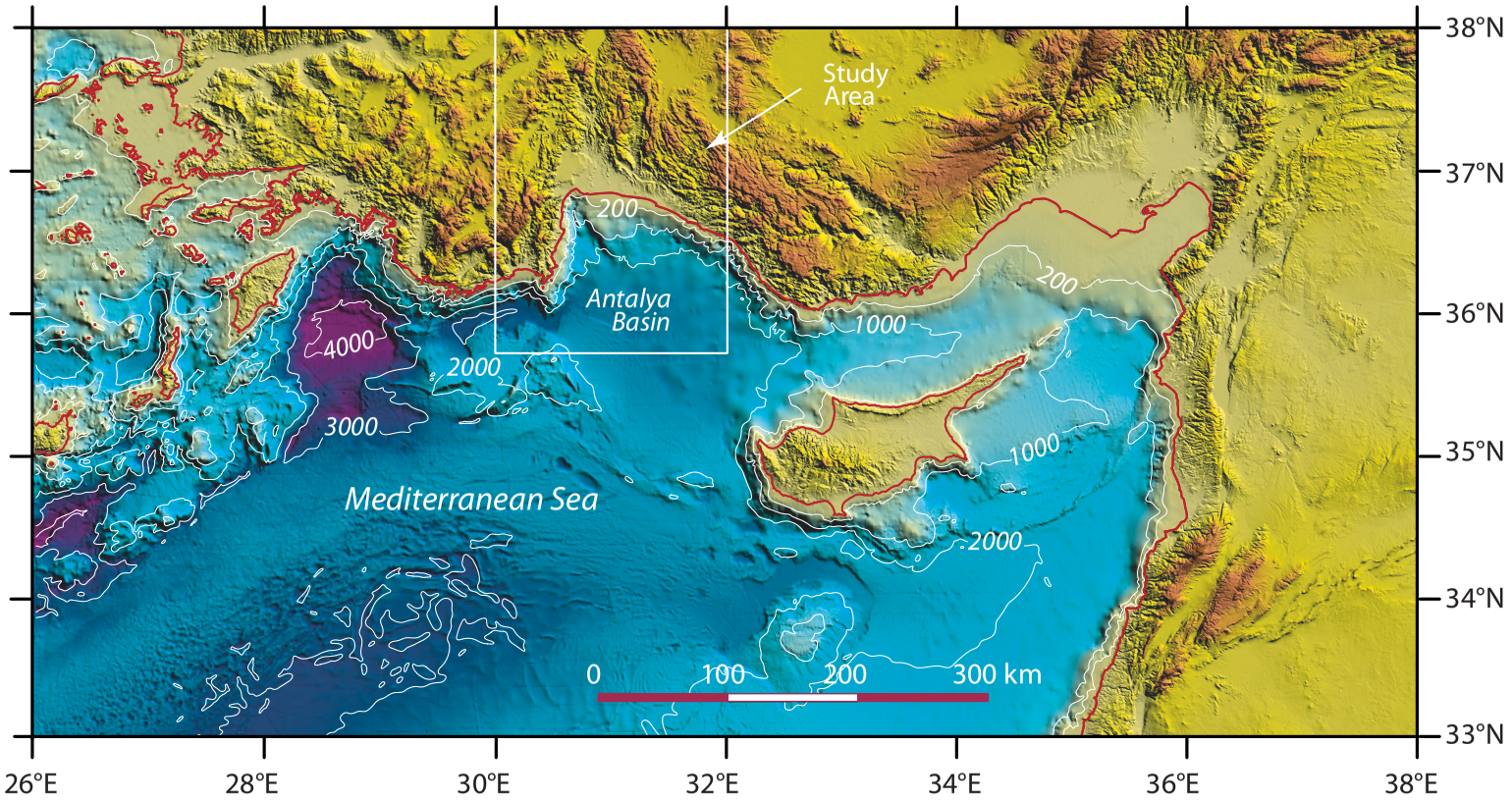

Figure 1.3: Physiography of the eastern Mediterranean showing the Antalya Basin and its relationship with the major tectonic elements in the region. The topography and bathymetry are compiled from GeoMapApp (Ryan et al., 2009), the coastline and the selected isobaths contours are from the International Oceanographic Commission (1981).

Arc; and onshore, these include the Isparta Angle, the Taurus Mountains, Kyrenia Range. The development of these structures is associated with the ongoing collision between the larger African and Eurasian plates and the squeezing and shuffling of the smaller Aegean-Anatolian and Arabian microplates, as well as continental fragments, such as the Hecataeus Ridge, Eratosthenes Seamounts and possibly the Anaximander Mountains (Fig. 1.4). The Antalya Basin is an L-shaped basin in the eastern Mediterranean with a very narrow continental shelf (2 to 6 km) and has a shelf-slope break at approximately 100-150 m depth. Steep continental slopes lead to the continental rise and abyssal plain. No multibeam data has been collected in the Antalya Basin, but the available bathymetric maps with 200 m isobaths show that the slope face is dissected by numerous submarine canyons, presumably feeding submarine fans, similar to those seen in continental slopes around the western Mediterranean (e.g., Droz et al., 2001; Lastras et al., 2002). The continental rise occurs between 1800 and 2000 m water depth, where the slope gradient decreases considerably (Fig. 1.3); the abyssal plain occurs at approximately 2400 m water depth. In the deepest part of Antalya Basin, at approximately 2600 m water depth, a quasi-circular depression is observed near the center of the basin.

1.3 Marine Miocene basins in the eastern Mediterranean and the Isparta Angle

The evolution of the Miocene basins in the eastern Mediterranean is controlled by the development of a large, broadly E-W-trending foredeep in front of the Tauride fold-thrust belt (Williams et al., 1995). The Tauride culmination was characterised by an arcuate thrust front that delineated a broad syntaxis, comprising several smaller thrust culminations which developed in the foredeep itself. The major thrust that

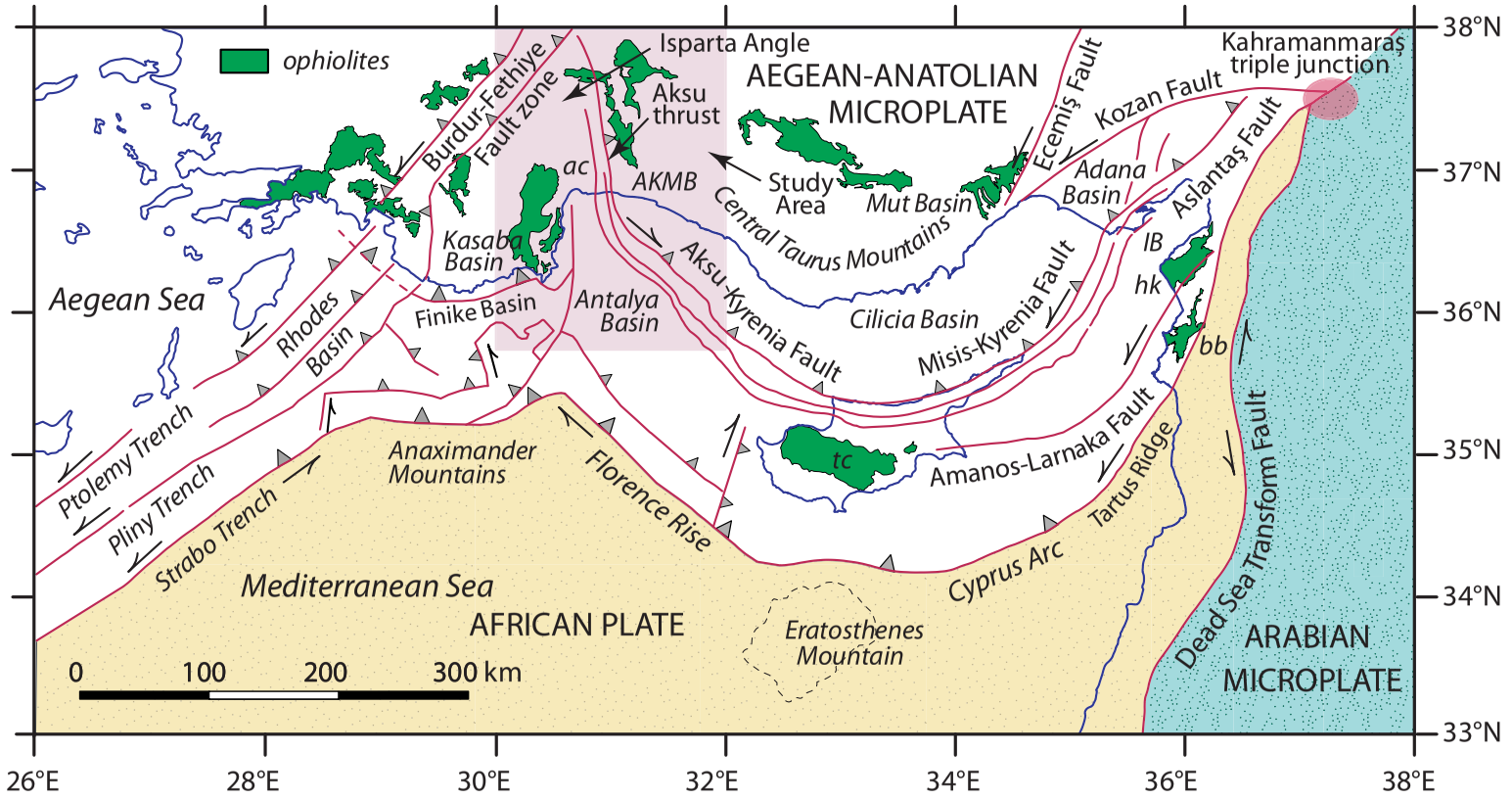

Figure 1.4: Simplified plate tectonic map of the eastern Mediterranean Sea and surrounding regions, showing major plate/microplate boundaries, ophiolitic and associated rocks (green fill: ac= Antalya complex, bb= Baér-Bassit complex, hk= Hatay and Kizildag complexes, tc= Troodos complex) and major tectonic elements. AKMB= Aksu, Köprüçay, Manavgat Basins, IB= Iskenderun Basin. Half arrows indicate transform/strike-slip faults.

defines the base of the present-day continental slope in the study area is likely the leading thrust, whereas the trailing thrust panels are located well onshore within the eastern limb of the Isparta Angle. There are remarkably similar marine Aquitanian-Tortonian successions in the now-onland Mut and Adana basins (Safak et al., 2005; Eris et al., 2005), Aksu, Köprüçay and Manavgat basins (Poisson et al., 2003a,b, Karabiyikoglu et al., 2005, Deynoux et al., 2005) and the Mesaoria Basin of central Cyprus (Robertson and Woodcock, 1986)(Locations shown in Fig. 1.4). Depositional similarities continue into the fold-thrust panels of the Misis Mountains (Gökçen et al., 1988) and the Kyrenia Range (Calon et al., 2005a,b), the Aksu Thrust (Poisson et al., 2003a,b), as well as the marine Cilicia, Iskenderun, Antalya and Finike basins (Uffenorde et al., 1990, Aksu et al., 2005a,b, 2009, Işler et al., 2005) (Locations shown in Fig. 1.4). These strong regional depositional similarities suggest the seemingly isolated basins in the eastern Mediterranean were once a single large basin in the Early Miocene. This large ancestral foredeep basin likely extended toward the east into the Karsanti and Maras Basins (Hall et al., 2005a, Calon et al. 2005a; Satur et al., 2005, Ilgar and Nemec, 2005) and toward the west into the Antalya and Kasaba Basins (Isler et al., 2005, Çiner et al., 2008). The development of northern and southern crustal-scale thrust culminations, together with onset of escape tectonics associated with the final collision of the Arabian and Aegean-Anatolian microplates in the latest Miocene and Pliocene-Quaternary (Şengör et al., 1985) basicaly split the foredeep into several large piggy-back basins: the Iskenderun-Latakia-Mesaoria basin complex, the Mut-Adana-Cilicia basin complex, and the Cyprus, Antalya, Finike and Rhodes basins (e.g., Hall et al., 2005a, 2009; Calon et al., 2005a; Aksu et al., 2009).

The Isparta Angle is a north-convex region located in onland western Turkey with limbs defined by two branches of the Alpine orogenic belt: a southwest-northeast trending western limb and a southeast-northwest trending eastern limb. The Bey-

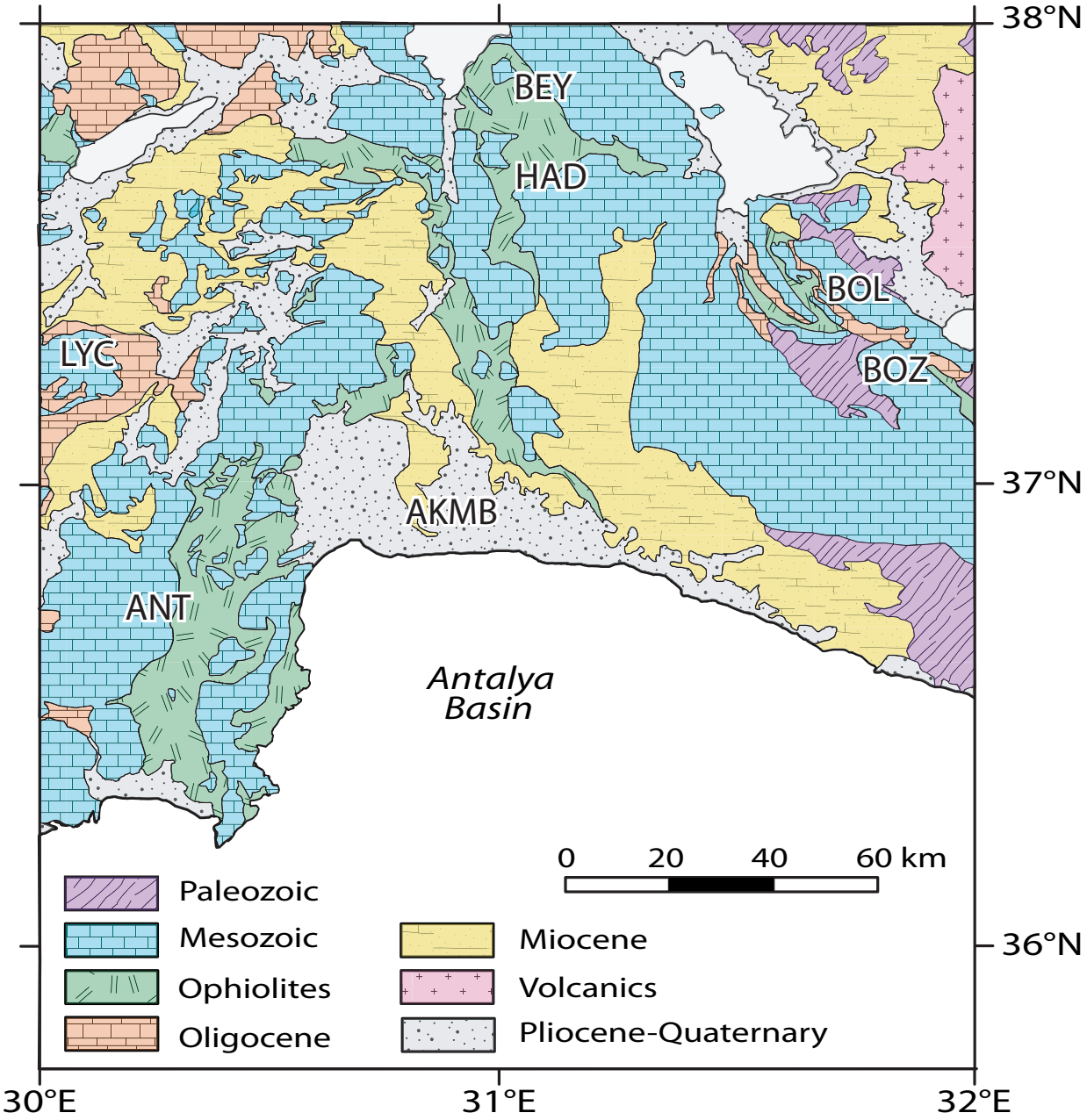

Figure 1.5: Simplified Geological map of the Western Taurus Mountains (simplified and redrawn from Blumenthal, 1963b). AKMB= Aksu, Köprüçay, Manavgat basins, ANT= Antalya complex, BEY= Beyşehir nappes, BOL= Bolkar nappes, BOZ= Bozkir nappes, LYC= Lycian nappes. Note that labels show approximate locations only.

dağları Platform, consisting of predominantly Jurassic to Miocene carbonates (Poisson, 1977), and the Anamas-Akseki Platform, consisting of Cambrian to Eocene carbonates (Dumont, 1976; Özgül, 1984; Monod, 1977), form the two main basement units of the Isparta Angle in the west and east, respectively (Waldron, 1984; Robertson and Woodcock, 1986; Dilek and Rowland, 1993).

The Isparta Angle was developed as the result of the Tertiary closure of the Pamphylian Basin which originally separated the Beydağları and the western Taurus platforms during the Mesozoic (Waldron, 1984; Poisson et al., 2003). It is bounded by the Lycian Nappes in the west and the Beyşehir, Hoyran and Hadim Nappes in the east (Monod, 1997). The Burder-Fetiye Fault zone, which transects the Lycian Nappes, is characterized by sinistral strike-slip faults with a considerable normal dip-slip component (Şaroğlu et al., 1987; Price and Scott, 1994; Barka et al., 1997). During the Late Miocene, the Isparta Angle underwent a compressional phase known as the Aksu Phase, with its western limb rotating 30° counterclockwise during the Miocene (Kissel and Poisson, 1987; Morris and Robertson, 1993) and its eastern limb rotating 40° clockwise since the Eocene (Kissel et al., 1990). Seismic reflection profiles and borehole data further document that the Tortonian (and older) successions are involved in the fold-thrust panels (see Chapters 4-6), suggesting that the Isparta Angle continued to evolve at least into the latest Miocene. This has significant impact on the study area and is further discussed in detail in Chapter 6.

1.4 Thesis objectives

The main focus of this thesis is the interpretation of high-resolution multichannel seismic reflection profiles from the western Antalya Basin acquired during three Memorial University of Newfoundland research cruises in 1992, 2001, and 2008 from

the Antalya Basin region of the eastern Mediterranean, and complemented by industry seismic reflection profiles. A secondary, but important, focus of this thesis is the processing of the multichannel seismic reflection profiles collected from the western Antalya Basin in 2008: these profiles provide denser grid spacing in the study area to assist in the interpretation of the complex western boundary of the Antalya Basin. The primary scientific objectives of this dissertation are:

- to establish a seismic stratigraphic framework for the Miocene to Recent successions observed in the seismic reflection profiles and establish a chronostratigraphy for these successions using correlations with the litho- and bio-stratigraphic data from an exploration well from the onland Manavgat Basin;

- to delineate and map the structural elements affecting the seismic stratigraphic units and to determine the age of deformation using the the growth-stratal architecture and progressive syn-tectonic unconformities observed in the seismic reflection profiiles;

- to relate the large-scale tectonic elements mapped within the marine Antalya basin with their counterparts in the Isparta Angle, and Beydağları and Antalya Complex regions of southwestern Turkey, as well as the Kyrenia Mountains of northern Cyprus and the Anaximander Mountains;

- to develop a tectonic and kinematic model for the Miocene to Recent structures of the western Antalya Basin that explains the evolution of the region within the context of the greater eastern Mediterranean.

Chapter 2

Methods: Acquisition, Processing and Interpretation of 2D Marine Seismic Data

In the seismic reflection method, elastic waves penetrate the earth and relay important stratigraphic and structural information back to the surface (Yilmaz, 2001). The resulting data is processed to fine-tune an image of the true subsurface geology and facilitate its stratigraphic and structural interpretation. This chapter contains a full discussion on data acquisition, commenting on both the general theory and also the specific survey parameters for the data processed for this thesis. The general concepts involved with data processing and interpretation are discussed in this chapter, but application of these concepts to thesis data is reserved for future chapters.

2.1 Acquisition of 2D marine seismic data

2.1.1 Basic theory of reflection seismology

Elastic waves can be subdivided into body waves and surface waves. Surface waves, such as Rayleigh waves, Stonely waves, Love waves and Tube waves, have applications in exploration seismology, but are beyond the scope of this thesis. Body waves include P-waves and S-waves: P-waves are longitudinal, propagating through both fluids and solids; S-waves are transverse, traveling only through solids. Discussion for this thesis will pertain mostly to P-waves, with mention of S-waves where necessary.

In three dimensions, an elastic wave travels as a spreading spherical front though an isotropic, homogeneous medium. In layered media, when the wave encounters a boundary separating two layers with differing elastic properties, part of the wave will be transmitted into the second layer and part of the wave will be reflected at the interface. The amplitude and polarity of the reflected energy is directly related to the elastic impedance contrast across the interface (Yilmaz, 2001).

Elastic impedance, Z, is an intrinsic property of a material which essentially measures its resistance to penetration by elastic waves. It is defined as the product of a material's elastic velocity,v, and its density, ρ:

$$Z = \rho v. \tag{2.1}$$

Moving from three dimensions to two dimensions (still in a homogenous, isotropic medium), the spreading front of an elastic P-wave becomes circular and can be approximated as raypaths. Consider the simple 2-layer interface shown in Figure 2.1. The Law of Reflection states that the incident ray is reflected at the same angle as it was incident on the interface, or:

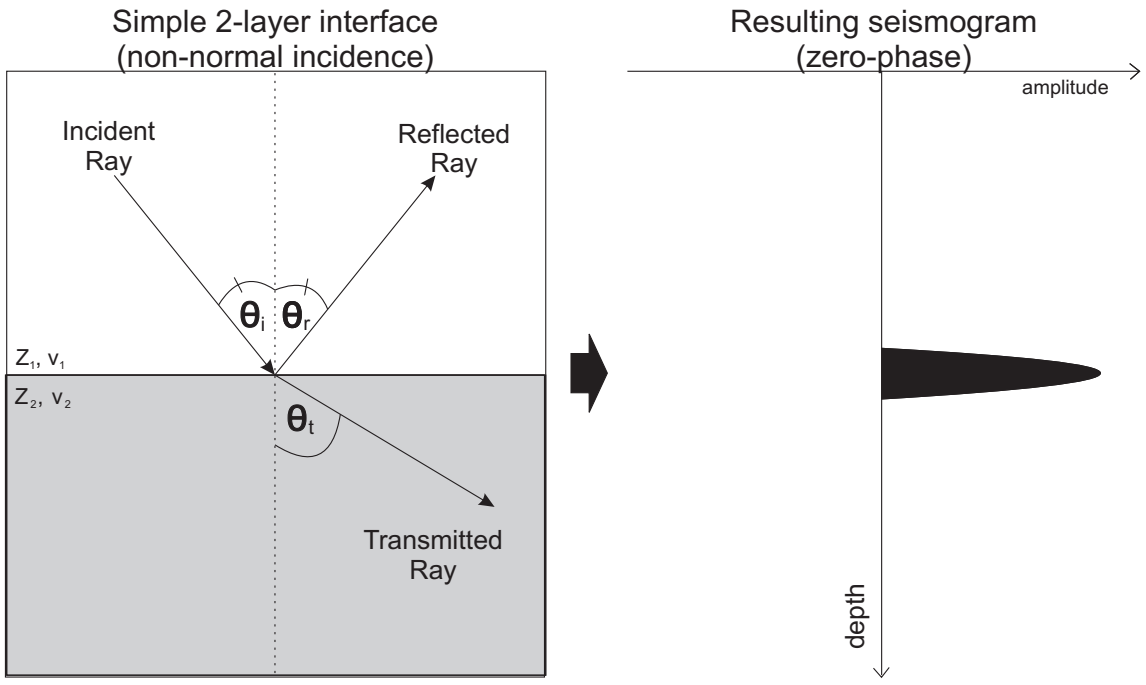

Figure 2.1: Reflection and transmission at a simple two-layer interface (Note: $Z_1 < Z_2$, $v_1 < v_2$). (a) The incident ray makes contact with the boundary t an angle θ_i. The reflected ray is reflected at $\theta_r = \theta_i$ back into layer 1 and the transmitted ray is refracted at angle θ_t into layer 2. (b) The resulting seismogram showing response with maximum amplitude at the boundary (zero-phase, simple wavelet).

$$\theta_i \;=\; \theta_r \tag{2.2}$$

where θ_i is the angle of of the incident ray and θ_r is the angle of the reflected ray. The remaining wave energy is transmitted, or refracted, into the second layer according to Snell's Law:

$$\frac{\sin\theta_i}{v_i} \;=\; \frac{\sin\theta_t}{v_2} \tag{2.3}$$

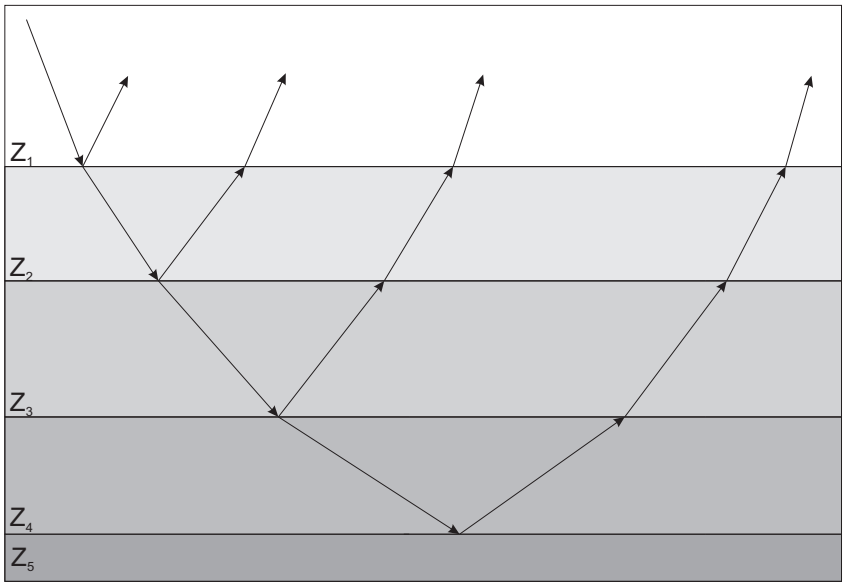

Figure 2.2: Reflection and transmission in multi-layered media, Z1<Z2<Z3<Z4<Z5. Note: for simplicity, wave-conversion at the boundaries is not taken into account.

where θ_t is the angle of the transmitted ray, v_1 is the velocity of the first layer and v_2 is the velocity of the second layer. As layering increases (e.g. Fig. 2.2), reflection and refraction continue at each interface allowing imaging of all layers.

The strength of a reflection can be measured by the reflection coefficient, R, and is dependent on both the angle of incidence and the impedance of the two layers. At normal incidence,

$$R \;=\; \frac{|Z_2 \;-\; Z_1|}{Z_2 + Z_1}\;, \tag{2.4}$$

which implies

$$R \;\alpha\; |Z_2 \;-\; Z_1|\,. \tag{2.5}$$

Therefore, high elastic impedance contrasts generate stronger reflections.

In practice, impedance contrasts strong enough to generate reflections imaging seismic profiles usually arise from geologically significant interfaces such as: (1) sedimentary reflectors (e.g. bedding planes); (2) non-sedimentary reflectors (e.g. fault planes, pore fluid contacts, mineral phase changes, etc.); and (3) unconformities; however, seismic records may also show events which are artifacts such as multiples, diffractions, or returns from out-of-plane geology. Special care must be taken to ensure these artifacts are not interpreted as geology.

2.1.1.1 Reflection seismology in the field

Implementation of the seismic reflection method in the field requires instrumentation including: source(s) (dynamite, vibroseis, air guns, etc.) to generate the elastic waves; receiver(s) (e.g. geophones, hydrophones, obs) to intercept the incoming reflections; and recorder(s) (e.g. seismographs) to record the information in a useable format. Typical setups for 2D marine seismic surveys are discussed below.

2.1.2 2D marine seismic surveys

In a conventional 2D marine seismic reflection survey, one ship tows the source and receivers behind it at constant speed (e.g. Fig. 2.3). Maintaining relatively constant speed is important for maintaining survey parameters.

The typical source used today on marine seismic vessels is the air gun. An air gun works by controlling the movement of high-pressure air through its chambers to send a large burst of pressured air into the water. Source signatures for single air guns are oscillatory (e.g. Fig. 2.4a) and can generate significant late bubble pulses (discussed later). To minimize this effect, air guns of varying sizes are often mounted in arrays with each gun contributing to the overall source signature (e.g. Fig. 2.4b). Pressure in the air gun is maintained by on-board compressors and shots are fired at fixed

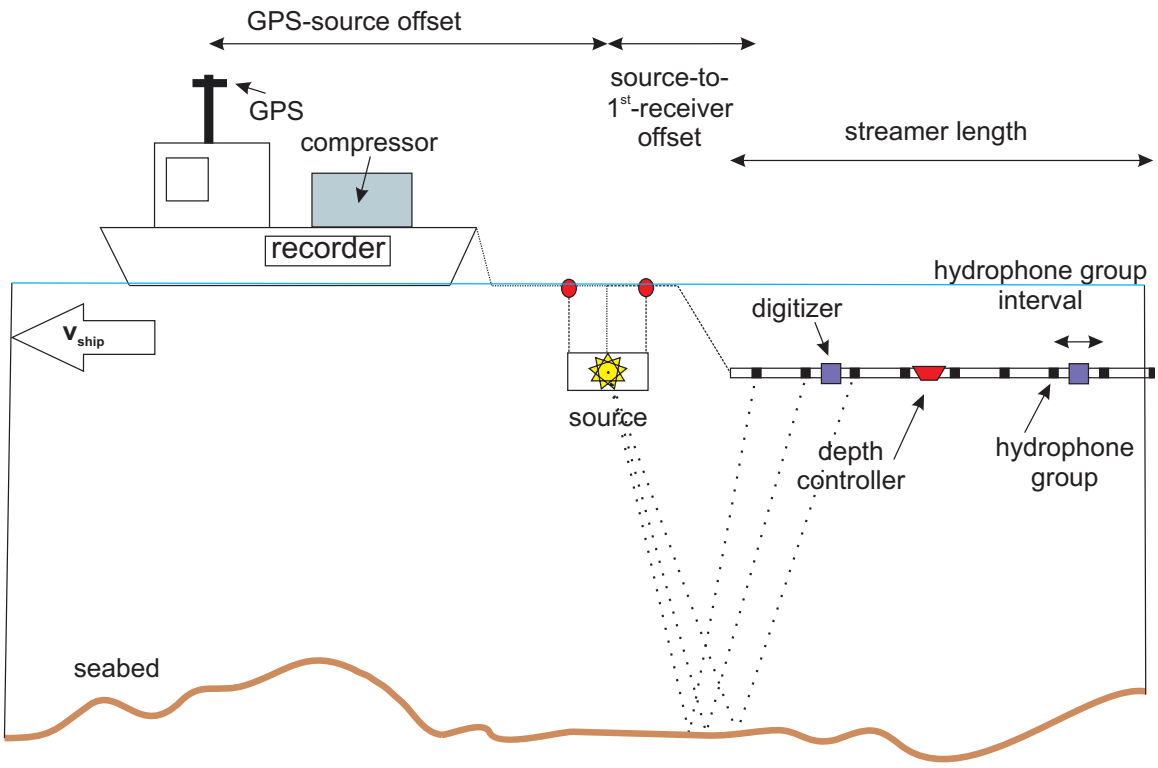

Figure 2.3: General marine 2D survey setup.

intervals. The distance between successive shots is called the shot interval. Seismic vessels require reliable navigation, such as GPS, to accurately map the location of each shot fired.

Receivers consist of hydrophone groups which are uniformly spaced at the group interval and embedded onto long streamers. Since S-waves do not travel through fluids, conventional hydrophones will only receive P-waves. Digitizers, located near the hydrophones, convert the analog signal to digital form at a set sampling interval, the sample rate, and relay the digital signal back to ship via fiber optic cables. Depth controllers can be used to maintain the streamer at a constant depth to minimize noise from near-surface turbulence.

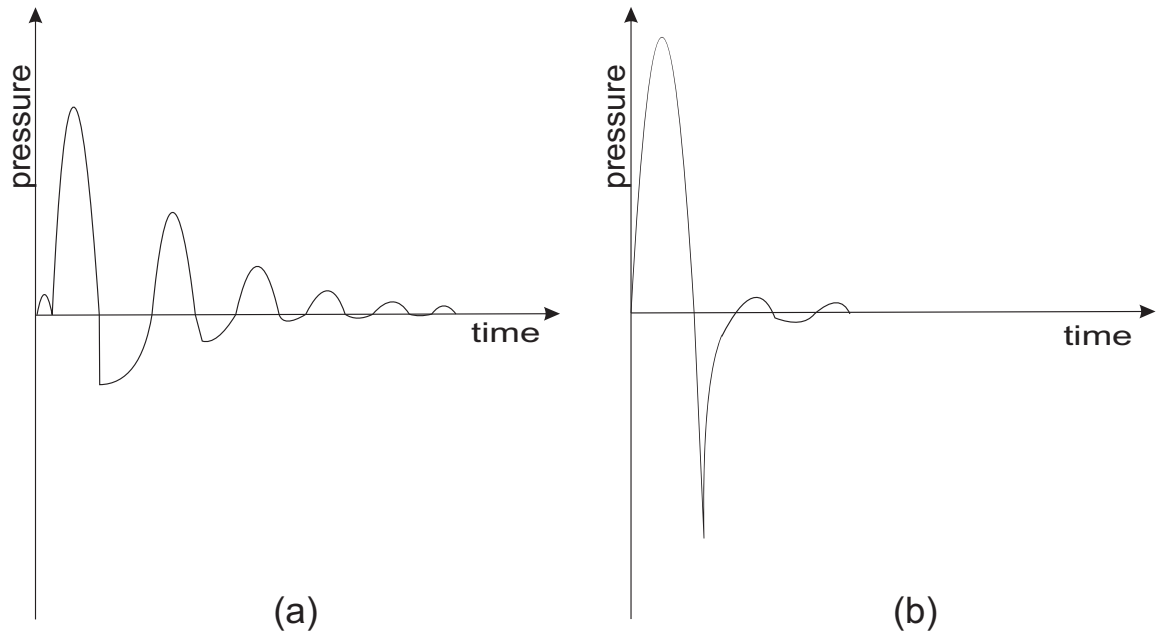

Figure 2.4: Cartoon illustrating source signatures associated with air guns. (a) A single air gun generates an oscillatory pulse. (b) An air gun array suppresses much of the oscillatory signature and better approximates a minimum phase wavelet.

Seismographs are located on-board and record the incoming digital signals on a separate channel for each hydrophone group. The data are monitored for quality and possible problems with the streamer and/or guns.

2.1.2.1 CDPs, CMPs, and seismic data fold

The sampling frequency of any one point on the seabed is directly related to survey geometry. The term *fold* is used to describe the maximum number of times one location is imaged by any of the hydrophone groups and is defined as:

$$\text{fold} = \frac{1}{2} \times (\text{number of channels}) \times \frac{\text{group interval}}{\text{shot interval}}. \tag{2.6}$$

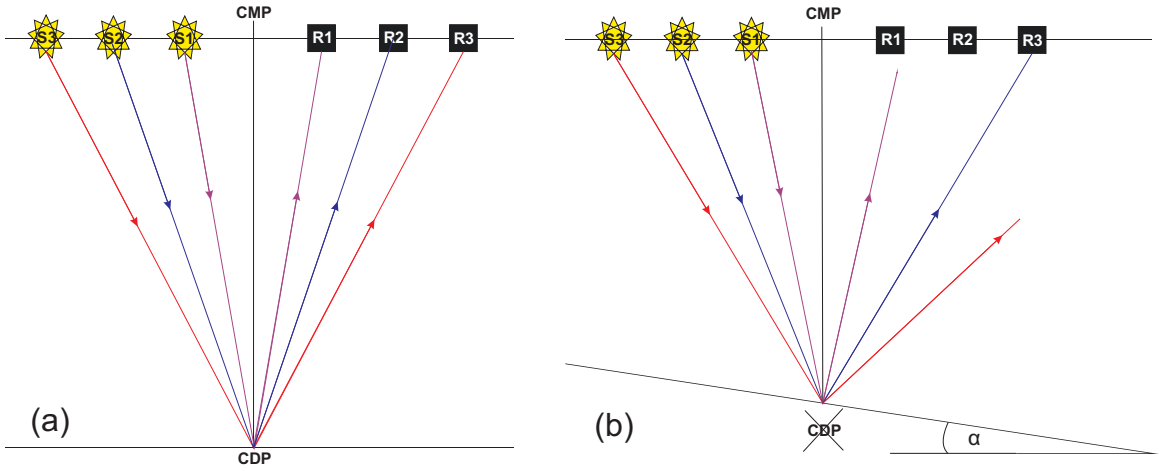

Figure 2.5: Illustration of CMP and CDP non-equivalency.

A higher fold results in higher sampling of subsurface points and improves the quality of the final image.

The point on the subsurface that has been sampled several times by different source-receiver pairs is called a common midpoint (or CMP). Spacing of the CMPs, assuming horizontal reflectors, is calculated by:

$$\text{CMP spacing} = \frac{1}{2}\,(\text{group interval}). \tag{2.7}$$

Note that when the subsurface reflectors are not horizontal, CMPs are not equivalent to common depth points (or CDPs; Fig. 2.5). The assumption of CMP and CDP equivalency in the CMP sorting process creates artifacts on the seismic record and requires an extra processing step to restore true subsurface locations of dipping reflectors (i.e. migration, discussed later).

2.1.2.2 Some issues associated with 2D marine surveys

- *Bubble pulses:* After the shot is fired, the gas bubble emitted by the source begins to rise to the surface. Pressure differences during ascent cause quasi-periodic collapse and expansion of the bubble. These oscillatory pulses, or

bubble pulses, can act as secondary sources generating superimposed profiles on the seismic section and obstruct primary reflections. If not properly identified, these bubble pulses can result in misinterpretation of subsurface geology. Occurrence of bubble pulses can be minimized by using air gun arrays in lieu of singular sources and/or placing the source close to the surface so that the air bubble escapes into the atmosphere before it begins to oscillate (Sheriff, 1995).

- *Near-sea-surface turbulence:* At the sea-surface and for a few meters below it, much turbulence is generated by both natural (e.g. waves) and mechanical (e.g. ships) disturbances. When recording marine seismic data, it is important to ensure the streamer is located below this zone of turbulence so that this noise is minimized.

- *Out-of-plane reflectors:* In areas of complicated geology, sometimes energy from nearby structures (which are not in the plane of the survey line) is recorded on the seismogram. This energy can be prominent and continuous enough to mimic an in-plane reflector and distort the real subsurface cross-section (examples shown in later chapters).

- *Multiples:* A multiple is an event on the seismic record that has been reflected more than once (Sheriff,1995). To be recognized as a distinct event on a profile, the multiple usually originates from a strong reflector with a large impedance contrast (Sheriff, 1995). Because the waves involved are reflected more than once and lose energy at each interface, multiples usually have lower amplitudes than primary reflections; exceptions to this are ghost reflections and water column reverberations. There are two types of multiples which we distinguish based on their travel paths in relation to the travel paths of the primary reflectors: short-period multiples and long-period multiples (e.g. Fig. 2.6).

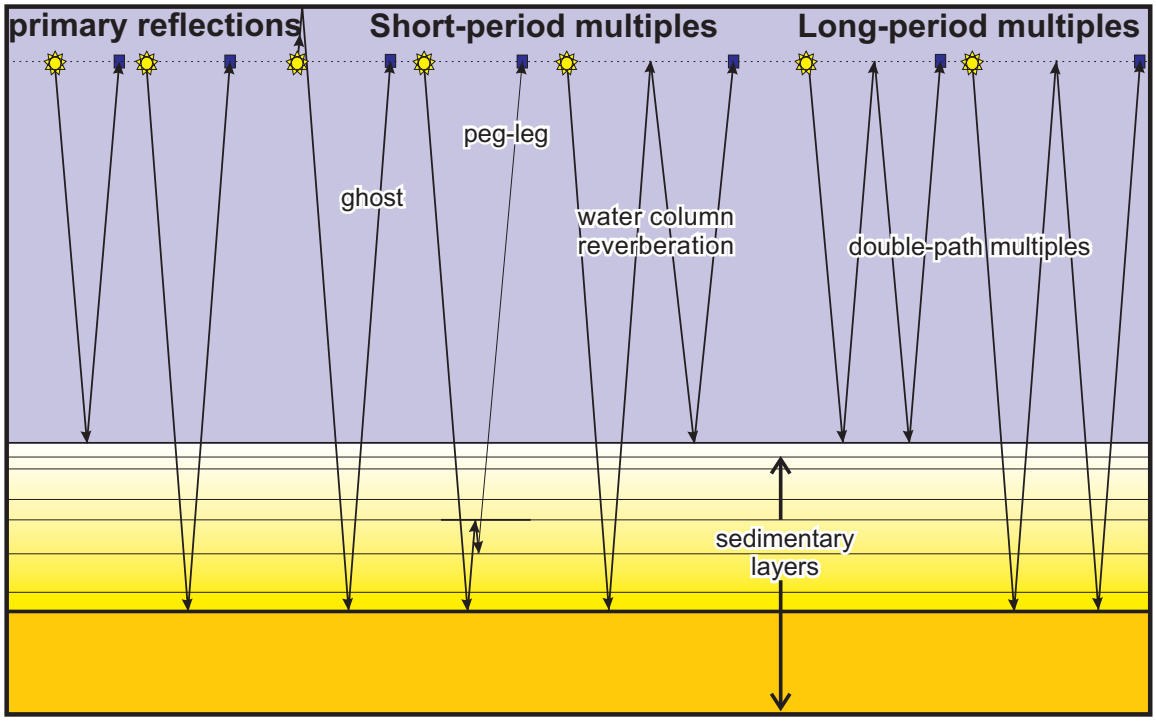

Figure 2.6: Cartoon illustrating various short- and long-period multiples generated during a 2D marine survey. Note that arrival time of multiples can be affected by water depth. For example, in deep water (as shown in this figure), the seabed multiples arrive much later than the primary arrivals making them relatively easy to distinguish. However, in shallower water, seabed multiples arrive soon after the primaries and can obscure interpretations.

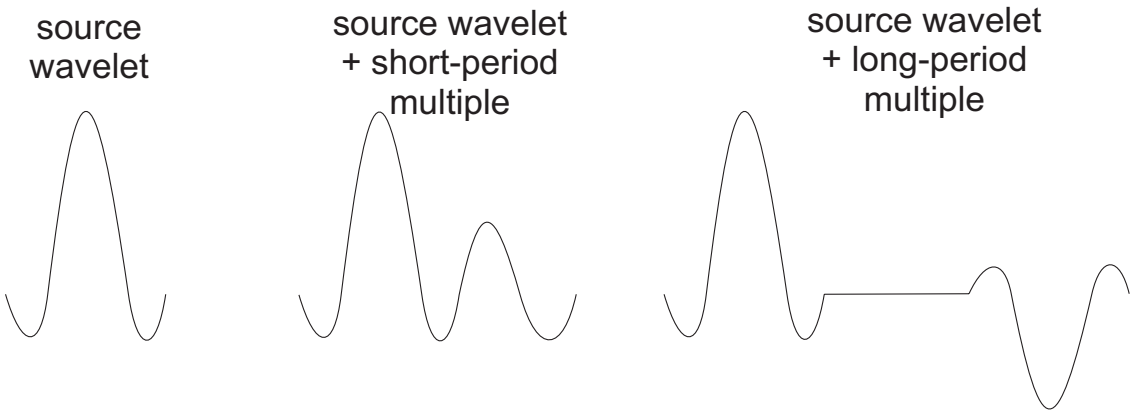

Figure 2.7: Effect of short- and long- period multiples on the seismic record. Short-period multiples essentially lengthen the wavelet while long-period multiples arrive as distinct events.

Short-period multiples

Short-period multiples have travel paths which are similar to the travel paths of primary reflections and thus arrive shortly after the primary energy. This type of multiple effectively lengthens the wavelet (e.g. Fig. 2.7) and causes ringing on the seismic record. Ghosts, so-called peg-leg multiples and water column reverberation (except for seabed multiple) are examples of short-period multiples (e.g. Fig. 2.6). If not properly identified, short-period multiples can be mistaken for primary energy, causing misinterpretation of the subsurface geology.

Long-period multiples

In contrast with short-period multiples, long-period multiples have travel paths which are sufficiently longer than those of the primary reflectors and arrive later on the seismic record as distinct events (e.g. Fig. 2.7). Double-path multiples (including the seabed multiple) are good examples of long-period multiples (e.g. Fig. 2.6). Long-period multiples can obstruct the image of primary reflectors (especially in shallow water) and should be removed where possible.

2.1.3 Survey parameters and geometry of the 2008 eastern Mediterranean cruise

The data processed for this thesis was acquired by the collaboration of Memorial University of Newfoundland (MUN), Canada, and Dokuz Eylül University (DEU), Turkey, during a 30-day cruise in the summer of 2008 on the DEU's RV Koca Piri Reis.

The seismic source for the 2008 cruise was a broad-band, high-frequency sleeve-gun array (MUN). The array consisted of seven sleeve-guns of differing volumes to yield a combined volume of 200-in^3: two 10-in^3 guns; one 20-in^3 gun; two 40-in^3 guns; and one 80-in^3 gun emulated by two 40-in^3. The combination of a 96-channel, 600 m Hydroscience Technologies Inc. streamer and 96-channel seismograph (DEU) recorded incoming reflections to 7000 ms two-way travel time (TWT) at a sample rate of 2 ms. Hydrophone arrays were arranged in group intervals of 6.25 m with shots fired every 10 s (an approximate distance of 25 m assuming a ship speed of $\sim$ 5 knots). From Eq. 2.6, we calculate the fold of this data to be 12; therefore each subsurface point has been sampled a maximum of 12 times. Source-to-first-receiver offset was 77 m. Digicourse streamer depth controllers were used to maintain constant streamer depth of approximately 3 m.

2.2 Processing 2D marine seismic data

Data processing is inherently iterative, with the success of future processes depending on the success of earlier processes. It is the goal of data processing to maximize signal-to-noise (S/N) ratio so that a readily interpretable image of the subsurface geology may be obtained. Noise, in the context of this thesis, is any energy other than the signal arising from primary reflectors in the subsurface. Noise can be random or coherent and each type distorts the image in a different way. Random noise, such as noise arising from recording equipment, stormy weather or scattering, distorts the overall image in an apparently random way; the effect of random noise on one trace cannot be predicted by observing the random noise on an adjacent trace. Coherent noise, on the other hand, like noise arising from sea-bed multiples or direct waves, can appear as reflections on seismic profiles.

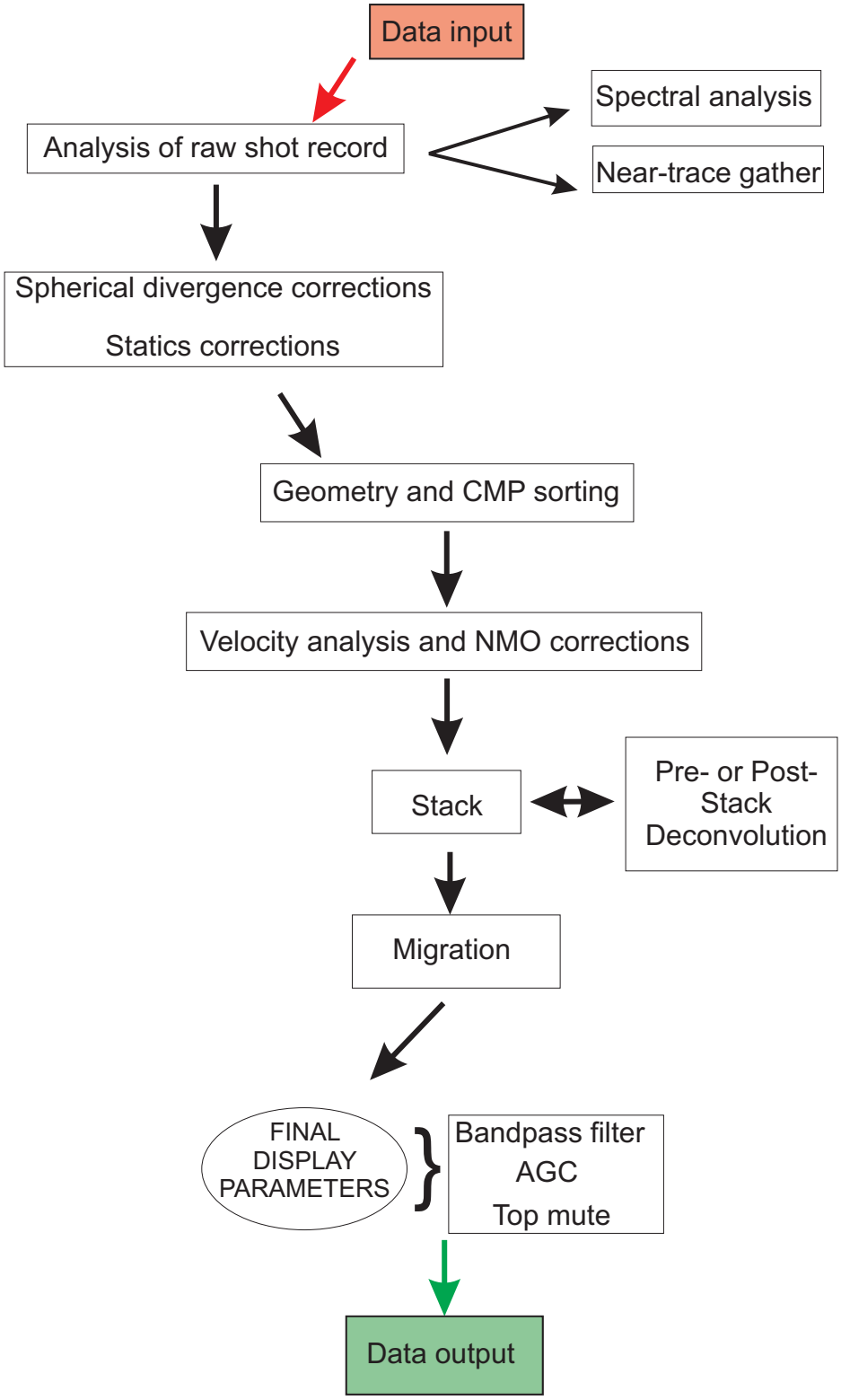

Figure 2.8: Typical processing flow for 2D seismic data.

A typical processing flow is shown in Fig. 2.8. Optimal processing parameters producing the best image are obtained through trial and error. Discussion within this chapter focuses on data processing in the most general sense. A detailed account of the author's specific processing flow can be found in Chapter 3.

2.2.1 Raw shot record analysis

A shot record contains the data recorded on all available channels following a single shot (e.g. Fig. 2.9). A typical shot record will contain both signal (i.e. hyperbolic primary reflections) and noise (e.g. linear direct wave, noisy traces, refractions, low-frequency noise from equipment, multiples, etc.).

2.2.1.1 Static corrections

The direct wave should arrive at the first receiver at t_1 where:

$$t_1 \; = \; \frac{x_1}{v_w} \tag{2.8}$$

and x_1 is the offset of the first receiver and v_w is the water velocity ($\sim$ 1500 m/s). The actual arrival time, t', can be checked on the raw shot gather (Fig. 2.9). If $t_1 \neq t'$, there is a static delay in the data inherent to the experimental setup. Each trace must be corrected for this by a static correction, SC, equal to:

$$SC = t' \; - \; t_1. \tag{2.9}$$

The static correction can also be determined by the onset of the first-pulse seen on a near-offset noisy trace from cross-feed (e.g. t_n in Fig. 2.9(a)).

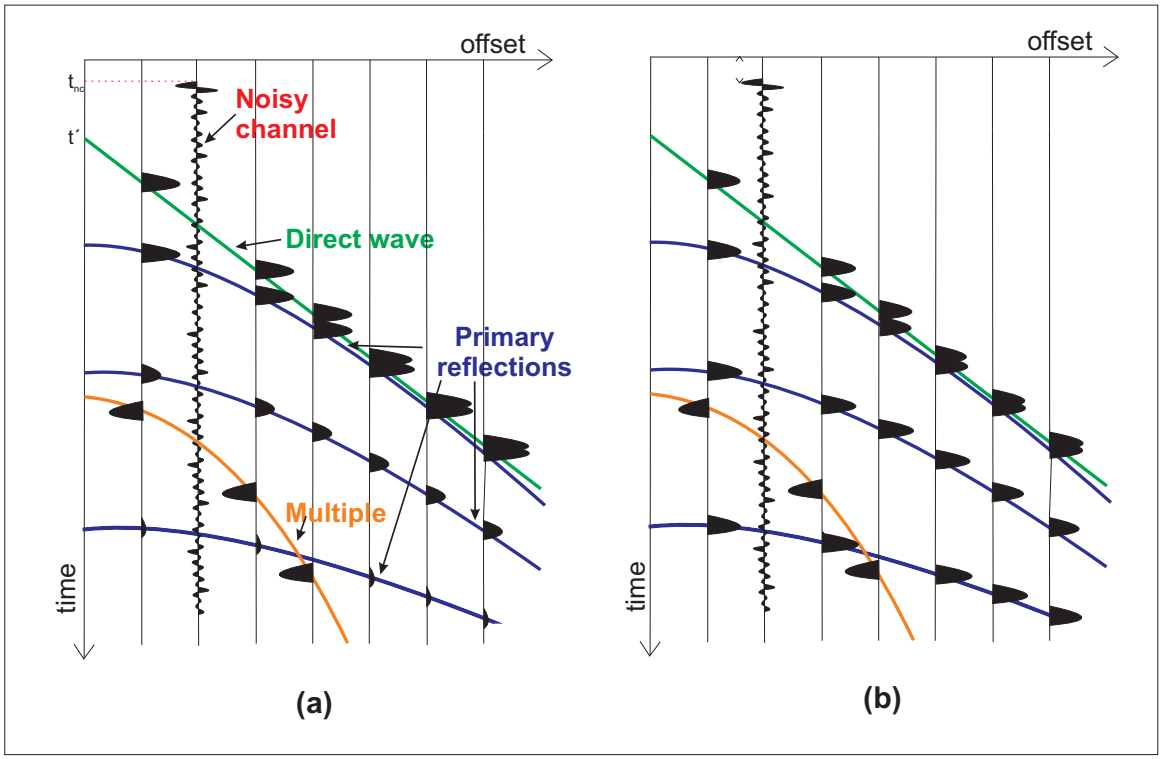

Figure 2.9: (a) Illustration of a marine shot record (bandpass filter applied, no AGC) showing several features including the direct wave, primary reflections, seabed multiple and a noisy channel; t_nc is the time associated with the onset of the first pulse of a near-offset noisy channel and t' is the actual arrival time of the direct wave. Note how the amplitude of reflections diminishes significantly with depth except the amplitude of the seabed multiple which is still very strong. Also note how the seabed multiple has the opposite polarity of the seabed reflector (first primary reflection). On the noisy channel, a large pulse can be seen shortly after the assumed zero-time. This indicates the time of shot (real zero-time) and therefore the static correction that must be made to the data. (b) Same shot record, but with AGC applied. Note how the stronger, shallower reflections are slightly scaled down and the weaker, deeper reflections are scaled up.

2.2.1.2 Spectral analysis and frequency filtering

Spectral analysis of a shot record displays the amplitude spectrum for the data set and provides initial information about the signal-to-noise (S/N) ratio. Single-frequency, high amplitude noise may be visible, signaling the need for notch-frequency filtering in the processing flow (discussed further in Chapter 3).

Frequencies of primary reflectors can be estimated from the raw shot gather:

$$F_r = \frac{1}{T_r} \tag{2.10}$$

where F_r is the dominant frequency of the reflection and T_r is the period of the waveform. This information can be used to construct a filter which will retain only this desired frequency range and attenuate the noise contained outside this range. A filter that retains certain frequencies while rejecting others is called a *bandpass filter*. One common bandpass filter is the Ormsby filter which uses four input frequencies, f_1 - f_2 - f_3 - f_4 to form a 4-sided polygon in F-K space:f_1 = low-cut frequency, f_2 = low-pass frequency, f_3 = high-pass frequency and f_4 = high-cut frequency. The range f_2 - f_3 is the bandpass and f_1 and f_4 determine how abruptly to cut off the filter. The sharp discontinuities at either shoulder of the filter can result in ringing in the filtered image. Special cosine filters can be applied to the upper corners of the polygon creating smoother ramps to reduce the ringing effect in the filtered image.

When applying a frequency filter, it is important to note that:

(1) successive filtering lengthens the wavelet and causes ringing and is best to avoid applying more than one filter if possible;

(2) the phase of the filter must be chosen to match the phase of the input signal. Mismatch causes severe distortion on the final image.

Aliasing

The digital sample rate of a survey directly affects the highest frequency that can be correctly recorded. It is necessary to sample a frequency at least twice in one period to properly digitize the waveform (Fig. 2.10). The maximum frequency which can be properly sampled in a particular survey is known as the Nyquist frequency, F_N:

$$F_N = \frac{1}{2\Delta t} \tag{2.11}$$

where Δt is survey sample interval.

Temporal aliasing, or mis-correlation of traces, occurs for any frequency higher than F_N and causes band folding in the frequency domain. It is important to ensure the high cut of the bandpass filter is below F_N to minimize temporal aliasing issues in the final image.

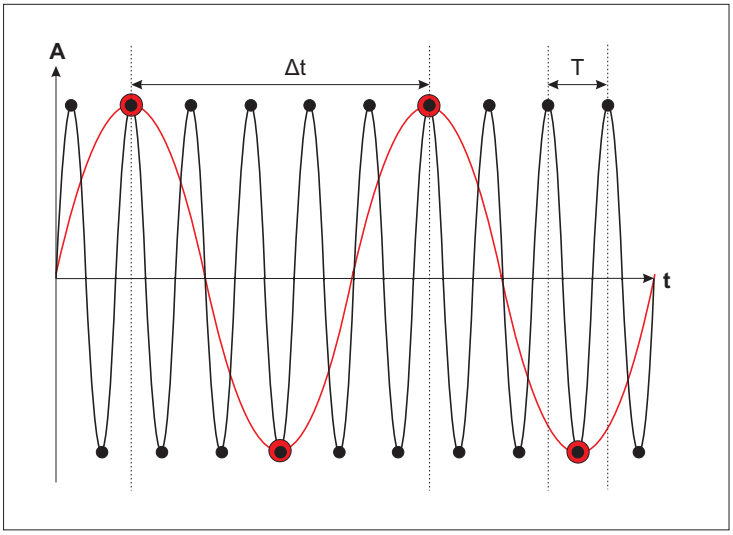

Figure 2.10: Here, A is the amplitude of the wave, t is elapsed time, and T is the period of the wave. T is the time is takes for a wave to complete one full cycle (e.g. peak to peak). In this figure, the sample interval, Δt, is too large to properly sample the high frequency waveform (black curve) and results in aliasing (red curve).

2.2.1.3 Near-trace gather

A near-trace gather displays all the data collected by a single channel for every shot fired during a particular seismic survey. Although the resolution is poor and subsurface reflectors are mispositioned (because they are at non-zero offset), it provides a first-look at the subsurface geology.

2.2.2 Amplitude control: Spherical divergence and AGC

The amplitude of a wave, A, is directly proportional to the square-root of the waves's energy density, u; so that:

$$A \; \alpha \; \sqrt{u}. \tag{2.12}$$

A spherical wave-front propagating in a homogeneous earth loses energy density, and hence, amplitude, by two major processes: (1) spherical divergence: energy density decreases proportional to $\frac{1}{r^2}$ where r, the radius of the wavefront, increases with depth and thus, from Eq. 2.12,

$$A \; \alpha \; \frac{1}{r}; \tag{2.13}$$

and (2) intrinsic attenuation in the rocks: causes higher frequencies (i.e. higher energies) to be more rapidly absorbed than lower frequencies (i.e. lower energies) (Yilmaz, 2001).

The combination of these processes along with other processes resulting from the non-homogeneity of the earth (e.g. scattering) creates seismic images with strong, high amplitude reflectors at shallow depth and increasingly weaker, lower amplitude

reflectors deeper in the seismic reflection profiles.

Spherical divergence correction

The spherical divergence correction is a simple algorithm that attempts to correct for energy spreading with depth. This function should be applied to the data early in the processing sequence.

Automatic gain control (AGC)

AGC is a function that attempts to correct for amplitude attenuation with depth by using a sliding window to scale-down higher amplitudes and scale-up lower amplitudes (e.g. Fig. 2.9). The choice of window is extremely important for the AGC function: a window that is too small will make strong reflections indistinguishable from weak reflections and all amplitude information is lost; a window that is too large will not scale amplitudes enough and amplitude of deeper reflections may still be too low. AGC does not discriminate between signal and noise and will amplify both equally. Permanent application of the AGC function means all original amplitude information is lost; such a function should not be applied to the data early in the processing flow. Like frequency filtering, it is better to use this function as a final tweak to the display before final output.

2.2.3 Geometry and CMP sorting

Survey geometry (shot point location, shot interval, receiver spacing, etc.) is entered into a spreadsheet. This information is used to regroup shot records into CDP bins. Location of shot points can be entered manually with a table of GPS coordinates generated onboard during acquisition or the shot points can be generated automatically by a computer using the acquisition parameters. Automatic geometry

generation is a more straightforward process and is sufficient when seismic lines are quasi-linear.

2.2.4 Velocity analysis and normal moveout (NMO) correction

Multifold coverage with non-zero offsets yields velocity information about the reflectors in the subsurface (Yilmaz, 2001). For a horizontal reflector, the two-way-travel time (TWT) at a given channel, t_x, is given by

$$t_x = \sqrt{{t_0}^2 + \frac{4x^2}{v_{RMS}^2}} \tag{2.14}$$

where x is the source-receiver offset, v_{RMS} is the RMS velocity of the first layer and t_0 is TWT at zero-offset. Normal moveout (NMO) is defined as the difference in TWT of t_x and t_0, or Δt_{NMO} where:

$$\Delta t_{NMO} = |t_x - t_0| \tag{2.15}$$

and moves non-zero-offset TWT to zero-offset TWT (Yilmaz, 2001). The effect of NMO is more pronounced for shallow refections and large offsets.

For horizontal layering and small offsets, seismic (RMS) velocity, NMO velocity and stacking velocity can be used interchangeably. NMO is often used to create velocity functions that will reposition traces in CMP gathers to zero-offset so that the traces may be later combined for maximum signal amplitude (i.e. stacking, discussed below).

The first step in creating a velocity function is choosing representative CMPs for analysis. Discerning NMO corrections for non-horizontal reflectors involves computa-

tion using a mathematically-complex algorithm. For this reason, in areas of complex geology, the horizontal sections of the reflectors are chosen for velocity analysis. Several neighbouring CMPs are combined into supergathers to increase offset-sampling for velocity semblance calculations.

Semblance between traces is calculated by dividing each trace in each supergather into discrete sections of time and using statistical measures to correlate each trace:

$$S = \frac{\sum_{i=1}^{n}\left[\sum_{j=1}^{m} A_{ij}\right]^2}{\sum_{j=1}^{m}\sum_{i=1}^{n} A_{ij}^2} \tag{2.16}$$

where A_ij is the amplitude of the j^{th} time-section of the i^{th} trace. Output from the semblance function yields a contour plot with high density areas representing location of maximum semblance. The velocity function for the data can be chosen by picking in these high density areas on the semblance plot (simplified as red dots in Fig. 2.11); interpolation between chosen functions creates a velocity function describing the entire seismic profile. If a velocity is chosen too high, the result is an under-correction of the reflector: the data curves upward; if a velocity is chosen too low, the result in an over-correction of the reflector: the data curves downward. When the correct velocity is chosen, reflectors will flatten and emulate zero-offset data (e.g. Fig. 2.11).

Where geology is complex, semblance analysis is often inaccurate and other methods, such as constant velocity panels (CVPs) or constant velocity stacks (CVSs), must be used in conjunction. Both the CVPs and and CVSs use NMO-corrected data to output results at varying velocities. The appropriate NMO velocity can be chosen from panel or stack which yields the flattest reflection(s). Both the CVP and the CVS method yield velocity results which are contingent on the test-velocity spacing (i.e.

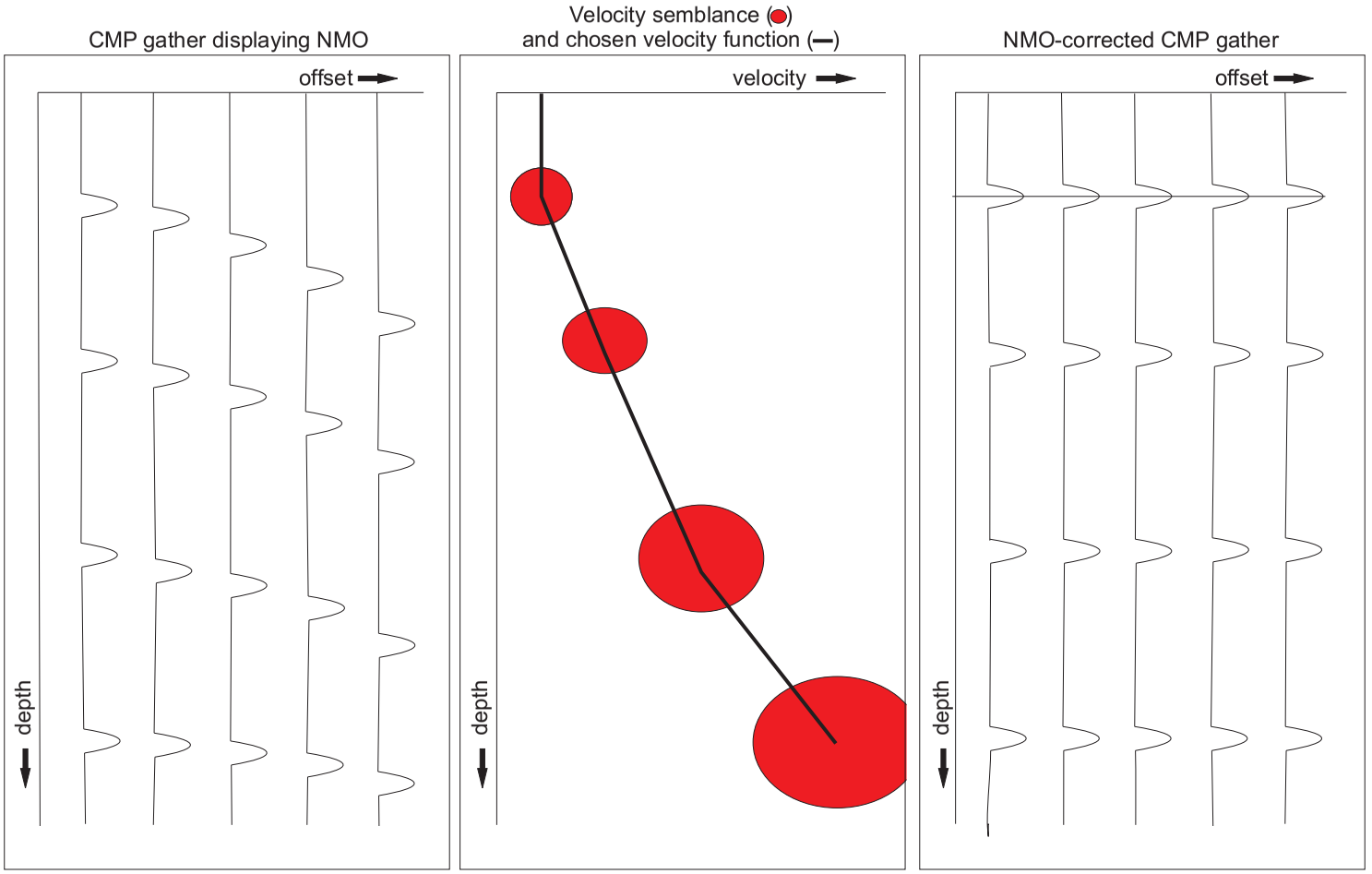

Figure 2.11: Cartoon depicting velocity analysis using semblance and the subsequent NMO correction of the CMPs

results can only be as precise as test velocities chosen). Further examples of these methods and the semblance method are shown in Chapter 3.

The resolution and accuracy of velocity estimation is limited by factors such as: reflector depth (deeper reflectors have less move-out); reflector dip (velocities are most accurate for horizontal reflectors, the more a reflector is dipping, the less accurate the velocity estimate); spread length (NMO is more pronounced at greater offsets, yielding better velocity-matching); fold (greater sampling of a CMP yields higher statistical probability of accurate semblance correlation); S/N ratio (data with higher S/N ratios produce more accurate velocity functions); and data set bandwidth.

NMO-stretching

NMO correction moves non-zero offset waveforms to zero-offset position by literally stretching the waveforms in the time domain from their original dominant period of $T\prime$ (and dominant frequency, f') to a new dominant period of T (and dominant frequency, f). Figure 2.12 shows that $T\prime < T$ and, from Eq. 2.10, this implies that $f' > f$. The results of this is a loss of temporal resolution and frequency

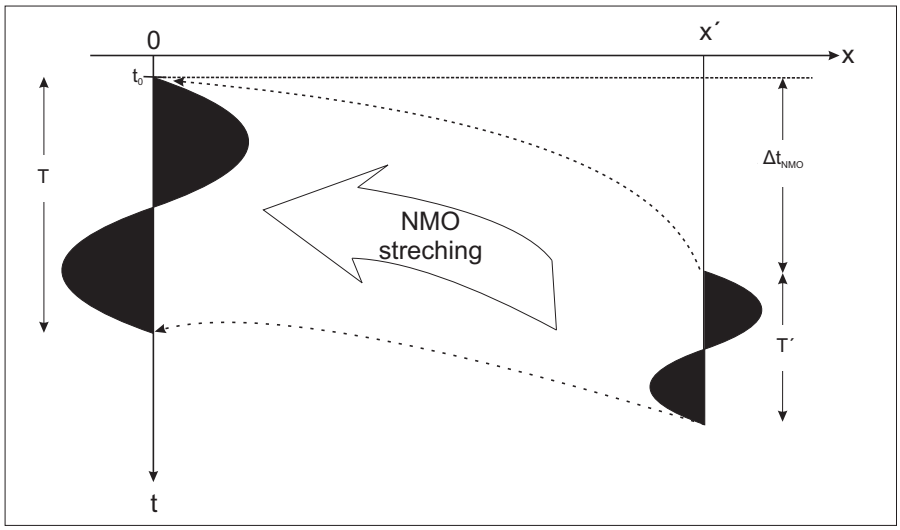

Figure 2.12: Illustration of NMO stretching.

distortion especially affecting shallow reflections and far-offset traces (Yilmaz, 2001). The amount of frequency distortion, Δf, is given by

$$\frac{\Delta f}{f'} = \frac{\Delta t_{NMO}}{t(0)}. \tag{2.17}$$

To minimize the distortion on the data set, a stretch-mute must be applied to the gathers prior to stacking.

Interval velocities and depth conversion

For this thesis it was assumed that $v_{NMO} \approx v_{RMS}$ (methodology for determining v_{NMO} described in previous section). The determination of the RMS velocities allows the calculation of interval velocity, v_{INT}, between one reflection with velocity v_{RMS_1} and a second reflection with velocity v_{RMS_2} using the Dix Equation:

$$v_{INT} = \sqrt{\frac{v^2_{RMS_2}\frac{t_2}{2} - v^2_{RMS_1}\frac{t_1}{2}}{\frac{t_2}{2} - \frac{t_1}{2}}} \tag{2.18}$$

where t_1 and t_2 are the zero-offset TWT for the first and second reflectors, respectively.

Once the interval velocity is determined, depth can be calculated using the simple relation

$$d = d_0 + v_{INT}(t_2 - t_1) \tag{2.19}$$

where d_0 is the depth to the first reflector (note that $v_{INT}(t_2 - t_1)$ gives the thickness of the layer). This process can be extended to calculate depth for multi-layered systems.

2.2.5 Stacking

The stacking process combines all traces in a CMP into a singular, high-amplitude trace, compacting the data-set and increasing reflection resolution (Fig. 2.13). A common summation for the stacked trace amplitude, S_T, for n traces is given by

$$S_T = \frac{1}{n}\sum_{i=1}^{n} A_i \tag{2.20}$$

where A_i is the amplitude of the i^{th} trace.

Stacking the data-set makes future procedures (such as migration) more manageable. It is also the single best process for maximizing the S/N ratio: coherent, primary

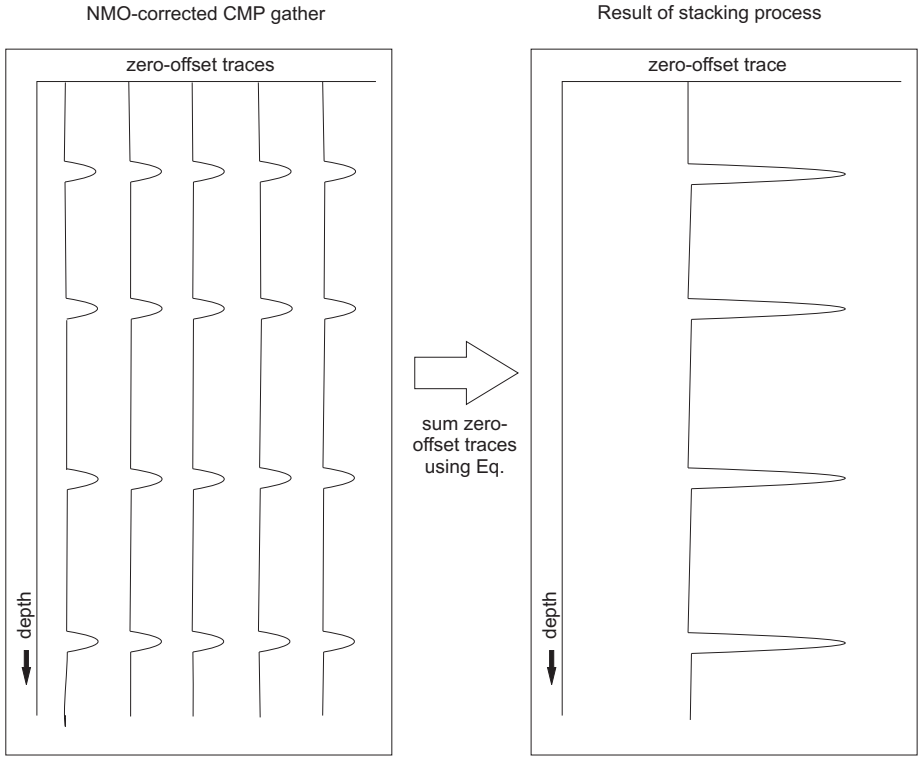

Figure 2.13: Illustration of the stacking process.

energy is amplified while both coherent noise (e.g. NMO over-corrected multiples) and random noise are reduced.

Stacked data is displayed as zero-offset data resulting from normal-incident P-waves reflected on horizontal layers (i.e. CDPs are treated as CMPs). This results in distortion of dipping reflectors and diffraction of point-sources. Dipping reflectors are imaged to be longer and less steep than they really are (Fig. 2.14). Geological features like anticlines, synclines, and faults are distorted in the stacked section. Anticlines appear broader and display reflector cut-off at either limb (Fig. 2.15). Synclines appear compacted and display "bow-tie" geometry(Fig. 2.16). Faults, sharp edges and dipping surfaces appear as series of diffractions on the seismic profile (Fig. 2.17). In order to correct for this distortion, the data must be migrated.

2.2.6 Migration

The migration process restores mispositioned subsurface reflectors to their proper locations (Fig. 2.18). Effects of migration include:

(1) diffractions are collapsed;

(2) dipping reflectors are steepened (dip increased), shortened and moved up-dip resulting in the steepening of anticlines and the broadening of synclines. Note that in a time-migrated section, dipping reflectors are not completely restored to their true subsurface position, this is only accomplished with depth-migration;

(3) bandwidth of the dataset is decreased.

Migration can be performed either pre- or post- stack. Where geology is complex, pre-stack migration produces better signal-retention, but the computational cost is high. Migration can executed in either in time or in depth. Time migration assumes

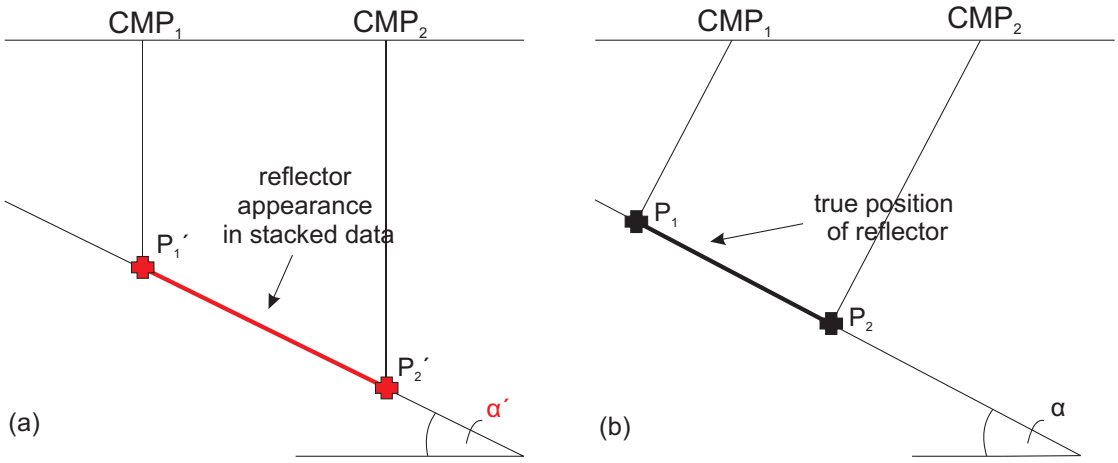

Figure 2.14: On a CMP stack, dipping reflectors are imaged longer and less steep than they really are. (a) Imagined positions of P_1 and P_2 on reflector with apparent dip $= \alpha'$. (b) True subsurface position of P_1 and P_2 on reflector with true dip, α. Actual depth positions are restored during the process of migration, discussed in the next section.

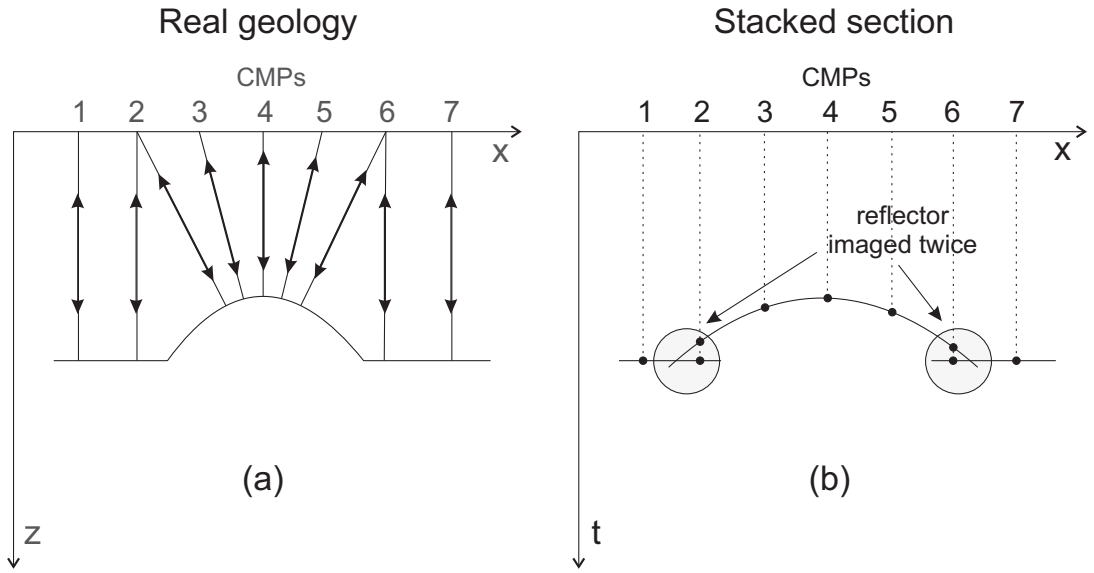

Figure 2.15: (a)Actual subsurface anticline. (b) Because of the curved surface, two reflections originating from the same reflector are recorded at CMPs 2 and 6. Note how the anticline appears broader on the CMP stack section.

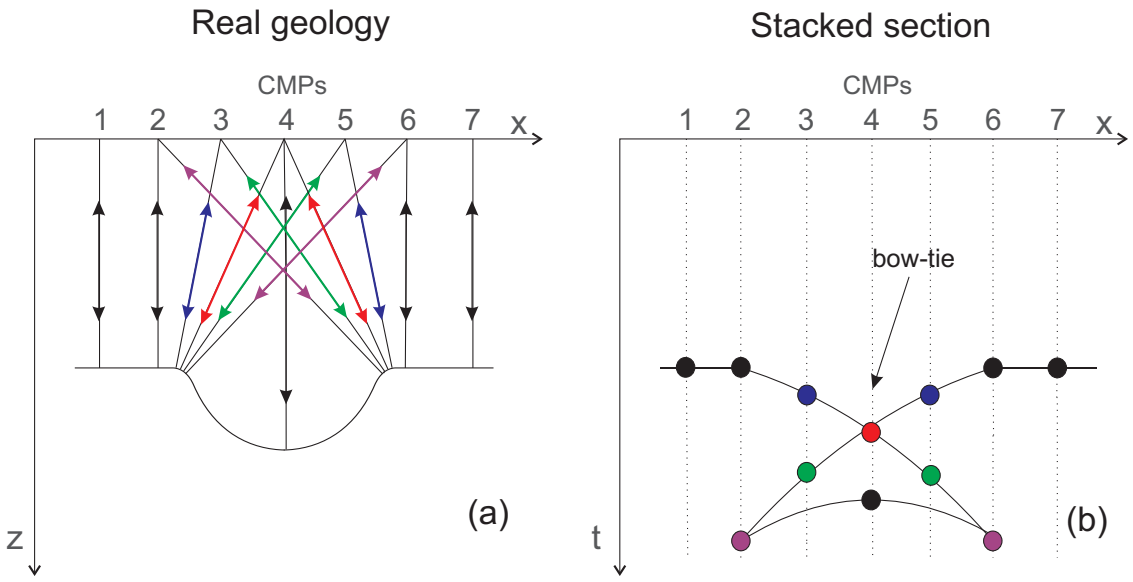

Figure 2.16: (a) Actual subsurface syncline. (b) Because of the curvature, the reflector is imaged several times at the CMPs, resulting in bow-tie geometry in the stacked section. Note how the syncline appears compressed in the stacked section.

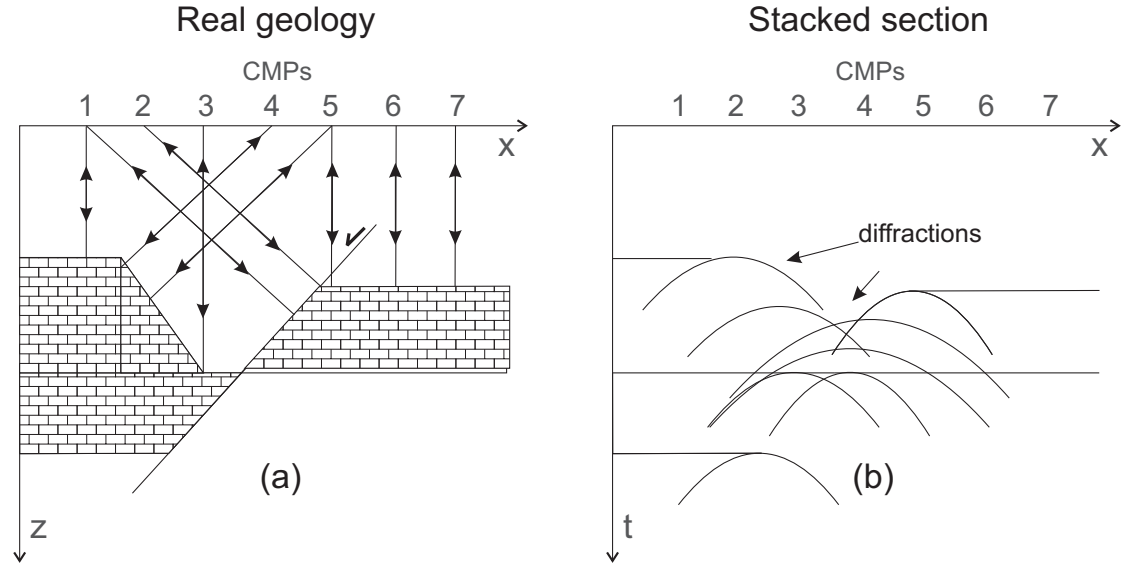

Figure 2.17: (a) Actual geology of a dipping reflector and an extensional fault. (b) Diffractions generated in stacked section.

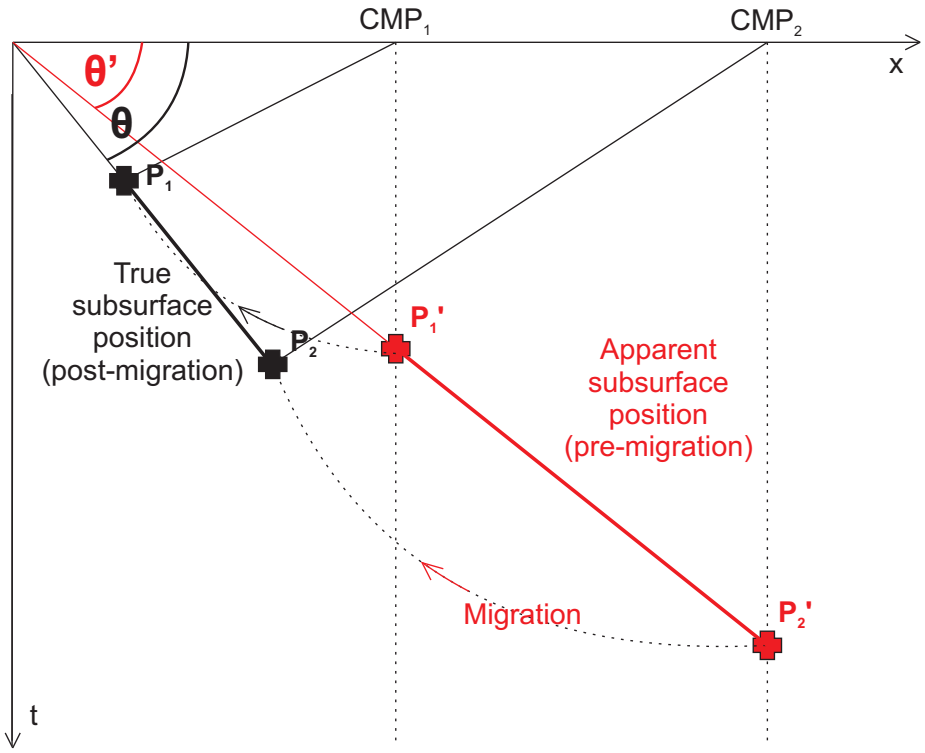

Figure 2.18: Illustration of migration principles. Note that after migration: reflector is shortened; dip increases (i.e. $\alpha < \alpha'$); and reflector is moved up-dip.

diffractions are hyperbolic and uses this to collapse diffractions while depth migration uses a known velocity model to more-correctly approximate diffraction shapes. Although depth migration provides a more accurate picture of the subsurface geology, it is more computationally intensive than time migration and requires an accurate velocity model for optimal results. For data with small folds, the accuracy of the velocity function decreases significantly with depth and is not suitable for depth migration. The two important (time) migration algorithms relevant to this thesis are Stolt migration and Kirchhoff migration are discussed below.

Stolt migration

The Stolt, or frequency-wavenumber (fk), migration algorithm is fairly simple and robust. Its fastest, and best, performance is at constant velocity where data is transformed into the fk domain, multipled by a scalar and then transformed back into the time domain. The Stolt stretch factor, W, is used to stretch the time axis and allow for non-constant velocity migration. This slows down the algorithm considerably and the end-result is not as good as other migration algorithms. For this reason, Stolt migration is best used as method to approximate migration velocities to be used as starting-point velocity models for other migration algorithms.

Kirchhoff time migration

Kirchhoff migration, or diffraction-stack migration, bases its algorithm on the assumption that every point on a reflector acts as a secondary point source generating hyperbolic TWT curves. The Kirchhoff migration algorithm collapses the diffraction hyperbolae visible on stacked sections by summing the amplitudes of the diffraction hyperbolae of all the secondary sources and placing them at the appropriate apex (Fig. 2.19). This is achieved by using a reliable migration velocity function. Mod-

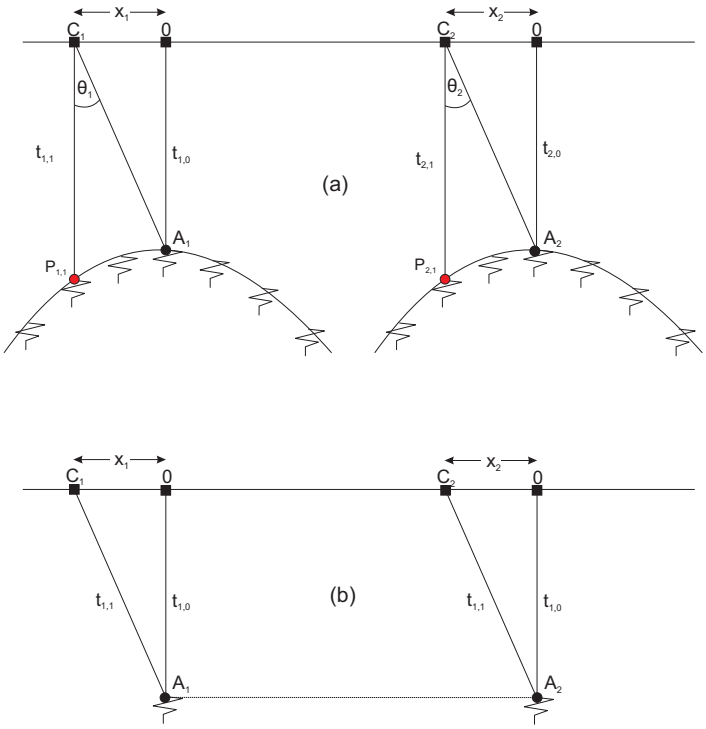

Figure 2.19: Illustration of Kirchhoff migration principles. (a) Zero-offset stacked section. (b) Kirchhoff migration maps the amplitude at points $P_{1,1}$ or $P_{2,1}$ to apexes A_1 and A_2 respectively.

erate temporal and lateral velocity gradients are tolerated within the Kirchhoff time migration algorithm, but severe gradients will produce unwanted migrational artifacts on the final image.

Kirchhoff migration can migrate all dips and the choice is available how large of a migration aperture is desired. The migration aperture specifies the range of data included in the migration of each point (Sheriff, 1995); deeper and steeper reflectors require larger apertures to migrate properly. Ideally, the aperture should be larger than twice the horizontal migration distance of the steepest dipping reflector (Yilmaz, 2001). The larger the migration aperture and the steeper the dip to migrate, the longer the computational cost of the process.

2.2.7 Deconvolution

The seismic record, $R(T)$ can be thought of as the convolution of the earth's impulse response function, $E(t)$ and the source signature, $S(t)$:

$$R(t) \;=\; E(t) \;*\; S(t). \tag{2.21}$$

If the source signature was a spike, then the convolution would generate a seismogram illustrating the impulse response of the earth. Of course, the seismic record is also superimposed with noise (both coherent and random). Denote a noise function, $N(t)$, to represent this noise, so now,

$$R(t) \;=\; E(t) \;*\; S(t) \;+\; N(t). \tag{2.22}$$

Deconvolution, then, is the attempt to reverse the convolution process and leave only the earth's impulse response. It can be used to attenuate both short-period wavelet reverberation (spiking deconvolution, short-gap predictive deconvolution) and long-period multiples with predictable periods (predictive deconvolution, adaptive deconvolution). Deconvolution can be applied either pre- or post- stack. Post-stack deconvolution is much less computationally intensive and it also benefits from the increased S/N ratio that stacking provides.

2.2.7.1 Spiking deconvolution

Spiking deconvolution is an inverse filter which attempts to remove the source wavelet from the siesmogram; it can suppress short-period multiples and increase temporal resolution by shortening the source wavelet and approximating it as a spike. A spike in the time domain is equivalent to a flat spectrum in the freqency domain

(this type of deconvolution is also referred to as *whitening*). At high frequencies, spiking deconvolution is especially prone to generating added noise in the section. Note: If the source wavelet is not perfectly minimum phase, spiking deconvolution will not be effective (Yilmaz, 2001).

2.2.7.2 Predictive deconvolution

Predictive deconvolution algorithms are based on five assumptions: (1) the source wavelet is both minimum phase and stationary (i.e. does not change in time); (2) subsurface reflectors are horizontal and have constant velocity; (3) noise is minimal (i.e. seismic record behaves more like Eq. 2.21 than Eq. 2.22); (4) the source generates P-waves which are reflected at normal incidence at interfaces (i.e. do not produce S-waves by shearing); (5) and the earth's reflectivity series is random (Yilmaz, 2001). Despite the many (often incorrect) assumptions used in these algorithms, predictive deconvolution is often very effective at removing both short- and long- period multiples from the data set. Unwanted data is deconvolved using a filter generated from parameters obtained from the autocorrelation of the seismogram.

An autocorrelation function is the correlation of the data set with itself (Fig. 2.20). Under the assumption that the source wavelet behaves as the seismogram does (assumption 5 above), the autocorrelation function can be used to estimate deconvolution parameters like prediction lag, α, and prediction operator length, n. For a source wavelet of length $n + \alpha$, the deconvolution alrgorithm will create a filter of length n which compresses the signal to a wavelet that is α samples long (Yilmaz, 2001).

The choice of prediction lag therefore directly affects the compression (i.e. amplitude spectrum) of the output wavelet. The shorter the prediction lag, the more the wavelet is compressed. In fact, spiking deconvolution is equal to choosing $\alpha = 1$

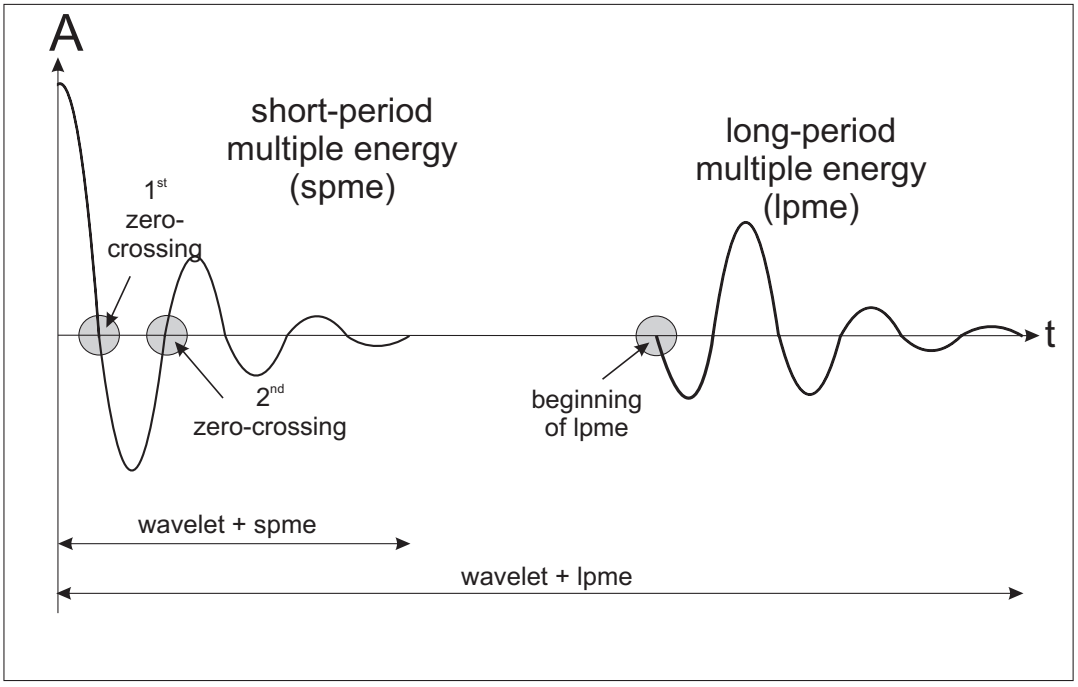

Figure 2.20: Autocorrelation function and choice of prediction lag and operator length.

so that the filter operates over only one sample in time, thus whitening the frequency spectrum. Predictive deconvolution can mimic spiking deconvolution for short-period multiple supression by chosing a short prediction lag equal to the 2^{nd} zero-crossing of the autocorrelogram (Fig. 2.20). For long-period multiple supression, the prediction lag should be equal to the beginning of the first multiple on the autocorrelation function (Fig. 2.20). Note that, in all cases, highly compressed wavelets boost both high and low frequency noise; therefore, longer prediction lags are best. The choice in operator length, n, affects the degree of multiple supression. The ideal operator length should be sufficiently long so that it does not leave much energy in the autocorrelation function, but not so long that it will begin to deconvolve geology. Note that deconvolution parameters should be tested extensively to obtain optimal parameters for the particular data set before applying a permanent deconvolution to the data.

Adaptive deconvolution is a sub-type of predictive deconvolution which adapts to the changing shape of the source wavelet as it travels through the earth by making multiple calculations of the autocorrelation function over many windows. This type of deconvolution can be very harsh and can leave unwanted, eraser-like marks on seismic sections, often eliminating primary energy, and must therefore be used very carefully, if at all (Yilmaz, 2001).

2.2.8 Multiple supression

Predictive deconvolution and stacking are the two most effective multiple removal tools. Other types of multiple removal processes include frequency-wavenumber (FK) - domain multiple removal and the wave equation multiple removal (WEMR). Because multiple removal techniques were not successful for this data set, a detailed discussion here is not required. Curious readers can find information on multiple removal techniques in texts such as Yilmaz, 2001.

2.3 Geological interpretation of 2D marine seismic data

If the goal in data processing is to produce an image which is the best reflection of the true subsurface geology; it is, then, the goal of interpretation to take this image and determine its geological significance. The three major aspects of geological interpretation are: 1-establishing a litho- and chrono-stratigraphic framework (Chapter 4); 2- identifying and mapping important structural markers across the study area (Chapter 5); and 3- generating models which explain the evolution of these features on a larger scale (Chapter 6). Initial small-scale observations from seismic profiles evolve and combine together to create the "big picture" of the regional tectonic framework.

2.3.1 Stratigraphy and chronology

Sequence stratigraphy is a methodology which uses a hierarchy of chronostratigraphically significant surfaces, or sequence boundaries, to subdivide the sedimentary record into relatively conformable and genetically-related strata (Mitchum et al., 1977). Sequence boundaries mark periods of lowstand and are marked by extensive erosion; they are unconformities. Unconformities are representative of large gaps in geological time and are, in general, diachronous. Reflectors between sequence boundaries can show characteristic terminations which aid in interpretaton (e.g. Figs. 2.21 and 2.22). Toplap is indicative of progradation and is commonly observed in deltaic environments, coastal barrier islands, and large sand waves. If the top-most layer is more thin than the temporal resolution of the seismic profile, toplap may be indistinguishable from an angular unconformity. Downlap involves the termination of more steeply dipping younger strata onto a less steeply dipping older surface. Onlap is characterized by shallowly-dipping younger strata overstepping each other and terminating on a steeper-dipping older surface. This is associated with the progressive infill of a structural low. Offlap occurs when the distance between strata becomes smaller than the temporal resolution of the wavelet; thus reflections terminate mid-section.

Major unconformities (i.e. sequence boundaries) form the boundaries of the stratigraphic units in the study areas. These units have similar reflectivity and internal characteristics as well as depositional ages. Detailed seismic interpretations of prominent reflections, unconformities, and structural features are traced by hand on paper sections. Crossover lines are integral in generation of a stratigraphic framework by facilitating the correlation of prominent reflections and unconformities across the study area. Stratigraphic unit apparent-thickness maps (isochore maps) are generated to illustrate the overall sedimentary evolution of the region and, later, aid in structural

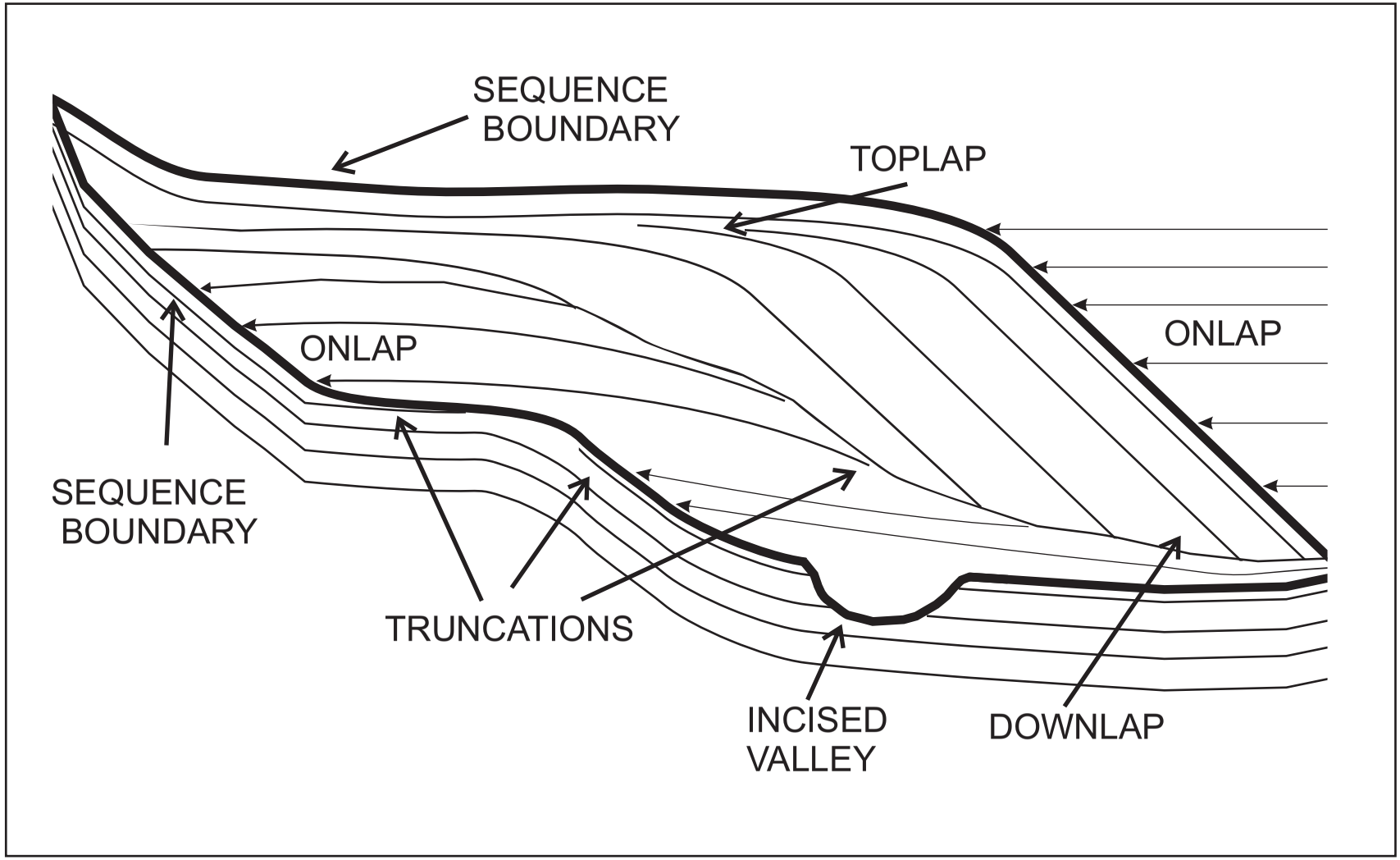

Figure 2.21: Schematic demonstration of reflector terminations used for interpretation (redrawn and modified from Vail et al., 1977)

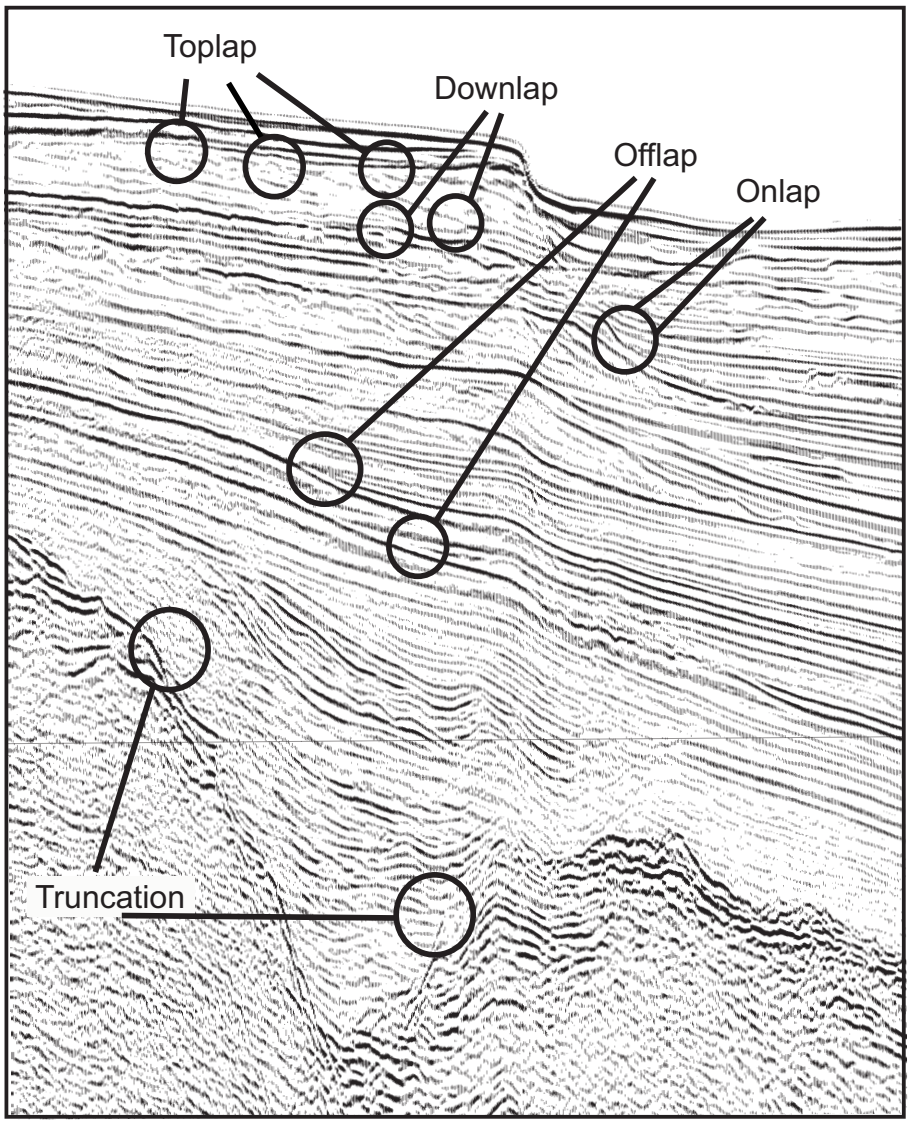

Figure 2.22: Seismic example from the 2008 Cilicia Basin survey demonstrating the various reflector terminations (from Walsh, 2012)

interpretation. Where possible, chronostratigraphic information of the identified units is derived by direct correlation of these units with existing well-log data. Where well-log correlation is not possible (e.g. to probe deeper into a section that a well-log has recorded, or where a well-log is not available), correlations with and extrapolations from surrounding areas are performed in order to establish the chrono-stratigraphic framework. Chapter 4 contains a detailed account of the establishment of the chrono-stratigraphic framework for the Antalya Basin.

2.3.2 Structural geology

Prominent structural features are highlighted on all seismic profiles. In the Antalya basin, these features include: faults (both normal and reverse), basins, ridges and salt structures. Where major structures are not immediately visible, minor structures are used to delineate the major structures (e.g. Fig. 2.23). For example, thrust surfaces are not always clearly imaged on seismic sections and, thus, minor structures (e.g. footwall and/or hangingwall ramps and flats) are used to trace thrust trajectories (e.g. Fig. 2.24). Sense of separation along a fault place was determined by identifying the apparent vertical and horizontal offsets of prominent reflections (Figs. 2.23, 2.24). Faults can have lateral movement in conjunction with vertical and horizontal displacement. These so-called strike-slip, or oblique, faults are very difficult to identify on seismic profiles and minor structures are vital in uncovering them; minor structures hinting at the presence of oblique faulting include positive and negative flower structures (e.g. Harding, 1985; Twiss and Moores, 1992; Moores and Twiss, 1995; Woodcock, 1986; Woodcock and Fischer, 1986). Inversion structures can be indicative of strike-slip faulting, but may instead be depositional effects. Evaporite sequences are identified by a very reflective upper boundary and moderately laterally continuous, sometimes chaotic internal reflections (e.g. Fig. 2.25). Sediments overly-

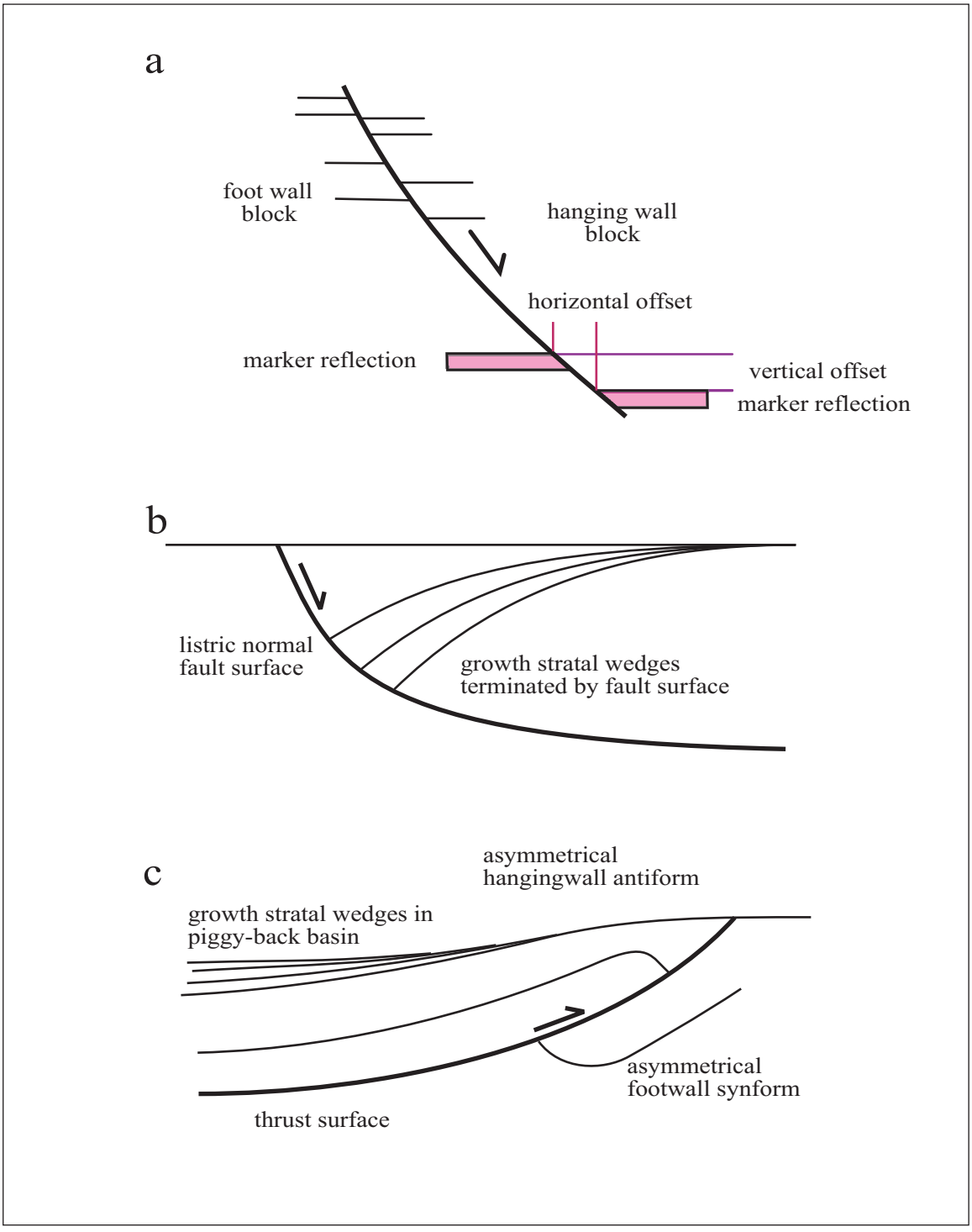

Figure 2.23: Minor structures associated with (a) horizontal and vertical separation of marker reflections in a normal fault, (b) growth strata wedges developed in a listric normal fault and (c) growth strata wedges developed as piggy-back basins in a thrust fault (from Walsh, 2012; modified from Aksu et al., 2009)

ing the evaporites are deformed as a result of salt migration, or halokinesis, and form signature structures including minibasins, turtle structures, and detachment surfaces (Hudec et al., 2011). Relative age of formation of structures is ascertained by observation, or lack thereof, of growth strata wedges in the strata immediately adjacent or overlying the structures (e.g. Fig. 2.25). Presence of growth strata indicates that deposition was syn-tectonic. It is important to be aware that planar fault surfaces can appear listric in time section due to velocity changes with depth. Interpretation of a listric fault surface must be made in consideration of this fact.

Structures were correlated across adjacent profiles and mapped by hand to reveal the overall structural trends in the study area. Line crossovers were used to confirm structural orientations for mapping. Two major structural maps were generated: one for the pre-Messinian Miocene interval; and one for the Pliocene-Quaternary interval. Chapter 5 contains a full discussion on the structures and their trends as identified in the seismic reflection profiles from Antalya Basin.

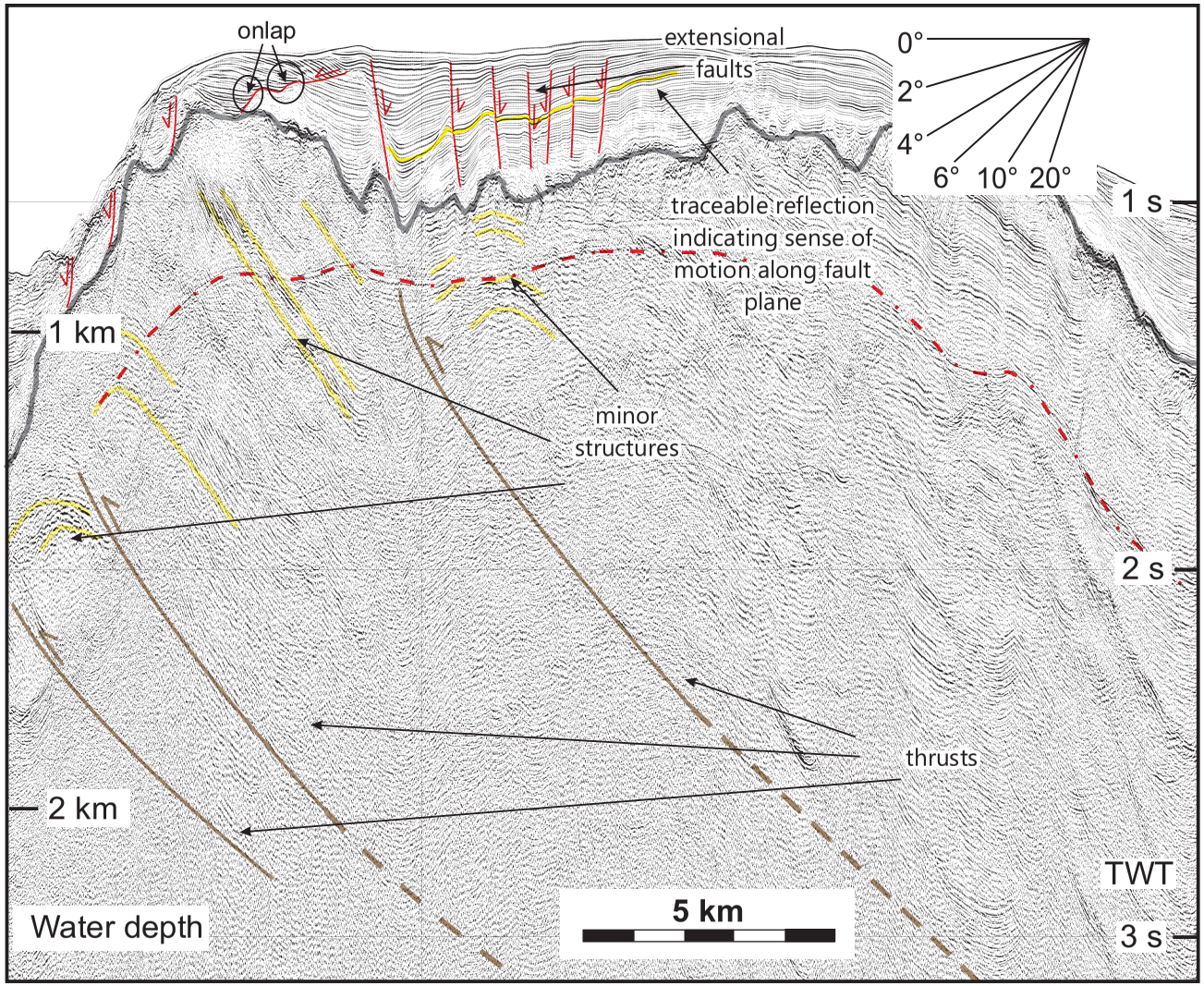

Figure 2.24: Seismic example from Antalya Basin showing reflector terminations and minor structures.

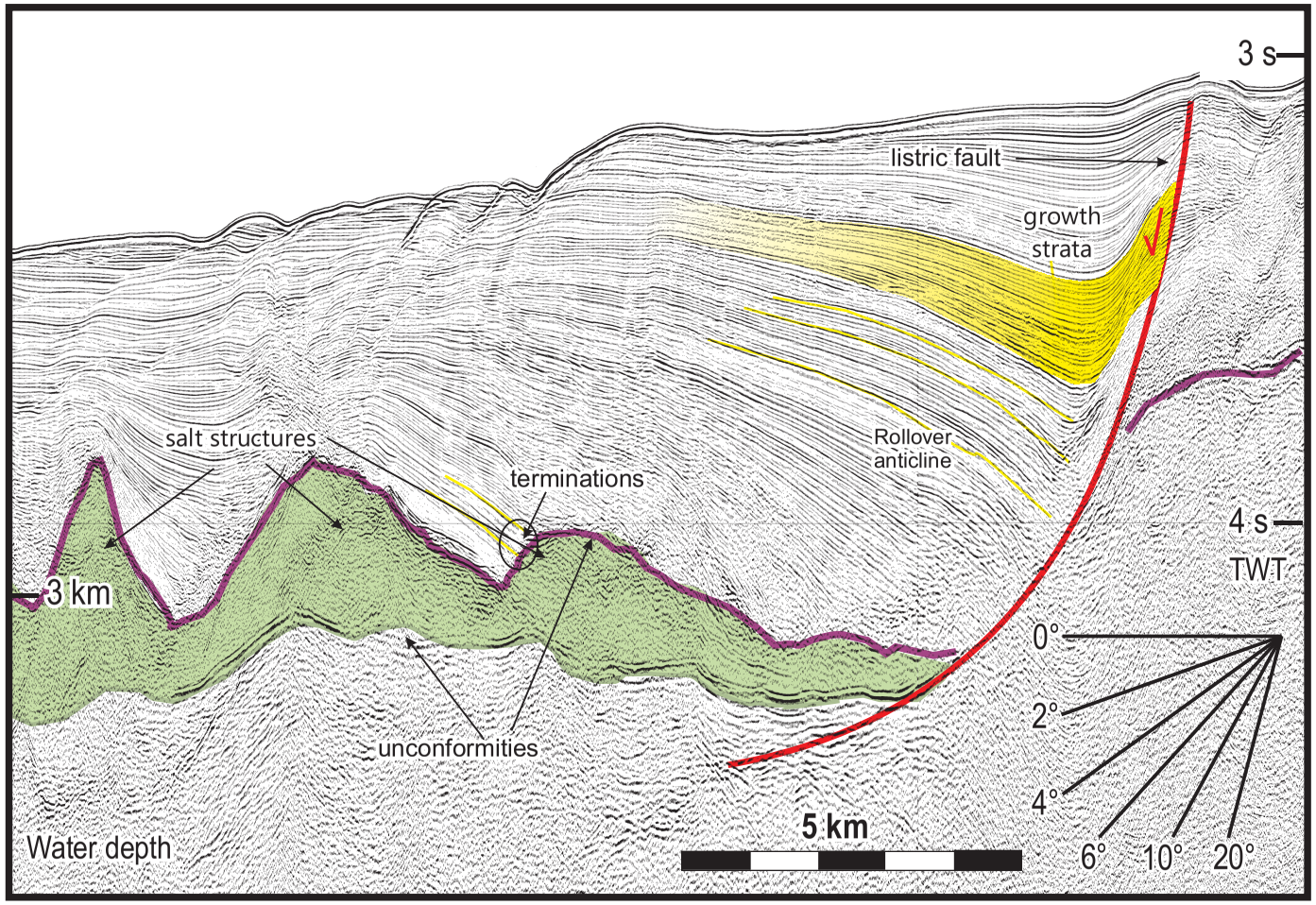

Figure 2.25: Seismic example from Antalya Basin showing reflector terminations and minor structures. Seabed multiple is highlighted with dotted red line.

Chapter 3

Data processing: 2008 eastern Mediterranean Sea survey, western Antalya Basin

The previous chapter described the theory behind the processing techniques used on 2D seismic reflection data. The current chapter outlines the processing flow and specific parameters generated by the author to obtain optimal S/N ratios for the 2008 western Antalya Basin seismic data.

Approximately 500 line-km of 96-channel, 12-fold seismic reflection data was acquired from the western Antalya Basin during the summer of 2008 (Fig. 3.1). Most of this data was processed by the author; however, approximately 90 line-km were processed by an author in a collaborative study (i.e. Çınar, unpublished thesis, 2012; see Fig. 3.1). Processing was done using Landmark's ProMAX software using the techniques described in Chapter 2. Various screenshots taken from ProMAX illustrate

the degree of success of the processing techniques. The processing flow used for the 2008 western Antalya Basin data is shown in Fig. 3.2.

For esthetic purposes, where required, screenshots were enhanced in CorelDraw by manipulating the brightness, contrast and intensity of the original bitmaps (e.g. Fig. 3.3). It is important to note that this manipulation of the bitmaps did not affect the outcome of the processing in any way. Further, no interpretation was done on these screenshots. All interpretation for this thesis was done on exported ProMAX bitmaps which were imported directly to CorelDraw and not enhanced prior to interpretation.

3.1 Raw shot record analysis

Figure 3.4 on page 61 shows raw shot records for shallow and deep water, respectively (from Line A in Fig. 3.1).

3.1.1 Spectral analysis and frequency filtering

Initial spectral analysis of the raw shot records indicated the data set contained frequencies in the range of 0 to >400 Hz (Fig. 3.5). To eliminate both high and low frequency noise while retaining optimal bandwidth for imaging, an Ormsby filter was used with the following operating parameters: low cut - 20 Hz; low pass - 60 Hz; high pass - 200 Hz; high cut - 250 Hz (i.e. 20 - 60 - 200 - 250). In addition to the regular bandpass, a 50 Hz notch filter with a 4 Hz ramp is applied to reduce inherent electrical noise. The bandpass filter is not permanently applied to the data until the very end where it is used as a final display parameter for output.

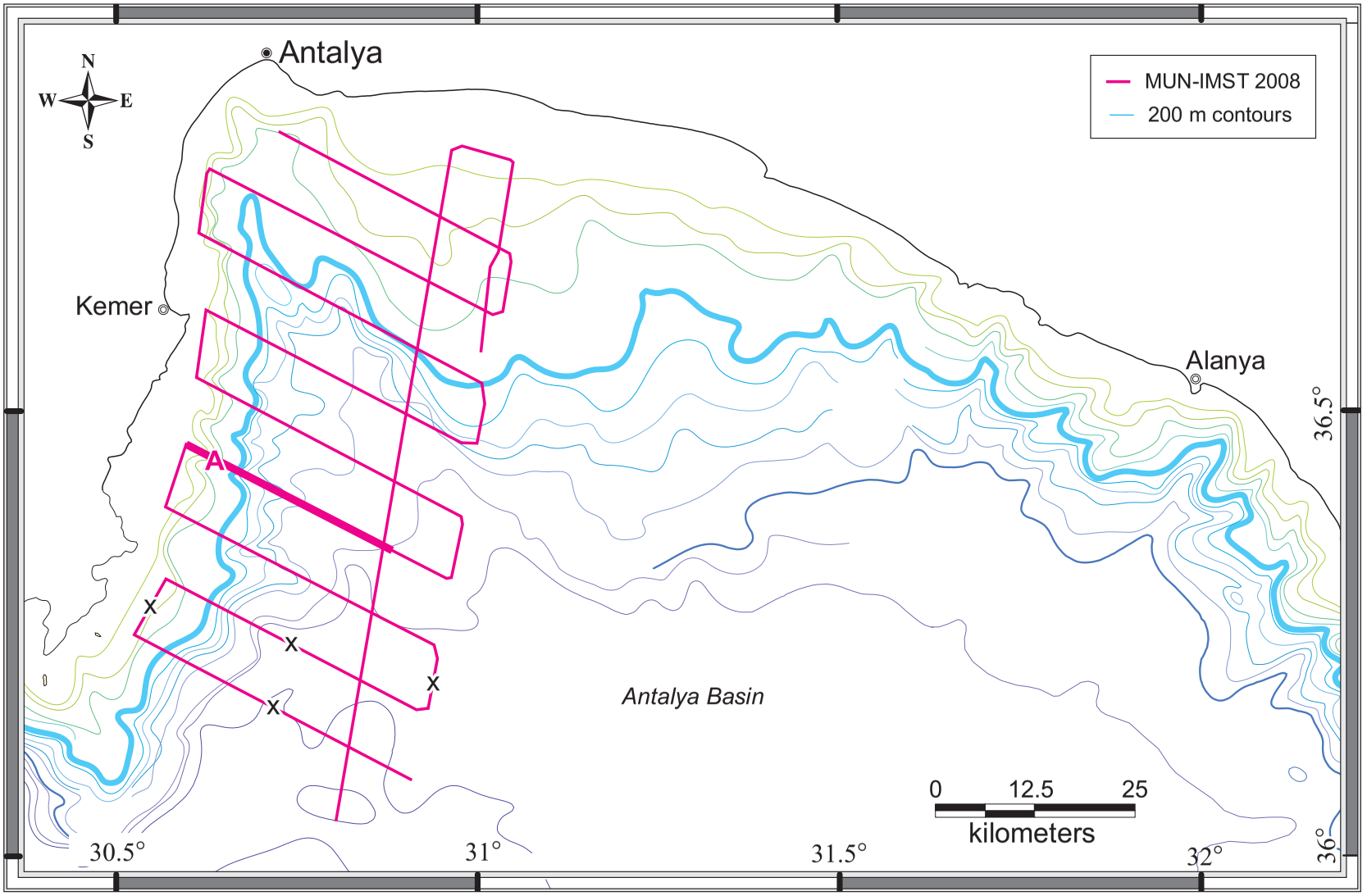

Figure 3.1: Seismic reflection survey grid in the western Antalya Basin from the 2008 Eastern Mediterranean survey (MUN-IMST 2008). Lines marked with x's were processed by an author in a collaborative study (i.e. Çınar, unpublished thesis, 2012). Line marked *A* is the example line used to generate the figures for this chapter. Thicker blue line represents the 1000 m contour. Modified from Gogacz (unpublished, 2010).

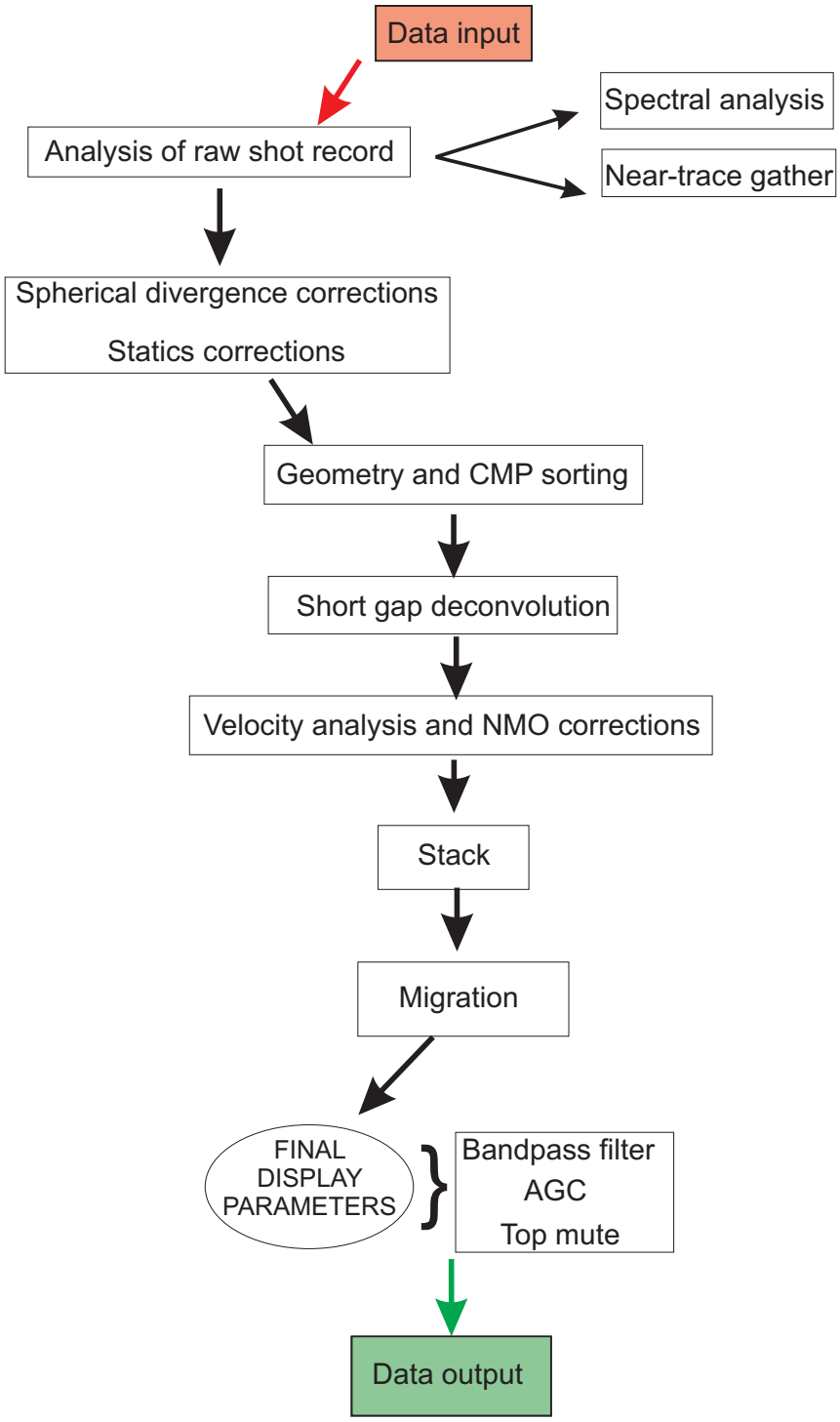

Figure 3.2: Processing flow for the 2008 western Antalya Basin seismic reflection data.

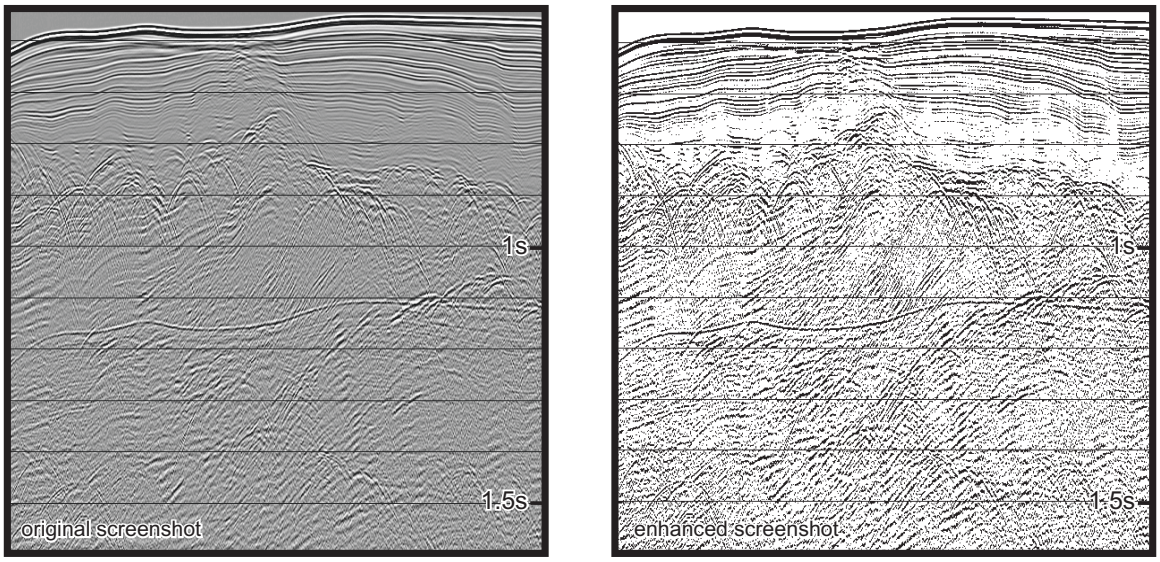

Figure 3.3: Original screenshot from ProMAX is very dark (left). For better visual display, screenshots were enhanced in CorelDraw by varying the brightness, contrast and intensity of the bitmap (right).

3.1.2 Near-trace gather

Displaying one channel for each shot record gives an preliminary impression of the subsurface geology. Because travel time increases with source-channel distance, channels closer to the source will give a more realistic image of seabed depth. Figure 3.6 shows a near-trace gather for Line A (location shown in Fig. 3.1). Once the data is sorted into CDP gathers, the near-trace gather is used to approximate the locations for velocity profiles (discussed further below).

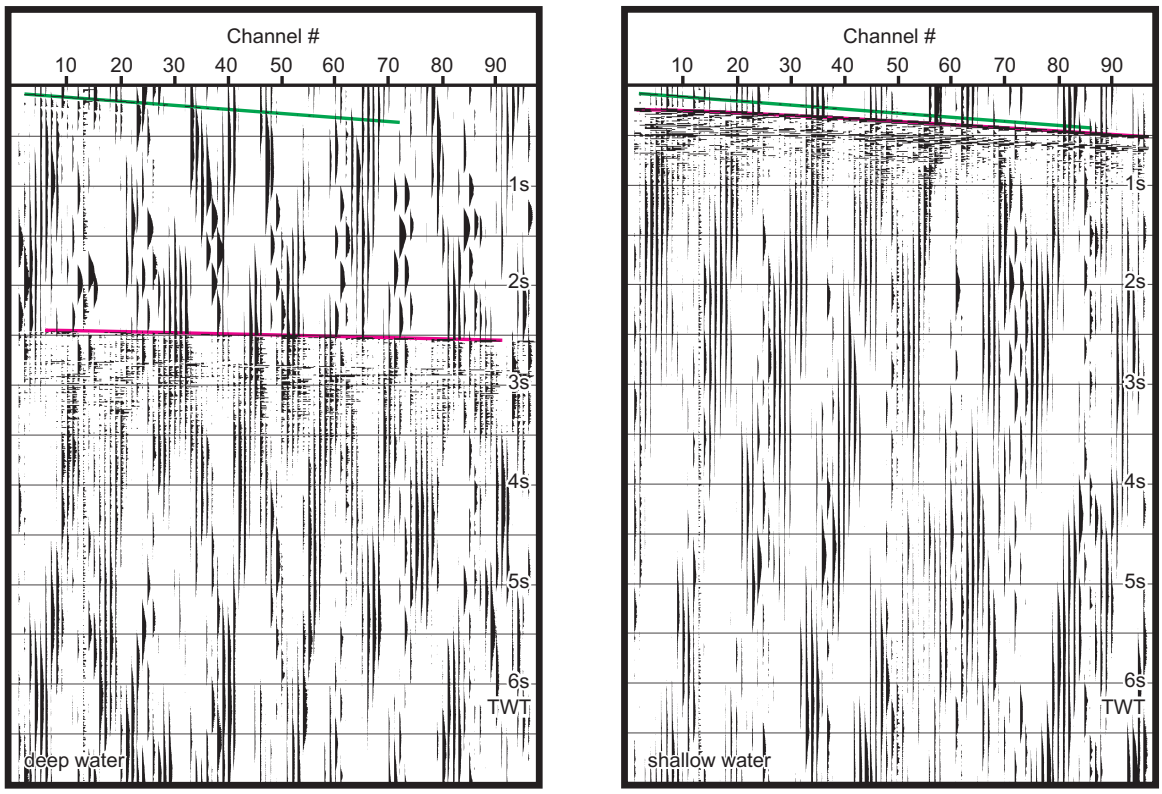

Figure 3.4: Shot records showing full 7 seconds of recording time from deep water (left) and shallow water (right). In both profiles, the direct wave is highlighted in green and the seabed is highlighted in pink. Note the low-frequency noise which dominates both shot records.

3.2 Primary processing: Hand statics and spherical divergence corrections

Primary data processing includes shifting the traces in time to account for lag between the shooting box and the recorder, and scaling the amplitudes of each trace to correct for signal attenuation with depth.

3.2.1 Static corrections

From Eq. 2.8, the calculated arrival time for the direct wave, t_1 should be:

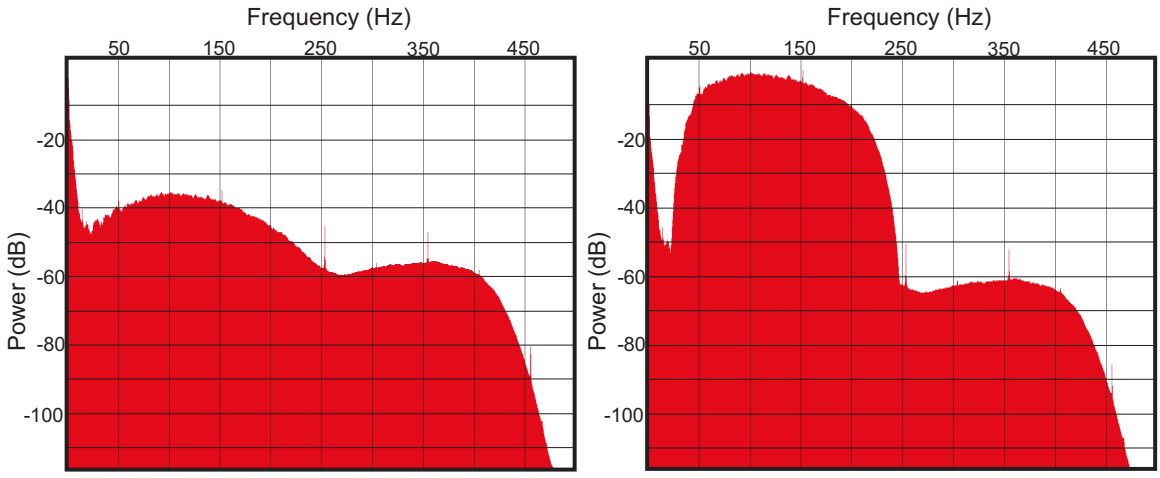

Figure 3.5: Spectral analysis of raw shot records (left) shows data set contains frequencies in the 0 - 400 + Hz range. After applying a 20 - 60 - 200 - 250 Ormsby frequency filter (right), the 50 - 250 Hz signal is amplified. Note the frequency spike every 50 Hz due to inherent electrical noise.

$$t_1 \;=\; \frac{77\ m}{1480\ m/s} \;\approx\; 50ms \tag{3.1}$$

As can be seen in Figure 3.7, the actual arrival time, t_a of the direct wave was approximately 80 ms. Using Eq. 2.9, the static correction, SC, required for the data set was:

$$SC \;=\; 80ms \;-\; 50ms \;=\; 30\ ms. \tag{3.2}$$

Static corrections were applied using the *Hand Static* function in ProMAX.

3.2.2 Spherical divergence and AGC

To reverse the effects of spherical spreading governed by Eq. 2.13, a spherical divergence correction (SDC) is applied to each trace. This is accomplished with the *True Amplitude Recovery* function and is applied permanently to the data set.

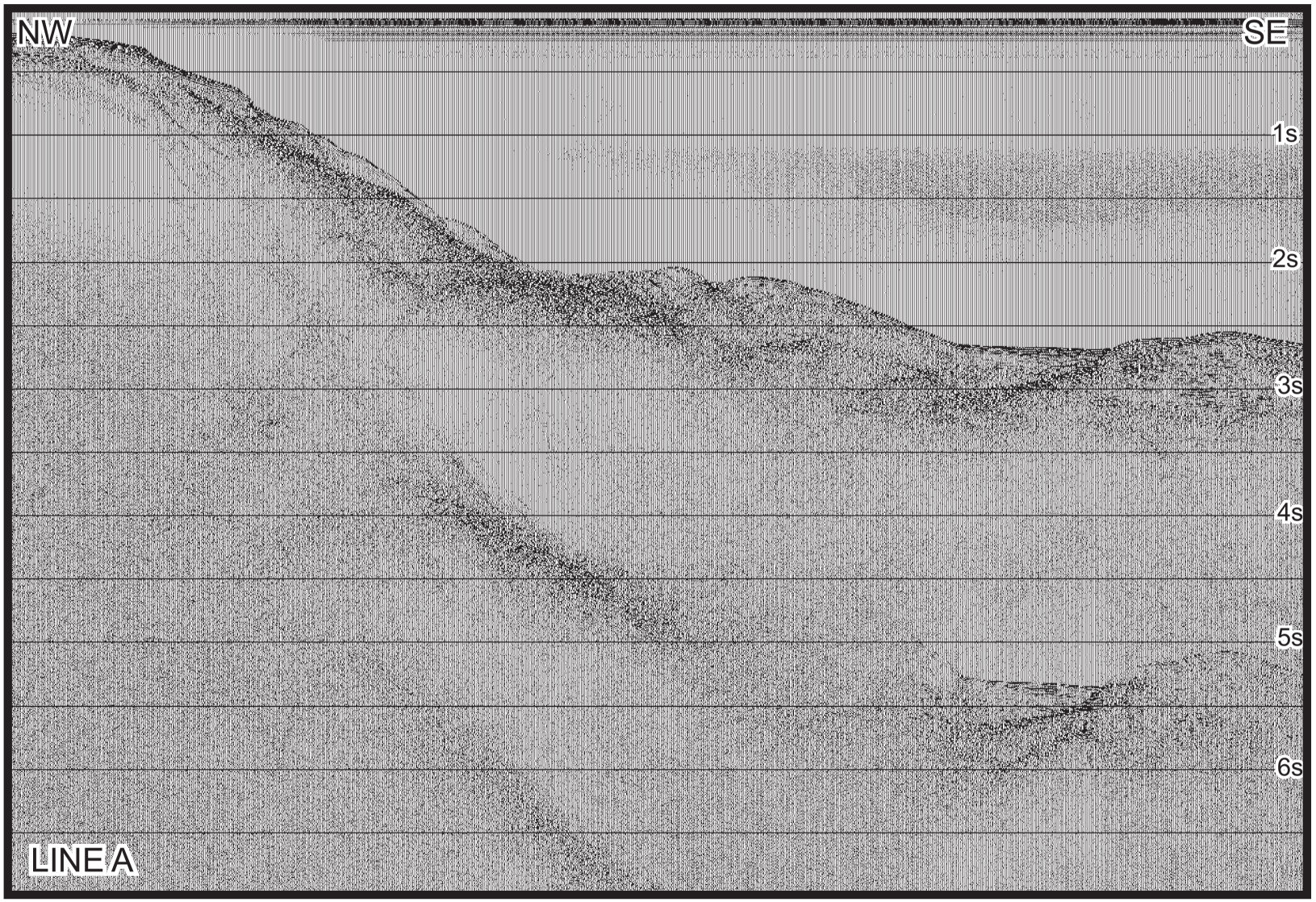

Figure 3.6: Near-trace gather for Line A showing first glimpse of sub-surface geology(location shown in Fig. 3.1).

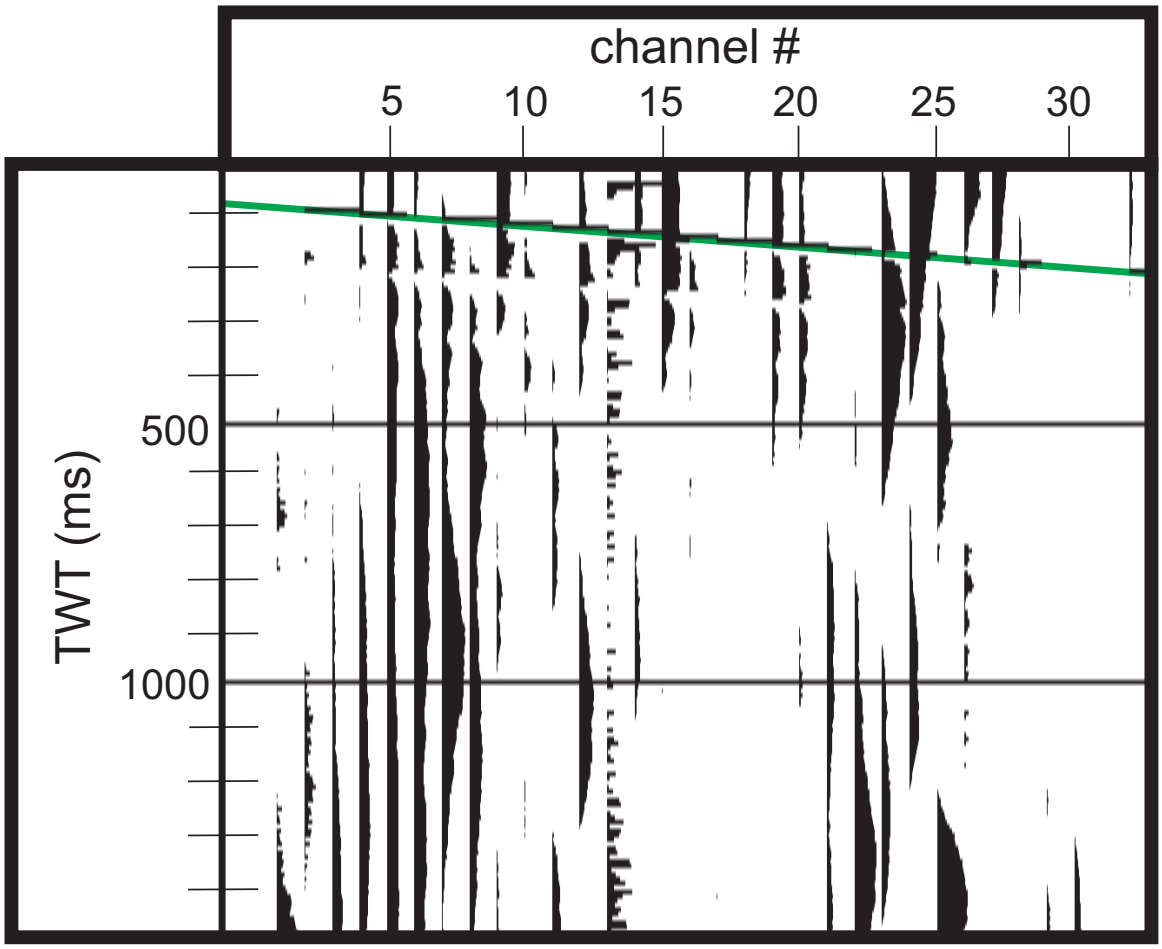

Figure 3.7: Zooming in on the deep water raw shot record shown in Fig. 3.4, it is seen that the actual arrival time of the direct wave is approximately 80 ms.

Automatic gain control (AGC) is also useful for amplifying attenuated signal at depth. For this data set, a 500 ms window is found to be ideal. Like the frequency filter, AGC is not permanently applied to the data early in the processing sequence; instead, it is used as a display parameter until it is applied to the image during the final output.

3.2.3 Results of primary processing

The results of primary processing on the raw shot gathers are shown in Figure 3.8.

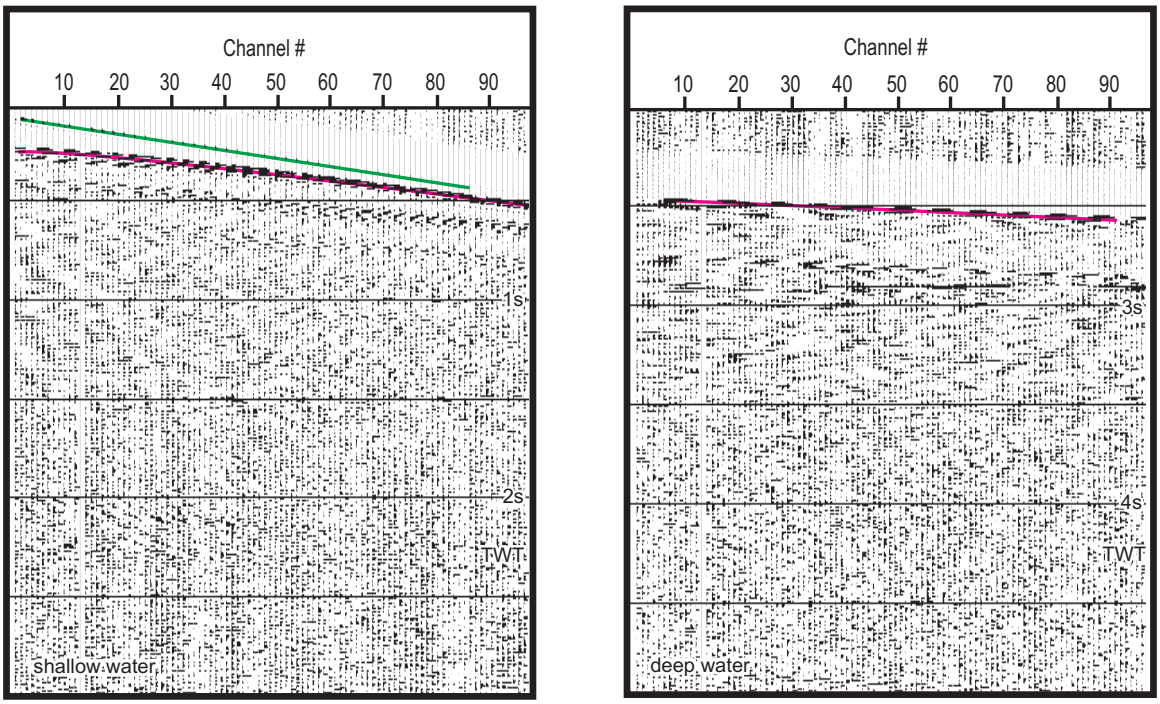

Figure 3.8: Shallow water (left) and deep water (right) shot gathers with AGC, frequency filtering and primary processing (spherical divergence and statics corrections) applied. Shot gathers have been enlarged to show only 3s recording time each. Note: (1) the low frequency noise which dominated the raw shot gathers in Fig. 3.4 has been attenuated; (2) low amplitude deeper reflections have been enhanced.

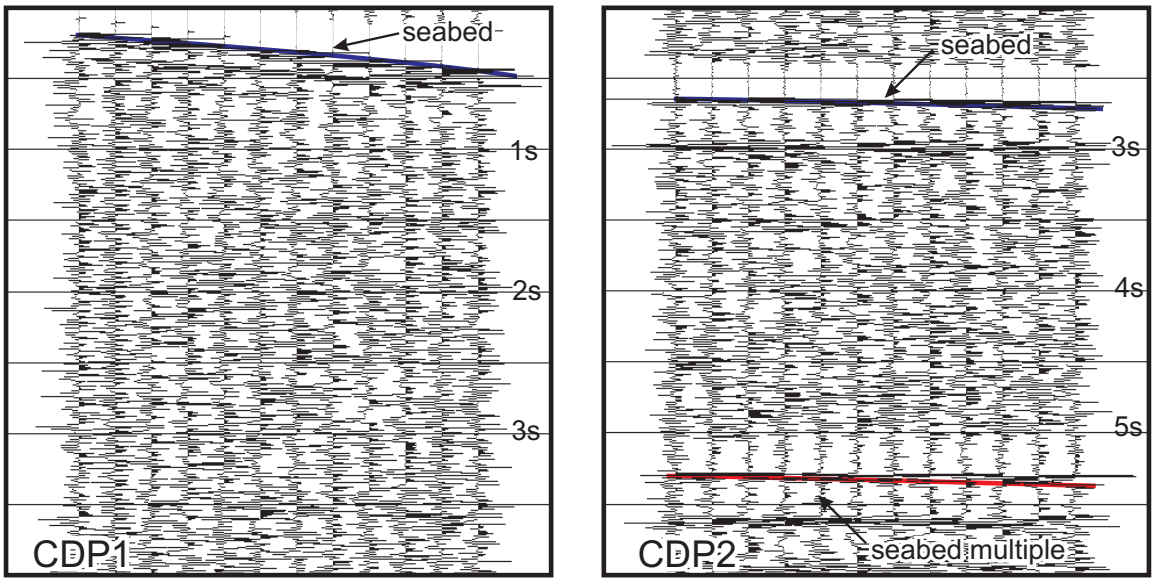

Figure 3.9: CDP gathers from shallow (CDP1) and deep water (CDP2). Seabed is highlighted in blue; seabed multiple is highlighted in red. Note how the normal move out observed in the seabed reflection is higher in shallow water (left).

3.3 Geometry and CDP sorting

Since the survey grid lines are approximately linear and sub-parallel, specific survey navigation coordinates were not required for processing this data set. Instead, the survey geometry was entered into ProMAX's *2D Marine Geometry Spreadsheet* and headers were created using relative floating coordinates. CDPs imaged by different shot-receiver pairs were grouped together (e.g. Fig. 3.9).

Note that the CDPs referred to in this context are actually CMPs (or common mid points). Processing these CMPs as though they were CDPs creates artifacts on the seismic record from mispositioned reflectors. Repositioning of the true locations of subsurface depth points does not occur until after stacking (further discussed below); however, for the purpose of this discussion it will be assumed that CDP $\approx$ CMP.

3.4 Velocity analysis and NMO correction

A near-trace gather with CDP labels was used to approximate the location of near-horizontal surfaces on the seafloor and other important reflectors. These representative CDPs were used as the central traces in nine-trace supergathers. When fold is small and dips are low (i.e. quasi-horizontal surfaces), supergathers generate more accurate velocity analyses by increasing S/N ratio. ProMAX calculates velocity semblance as well as constant velocity stacks for each input CDP location (e.g. Figs.3.10 and 3.11). For shallow depths, choosing the peaks in the velocity semblance is generally trivial and often generates a good velocity function. However, as seen in Figures 3.10 and 3.11, velocity semblance spreads out with depth and it becomes progressively more difficult to obtain accurate velocity functions deeper in the seismic sections. Because of this, picking good velocity functions was extremely tedious as it was necessary to simultaneously compare results for the velocity semblance, constant velocity stacks and the CDP gather.

ProMAX interpolates between each velocity pick to obtain a continuous velocity function for the data set. Abrupt velocity changes (either temporal or lateral) were not well-tolerated; simple velocity functions, where possible, were best and yielded the best stacks.

3.5 Stacking

Each CDP in the data set was NMO-corrected and stacked using the velocity functions obtained during velocity analysis (e.g. Fig. 3.13); a 30% mute was applied during the stacking process to eliminate noise from NMO-stretching. While the stacked section has a higher S/N ratio, it was distorted by mispositioned dipping

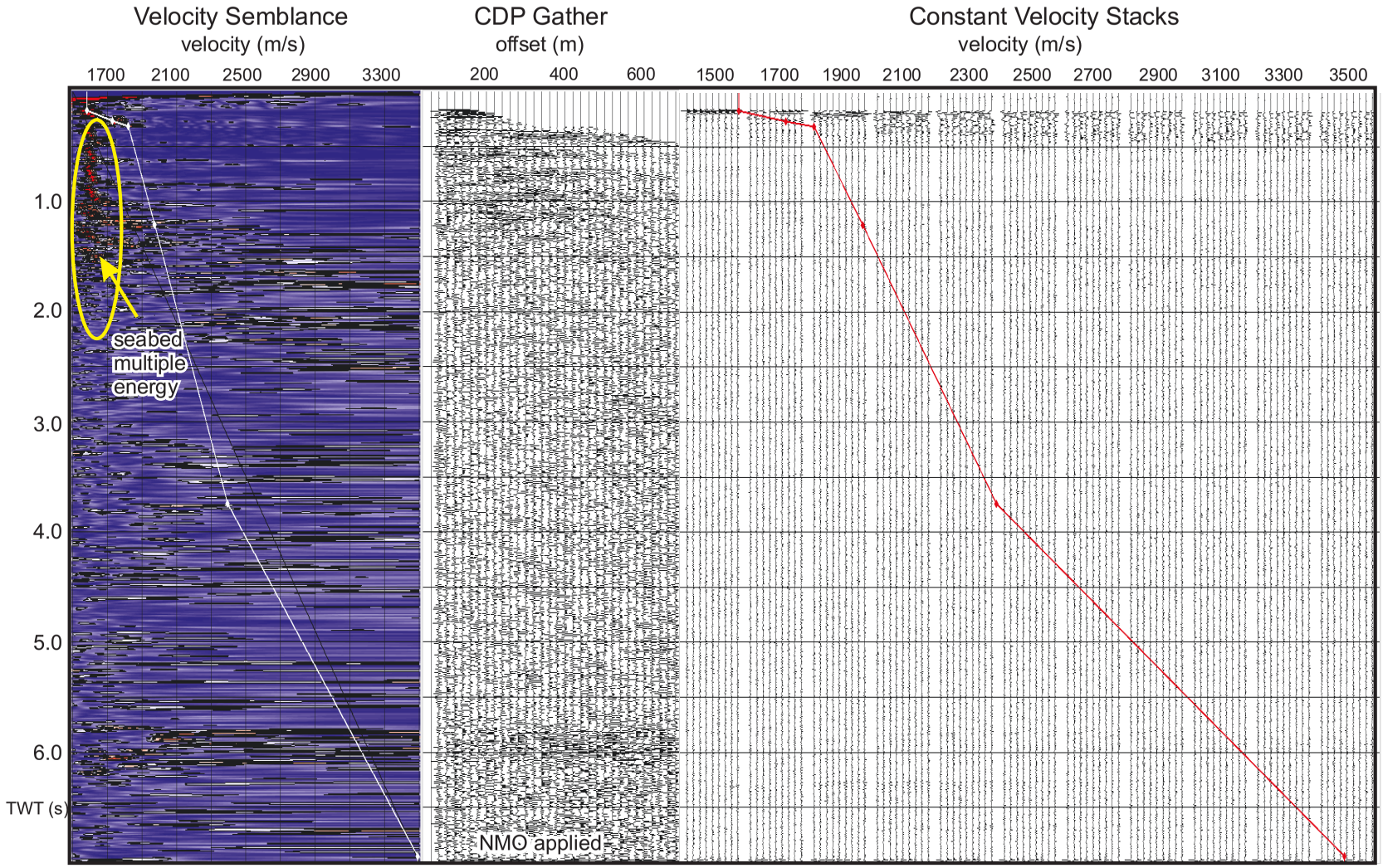

Figure 3.10: Velocity analysis in shallow water. Note the energy from the seabed multiples in the shallow section of the velocity semblance. It is important here to choose velocities which are a little high to ensure maximum multiple suppression.

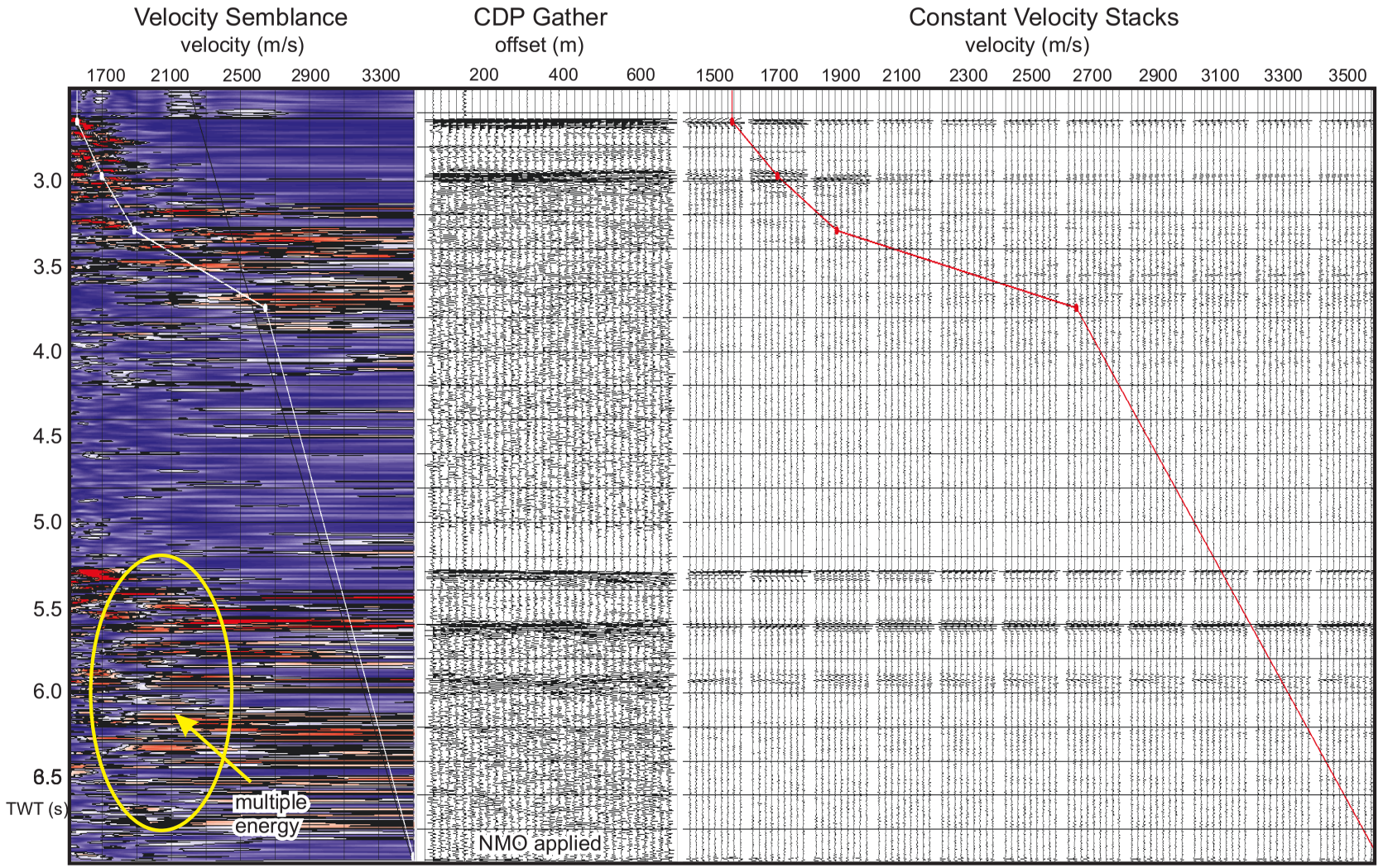

Figure 3.11: Velocity analysis in deep water.

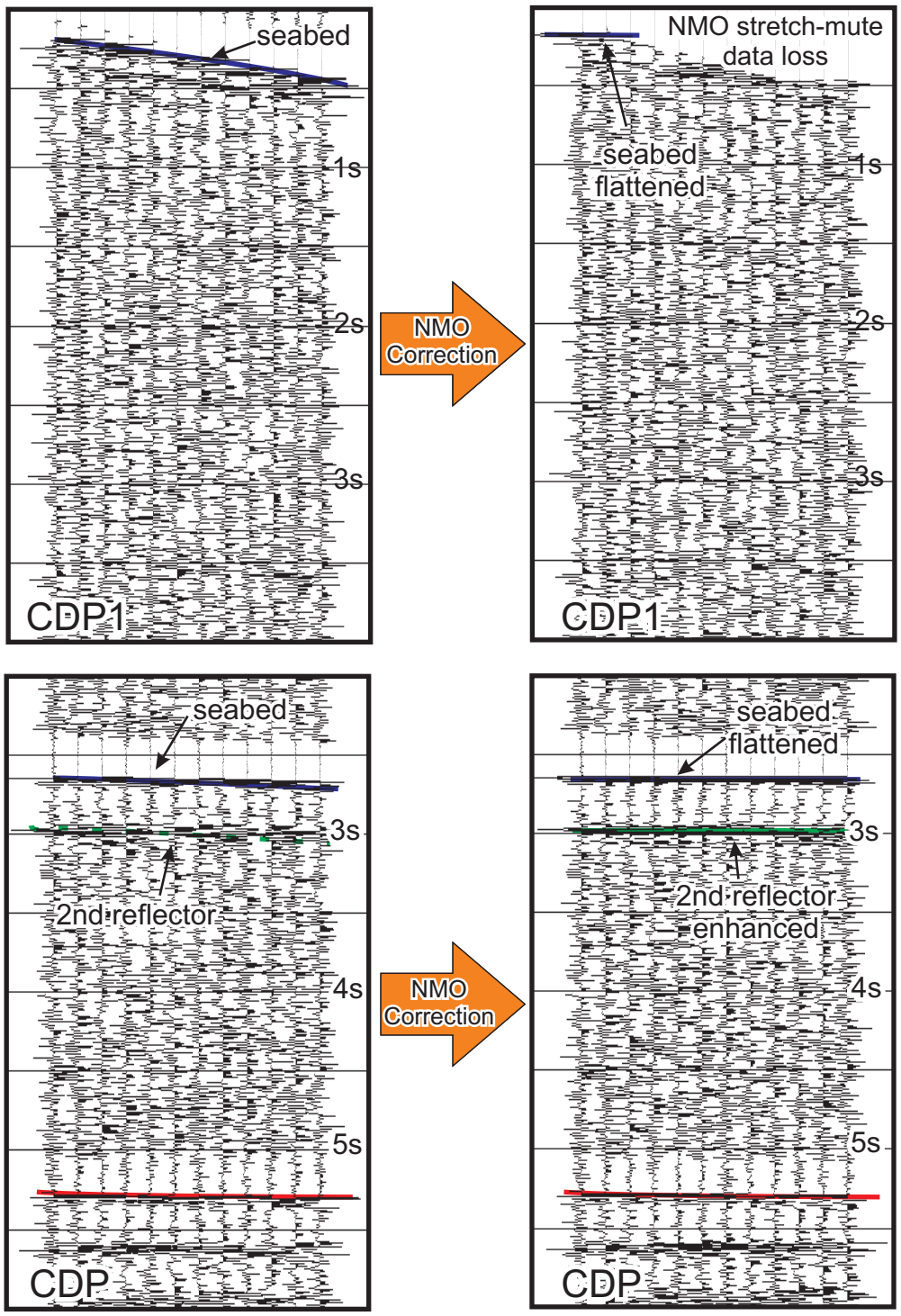

Figure 3.12: NMO-corrected CDP gathers in shallow water (top, CDP1) and deep water (bottom, CDP2)

reflectors, bowties, and diffraction hyperbolae generated by point sources (e.g. Fig. 3.14). Migration was required to reposition data points for a best approximation to the true subsurface geology.

3.6 Migration

Compared to other processing flows, migration is quite computationally intensive. Because it is also iterative, obtaining a well-migrated section can be very time consuming. In the interest of saving time, Stolt migration can be used to estimate the migration-velocity model for the much slower, but more effective, Kirchhoff algorithm. In this method, the stack is quickly Stolt-migrated at various relevant velocites (e.g. 1500 m/s, 1600 m/s, 1700 m/s, etc) and estimates of migration velocities for pertinent reflectors are obtained by careful examination of each of the migration outputs. This first estimate is then input into the Kirchhoff migration flow. The Kirchhoff-migrated image is then checked for improperly migrated features such as bowties (if the migration velocity is too low) and smiles (if the migration velocity is too high), and the velocity function is edited accordingly. The Kirchhoff migration is re-run after appropriate velocity edits until an acceptable final image is obtained (e.g. Fig. 3.14).

While Stolt migration is indeed less computationally intensive than Kirchhoff, the migration algorithms are also sufficiently different that the constant-velocity estimates obtained from Stolt migration consistently over-migrate in the Kirchhoff flow. With practice, it is possible to skip the Stolt migration step entirely by identifying several prominent marker reflectors and using migration velocities determined for similar marker reflectors on adjacent seismic reflection profiles for the initial velocity estimate (e.g. in the western Antalya Basin, the M-reflector is found to migrate at approximately 1650 m/s). Of course, migration velocities for the same reflector will

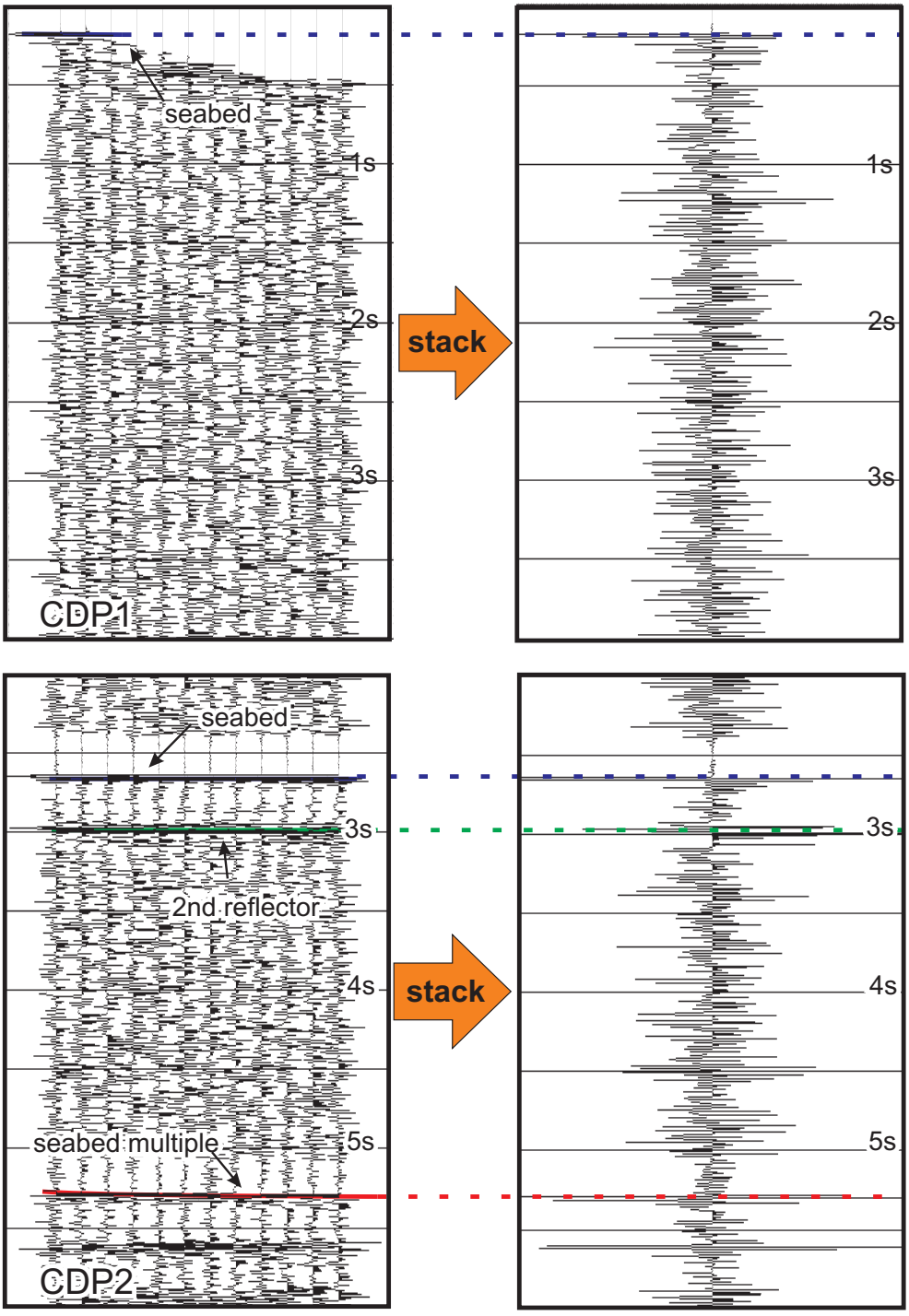

Figure 3.13: NMO-corrected CDP gathers are stacked to increase S/N ratio.

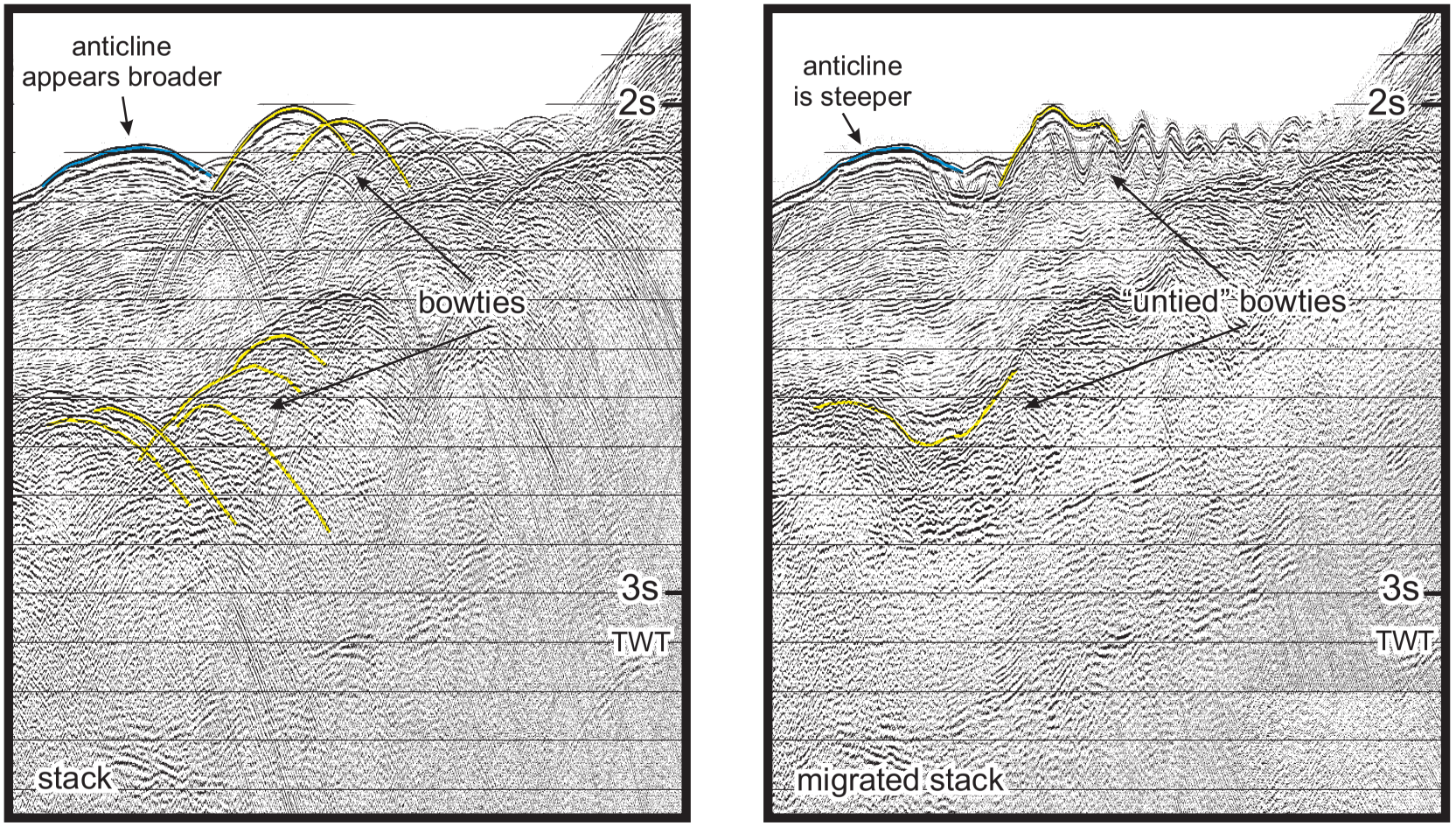

Figure 3.14: The stacked section (left) shows bowties and reflectors dip at incorrect angles. In the migrated section (right), diffraction hyperbolae are collapsed and reflectors are repositioned nearer to their true subsurface locations.

vary slightly depending on the location, depth, etc., but quite often it will only require a few small tweaks to obtain a good migration. Like the stacking velocity function, a simple migration velocity function yields the best results. Abrupt lateral or temporal velocity variation produces undesirable results and increases computational time.

3.7 Deconvolution

The wavelet generated by the 2008 source was not minimum phase; therefore, spiking deconvolution was not attempted on this data set. Predictive deconvolution has been previously found to be ineffective in eastern Antalya Basin due to the complex geology in the region (Işler, 2005). Although it was likely that results from deconvolution would be similar in the similarly complex western Antalya Basin, several predictive deconvolution trials are performed. These trials included both pre- and post- stack deconvolutions where operator length and prediction distance relative to the seafloor are varied.

A short-gap (small operator length) deconvolution was applied to the data pre-stack. An operator length of 8 ms was chosen (from second zero-crossing of autocorrelation function) to compress the wavelet and reduce ringing on the seismic reflection profiles. Predictive deconvolution aimed at multiple removal (by increasing the operator length) was minimally effective and sometimes introduced very strange noise which obscured primary reflections (e.g. Fig. 3.15). Because of the ineffectiveness in this study area and the introduction of noise, no longer-gap deconvolution is applied to any of the 2008 seismic reflection profiles in the western Antalya Basin.

Adaptive deconvolution had been particularly effective for seabed multiples in the Cilicia Basin (e.g. Piercey, M.Sc. thesis, 2010). Unfortunately, in the western

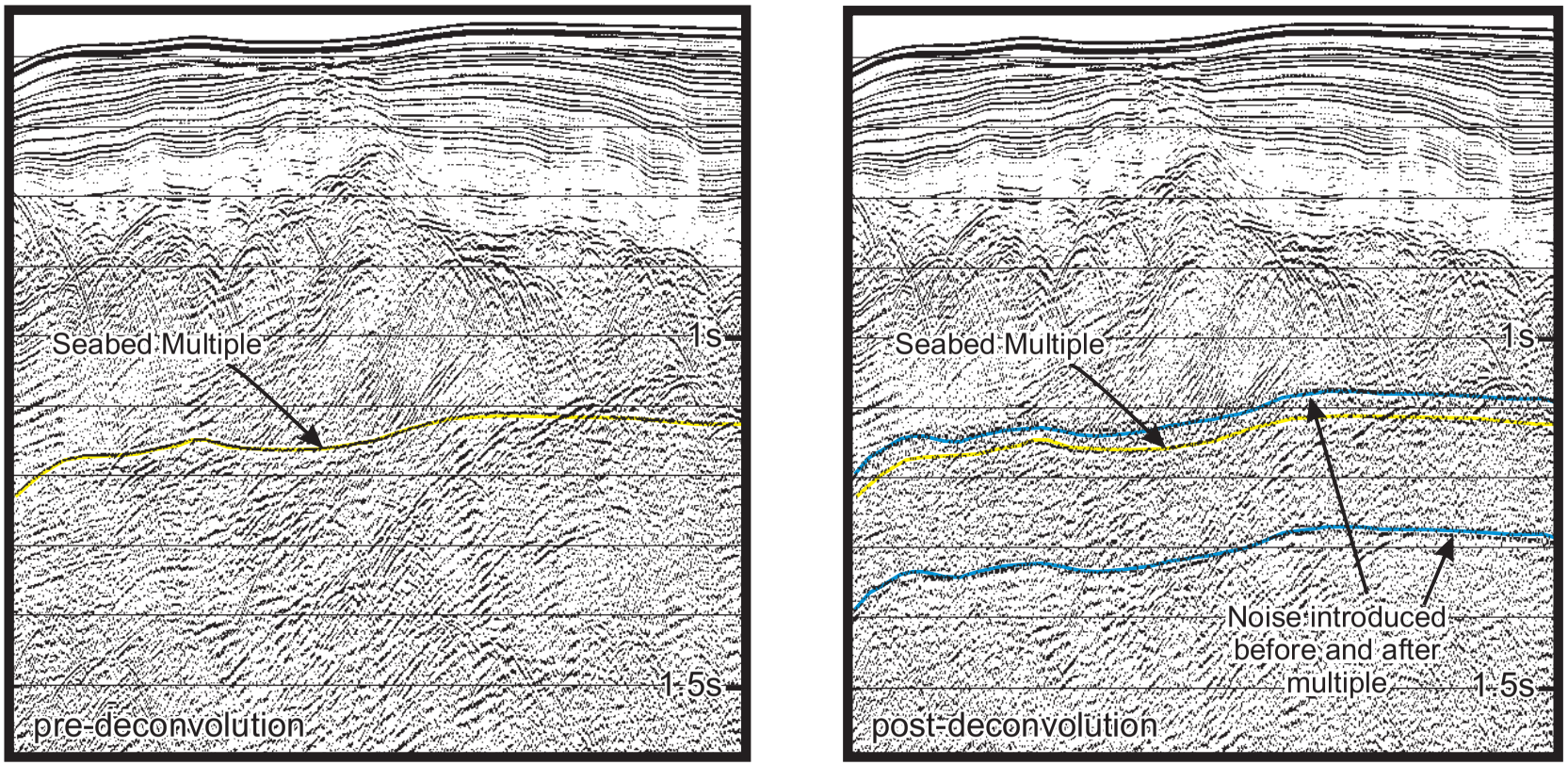

Figure 3.15: Pre-deconvolution screenshot (left) and post-deconvolution screenshot (right) show strange noise (blue) introduced to the data by the deconvolution algorithm. Note first seabed multiple (yellow).

Antalya Basin, parameters which were very successful in multiple attenuation caused considerable signal loss and were therefore not used.

3.8 Multiple removal

In addition to deconvolution, various other multiple removal techniques were attempted on the data including WEMR and FK-filtering. While WEMR was quite effective at estimating the location of the seabed multiples, the algorithm for subtracting the appropriate amplitudes from the data was poor. Consequently, the application of WEMR to the data set did not result in any measurable multiple suppression and was therefore not applied to any line.

Due to either (a) ineffectiveness at multiple suppression or (b) introduction of noise obscuring primary reflections, no multiple-removal processes were applied to the 2008 western Antalya Basin data set. Multiple suppression in this data set was achieved in varying degrees with careful choice of NMO velocities during the stacking process. Because the bulk of the data is in deeper water, most of the multiples arrive near the end of recording time and do not obscure pertinent primary reflections; thus, for this data set, multiple removal was, generally, not integral to the success of the processing sequence. Where multiple removal would have been beneficial is near the continental shelf and slope where seabed multiples in the shallower water sometimes cause significant interference with primary reflections.

3.9 Processing difficulties

The geology of the western Antalya Basin is complex and varied. Seabed TWTs in a single seismic reflection profile range from approximately 100 ms along the shelf to 3000 ms and greater toward the basin (e.g. Fig. 3.16). This marked

bathymetric variation is echoed in the underlying sediments and generates steeply dipping reflectors on the present-day seabed as well as the paleo-seabed surface (e.g. Fig. 3.16). Steeply dipping reflectors make processes such as deconvolution and other multiple removal processes extremely challenging and quite often, as in the case for this data set, completely unsuccessful. However, multiples which remain on the seismic record are generally readily identifiable and highlighted during interpretation; seabed multiples are generally readily recognised from their travel time being exactly double that of the seabed reflection.

3.10 Depth conversion

Good depth conversion required reliable interval velocity functions. While results from stacking were generally good, velocity functions obtained from this data set are not very accurate. This is due in part to the short streamer and subsequent low fold and small spread length. Furthermore, most of the seismic reflection profiles are located in deeper water where NMO is already low. Due to poor resolution of the velocity functions (especially at depth), depth conversion is not especially useful for this dataset. Lack of depth conversion means decreasing vertical exaggeration in time. This is especially important to keep in mind when interpreting growth strata or fault trajectories within Unit 3. For example, a planar fault would appear as a straight line in a depth section, but would appear listric (concave upward) in a time section. If required, depth can be approximated using the following interval velocities reported elsewhere in the eastern Mediterranean: Unit 1 - 2000 m/s; Unit 2 - 4200m/s; and Unit 3 - 3000-3500m/s.

3.11 Final display

A top-mute 20 ms above the seabed was constructed for each seismic reflection profile. This ensured a cleaner-looking final image. Before final output, the top-mute was applied to the data along with the 20 - 50 - 200 - 250 Ormsby bandpass filter and the 500 ms AGC filter. Figure 3.16 shows the final display for the fully processed Line A (location shown in Fig. 3.1). All seismic reflection profiles processed by the author are found in Plates 1-14 in the back of this thesis.

3.12 Summary

All data from the 2008 western Antalya Basin survey processed by the author has spherical divergence and static corrections permanently applied during the primary processing flow. All data is stacked and time-migrated using the iterative methods described above. Due to the lack of accurate velocity information deeper in the seismic sections, depth conversion is not performed on any lines. A pre-stack short-gap predictive deconvolution was applied to the dataset to reduce ringing at the seabed; however deconvolution at longer operator lengths was not applied because the process introduced noise and other artifacts which obscured primary reflections. For similar reasons, no multiple attenuation processes (e.g. WEMR, FK) were permanently applied on any of the 2008 seismic reflection profiles processed by the author. Final display parameters for the 2008 data processed for this thesis are a 20-50-200-250 Ormsby bandpass filter, a 500ms-window AGC and a 20 ms top mute above the seabed.

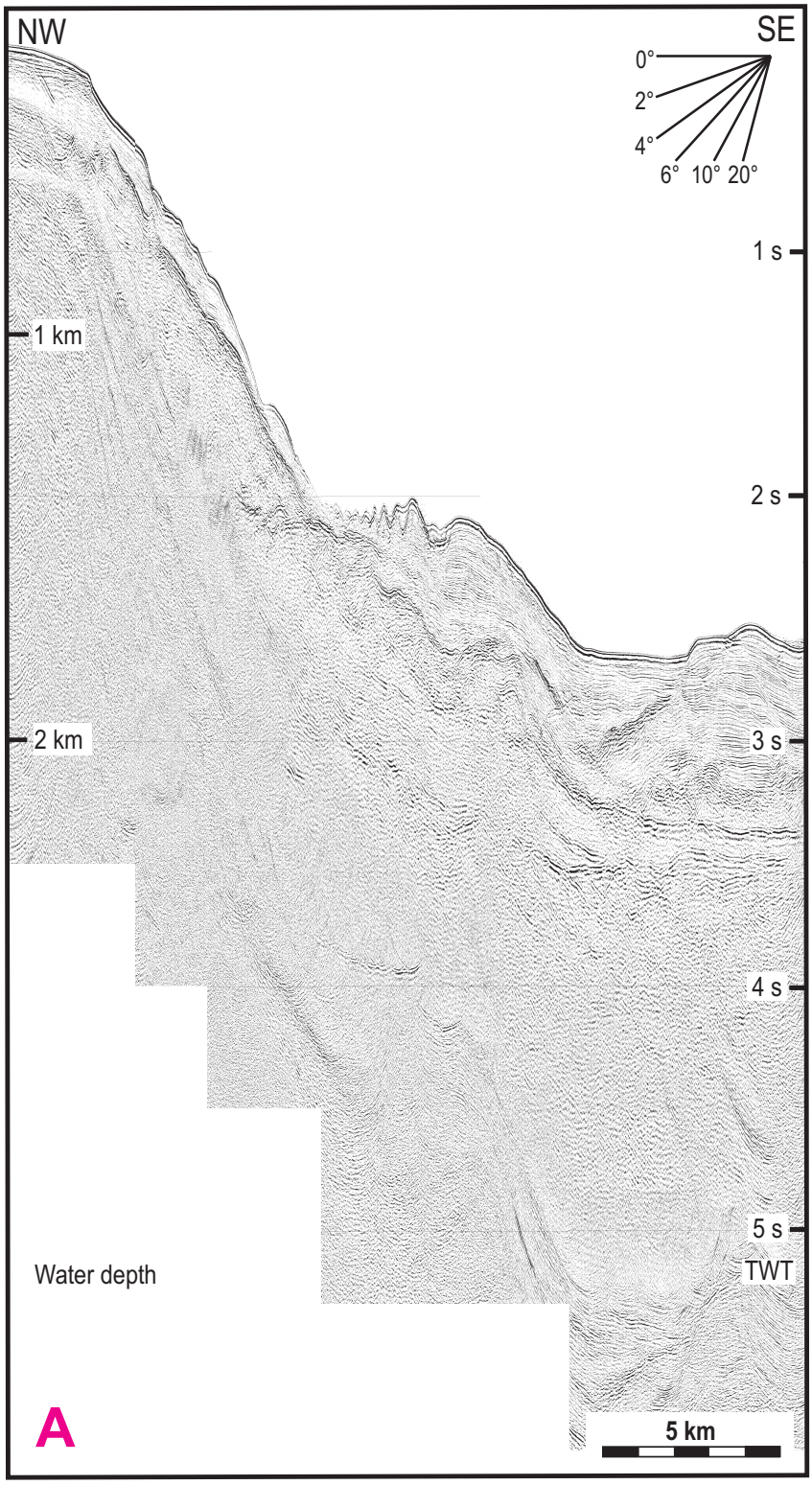

Figure 3.16: Fully processed Line A with final display parameters which include a 20 ms top-mute, a 20 - 50 - 200 - 250 Ormsby bandpass filter and a 500 ms AGC.

Chapter 4

Stratigraphy and chronology for the western Antalya Basin

The previous chapter outlined the methods for the acquisition, processing and geological interpretation of 2D seismic data. All data from the 2008 western Antalya Basin survey processed by the author has spherical divergence and static corrections permanently applied during the primary processing flow. All data was stacked and time-migrated using the iterative methods described above. Due to the lack of accurate velocity information deeper in the seismic sections, depth conversion was not performed on any lines. A pre-stack short-gap predictive deconvolution was applied to the dataset to reduce ringing at the seabed; however, deconvolution aimed at multiple removal was not applied to the data due to the introduction of noise and other artifacts which obscured primary reflections. For similar reasons, no multiple attenuation processes (e.g. WEMR, FK) were permanently applied on any of the 2008 seismic reflection profiles processed by the author. Final display parameters for the 2008 data processed for this thesis include a 20-50-200-250 Ormsby bandpass filter, a

500ms-window AGC and a 20 ms top mute above the seabed. Note that approximate velocities for depth conversion derived interval velocities reported elsewhere in the eastern Mediterranean are: Unit 1 - 2000 m/s; Unit 2 - 4200m/s; and Unit 3 - 3000-3500m/s.

This chapter describes how the chronostratigraphic framework for the region is established. This is accomplished using the seismic reflection profiles processed by the author with other archived seismic reflection profiles both from the Eastern Mediterranean Research Group and from industry. Fig. 4.1 shows all seismic lines used for this task. On the basis of acoustic character, stratigraphic position and location of the M- and N- unconformities, three distinct seismic units are identified in the Antalya basin: (1) Unit 1 - Pliocene-Quaternary siliciclastic successions; (2) Unit 2 - Messinian evaporites and interbedded siliciclastic successions; and (3) Unit 3 - undifferentiated pre-Messinian siliciclastic and carbonate successions. The lithostratigraphic composition and chronology of these units is determined through correlation with an onshore exploration well (location shown in Fig. 4.1). These units are further correlated with sedimentary successions identified in adjacent basins (e.g. Adana, Mesasoria, Cilicia, Latakia and onshore Antalya Basins; discussed in detail below).

4.1 Unconformities and seismic units in western Antalya Basin

4.1.1 The M- and N- reflectors

The M - and N - reflectors represent distinctive unconformities observed in seismic records across the entire eastern Mediterranean. The M-reflector, named by Ryan in 1969, marks the erosional surface which existed during the late Miocene

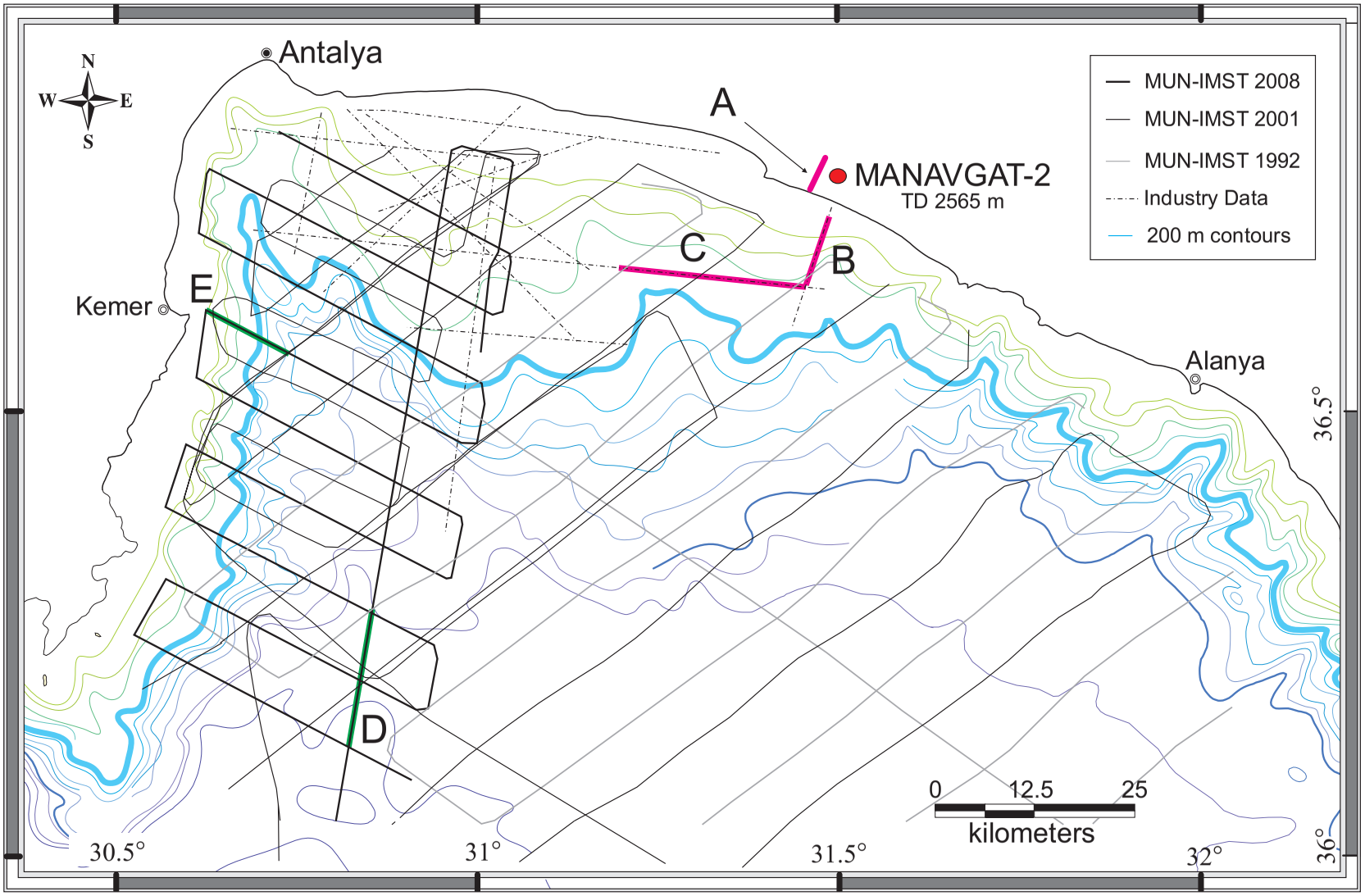

Figure 4.1: Map of the western Antalya Basin showing the location of the onshore industry exploration well and seismic reflection profiles presented in this chapter. Modified from Gogacz, unpublished.

(Messinian) when the closing and re-opening of the Gibraltar Straight caused a cyclic, nearly-complete desiccation of the entire Mediterranean Sea. Previous studies have shown that the M - reflector is a major unconformity separating the latest Miocene sequences from the younger Pliocene sedimentary successions (e.g. Hsü et al., 1978; Robertson, 1998a). In most of the Antalya Basin, the M-reflector images as a bright, laterally continuous, marker on almost all seismic profiles and serves as an important stratigraphic marker separating older, Miocene depositional sequences from younger, Pliocene-Quaternary sequences. In northwestern sections of the study area, however, extensive deformation of the subsurface makes this usually prominent marker more difficult to discern. In this area, the placement of the M-reflector is inferred using stratigraphic cut-offs and the thicknesses and acoustic character of the overlying and underlying sedimentary sequences (discussed further in Chapter 5). The N-reflector, where present, marks the base of the Messinian evaporites sequences associated with the repeated desiccation of the Mediterranean Sea. In the western Antalya Basin, the N-reflector images as a bright, continuous event on the seismic record and usually displays the opposite polarity of the M - reflector. Where present, the N-reflector marks the important stratigraphic marker which separates Upper Miocene depositional sequences from Middle-Lower Miocene sequences.

4.1.2 Seismic units of the western Antalya Basin

Based on their locations relative to the M - and N - reflectors, three distinct seismic units are identified in the western Antalya Basin (e.g. Fig. 4.2). Unit 1 is defined as the highly reflective package bounded below by the M-reflector; Unit 2 is the weakly reflective package confined between the M - and N - reflectors; and Unit 3 includes all reflectors below Unit 1 and Unit 2. These units and their chrono-stratigraphic correlations are discussed in further detail in the sections below.

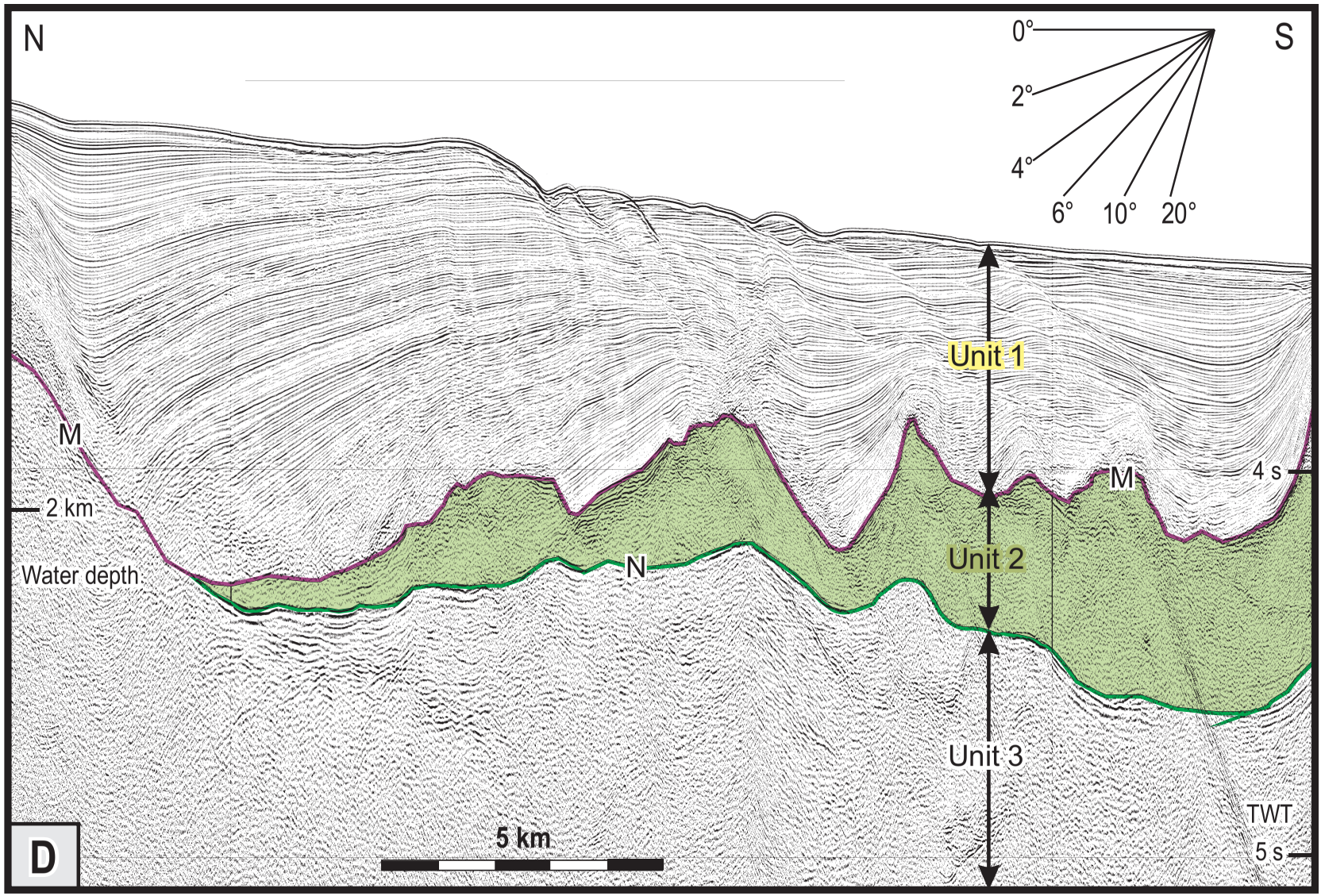

Figure 4.2: Seismic units of the western Antalya Basin. Location of profile shown in Fig. 4.1.

4.2 Establishing a chrono- and lithostratigraphic framework for the western Antalya Basin

The chrono- and litho- stratigraphic framework for the seismic units identified in the western Antalya Basin is established by the onshore - to - offshore seismic correlation of an industry exploration well (i.e. Manavgat-2 in Fig. 4.3) as well as direct comparison to the chrono-stratigraphic framework described in the literature for basins adjacent to the study area.

4.2.1 Manavgat-2 Well

The Manavgat-2 well was drilled to a total depth of 2248 m. It recovered approximately 204 m of loosely consolidated to unconsolidated claystone with a few sandstone interbeds. The succession is assigned to the Yenimahalle Formation with a Pliocene to ?Quaternary age (Fig. 4.3; Turkish Petroleum Corporation, unpublished data). Below this upper veneer, is an approximately 290 m-thick coarse siliciclastic succession composed of sandstones and shales with several volcanic tuff horizons. Although the sediments drilled in the Manavgat-2 well did not include any evaporites (such as the gypsum, anhydrite and carbonate alternates seen on outcrops, Deynoux et al., 2005; Çiner et al., 2008), on the basis of biostratigraphic information, this succession is correlated with the Upper Miocene Eskiköy Formation. The Eskiköy Formation is underlain by a 445 m thick siliciclastic succession consisting of sandstone, siltstone and claystone interbeds (Fig. 4.3). This succession is correlated with the Upper Miocene (i.e., Tortonian) Karpuzçay Formation (Turkish Petroleum Corporation, unpublished data). Below the Karpuzçay Formation the well recovered a siliciclastic succession, approximately 298m thick, with several well-defined lime-

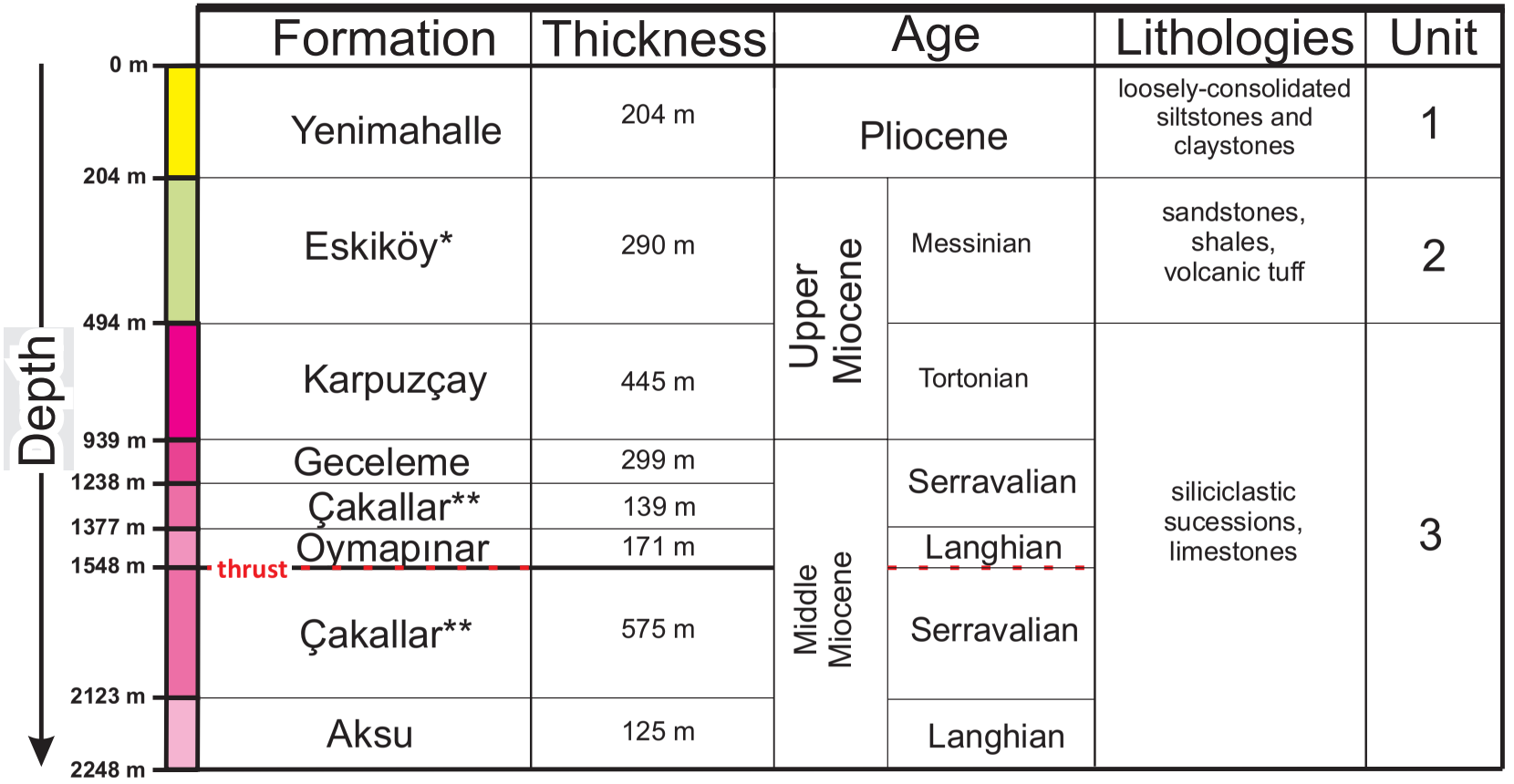

Figure 4.3: Lithologies recovered from the Turkish Petroleum Corporation Manavgat-2 exploration well with their approximate thicknesses and ages. Note the stratigraphic age reversal at 1548 m depth; this is interpreted by the Turkish Petroleum Corporation as evidence that a major Miocene thrust is intercepted by the Manavgat-2 exploration well.

stone beds, which in turn is underlain by a 138 m-thick siliciclastic succession with limestone interbeds (Fig. 4.3; Turkish Petroleum Corporation, unpublished data). These two successions are correlated with the Middle Miocene (Burdigalian Serravallian) Geceleme Formation and the Lower Miocene (Aquitanian to Langhian) Çakallar Formation (Fig. 4.3; Turkish Petroleum Corporation, unpublished data). These sediments are underlain by a 171 m-thick prominent limestone unit, which is well known in the Antalya Basin and its environs as the Oymapınar Formation (e.g. Çiner et al., 2008). At the base of the Oymapınar Formation the well recovered an additional 575 m thick siliciclastic succession which shows numerous limestone interbeds, correlated with the Çakallar Formation. This stratigraphic reversal is interpreted by the Turkish Petroleum Corporation as evidence that a major Miocene thrust is intercepted by the Manavgat-2 well. The well further recovered 125 m thick arenitic sandstone with limestone interbeds. This lower unit is correlated with the predominantly Langhian Aksu Formation (Turkish Petroleum, unpublished data (Fig. 4.3).

These lithologies can be separated into three distinct chrono-stratigraphic units which can be correlated to the seismic units seen in the western marine Antalya Basin: (1) Pliocene-Quaternary siliciclastics; (2) Messinian evaporites with interbedded siliciclastics; and (3) pre-Messinian Miocene siliciclastics and carbonates.

4.2.2 Correlation with seismic data

To facilitate correlation of the onshore stratigraphic units found in the Manavgat-2 well with the seismic units identified in the marine Antalya Basin, three industry seismic reflection profiles are used (i.e. A, B and C shown in Fig. 4.1). Depth-to-time conversion of the well depths is executed using RMS velocities reported in the industry data, allowing an immediate correlation of the exploration well with the onshore industry seismic reflection profile (i.e. A in Fig. 4.1). Using crossover points of the

industry profiles, the M- and N- reflectors are correlated across industry profiles in the northeastern Antalya Basin (i.e. B and C in Fig. 4.1) into the study area. Jump correlation based on seismic reflection character is used to cover gaps in the continuity of the Messinian sequences. The three chrono-stratigraphic units identified in the exploration well correlate to the three seismic units identified in the study area: seismic Unit 1 correlates to the Pliocene-Quaternary silicilastic successions; seismic Unit 2 correlates to the Messinian evaporite and interbedded siliciclastic successions: and seismic Unit 3 correlates to the pre-Messinian Miocene siliciclastics and carbonates.

4.2.3 Correlation with surrounding areas

There is some confusion surrounding the nomenclature of the litho-stratigraphic Neogene successions of the Antalya Basin and its surrounding area where successions of the same age have been given varying formation and member names by different authors. Therefore, the chrono-stratigraphic chart displayed in Figure 4.5 is a best summary of the pre-existing stratigraphy of the greater Antalya Basin area. What is reported as the Eskiköy Formation in the Manavgat-2 well (Turkish Petroleum, unpublished data) is also commonly referred to as the siliciclastic Taşlık Formation and its lateral evaporitic equivalent the Gebiz Formation (Akay et al., 1985a,b). Similarly, the Yenimahalle Formation in the Manavgat-2 well must also contain the stratigraphic equivalent sediments of the Antalya Tuffa and Alakilise Formations described in the Aksu, Köprü and Manavgat Basins. The use of Çakallar Formation by the Turkish Petroleum is actually incorrect, because Çakallar has been since described, instead, as a member located within the lowermost portion of the Geceleme Formation, immediately above the Oymapinar Formation (Karabiyikoglu et al., 2000).Further discussion of regional correlation can be found in §4.3.

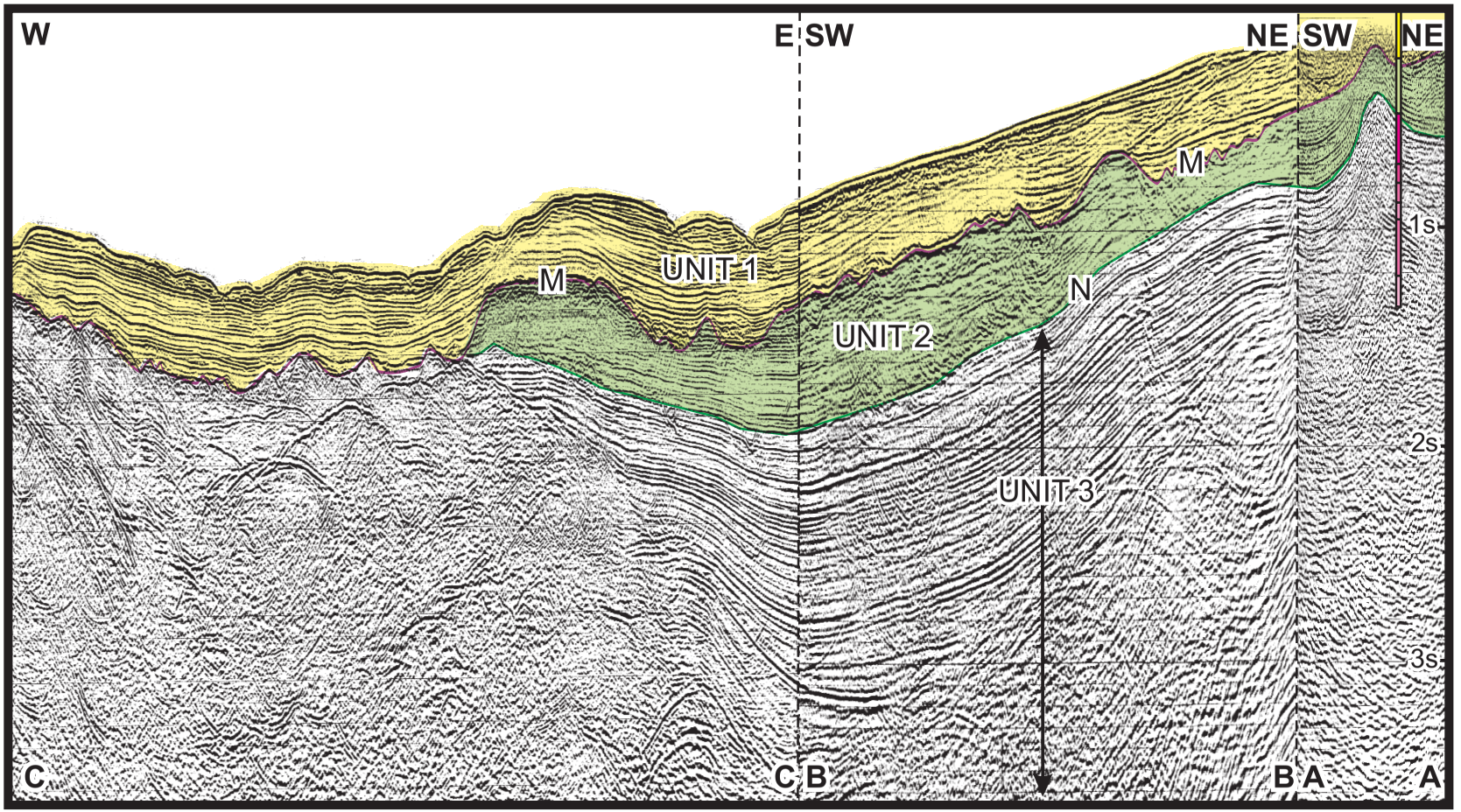

Figure 4.4: Correlation of the stratigraphic units of the Manavgat Basin to the seismic units observed in the marine Antalya Basin (unpublished industry data). Location of profiles shown in Figure 4.1 Modified from Gogacz, unpublished thesis.

.

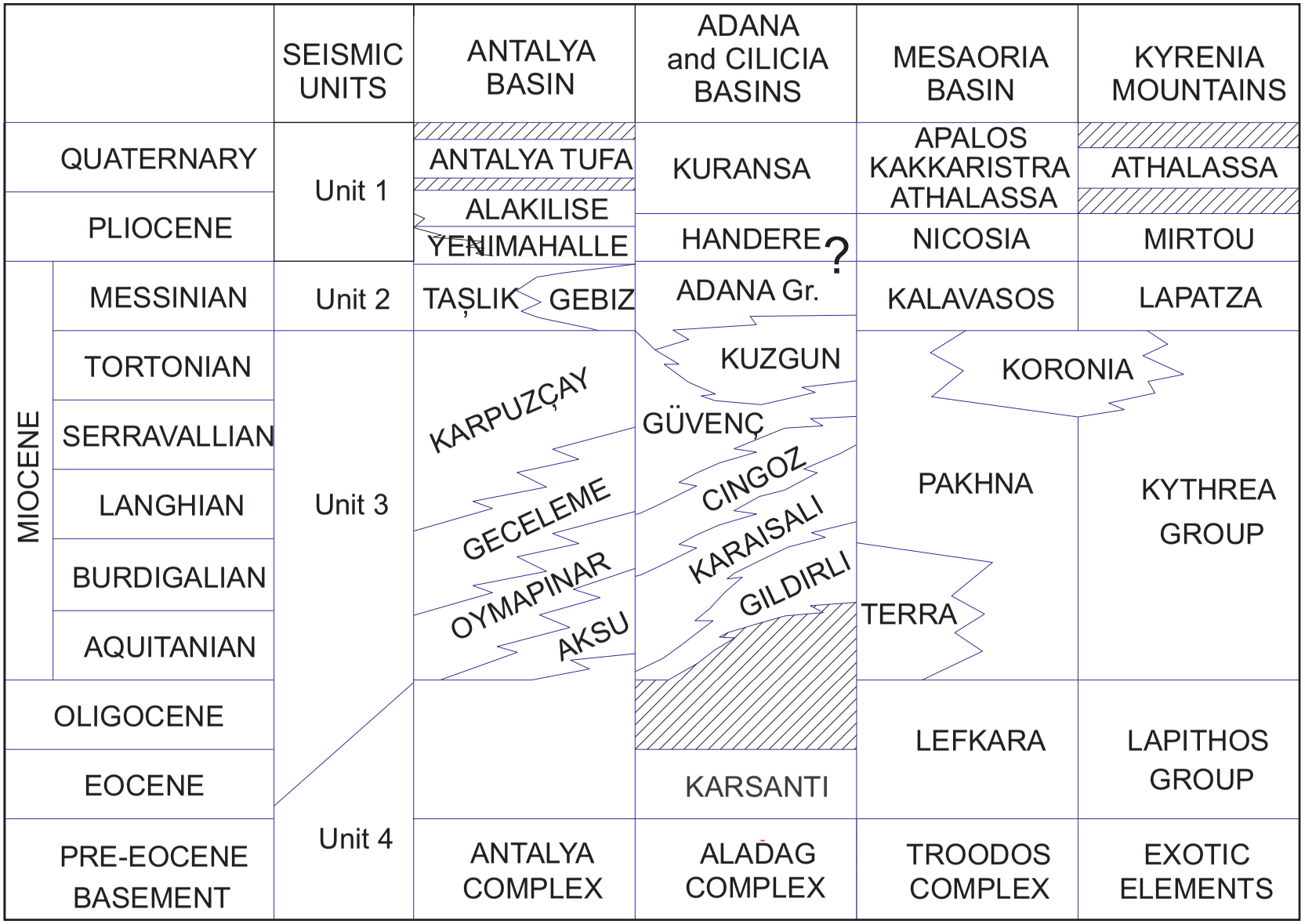

Figure 4.5: Chrono-stratigraphic chart summarizing the reported stratigraphy of the greater Antalya Basin area including the onshore Antalya Basin (Yalcin and Gorur 19 ; Kozlu, 1987), the Adana Basin (Gokcen et al., 1988), the Cilicia Basin (Kozlu, 1987), the Mesaoria Basin (Kozlu, 1987; Yilmaz et al., 1988) and the Kyrenia Mountains (Yilmaz et al., 1988).

4.3 Chronostratigraphic units of the western Antalya Basin

Figure 4.2 shows the three seismic units identified in the western Antalya Basin: Unit 1 - Pliocene Quaternary siliciclastics; Unit 2 - Messinian evaporites; and Unit 3 - pre-Messinian Miocene siliciclastics and carbonates. These units are discussed in detail below.

Note that there is evidence in the literature that the lower part of Unit 1 may contain sediments deposited during the latest stage of the Messinian Salinity Crisis, the *LagoMare* event (e.g. Cipollari et al., 2013; Cosentino et al., 2013). Although this thesis proceeds as though the first siliciclasic deposits above the M-reflector are Pliocene, the reader is cautioned that they may, instead, be of latest Messinian age.

4.3.1 Unit 1: Pliocene-Quaternary siliciclastics

The youngest succession identified in the Antalya Basin is characterized by a strong reflections, laterally continuous package of high-frequency reflections extending from the seabed to the M-reflector (e.g. Fig. 4.2). This unit is imaged on all seismic profiles. Based on well data, this unit is composed of the predominantly siliciclastic successions correlated with the Yenimahalle Formation of the onland Aksu, Köprü and Manavgat Basins (Figs. 4.3 and 4.5). In a more regional context, this unit is further correlated with: Kuranşa and Handere Formations of the Adana and Cilicia Basins; the Anthalassa and Nokosia Formation of the Mesaoria Basin; and the Mirtou Formation of the Kyrenia Mountains in Northern Cyprus.

The thickness of the Pliocene-Quaternary package varies across the study area (Fig. 4.6). In general, Unit 1 is thinnest along the continental shelf and slope and

thickest toward the basin. The thickest package of Pliocene-Quaternary sediments in the study area is found along the broadly NW-SE-trending axis of the bathymetric channel in the western Antalya Basin. There is also a thick package of Unit 1 sediments in the shallower northern continental shelf area.

4.3.2 Unit 2: late-Miocene, Messinian evaporites

Visible on many, but not all, seismic profiles from the study area, is a unit characterized by a weakly reflective package displaying complex internal architecture with often discontinuous and chaotic reflections that is bounded above by the M-reflector and below by the N-reflector (e.g. Fig. 4.2). Reflections in with this unit have, in general, lower frequencies than the overlying Pliocene-Quaternary successions. Based on correlations with the Manavgat-2 well and the existing work onland (Akay et. al., 1985; Karabıyıkoğlu et. al., 2000), this unit is inferred to be composed mainly of halite, with alternating smaller layers of anhydrite and limestone, deposited in the Late-Miocene (Messinian). Unit 2 is correlated with the siliciclastic successions which show interbeds of anhydite, gypsum (and/or gypsiferous siliciclastics) and calcareous sediments of the Taşlık and Gebiz formations described in the onland Aksu, Köprü and Manavgat Basins (Akay et. al., 1985; Karabıyıkoğlu et. al., 2000). In a regional context, this unit is further correlated with the Adana Group of the Adana and Cilicia Basins; the Kalavasos Formation of the Mesaoria Basin; and the Lapatza Formation of the Kyrenia Mountains (i.e. Fig. 4.5).

Outside of a small southern region of the study area (discussed in detail in Chapter 5), the presence of Messinian evaporites in the study area is sporadic. Where Unit 2 can be identified on one profile, it often appears to be completely absent on an adjacent profile. This makes mapping the Messinian sequences across the

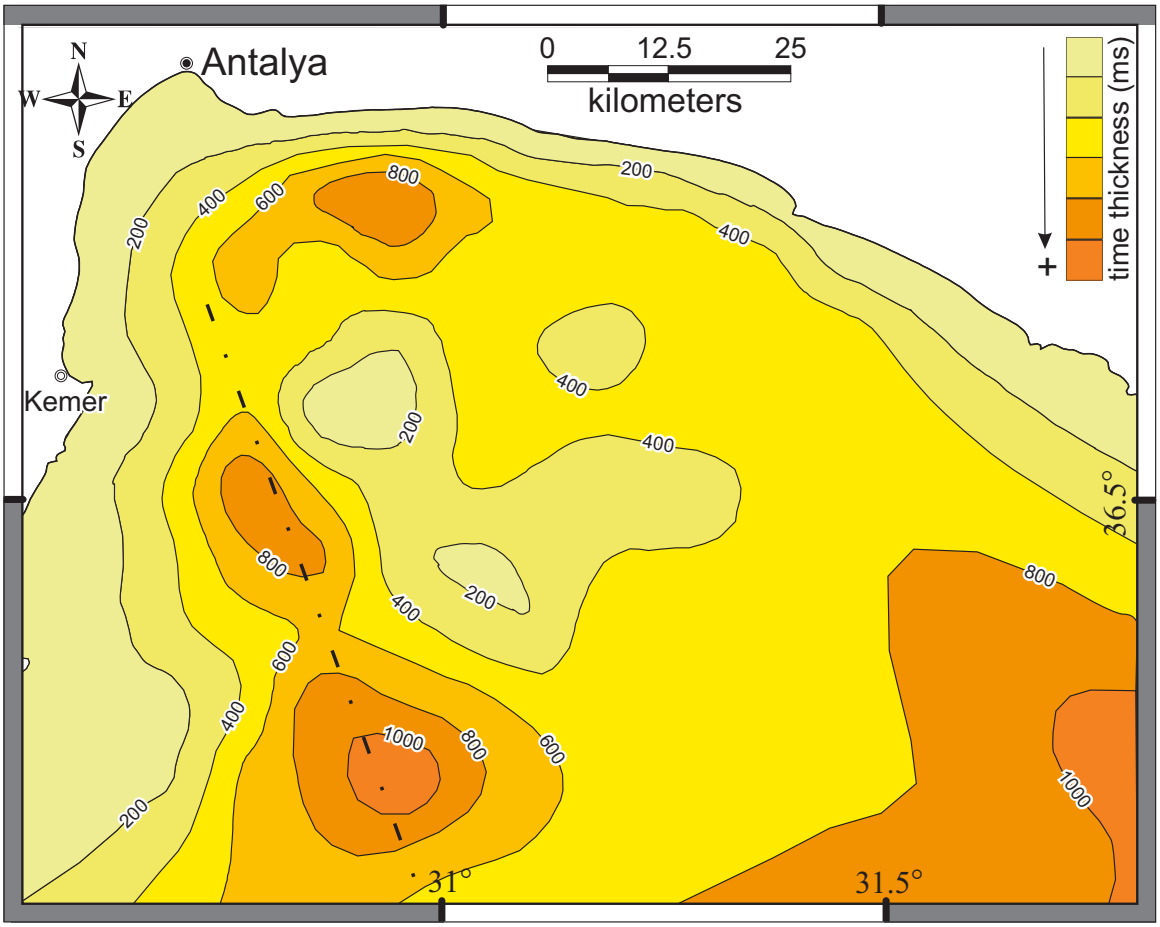

Figure 4.6: The thickness of the Pliocene-Quaternary successions offshore is varied across the study area. In general, Unit 1 is thickest toward the basin and thinnest along the continental shelf and slope. The axis of the bathymetric channel in the western Antalya Basin is shown as a dotted line. Time thicknesses were calculated from the MUN seismic data shown in Fig. 4.1. NB: The coastline, outlined in black, does not represent the true zero-thickness contour.

western Antalya Basin very difficult and does not provide for insight on the thickness variability of Unit 2 throughout the study area.

4.3.3 Unit 3: pre-Messinian Miocene siliciclastics and carbonates

Unit 3 comprises of the oldest succession(s) imaged in the Antalya Basin. In most of the study area, i.e. the eastern and central areas of the study area, seismic reflection profiles show this unit is predominantly characterized by of a series of strongly reverberatory, high reflective, low amplitude reflections with significant lateral continuity (e.g. Fig. 4.2), juxtaposed with regions of intense deformation where lateral continuity is moderate, at best. Based on correlation with well data, this unit is inferred to be composed of siliciclastic and carbonate successions of the pre-Messinian Miocene age or older. There are several marker reflectors within Unit 3, but the sparse line spacing of industry seismic data combined with the lower penetration of the MUN seismic data prevents the regional mapping of these markers. However, the existing well data show that the uppermost layer of this unit is correlated with the Upper Miocene Tortonian Karpuzçay Formation while deeper layers of this unit are correlated with the Middle Miocene Geceleme, Oymapınar and Aksu Formations of the onland Aksu, Köprü and Manavgat Basins (Figs. 4.3, 4.4 and 4.5). In a regional sense, this unit is further correlated with: the Pakhna Formation (including the Koronia, Terra members) of the Mesasoria Basin; the Kythrea Group of the Kyrenia Mountains in Northern Cyprus (Bagnall, 1960; Follows and Robertson, 1990); and also the Elekdağ, Kasaba and Sinekli formations of the Kasaba Basin (Şenel, 1997; Şenel and Bölükbaşı, 1997; Fig. 4.5).

In the westernmost region of the study area on the continental slope/shelf, east of the Beydağları and Antalya ophiolitic complexes, Unit 3 is characterized by a

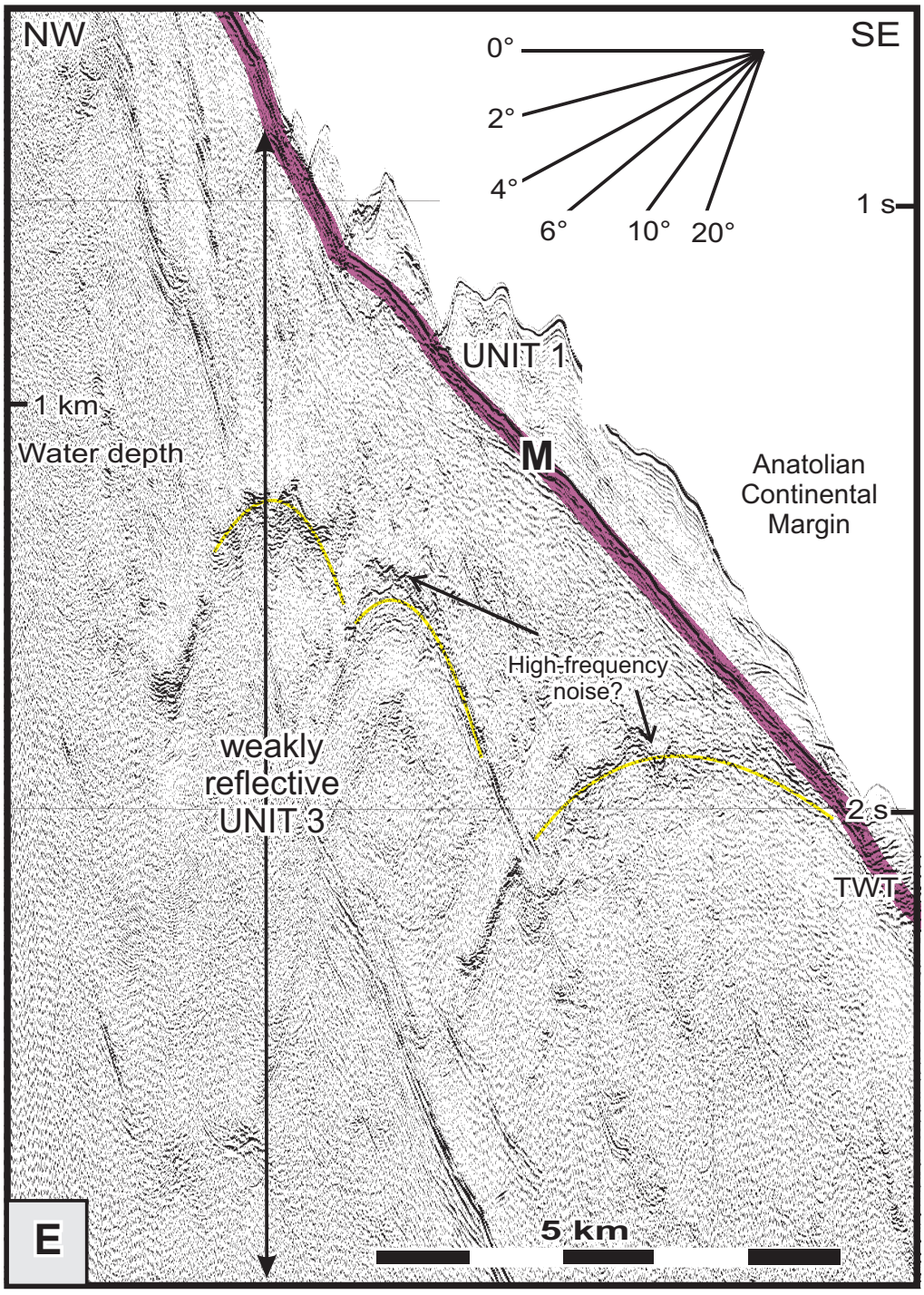

Figure 4.7: A seismic reflection profile from the westernmost Antalya Basin showing that Unit 3 in this region displays reverberatory and low-amplitude reflections which lack any significant lateral continuity.

reverberatory, low-amplitude package showing chaotic reflections without significant lateral continuity (e.g. Fig. 4.7). The chaotic nature of the unit with little coherent reflections is seen in both the industry and MUN seismic reflection profiles that are acquired both parallel and roughly orthogonal to the slope. There is no well data in the region to provide insight on the lithologies imaged in the western Antalya Basin, so their compositions are inferred based on the chaotic acoustic character of the unit in the region. It is speculated that the rocks that constitute the cores of the Beydağları and Antalya ophiolitic complexes extend into the western fringes of the marine Antalya Basin and that Unit 3 in this area includes the pre-Eocene basement rocks, including the Mesozoic shallow-water carbonates that form the core of the Beydağları and the Mesozoic ophiolitic and sedimentary successions of the Antalya Complex (e.g. Waldon, 1984).

The upper boundary of the pre-Messinian Miocene package is either the M- or N- reflector depending on the presence or absence, respectively, of the Messinian evaporite sequence in the area. The lower boundary of this unit is never clearly imaged in any of the seismic profiles studied for this thesis. This is likely due to decreasing resolution with depth or because the lower boundary is located deeper in the Earth than the seismic profiles have recorded. Lack of a lower boundary prevents any comment on the thickness evolution of Unit 3 throughout the study area.

Chapter 5

Structural geology of the western Antalya Basin

In the previous chapter, the chronostratigraphic framework for the western Antalya Basin was established through the correlation of seismic units identified in the study area with the lithology and chronostratigraphy recovered in an onshore industry exploration well. Further correlation with the literature firmly established that three distinct chronostratigraphic units, separated by the M- and N- reflectors, are present in the western Antalya Basin. Unit 1 houses the youngest sedimentary sequences in the study area. It is bounded at its base by the M-reflector and contains Pliocene-Quaternary siliciclastic rocks. Unit 2 and Unit 3 are found below the M-reflector. Unit 2 is not found consistently in the study area, but when present it is sandwiched between the M- and N-reflectors. This unit is composed of siliciclastic and carbonate successions interbedded with evaporites arising from the cyclical near-desiccation of the eastern Mediterranean during the Messinian. The oldest rocks in the study area are found in Unit 3. This unit has no identifiable base within the

seismic reflection profiles in this study, but it is bounded above by the M-reflector, or the N-reflector where Unit 2 is present. Unit 3 contains both siliciclastic and carbonate successions from the pre-Messinian Miocene. Establishing this time frame for the observed seismic units is the essential first step toward deciphering the complex structural history of the study area. Approximate subsurface depths can be calculated using the following interval velocities: Unit 1 - 2000 m/s; Unit 2 - 4200m/s; and Unit 3 - 3000-3500m/s.

In this chapter, the structural architecture of the study area is investigated using seismic reflection profiles processed by the author as well as archived profiles from the Eastern Mediterranean Research Group and from industry (Fig. 5.2). Mapping prominent features across various profiles in the study area revealed that strain in this region is partitioned both temporally and spatially. The structural architecture of the western Antalya basin can best be described under the same three time intervals that defined the chronostragraphy described in Chapter 4: (1) pre-Messinian Miocene; (2) Messinian; and (3) Pliocene-Quaternary. Each of these time intervals is recorded in data across the entire western Antalya Basin, east of the onshore Beydağları and Antalya Complexes. Within the pre-Messinian Miocene and the Pliocene-Quaternary intervals, there is further division into a number of spatial domains. These three time intervals and their spatial domains, when present, are discussed in detail below. Note that halokinetic structures, despite being the product of the motion of the Unit 2 Messinian evaporite sequences, are generally described (where present) within the Pliocene-Quaternary domains since the loading of these sediments is what initiated their displacement. Interested readers can find uninterpreted profiles for the sections processed by the author in the *Plates* section of this manuscript (available profiles are noted in figure captions).

5.1 Interval 1: pre-Messinian Miocene

Interval 1 is characterized by structures developed during the pre-Messinian Miocene and is associated with a period of protracted contractional deformation (Fig. 5.1). The locations of the profiles used for illustration purpose while describing this interval are shown in Fig. 5.2. On the basis of the predominant morphotectonic elements and their trends and, to a lesser extent, their deformational style, the pre-Messinian Miocene interval can be further subdivided into three spatial domains: in the east, an domain of arcuate mainly NW-SE- trending structures (1A); in the west, a domain of primarily N-S- trending structures (1B); and, in the south and central region, an arrowhead-shaped domain (1C) sandwiched between domains 1A and 1B.

Faults are interpreted as thrust faults based mainly on associated minor structures such as hangingwall antiforms and footwall synforms (e.g. highlighted yellow reflections in the pre-Messinian Miocene sequences in Figs. 5.3 and 5.4). Trajectories are interpreted to be listric based on the thrust surface seen in Figure 5.3. At depth, this surface becomes sub-horizontal; thus, this cannot be simply a velocity artifact. Further, within the pre-Messinian Miocene package, the velocity might increase by 1000 m/s over approximately three seconds, leading to an increase in apparent gradient from 1 in 4 to 1 in 3 deeper in the section. Observed gradient changes are much larger than this (e.g Figs. 5.3 and 5.4), suggesting velocity increase with depth is only a minor contributor to apparent listricitiy.

5.1.1 Domain 1A: Arcuate contractional structures

Domain 1A is a NW-SE- trending zone occupying the shallow continental shelf and slope in the easternmost region of the study area (Figs. 5.2 and 5.1). It is characterized by an arcuate SW- and SSW- verging, NW-SE- and N-S- trending fold-thrust belt

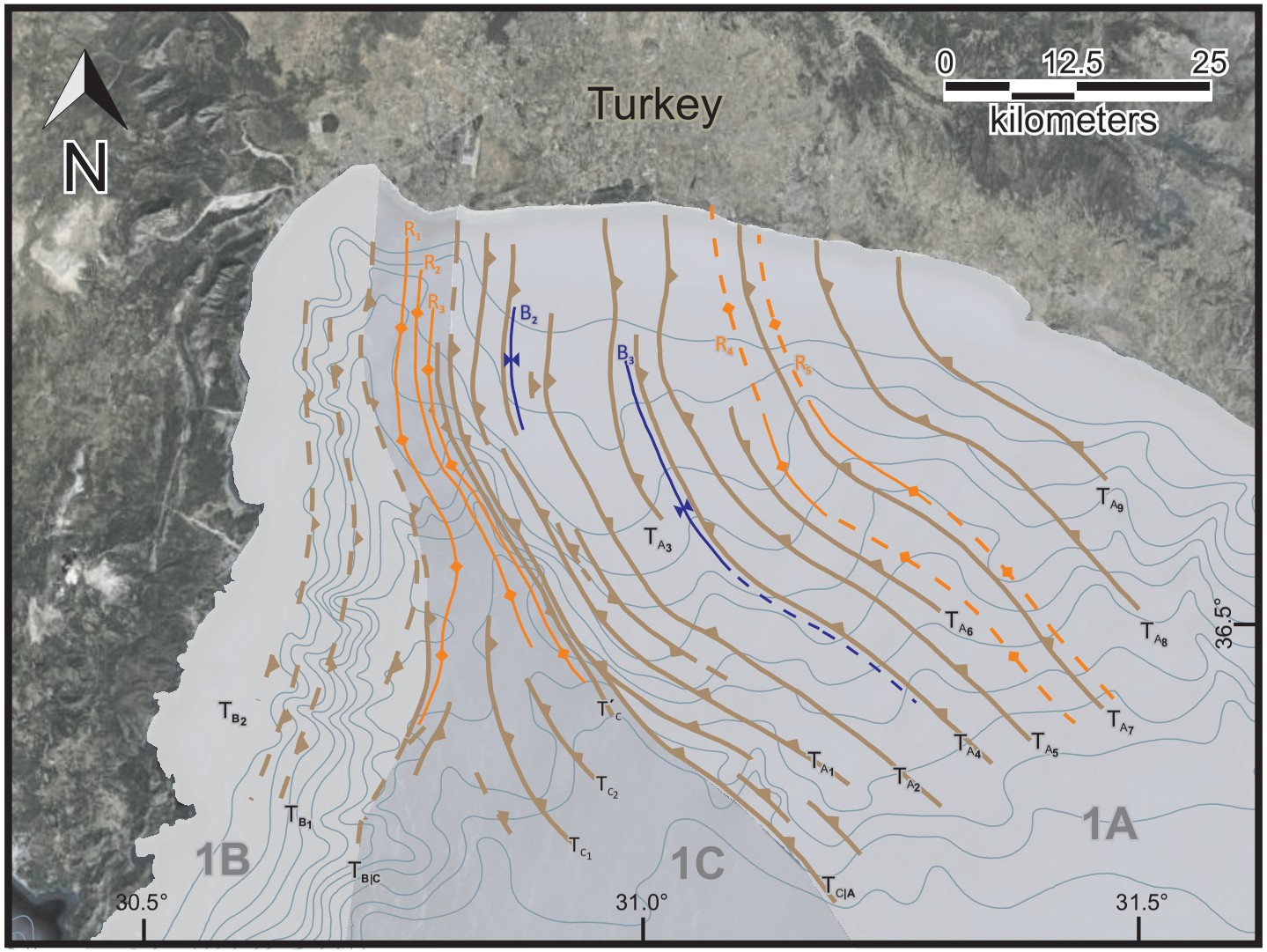

Figure 5.1: Detailed pre-Messinian Miocene tectonic map of the western Antalya Basin showing major structures including: thrust faults, shown with filled triangular ticks; crests of prominent ridges, shown with diamond ticks; and trough lines of major piggy-back basins developed on the backlimbs of major thrusts, shown with bow-tie ticks. Structural domains 1A, 1B, 1C are highlighted.

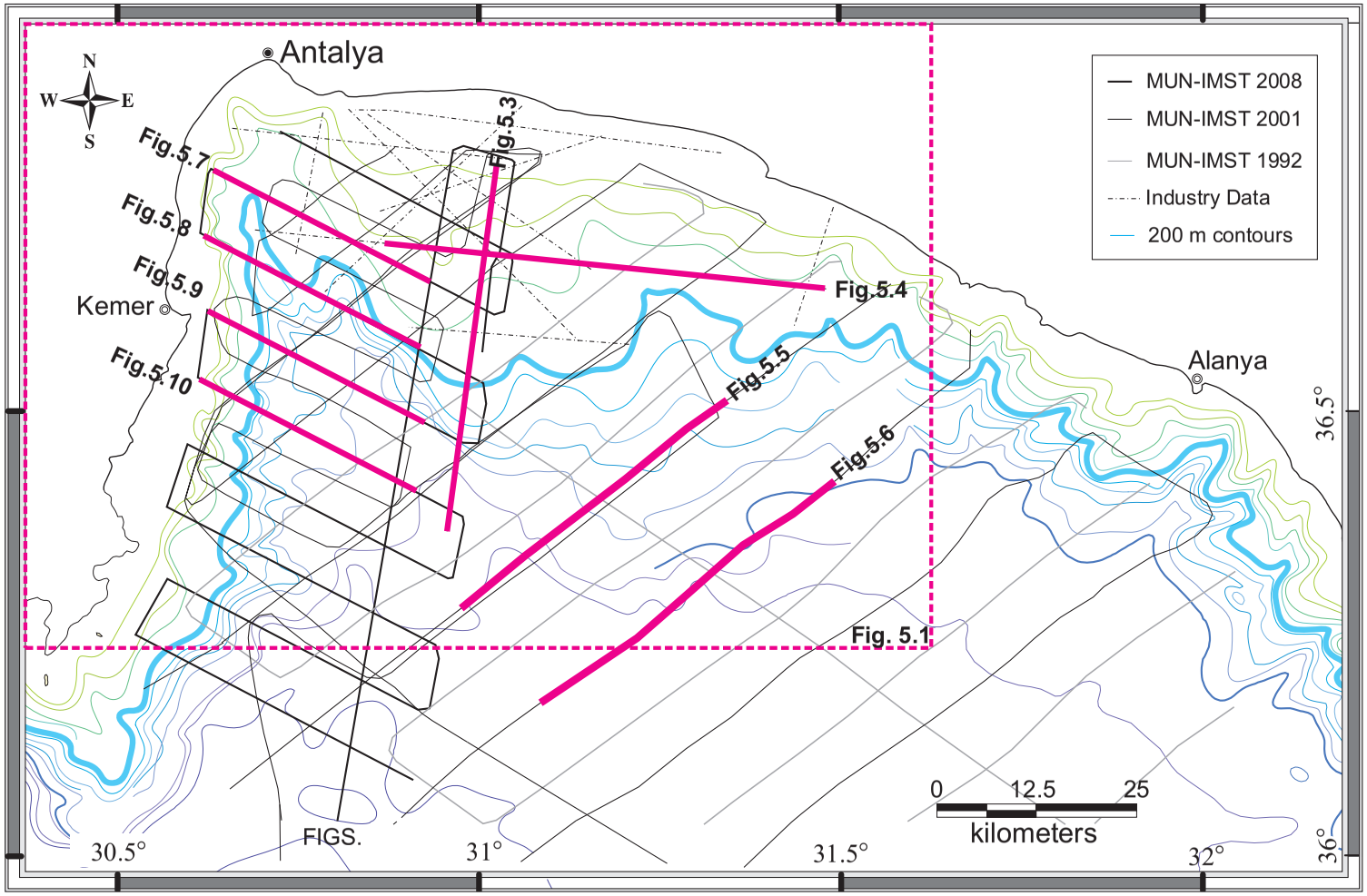

Figure 5.2: Index map showing the locations of all the seismic reflection profiles used for structural interpretation. Location of profiles used for figures for the Miocene interval are highlighted in pink. Area shown in Fig. 5.1 is highlighted in the dotted pink box. Thick blue line indicates the 1000m contour.

composed of 9-12 prominent thrust panels extending from the central Antalya Basin toward the present-day coastline (i.e. thrusts $T_{C|A}$ - T_{A_9} in Fig. 5.1). Traced toward the northwest, these thrusts progressively swing clockwise to assume a broadly N-S orientation in the northern segment of the domain. These are immediately south of, and collinear with, the prominent thrust panels mapped onland that are associated with the southeastern structures of the Isparta Angle (Poisson et al., 2003).

The fold-thrust belt which characterizes this domain is best imaged in the industry seismic reflection profiles (e.g. Figs. 5.3 and 5.4). Within Domain 1A, the M-reflector is a very distinctive marker defining a prominent erosional unconformity which separates the Pliocene-Quaternary sediments from the underlying pre-Messinian Miocene successions. In this area, the gently N-dipping pre-Messinian Miocene sediments are clearly truncated by erosion at the M-reflector. The leading thrust of the belt, and the bounding thrust of the sub-domain, is located at the base of the continental slope in the east-central section of the study area (i.e. the $T_{C|A}$ thrust in Fig. 5.1, 5.3, 5.4, 5.5, 5.6). The footwall and hangingwall cutoffs of this fault are clearly visible in the industry seismic reflection profiles. The thrust trajectory can be traced from close to the seabed to at least 5000 ms depth, defining a prominent listric surface (e.g. Figs. 5.3 and 5.4). At depth, this surface defines a 200-300 ms thick sub-horizontal reflector bundle that gently dips northward; based on the interpreted fault trajectory observed in Figure 5.3, this surface likely soles at a depth greater than 6000 ms. Thrust trajectories can also be traced on non-industry profiles, however, the actual surfaces are highly interpretive and are largely delineated by the geometries of the adjacent sedimentary layers (e.g. Figs. 5.5 and 5.6). An approximation using a time depth of 6000 ms (as estimated from the industry profiles) and sediment velocitiy of 3500 m/s in Unit 3, finds the corresponding maximum depth of this surface to be over 10km, suggesting that this pre-Messinian Miocene fold-thrust belt defines a crustal-scale

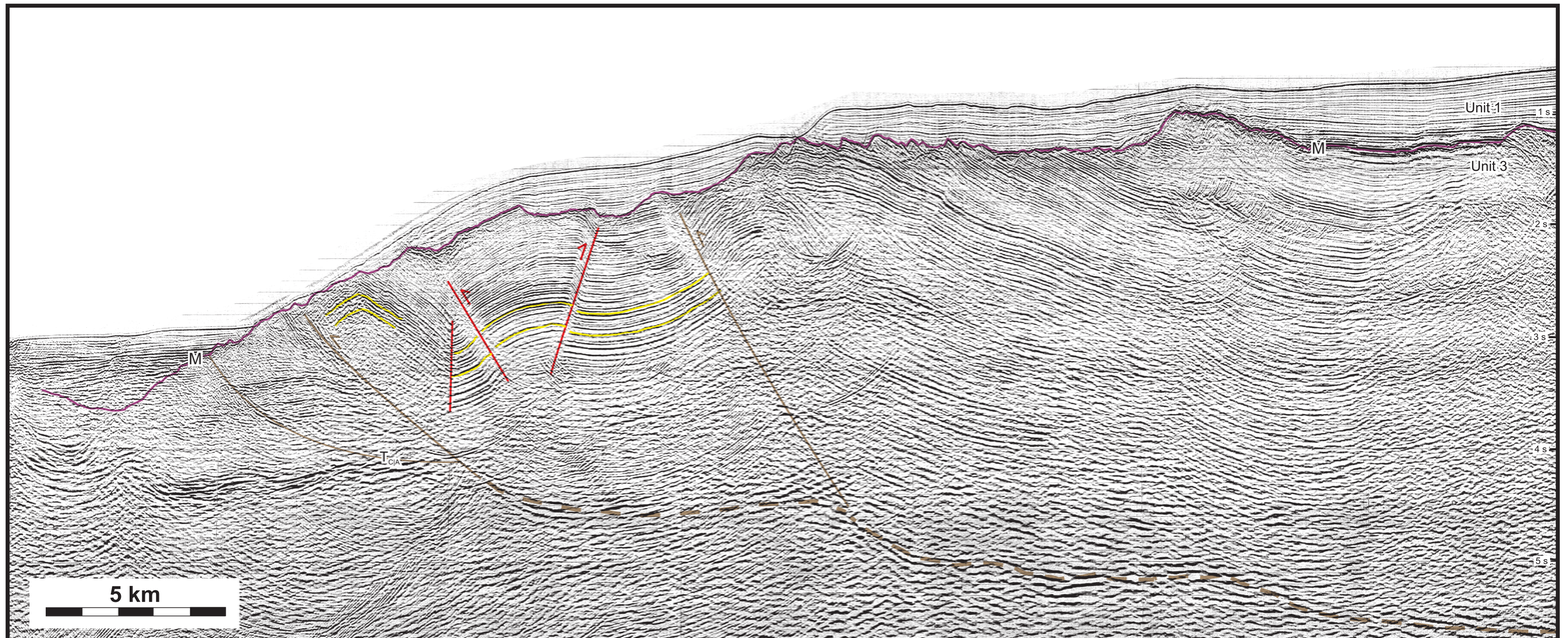

Figure 5.3 Industry multi-channel seismic reflection profile showing the Miocene structural architecture of the western Antalya Basin. Note that the M-reflector is a prominent erosional unconformity separating the Pliocene-Quaternary successions of Unit 1 from the pre-Messinian Miocene successions of Unit 3. Further note that the leading thrust of the fold thrust belt delineates the base of the slope in the western Antalya Basin and that the slope face is the forelimb of a huge thrust culmination. Geometries of sedimentary layers are highlighted in yellow. Profile is kindly provided by the Turkish Petroleum Corporation. Location is shown in Figure 5.1.

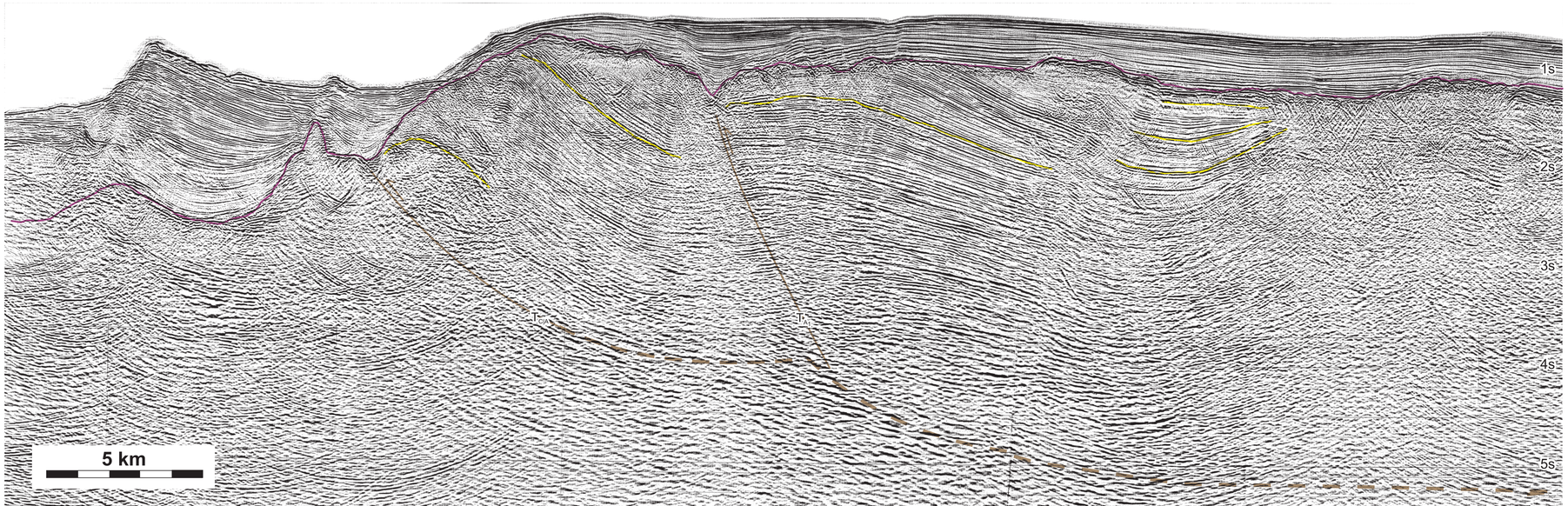

Figure 5.4 Industry multi-channel seismic reflection profile showing the Miocene structural architecture of the western Antalya Basin Domain 1A. Note that the M-reflector is a prominent erosional unconformity separating the Pliocene-Quaternary successions of Unit 1 from the pre-Messinian Miocene successions of Unit 3. Also note the Pliocene-Quaternary reactivation of Miocene thrusts on the western section of the profile (Domain 1B). Geometries of sedimentary layers are highlighted in yellow. Profile is kindly provided by the Turkish Petroleum Corporation. Location of profile shown in Figure 5.1.

feature in front of the western Tauride Mountains of south-central Turkey (further discussed in Chapter 6).

There are generally no growth strata imaged in the pre-Messinian Miocene piggy-back basins in this thrust belt, although there are occasional minor exceptions to this (e.g. Figs. 5.3 and 5.4). However, there is a prominent angular unconformity at the M-reflector between the dipping pre-Messinian Miocene sediments immediately behind a thrust and relative undeformed overlying Pliocene-Quaternary sediments (e.g. Fig. 5.5). This, coupled with the widely accepted notion that the late Miocene (Messinian) was a period of tectonic quiescence in the eastern Mediterranean region, affirms that the thrusting must have begun at least in the latest pre-Messinian Miocene and any growth strata therein may have eroded away during the formation of the M-reflector.

5.1.2 Domain 1B: Poorly-imaged contractional zone

Domain 1B is situated across the continental shelf and slope of the westernmost area of the Antalya Basin. It is characterized by a broadly N-S-trending W-verging fold-thrust belt bounded to the east by the thrust $T_{B|C}$ (i.e. Fig. 5.1; e.g. Figs. 5.7, 5.8, 5.9 and 5.10). A series of NW-SE trending high-resolution seismic reflection profiles suggest that the belt consists of two to three thrust panels which are poorly imaged in this region (i.e. dashed thrusts T_{B_1} and T_{B_2} in Figs. 5.2 and 5.11).

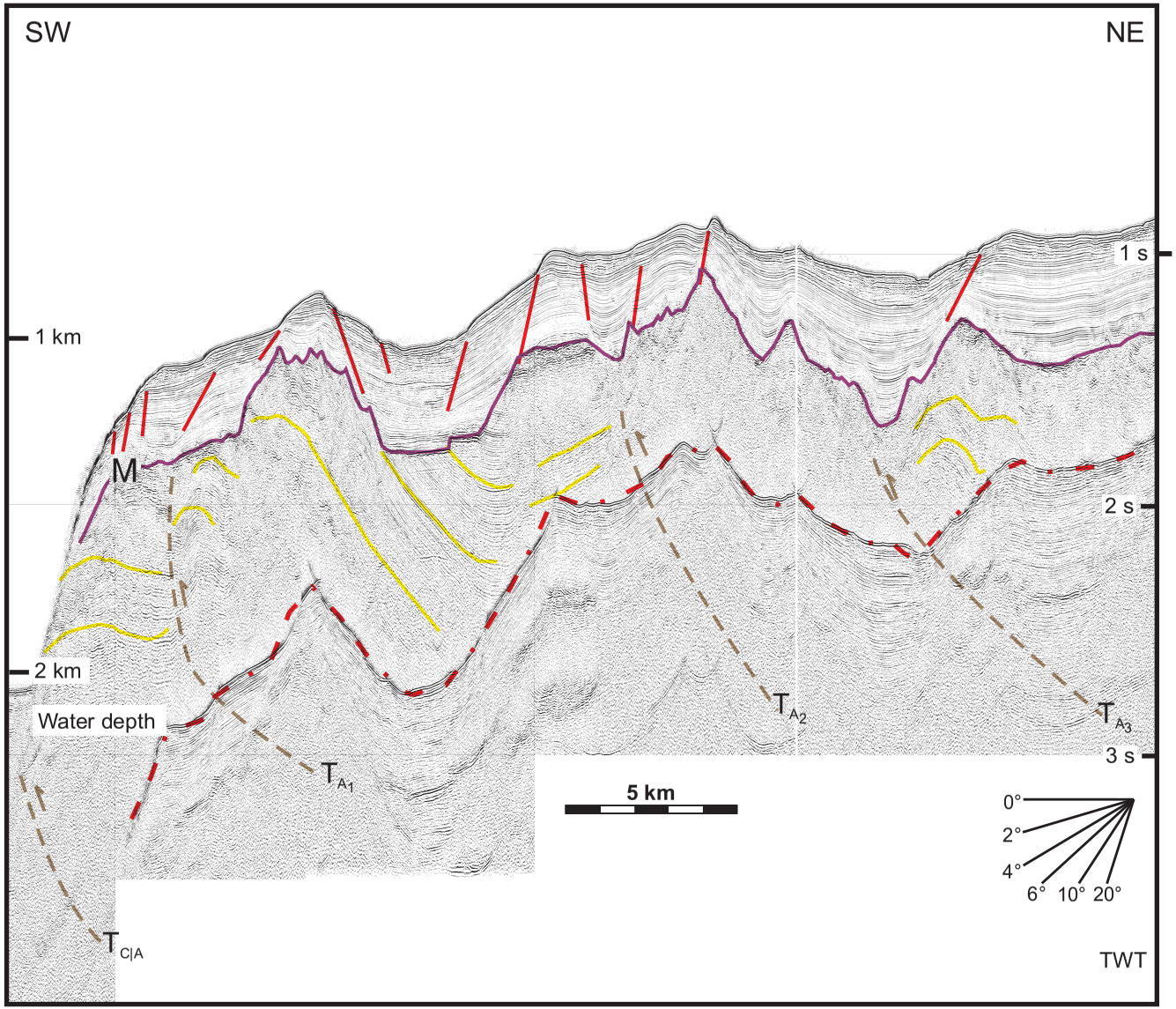

Figure 5.5: High resolution multichannel seismic reflection profile showing the detailed structural architecture of Domain 1A. Note that the M-reflector defined a major erosional unconformity across the shelf region of the Antalya Basin and that the Messinian evaporites of Unit 2 are absent in the area. Note the highlghted sedimentary layers (yellow) whose geometries help define the thrust surface. Note that these surfaces are highly interpretive at depth. Seabed multiple highlighed in dotted red. Location shown in Figure 5.2. Note that the angular scale was calculated at seismic water velocity (1500 m/s) and is not valid at depth.

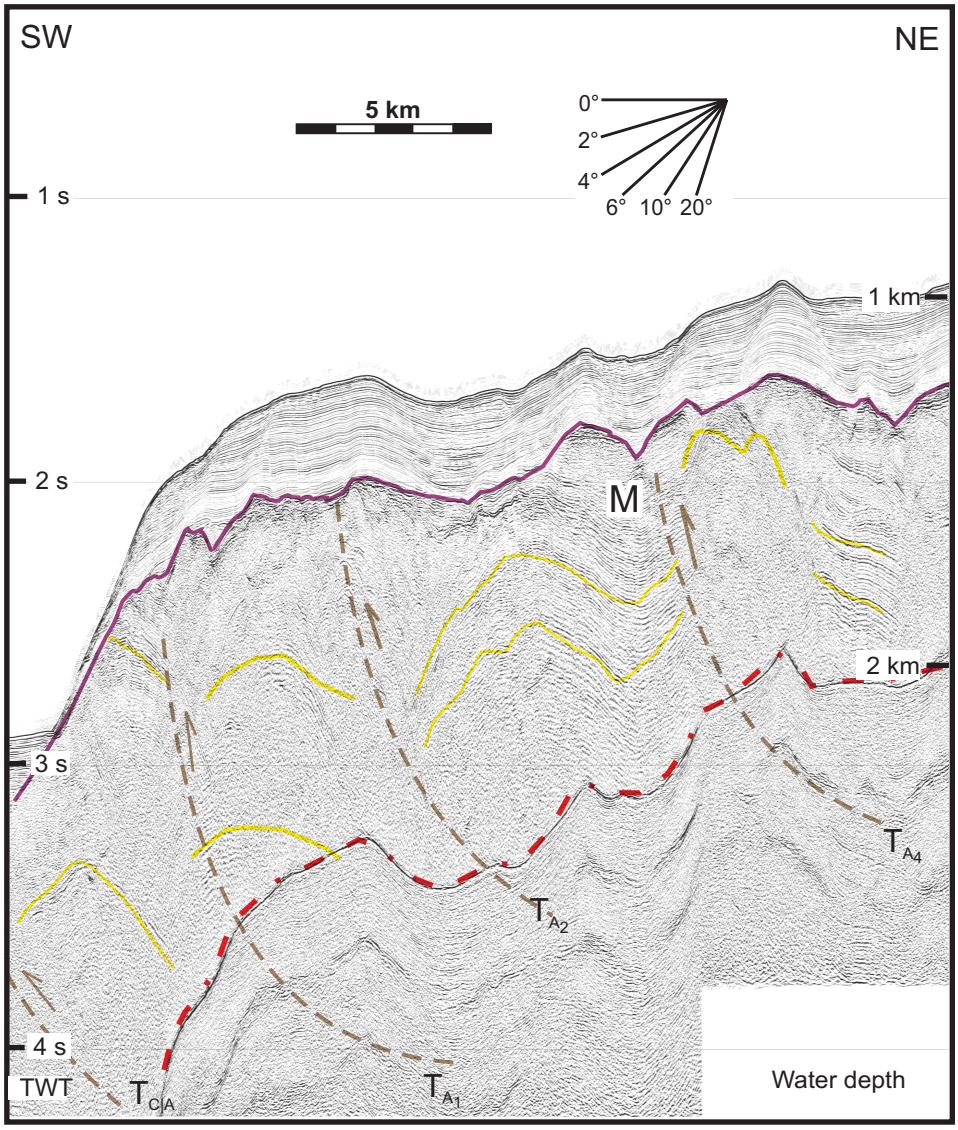

Figure 5.6: High resolution multichannel seismic reflection profile showing the detailed structural architecture of Domain 1A. Note that the M-reflector defined a major erosional unconformity across the shelf region of the Antalya Basin and that the Messinian evaporites of Unit 2 are absent in the area. Note the highlghted sedimentary layers (yellow) whose geometries help define the thrust surface. Note that these surfaces are highly interpretive at depth. Seabed multiple highlighed in dotted red. Location shown in Figure 5.2. The angular scale was calculated at seismic water velocity (1500 m/s) and is not valid at depth.

In the northernmost portion of the sub-domain, the belt is well-imaged. Immediately west of thrust $T_{B|C}$, the seismic architecture of the pre-Messinian Miocene suggests the presence of another west-verging thrust (i.e. T_{B_1} in Fig. 5.9). This thrust has a well-developed ramp anticline delineated in the pre-Messinian Miocene successions as well as by the M-reflector. T_{B_1} appears to cut the M-reflector and tip within the overlying Pliocene-Quaternary successions (e.g. Fig. 5.7). This thrust soles deeply into the pre-Messinian Miocene successions and appears to link with the major thrust, $T_{B|C}$. Immediately west of this thrust, the seismic architecture of the Miocene successions suggests the presence of another W-verging thrust (i.e. T_{B_2} in Figs. 5.1, 5.8 and 5.9), however this is not well imaged in the seismic reflection profiles.

Further southward, the structural architecture becomes progressively more complicated as structures become buried beneath the steep continental slope. However, the structural elements observed in the northernmost portion of the sub-domain can still be mapped using secondary structures and the thrust $T_{B|C}$ as a guide. For example, two small, but notable ramp anticlines at the base of the continental slope are interpreted to have west-verging thrusts bounding their western margins (i.e. T_{B_1} and T_{B_2} in Figs. 5.1 and 5.9). Unfortunately, in this area, the two ramp anticlines appear to have been overprinted by high-frequency reflections possibly arising from nearby out-of-plane geology. Even further south, disconnected and sporadic lower frequency reflector bundles give only hints of possible structure elements (e.g. Fig. 5.12). This region is also dissected by high-angle E-dipping normal faults with possible strike-slip components, surmised to be Pliocene-Quaternary in age (discussed in detail in Sub-Domain 3B below). It is, therefore, speculated that the N-S-trending fold-thrust belt mapped in the northern and central portion of the western Antalya Basin also continues south along the similarly-trending continental margin in this area. Because

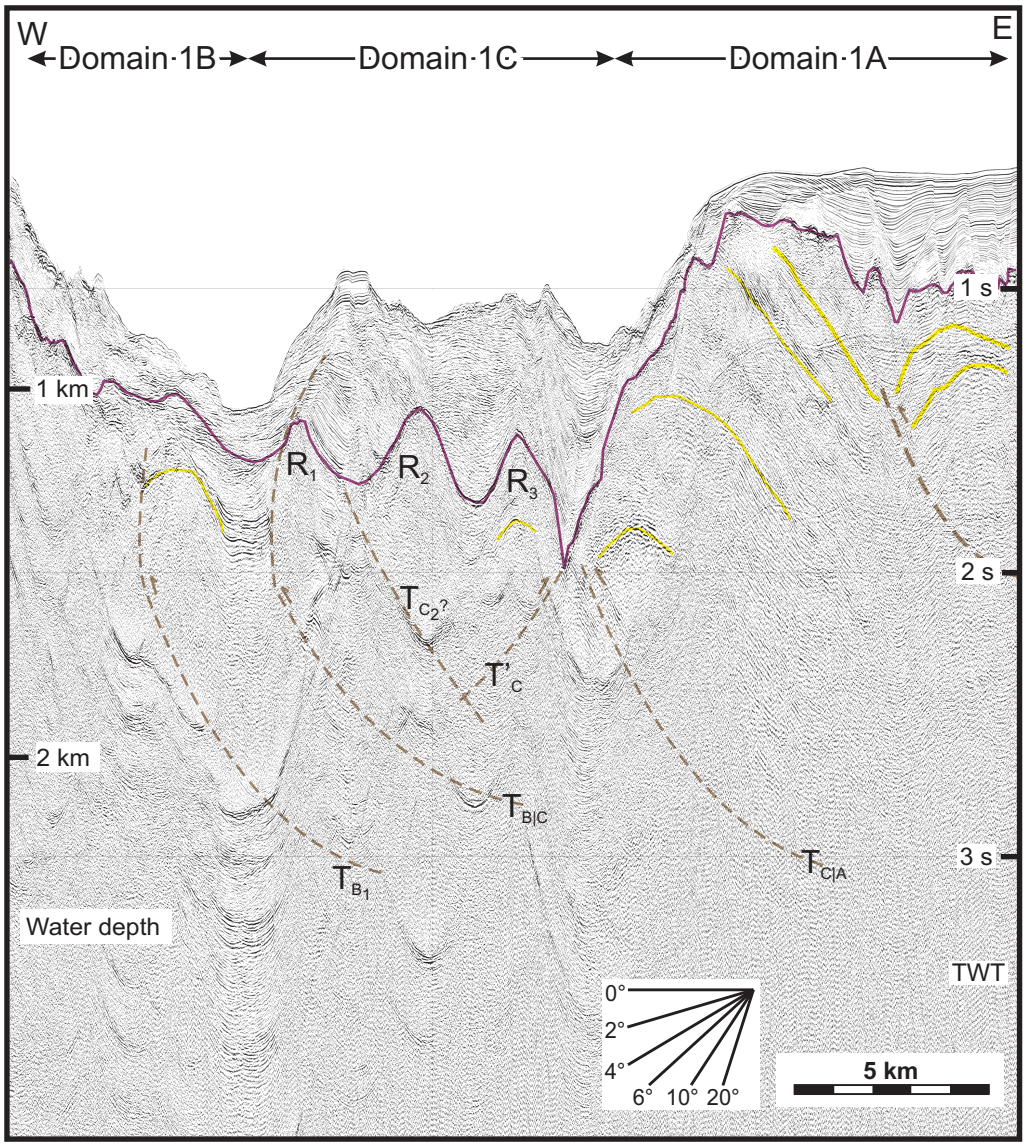

Figure 5.7: High resolution multichannel seismic reflection profile showing the detailed structural architecture of Domains 1B and 1C in the northernmost segment of the western Analyta Basin. Note that 2-3 large N-S-trending, W-verging thrusts define the core of Domain B in the Miocene successions of Unit 3. Note that the M-reflector defined a major erosional unconformity across the shelf region of the Antalya Basin and that the Messinian evaporites of Unit 2 are absent in the area. Location shown in Figure 5.2. The angular scale was calculated at seismic water velocity (1500 m/s) and is not valid at depth. Uninterpreted seismic profile can be found in Plate 5, Fixes 144 - 125.

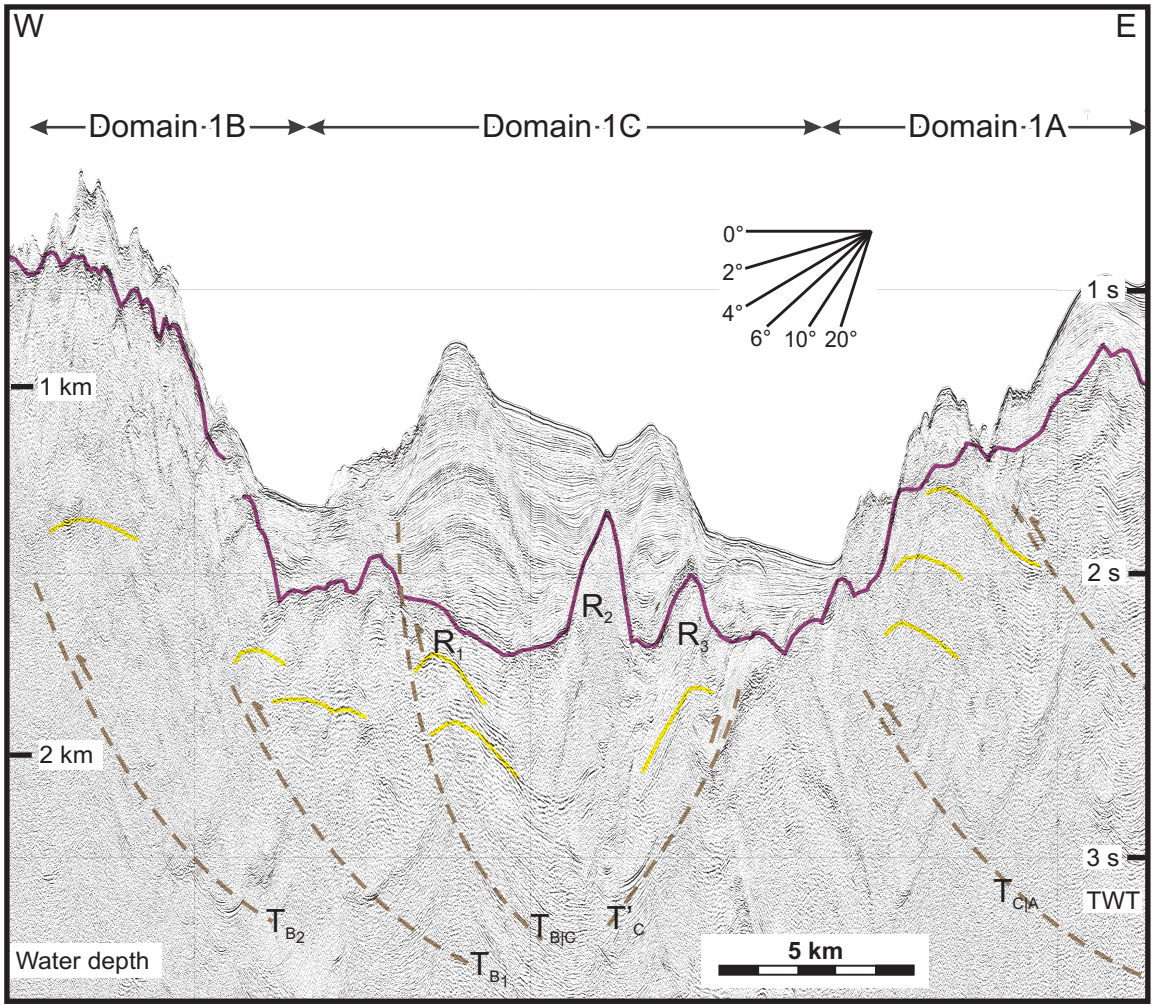

Figure 5.8: High resolution multichannel seismic reflection profile showing the detailed structural architecture of Domains 1B and 1C in the northern segment of the western Analyta Basin. Note the steep slope which defines the western margin of Antalya Basin, which is covered by a thin veneer of Pliocene-Quaternary deposits above the M-reflector. Also note that several west-verging thrusts control the deeper structural framework of the margin in the Miocene successions of Unit 3. Location shown in Figure 5.2. The angular scale was calculated at seismic water velocity (1500 m/s) and is not valid at depth. Uninterpreted seismic profile can be found in Plate 7, Fixes 125 - 172.

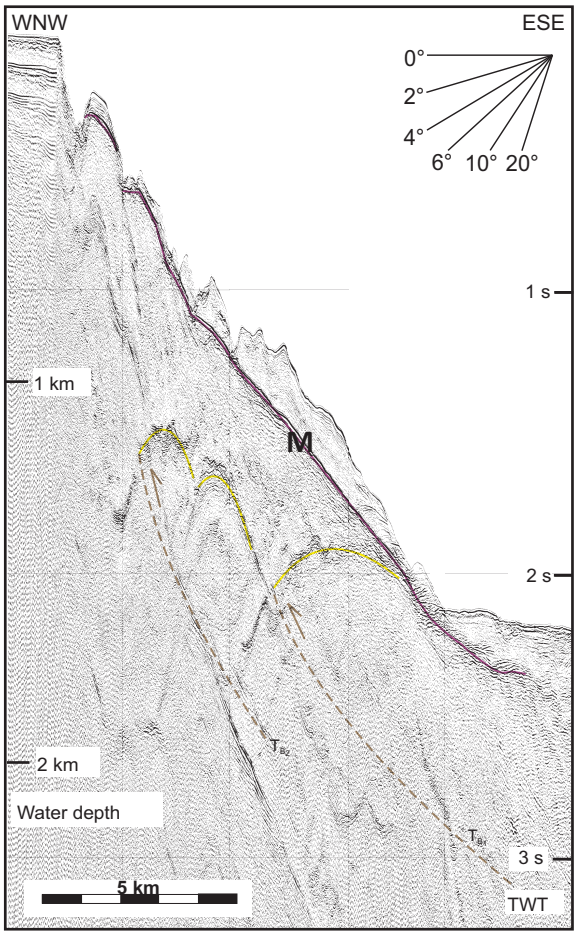

Figure 5.9: High resolution multichannel seismic reflection profile showing the detailed structural architecture of Domain 1B. Note the steep slope which defines the western margin of Antalya Basin, which is covered by a thin veneer of Pliocene-Quaternary deposits above the M-reflector. A west-verging thrust system is poorly imaged beneath the M-reflector. Location shown in Figure 5.2. The angular scale was calculated at seismic water velocity (1500 m/s) and is not valid at depth. Uninterpreted seismic profile can be found in Plate 9, Fixes 211 - 200.

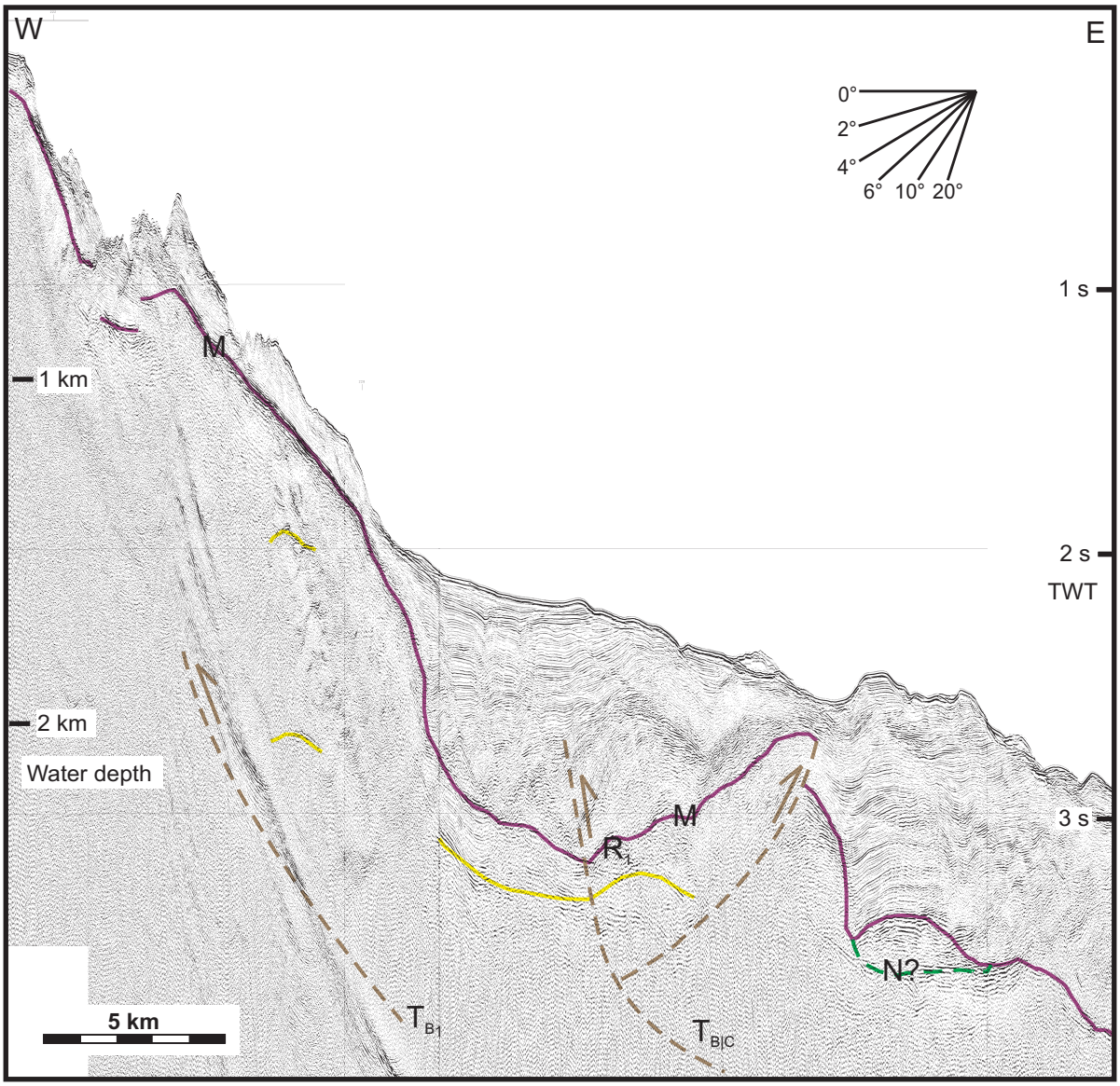

Figure 5.10: High resolution multichannel seismic reflection profile showing the detailed structural architecture of Domains 1B and 1C. Note the steep slope which defines the western margin of Antalya Basin, which is covered by a thin veneer of Pliocene-Quaternary deposits above the M-reflector. Also note the Messinian evaporites of Unit 2 are only present in the deeper Antalya Basin, forming halokinetic structures (discussed later). The west-verging thrust system of Domain 1B is not well imaged in this profile, possibly because the thrusts became reactivated as normal faults with strike-slip components in the Pliocene-Quaternary (discussed later). Location shown in Figure 5.2. The angular scale was calculated at seismic water velocity (1500 m/s) and is not valid at depth. Uninterpreted seismic profile can be found in Plate 11, Fixes 220 - 242.

of imaging difficulties, we only tentatively correlate thrusts T_{B_1} and T_{B_2} across the sub-domain.

5.1.3 Domain 1C: Transitional zone

Domain 1C occupies the narrow bathymetric channel in the northwestern Antalya Basin and widens considerably toward the abyssal plain in the south (Fig. 5.1). This domain can be considered a transitional zone sandwiched between Domain 1A in the east and Domain 1B in the west. The structural architecture of Domain 1C is characterized by two broadly W-verging, NS-trending thrust panels (i.e. thrusts $T_{B|C}$ and T_{C_1} in Figure 5.1), one similarly trending, but E-verging backthrust (i.e. thrust T'_C in Figure 5.1), and three prominent ridges (i.e. ridges R_{C_1}, R_{C_2}, and R_{C_3} in Figure 5.1).

The western boundary of Sub-Domain 1C is marked by the thrust $T_{B|C}$ (Figs. 5.1; e.g. Fig. 5.7 and 5.8 and 5.10). A prominent ramp anticline is developed on the hanging wall of $T_{B|C}$ which is readily mappable along the western margin (R_1 in Figs. 5.1, 5.7 and 5.8). Thrust $T_{B|C}$ appears to impact the M-reflector as well as (possibly) the overlying Pliocene-Quaternary sediments (e.g. Figs. 5.7 and 5.8) suggesting the activity of this thrust might have either continued into, or have been reactivated during, this time period (discussed further below).

East of thrust $T_{B|C}$ and ridge R_1, there is another distinctive ridge which affects the pre-Messinian Miocene sediments as well as the M-reflector (i.e. ridge R_2 in Figs. 5.1, 5.7 and 5.8). In the north, the seabed immediately above the ridge shows a marked dip (with no erosional artifacts which would indicate a submarine channel) suggesting that there might be lateral movement along this ridge (e.g. Fig. 5.8). It is speculated this may be related to salt trapped in this area which, due to imaging difficulties, could not be correlated across profiles.

Immediately east of R_2, there is another prominent ridge (i.e. R_3 in Figs. 5.1, 5.7 and 5.8). The R_3 ridge appears to be a ramp anticline of a backthrust (i.e. $T_C{}'$ in Figs. 5.1, 5.7 and 5.8). Using R_3 as a guide, this backthrust is mapped across the domain to show a broadly arcuate NW-SE-trend reminiscent of the thrust belt mapped in Domain 1A. Note that this backthrust interpretation is speculative and it is possible, instead, that the displacement seen between Domain 1A and 1C is the result of a normal fault.

Southward, two thrusts are mapped which are tentatively assigned to the pre-Messinian Miocene interval (i.e. T_{C_1} and T_{C_2}). Due to imaging issues, no marker reflectors in the pre-Messinian Miocene sediments could be traced. These thrusts were identified based on large offsets in the M-reflector as well as the visible impact on the seabed. The T_{C_1} thrust appears to carry the $T_C{}'$ backthrust discussed above, but cannot be confidently mapped as far northward due to complex deformation in the region. However, there is some evidence that T_{C_2} is present northward (e.g. Figs. 5.7 and 5.8). The T_{C_1} and T_{C_2} are clearly active during the Pliocene-Quaternary and are discussed in detail in Domain 3C below.

It is here, in the south-central region of the domain that there appears to be a junction where morphotectonic style changes from the arcuate NW-SE-trending architecture of Domain 1A to the broadly N-S-trending architecture of Domain 1B. A similar region is also identified within the Pliocene-Quaternary domains (discussed below). It is inferred that this may be evidence of an important crustal-scale structure in the region related to the evolving Isparta Angle (further discussed in Chapter 6).

5.2 Interval 2: late-Messinian, Miocene

The Messinian was a period of significant changes in the eastern Mediterranean Sea, both in tectonic style as well as the morphology of the basins and their surrounding landmass. From the late Tortonian into the Messinian, the progressive evaporation of the western extension of the Tethys Ocean exposed the continental shelves and slopes to subaerial processes. Consequently, during the Messinian, the entire Antalya Basin became a deep, exposed basin with very shallow water in its deepest parts. Periodic innundation throughout the Messinian resulted in the sedimentation of approximately 2 km of evaporite successions within the deeper portion of the erosional basin. First-order calculations suggest that between 70 and 75 volumes of the present-day Mediterranean Sea would be needed for the deposition of these thick evaporite sequences (Işler et al., 2005).

Due to a lack of coherent reflectors within the Messinian sedimentary sequence, it is not possible to say if there was active tectonism in the region during this time. Furthermore, tip points of the pre-Messinian Miocene thrusts occur at varying points below, at, or above the M-reflector; in fact, in many places the M-reflector is greatly offset by these thrusts (discussed further below). The Messinian was possibly a period of tectonic quiescence, but it is speculated that thrusting from the pre-Messinian Miocene may have continued, to some extent, during this time and then well into the Pliocene-Quaternary. Because of the halokinetic activity during the Pliocene-Quaternary, the migration of Messinian evaporites as well as the subsequent deformation of overlying Pliocene-Quaternary sediments is dicussed in the next section (Domain 3C).

5.3 Interval 3: Pliocene-Quaternary

The Pliocene-Quaternary structures in the Antalya Basin are largely overprinted on the older Miocene structures; some of these younger structures appear to have developed completely independently of the older structures, yet others have clearly evolved by the re-activation or continued activity of older structures (see Figs. 5.1 and 5.11). There are three spatial domains which each display a distinctive set of characteristics including style and depth of deformation as well as structural trend: in the east, an arcuate mainly NW-SE- trending sub-domain which is characterized by a broadly arcuate superficial extensional fault system which, on its more westerly margin, also contains a couple of re-activated pre-Messinian thrusts (3A); in the west, a broadly N-S- trending sub-domain which appears to be controlled by a deeply-rooted extensional fault system (3B); in the central region, a complex, arrowhead-shaped sub-domain displaying both extensional and contractional features as well as halokinetic activity (3C). These domains have similar locations to the three zones described in Interval 1, and the correspondence is likely not fortuitous. Locations of profiles used in figures are shown in Fig. 5.12.

5.3.1 Domain 3A: Arcuate superficial extensional fault zone with reactivated (?) Miocene thrusts

The structural architecture of Domain 3A is characterized by an arcuate belt of superficial extensional faults which has a predominantly NW-SE trend in the south, but progressively swings clockwise to assume a N-S trend in the north (Fig. 5.11). This morpho-tectonic character appears to loosely overprint the pre-existing compressional structures of the pre-Messinian Miocene Domain 1A while displaying a

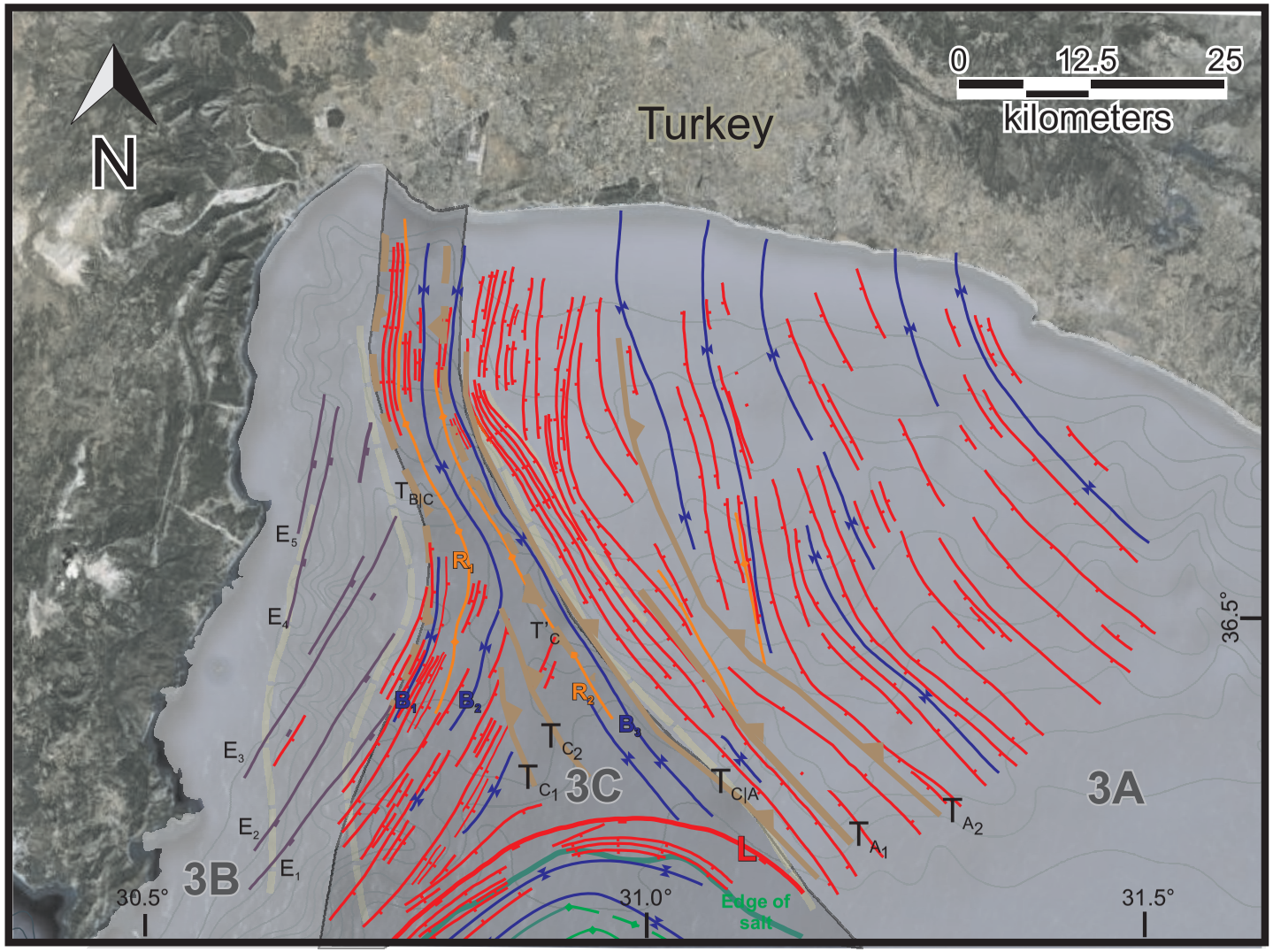

Figure 5.11: Detailed Pliocene-Quaternary tectonic map of the western Antalya Basin, showing major structures including: normal faults, shown with filled rectangular ticks on the hanging walls; thrust faults, shown with filled triangular ticks on the hanging walls; the crestal hinge lines of prominent ridges, shown with diamond ticks; and trough lines of major basins, shown in bow-tie ticks. Structural domains 3A, 3B, and 3C and highlighted.

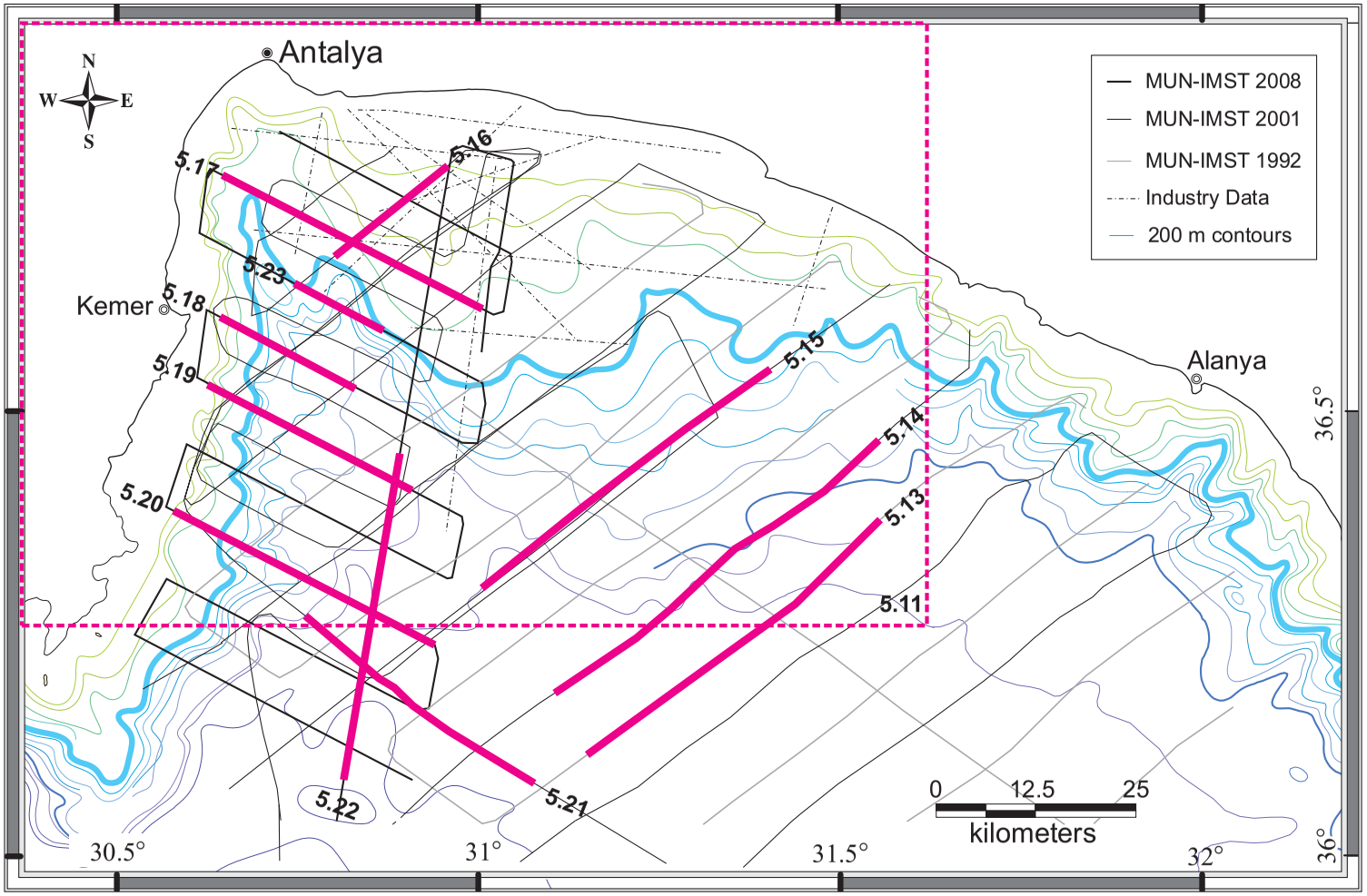

Figure 5.12: Index map showing the locations of all the seismic profiles used for structural interpretation. Locations of figures for the Pliocene-Quaternary interval are highlighted in pink. Area shown in Fig. 5.11 is highlighted in the dotted pink box. Thick blue line indicates the 1000m contour.

completely different deformational style (e.g. Figs. 5.1 and 5.11). There is also evidence of re-activated pre-Messinian Miocene thrusts along the westernmost margin of the sub-domain (discussed in detail below).

In the southern region of 3A, numerous NW-SE-trending and NE-SW-dipping extensional faults define a series of horst and graben structures (e.g. Fig. 5.13). Most of these faults cut the entire Pliocene-Quaternary successions, extending to the depositional surface where they create distinctive steps on the seafloor. Marker reflectors across the footwalls and hanging walls of the extensional faults show very little (if any) sedimentary growth across these faults. This suggests the faulting is quite recent and must post-date the development of the most of the Pliocene-Quaternary successions. Because of the morphology of the M-reflector and the concordance of the overlying successions, formation of these horst and graben structures is speculated to have been initiated by the reactivation of several pre-Messinian Miocene thrusts in the region (e.g. T_{A_1} and T_{A_2} in Figs. 5.11 and 5.14).

In the central portion of Domain 3A, the base of slope becomes a prominent surface rising from the Antalya abyssal plain; Pliocene-Quaternary sediments resting on the continental slope are cut by a series of 4-5 NW-SE-trending, SW-dipping extensional faults (e.g. Figs. 5.13, 5.14, and 5.15). These faults extend from the seabed onto the M-reflector and create steps on the seafloor. Landward of this frontal margin, the morphology of the domain is very similar to that described to the south. This region is characterized by numerous well-developed horst and graben structures bounded on their sides by steep, planar extensional faults which tip at or near the seabed and create steps on the seafloor (e.g. Fig. 5.15). Some of these faults show growth within the Pliocene-Quaternary sediments (e.g. Fig. 5.15).

The northern portion of Domain 3A is characterized by numerous broadly N-S-trending, E- and W- dipping high-angle extensional faults (e.g. Figs. 5.16 and

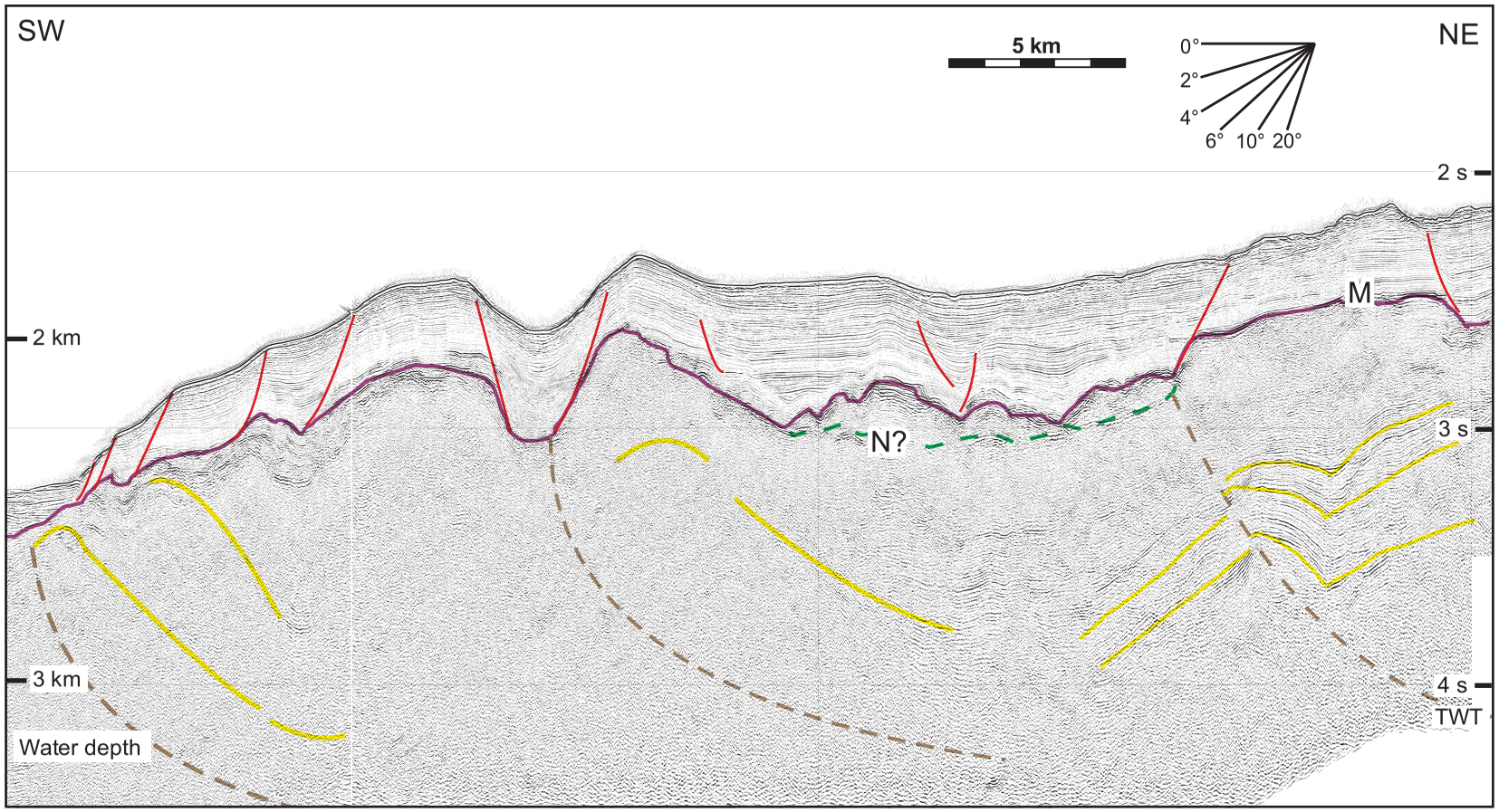

Figure 5.13: High-resolution multichannel seismic reflection profile showing the detailed structural architecture of Domain 3A. Note the prominent horst and graben structures developed within the Pliocene-Quaternary sediments. Location is shown in Figure 5.12. The angular scale was calculated at seismic water velocity (1500 m/s) and is not valid at depth.

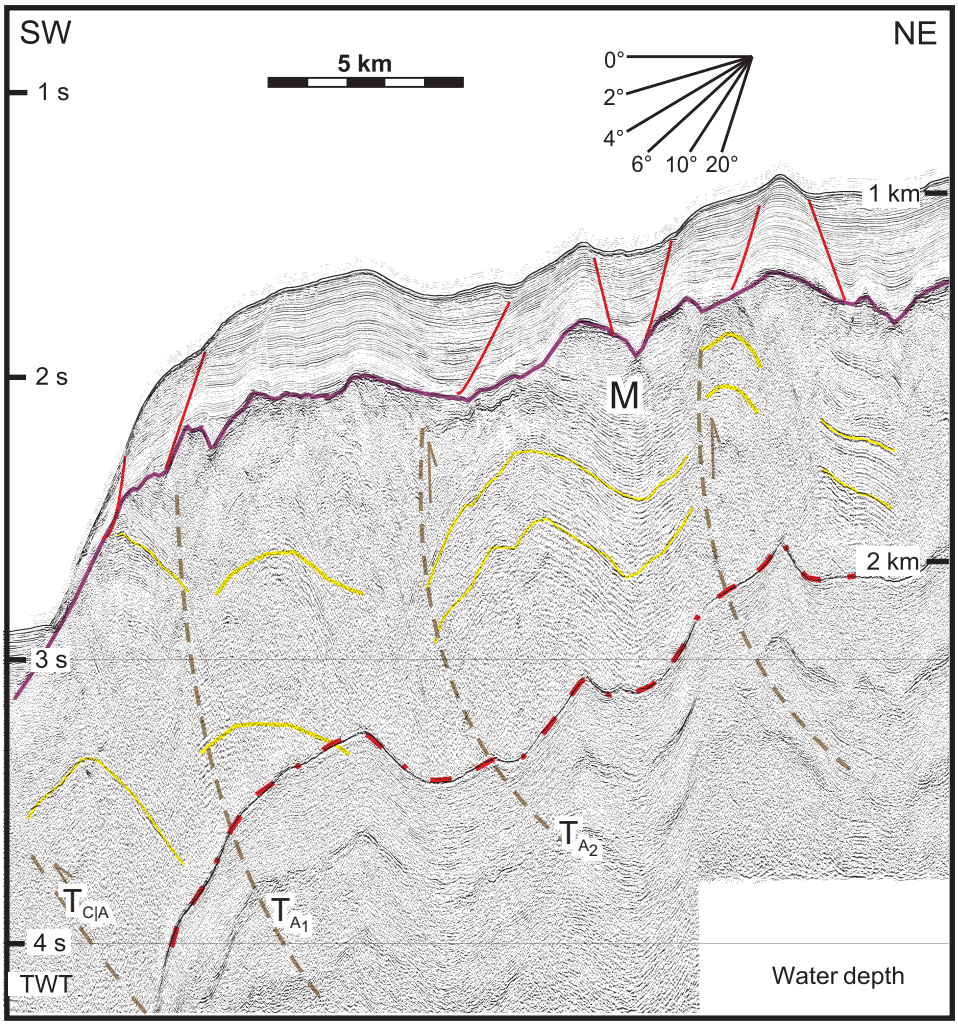

Figure 5.14: High-resolution multichannel seismic reflection profile showing the detailed structural architecture of Domain 3A. Note the extensional faults bounding the horst and graben structures create notable corrugation on the seafloor. Location is shown in Figure 5.12. The angular scale was calculated at seismic water velocity (1500 m/s) and is not valid at depth. Seabed multiple is highlighted in dotted red.

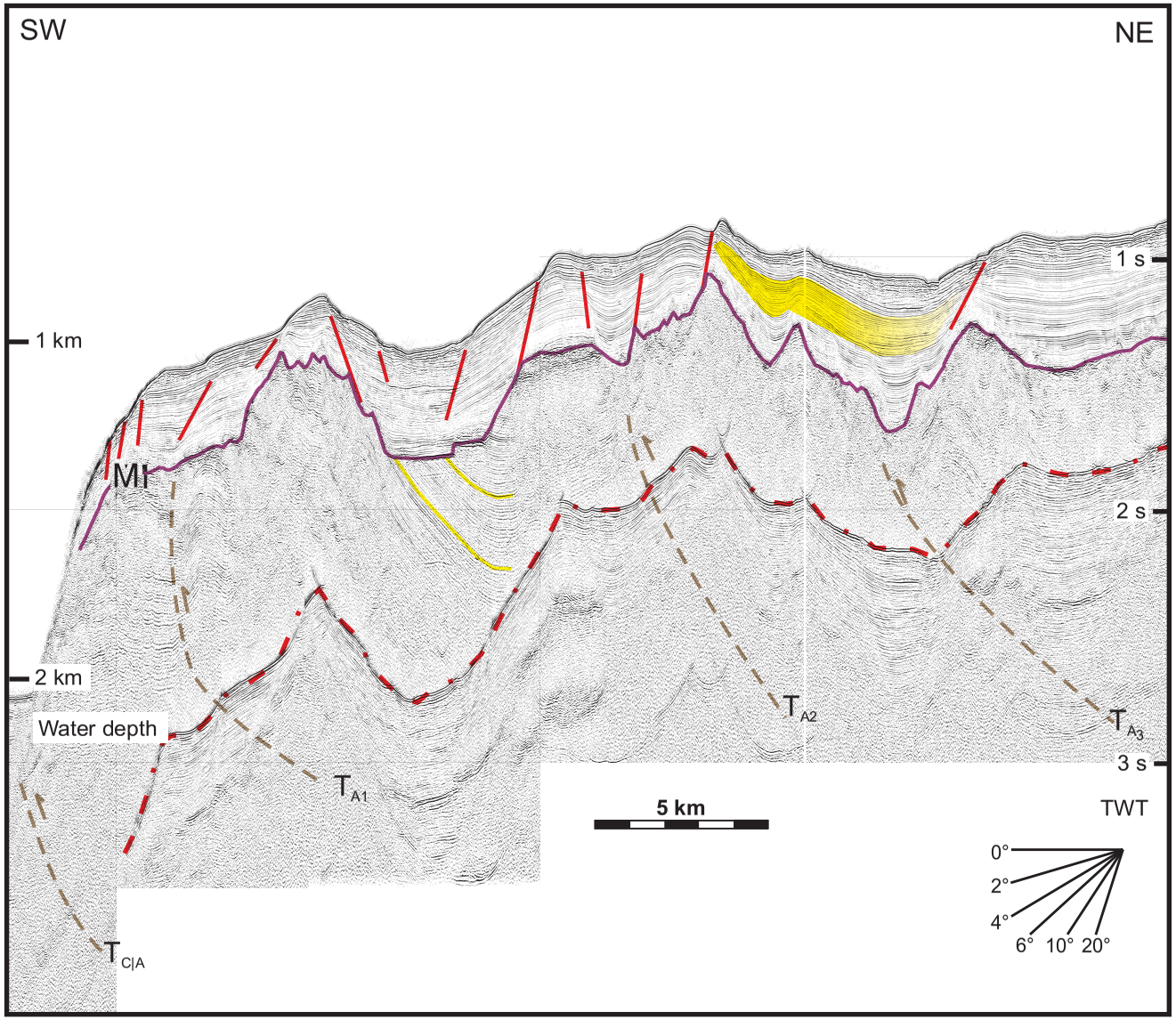

Figure 5.15: High-resolution multichannel seismic reflection profile showing the detailed structural architecture of Domain 3A. Note the extensional faults bounding the horst and graben structures create notable corrugation on the seafloor. Two small piggy-back basins show minor growth. Location is shown in Figure 5.12. The angular scale was calculated at seismic water velocity (1500 m/s) and is not valid at depth. Seabed multiple is highlighted in dotted red.

5.17). The horst and graben structures which are predominantly imaged in the south become progressively less defined toward the north. High-angle extensional faults extend almost to the seabed but do not appear to cut the M-reflector (e.g. Figs. 5.16, 5.17). The continental slope is steep and is similarly cut by numerous steep superficial faults which form bathymetric steps on the seafloor (e.g. Figs. 5.16 and 5.17).

The general structural architecture described above suggests that, in this region, the pervasive fold-thrust activity predominant in the pre-Messinian Miocene largely ceased during the Messinian and then, in the Pliocene-Quaternary, a completely different deformational style, resulting in basin-wide extensional faulting, commenced. The fact that these extensional faults do not appear to cut the M-reflector suggests that they are a superficial response in a rheologically distinct Pliocene-Quaternary cover to minor recurring deformation in the basement. There is some evidence of continued (or re-activated) thrusting during this time, at least into the lowermost portion of the Pliocene-Quaternary and along the western margin of the domain (e.g. Figs. 5.11 and 5.15).

5.3.2 Domain 3B: Deep-rooted extensional fault zone

Domain 3B is situated in the westernmost region of the study area (Fig. 5.11) and occupies the shelf and slope of the western Antalya Basin. This sub-domain is characterized by 5 major NE-SW and NNE-SSW- trending, high-angle normal faults (e.g. E_1 - E_5 in Fig. 5.11). Even though line spacing was relatively tight (approximately 4-5 km), correlating these faults was not easy. The combination of a steep continental slope (with numerous large slide and slump masses, see Fig. 5.18) and a shallow seabed in this region render poorer temporal and lateral resolution of seismic markers below the M-reflector than in other regions in the study area. It has also been speculated that in at least some of this region, the poor reflectivity below

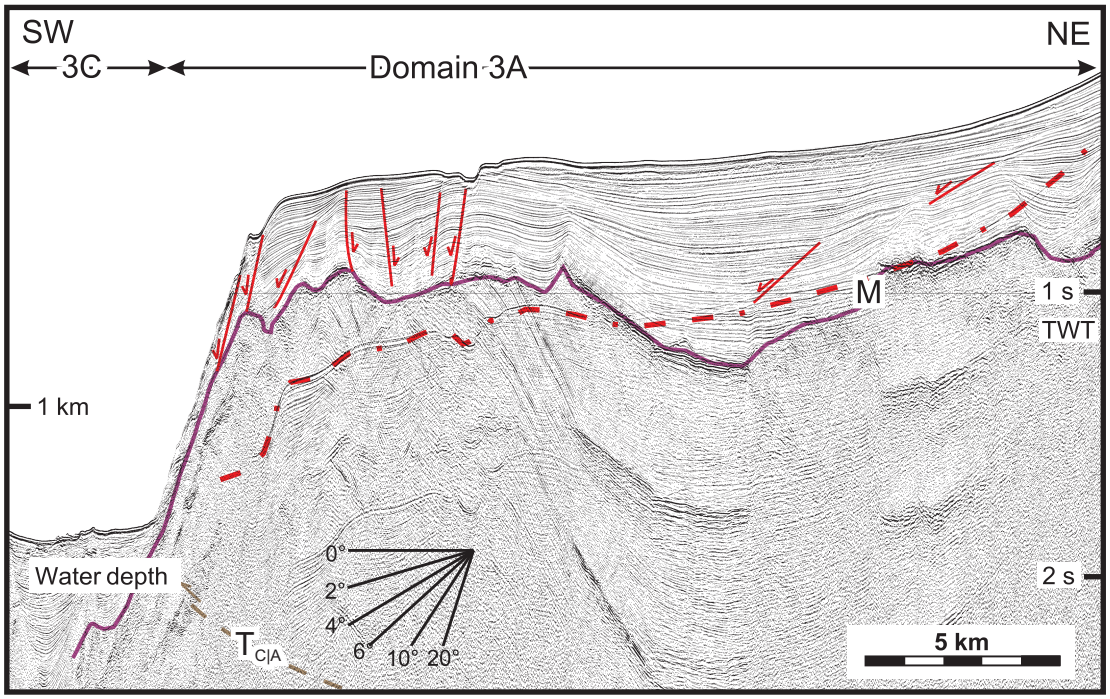

Figure 5.16: High-resolution multichannel seismic reflection profile showing the detailed structural architecture of the more northern region of Domain 3A. Note the steep SW margin of Domain 3A, where several steeply dipping extensional faults create distinct steps of the seafloor. Location is shown in Figure 5.12. The angular scale was calculated at seismic water velocity (1500 m/s) and is not valid at depth. Seabed multiple is highlighted in dotted red.

!p]

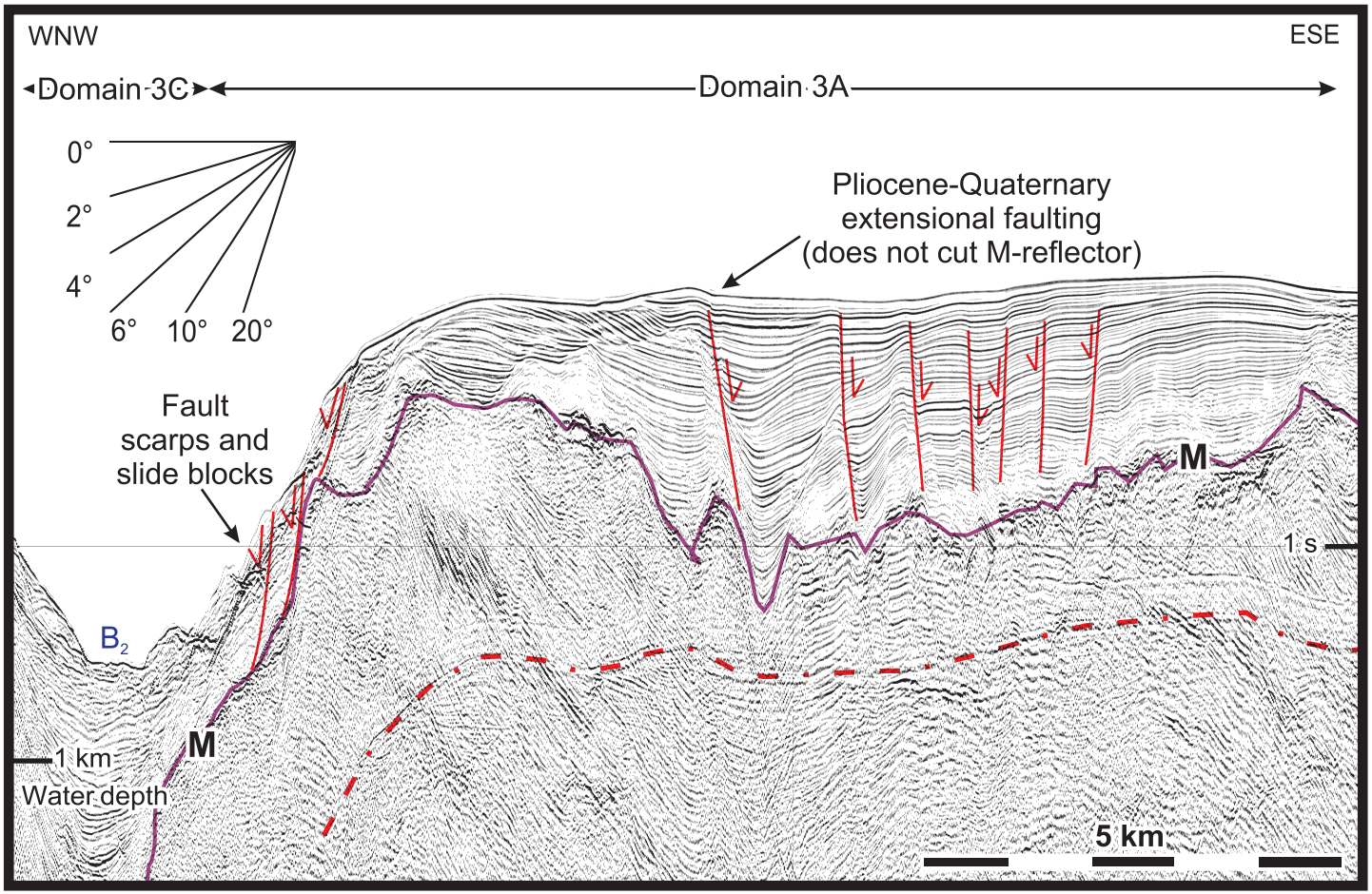

Figure 5.17: High-resolution multichannel seismic reflection profile showing the detailed structural architecture of the northernmost portion of Domain 3A. Note the high angle planar faults that that cut the Pliocene-Quaternary sediments and sole onto the M-reflector. Location is shown in Figure 5.12. The angular scale was calculated at seismic water velocity (1500 m/s) and is not valid at depth. Seabed multiple is highlighted in dotted red. Uninterpreted seismic profile can be found in Plate 5, Fixes 133 - 122.

the M-reflector is attributed to the presence of limestones or igneous basement rock. Locations of the high-angle extensional faults can still be delineated, however, using features such as present-day seabed, M-reflector morphology (e.g. Figs. 5.18, 5.19, and 5.20) as well as interpreting tie-lines connecting the NW-SE-trending profiles.

The eastern boundary of Domain 3B is delineated by the reactivated Miocene $T_{B|C}$ thrust (see Fig. 5.11). Fault E_1 marks the first extensional fault in a series five NE-SW-trending, SW-dipping deeply-rooted extensional faults which dominate the domain. The northenmost extensional faults (i.e. E_4 and E_5 in Figs. 5.11, 5.18, 5.19) assume a slightly more N-S orientation than those southward in the region (i.e. E_{B_1}, E_{B_2} and E_{B_3} in Figs. 5.11, 5.20). This appears to correlate with the present-day shoreline and shelf edge.

In the more northerly region of the domain, the shelf edge is well defined and is marked by a prominent broadly NNE-SSW- trending and SSE-dipping normal fault which clearly offsets the depositional surface and creates a distinctive step on the seafloor (e.g. E_5 in Fig. 5.18). The slope face in this area is marked by several large lenticular units, bounded at their upslope ends by numerous superficial listric detachment surfaces that rest over the steeply ($10° - 15°$) SE-dipping M-reflector (e.g. Fig. 5.18). These shallow structures are very similar in morphology and internal seismic architecture to the submarine slide and slump masses described elsewhere (e.g. Hiscott and Aksu, 1994).

Further southward, the domain is noticeably broader and the deeply-rooted extensional fault system appears to swing slightly counter-clockwise to assume a more NE-SW orientation aligning with the coastline in the area (e.g. E_1-E_3 in Figs. 5.11, 5.20). Of further note in this region of the sub-domain, a number of surficial extensional faults are readily mappable across the seismic reflection profiles. The strike of these surficial faults appear to be consistent with the strike of the deeply-rooted

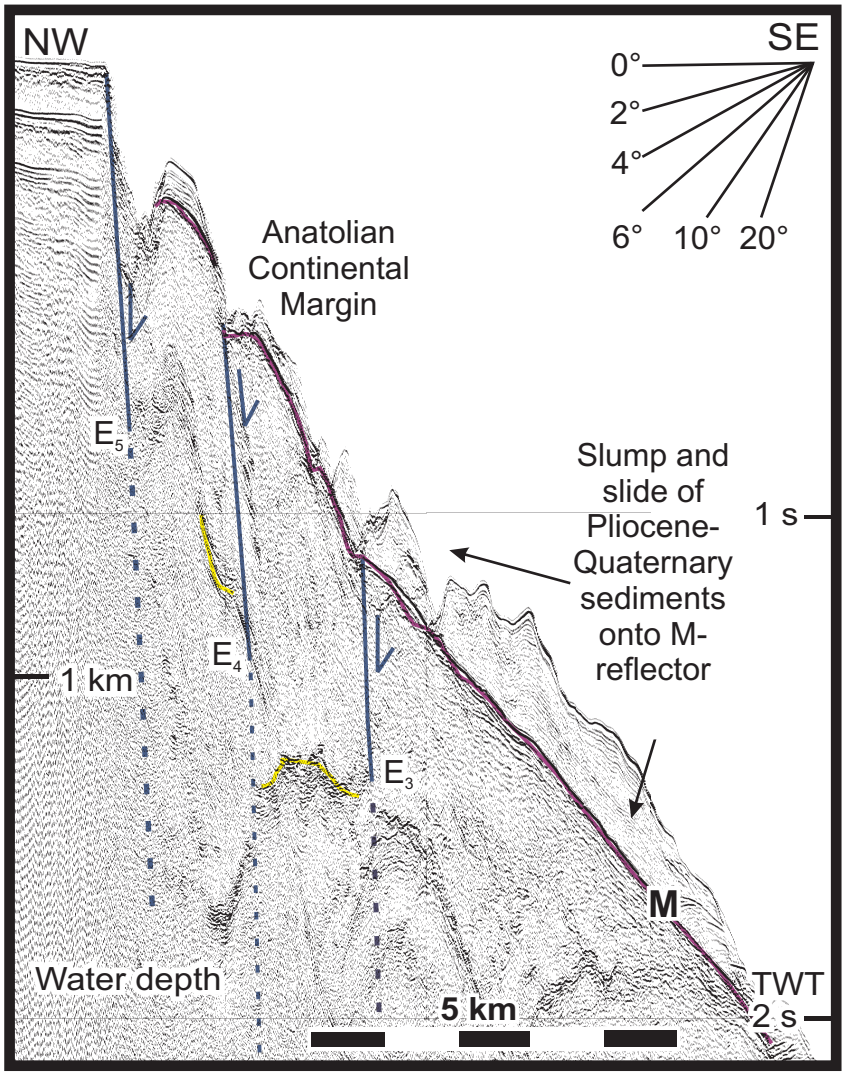

Figure 5.18: High-resolution multichannel seismic reflection profile showing the detailed structural architecture of the northernmost portion of Domain 3B. Note the high-angle normal faults that define the morphology of the shelf-edge. Location is shown in Figure 5.12. The angular scale was calculated at seismic water velocity (1500 m/s) and is not valid at depth. Uninterpreted seismic profile can be found in Plate 9, Fixes 211-202.

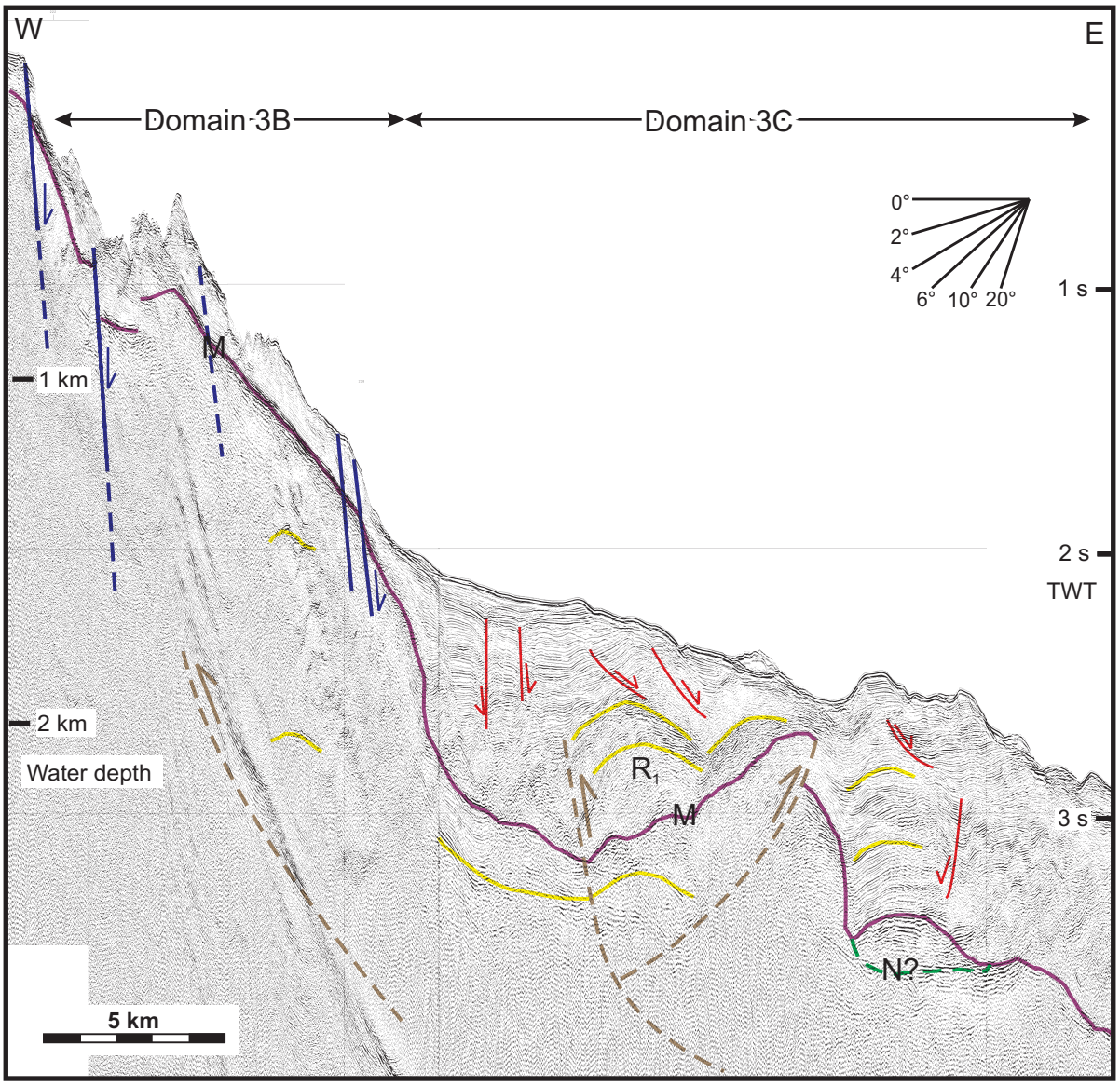

Figure 5.19: High-resolution multichannel seismic reflection profile showing the detailed structural architecture of the northernmost portion of Domains 3B and 3C. Note the high-angle normal faults that define the morphology of the shelf-edge. Also note the shallow-rooted normal faults within the Pliocene-Quaternary successions of Domain 3C, as well as the reactivated Miocene thrust. Location is shown in Figure 5.12. The angular scale was calculated at seismic water velocity (1500 m/s) and is not valid at depth. Uninterpreted seismic profile can be found in Plate 11, Fixes 220-242.

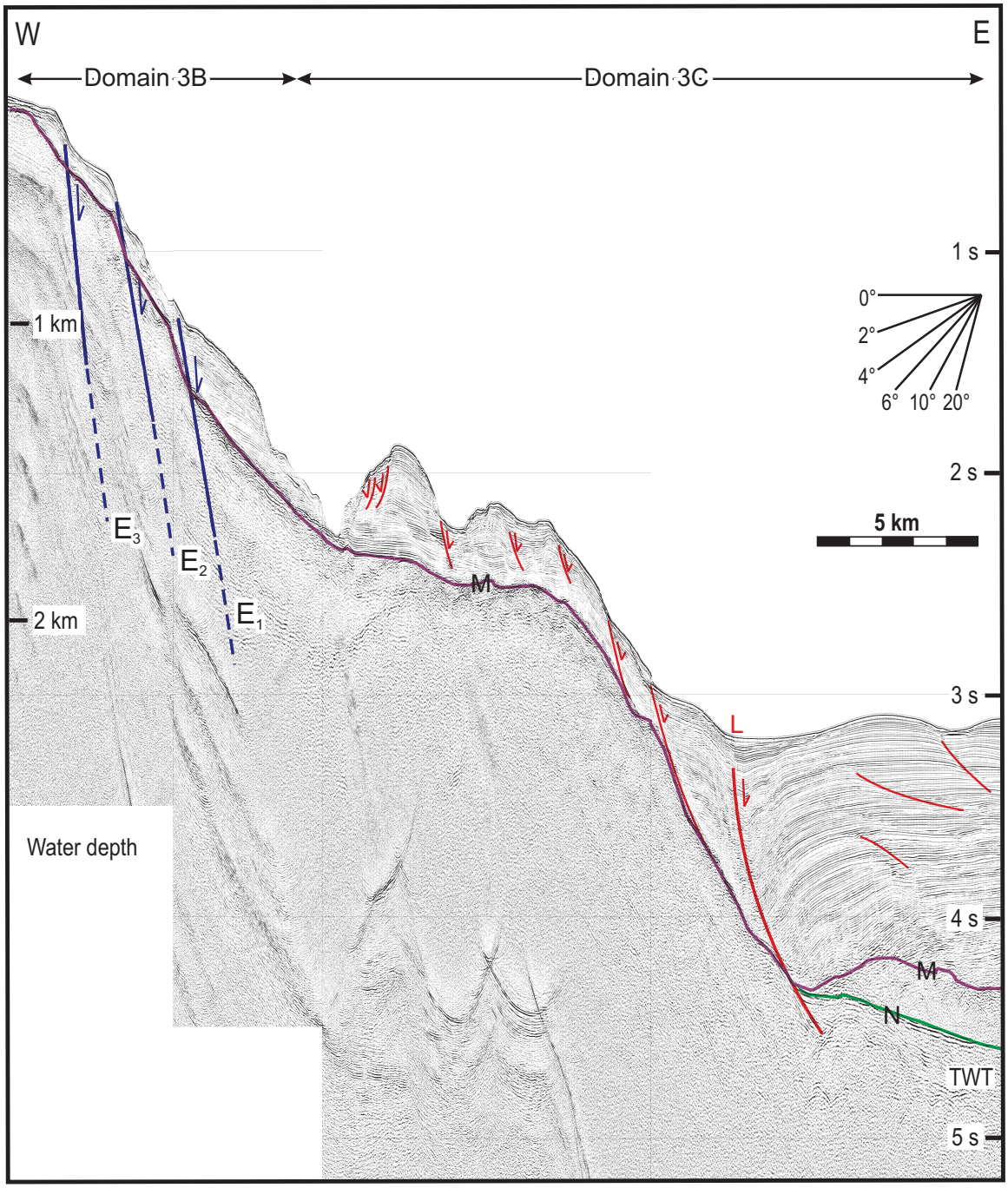

Figure 5.20: High-resolution multichannel seismic reflection profile showing the detailed structural architecture of Domains 3B and 3C. Note the high-angle faults which define the morphology of the slope. Also note the shallow-rooted extensional faults within the Pliocene Quaternary sediments and the listric extensional fault, *L*, that bounds the salt-controlled basin in the south. Location is shown in Figure 5.12. The angular scale was calculated at seismic water velocity (1500 m/s) and is not valid at depth. Uninterpreted seismic profile can be found in Plate 15, Fixes 292 - 319.

extensional faults (Fig. 5.11); this suggests that one of the triggering mechanisms may be the development of the high-angle faulting along the western margin of the study area (discussed in Chapter 6).

5.3.3 Domain 3C: Halokinetic and transitional zone

Domain 3C is a roughly arrowhead-shaped zone situated between the arcuate thrusts and superficial extensional faults of Domain 3A in the east and the NE-SW-trending high-angle extensional faults of the Domain 3B in the west (Fig. 5.11). This region exhibits complex structures involving re-activation of pre-Messinian Miocene thrusts, displacement of Messinian evaporites and the development of prominent fans of superficial extensional faults. These complex and diverse structures form an internally coherent spatial framework with extensional and contractional structures developing in association with one another and having similar orientations and trends (implications of which is discussed in Chapter 6).

In the south, the domain is characterized by large, deep Pliocene-Quaternary basin bounded to the north by a south-dipping north-convex, arcuate listric extensional fault L (e.g. Fig. 5.11, 5.20, 5.21, 5.22). L appears to cut the M-reflector; it extends from the seafloor, where it creates an inflection on the seabed, and follows a listric trajectory into the pre-Messinian Miocene successions (e.g. Fig. 5.20, 5.21, 5.22). Exactly where below the M-reflector this fault terminates is not clear from the seismic profiles, but it is possible that it soles into the evaporite sequences. A large, roll-over anticline is located on the hanging wall of fault L (e.g. Figs. 5.20, 5.21, 5.22); this could have formed as a result of salt expulsion. Spectacular minibasins and detachment surfaces in the Pliocene-Quaternary sediments are formed by the displacement of the Messinian evaporites described in Chapter 4 and in Section 5.2. Growth strata in the Pliocene-Quaternary sediments confirm that the migration of salt continued throughout the

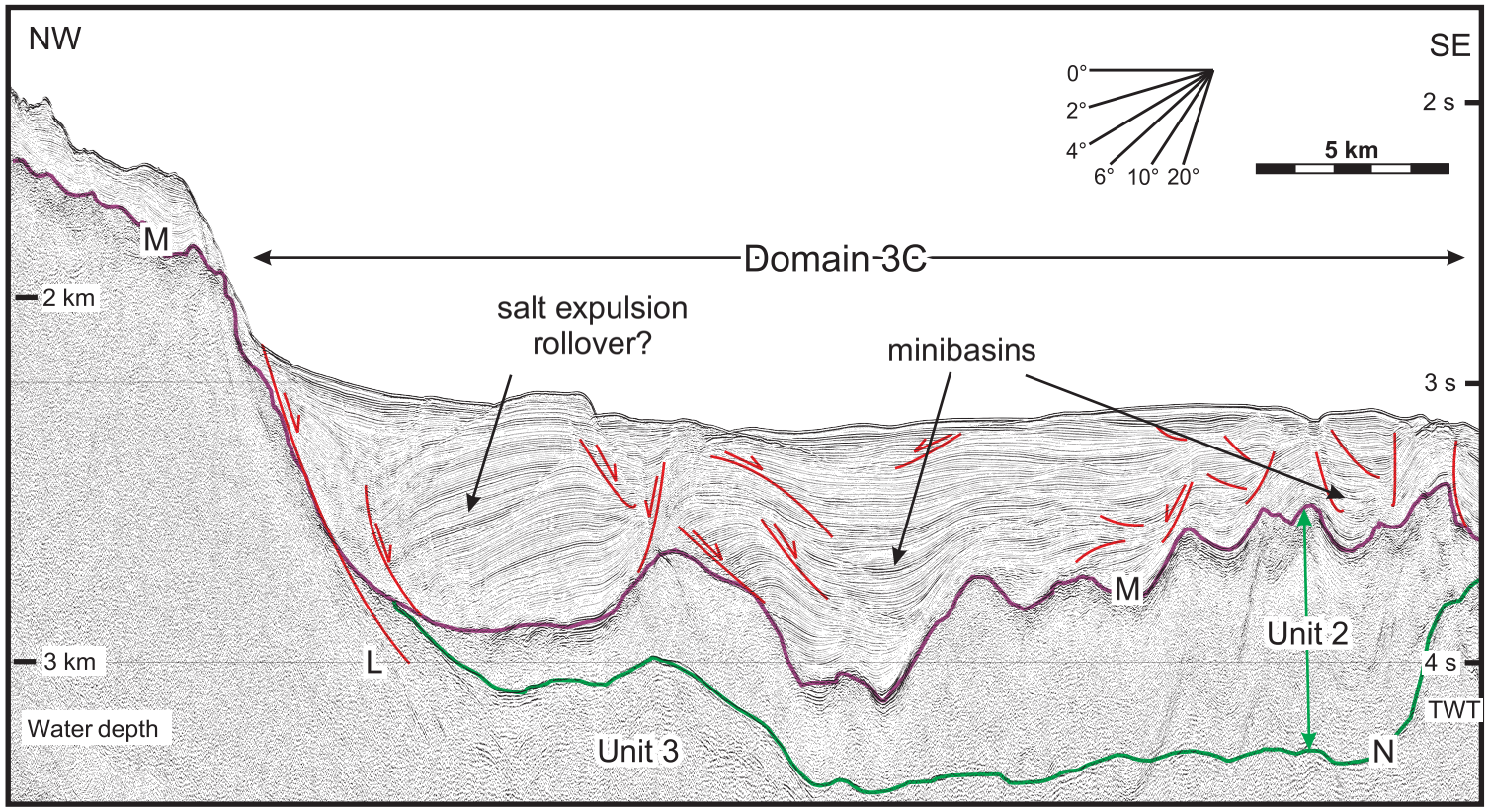

Figure 5.21: High-resolution multichannel seismic reflection profile showing the detailed structural architecture of Domain 3C. Note the prominent listric fault, L, that delineates the edge of the salt-controlled deeper Antalya Basin. A large rollover anticline is adjacent to L and may be the result of salt expulsion. Note the minibasins and detachment surfaces in the Pliocene-Quaternary sediments which were formed due to the displacement of the Messinian evaporite sequences. The angular scale was calculated at seismic water velocity (1500 m/s) and is not valid at depth. Location is shown in Figure 5.12.

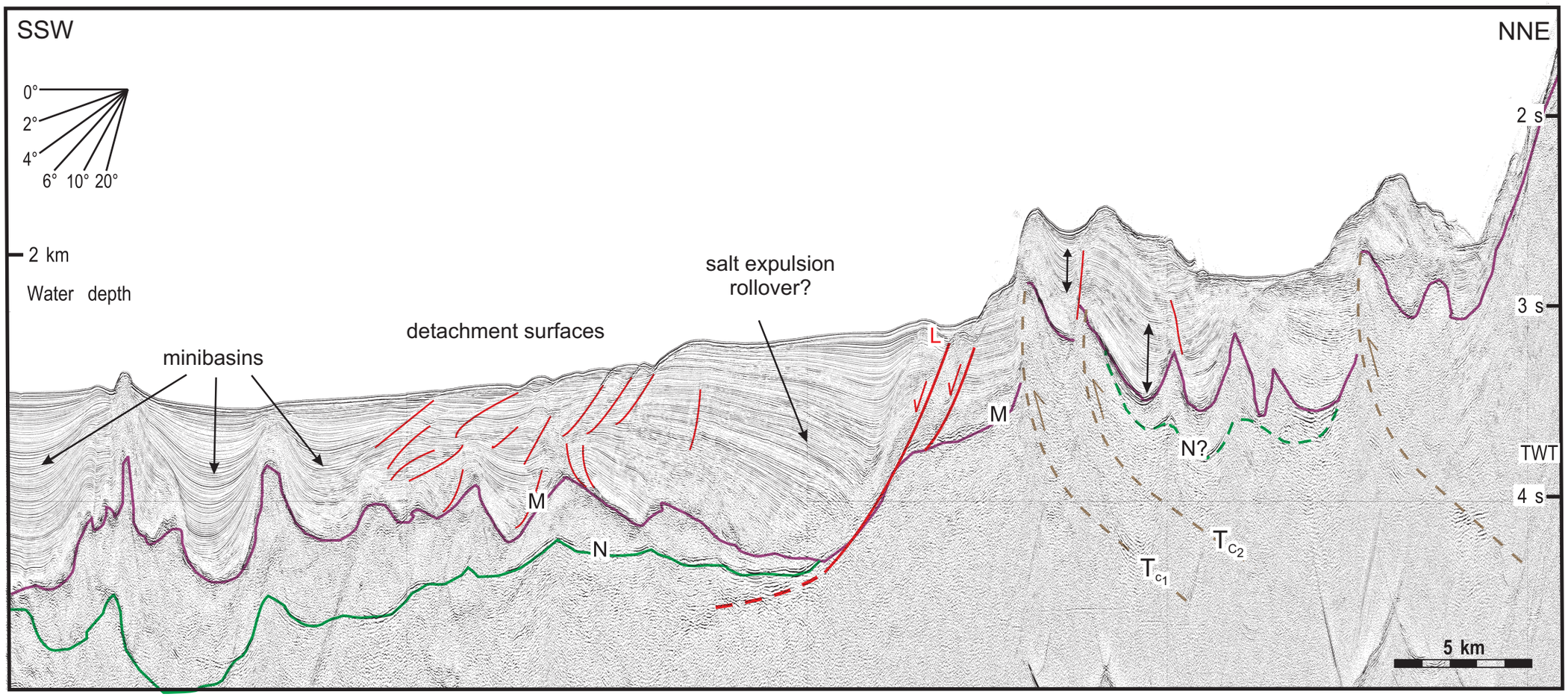

Figure. 5.22 High-resolution multichannel seismic reflection profile showing the detailed structural architecture of Domain 3C. The arcuate listric fault, L, bounds the northern edge of the deep Pliocene-Quaternary salt-controlled basin and appears to sole somewhere below the M-reflector, possibly into the evaporite sequences. A large rollover anticline has formed on its hangingwall; this could be largely driven by salt expulsion. Displacement of the Messinian evaporites has formed various detachment surfaces and superficial extensional faults within the Pliocene-Quaternary sediments. Further northward, large offset of the M-reflector and the growth in the Pliocene-Quaternary sediments indicate thrusts T_{c1} and T_{c2} are active during this time. Bright reflectivity characteristic of the N-reflector is imaged here, thus the presence of Messinian evaporites in the region is likely. Location is shown in Figure 5.12. The angular scale was calculated at seismic water velocity (1500 m/s) and is not valid at depth. Uninterpreted seismic profile can be found in Plate 1, Fixes 1 - 43)

entirety of the interval (e.g. Figs. 5.21 and 5.22). Note that although comment on the geometric trajectory of a fault is tedious in a time section, it is reasonable to argue that L is indeed a listric fault, as a rollover anticline would not be expected adjacent to a planar fault. The edge of salt is mapped in thick green on Figure 5.11 and it should be noted that very few extensional structures are mapped within this sub-domain south of this marker. Poor correlation between faults in this region is due, largely, to the complexity of the superficial faulting and detachment surfaces here.

Immediately north of this salt-controlled basin, there are two active thrusts (i.e. T_{C_1} and T_{C_2} in Fig. 5.11); discussed briefly in Domain 1C. Growth strata within the Pliocene-Quaternary sequences and large offsets in the M-reflector are evidence that these thrusts were indeed active during the Pliocene-Quaternary (e.g. Fig. 5.22). In fact, inflections on the seabed and growth strata within the youngest Pliocene-Quaternary sequences suggest that these thrusts are active at present. Figure 5.22 also shows reflectivity below the M-reflector characteristic of the N-reflector, hinting that Messinian evaporites may be present here. Unfortunately, due to complex geology in this area, it was not possible to correlate the (possible) salt diapirs across seismic reflection profiles. There is evidence of reactivation of several other Miocene thrusts as well including the pervasive domain-bounding $T_{B|C}$ thrust (e.g. Figs. 5.11, 5.19). The remainder of the central region of this sub-domain is dominated by by a series of superficial NE-SW- trending extensional faults (e.g. Figs. 5.11, 5.19, 5.20). The orientation of these faults appears to mirror that of the surficial extensional faults of Domain 3B.

Northward, the domain becomes a narrow belt extending toward the present-day shoreline along northwestern Antalya Bay (Fig. 5.11). Two prominent, broadly N-S trending, ridges also emerge in this region (i.e. R_1 and R_2 in Fig. 5.11). The R_1 ridge is especially interesting because it appears to change character from south to

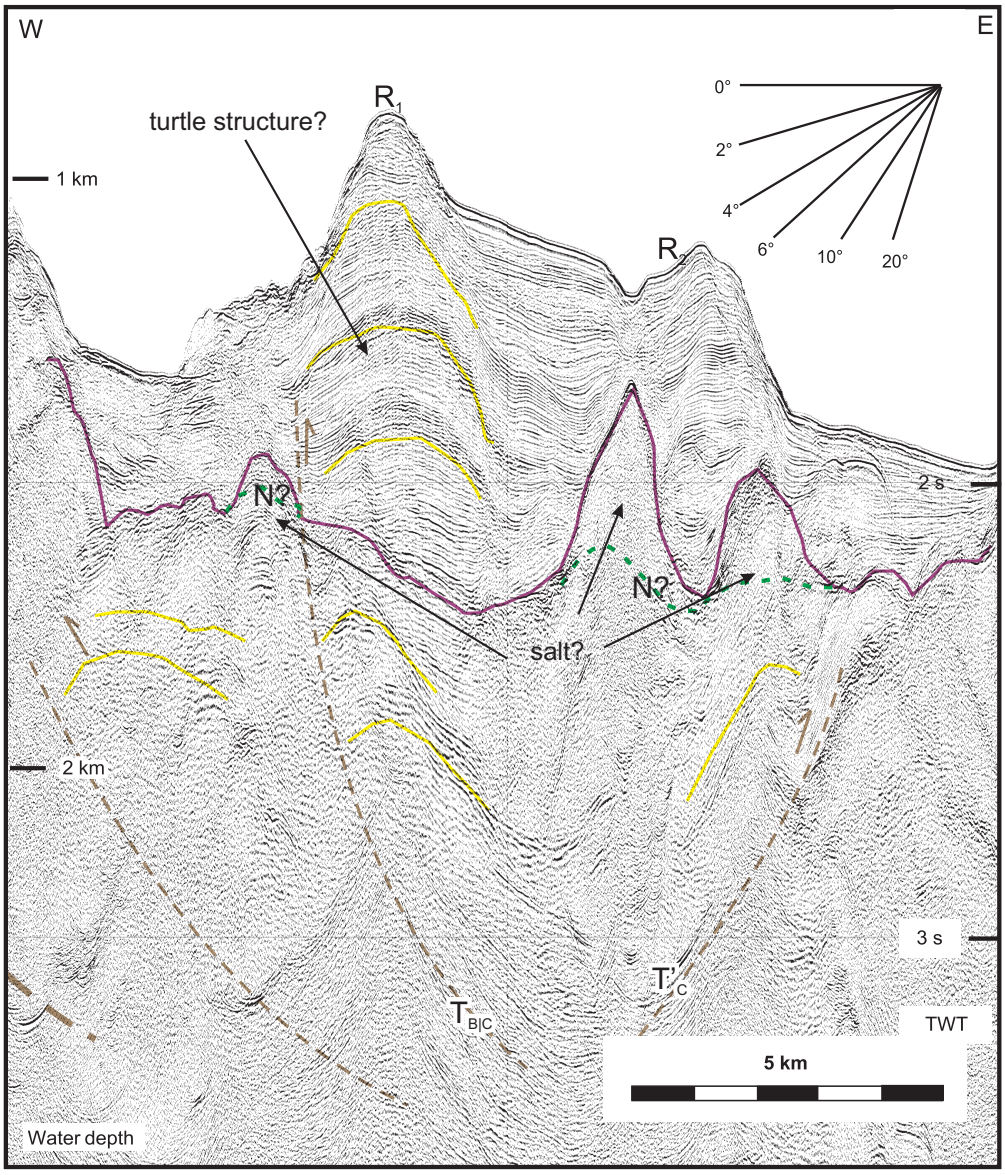

Figure 5.23: High-resolution multichannel seismic reflection profile showing the detailed structural architecture of Domain 3C. Note the presence of extensional faults superimposed on re-activated(?) Miocene thrusts. Antiform above the M-reflector suggests possible turtle structure; is there salt in the core of the adjacent M-reflector antiforms? Location is shown in Figure 5.12. The angular scale was calculated at seismic water velocity (1500 m/s) and is not valid at depth. Uninterpreted seismic profile can be found in Plate 7, Fixes 156 - 167.

north. Furthest south, this ridge is buried and does not affect the morphology of the seabed (e.g. Fig.5.23); however, moving northward, the ridge emerges and creates a prominent inflection on the seafloor (e.g. Fig. 5.23). Based on the morphology and growth of the Pliocene-Quaternary sediments imaged in Figure 5.23, R_1 appears to be the thrust culmination of the reactivated (?) $T_{B|C}$ thrust (e.g. Figs. 5.19, 5.23). It is possible, however, that this ridge formed as the result of salt expulsion and, as such, is a turtle structure. Although the N-reflector is not obvious here in the seismic reflection profiles, there may indeed be salt in the core of the M-reflector anticlines adjacent to the R_2 ridge. The R_2 ridge is easily mapped across this region of the sub-domain (i.e. Fig. 5.11). This ridge shows growth strata along its western flank, hinting at the Pliocene-Quaternary activity of the pre-Messinian back thrust $T_C{}'$ (e.g. Fig. 5.23).

As in Domain 1C of the pre-Messinian Miocene, this domain represents a region of complex deformation which appears to be the junction of (at least) two morphotectonic styles. Implications of this and its possible relation to the Isparta Angle are discussed in Chapter 6.

Chapter 6

Discussion

The previous chapter described the detailed structural architecture of the Antalya Basin in terms of three time intervals: 1- pre-Messinian Miocene, 2- Messinian, and 3- Pliocene-Quaternary. Tectonism during the pre-Messinian Miocene was largely contractional and spatial partioning during this interval is based primarily on the trends and vergence directions of the thrust systems. During the Messinian, there was likely a period of relative quiescence in the tectonic activity across the western Antalya Basin. The period coincides with a major tectonic reorganization in the eastern Mediterranean Sea: the collision of the Arabian Microplate with the Eurasian Plate and its final suturing along the Bitlis-Zagros belt (e.g. Şengör, 1979; Şengör et al., 1985; Dewey et al., 1986). At some time between the later Miocene and the Pliocene, the tectonic regime changed to include elements of extensional tectonics, especially in the western area where evidence suggests deeply-rooted extensional faulting. The easternmost domains of the pre-Messinian Miocene and Pliocene-Quaternary (i.e. Domains 1A and 3A, respectively) are predominantly characterized by NW-SE-trending, SW-verging structures. In the pre-Messinian Miocene, this region was dominated by

a large arcuate fold-thrust belt (i.e. Fig. 6.1). During the Pliocene-Quaternary, a complex, similarly-trending arcuate superficial extensional fault system was developed within these younger sediments and recent activity of some of the pre-Messinian thrusts is evident (i.e. Fig. 6.2). The structures within the westernmost domains are poorly imaged in both the pre-Messinian Miocene and Pliocene-Quaternary but are both found to be broadly N-S- trending (i.e. domains 1B and 3B, respectively, in Figs. 6.1 and 6.2). Poor lateral continuity of reflectors within the pre-Messinian unit allows only for speculation for Miocene thrusting based on inferred minor structures visible in the seismic reflection profiles. During the Pliocene-Quaternary, tectonic activity in this region appears to have completely shifted to an extensional fault system. Based on markers in the pre-Messinian successions and the offset of both the M-reflector and the seafloor, these faults are speculated to have deep roots somewhere within the pre-Messinian unit. The presence of a deeply-rooted extensional fault system in the Pliocene-Quaternary is further evidenced by the morphology of the present-day coastline. In both the pre-Messinian Miocene and the Pliocene-Quaternary intervals, there appears to be a central transitional spatial domain (i.e. Domains 1C and 3C, respectively, in Figs. 6.1 and 6.2) linking the arcuate SW-verging system in the east with the broadly N-S system in the west. In the pre-Messinian Miocene, this transitional domain contains poorly-imaged Miocene thrusts. In the Pliocene-Quaternary, some of these thrusts appear to be still active (or possibly reactivated) and impact the overlying sediments as well as the seafloor; there is also evidence of halokinetic influence throughout the Pliocene-Quaternary, especially in the southern region of this transitional zone. In both the pre-Messinian Miocene and the Pliocene-Quaternary, this is a region of very complex deformation and has important significance for the structural evolution of the area.

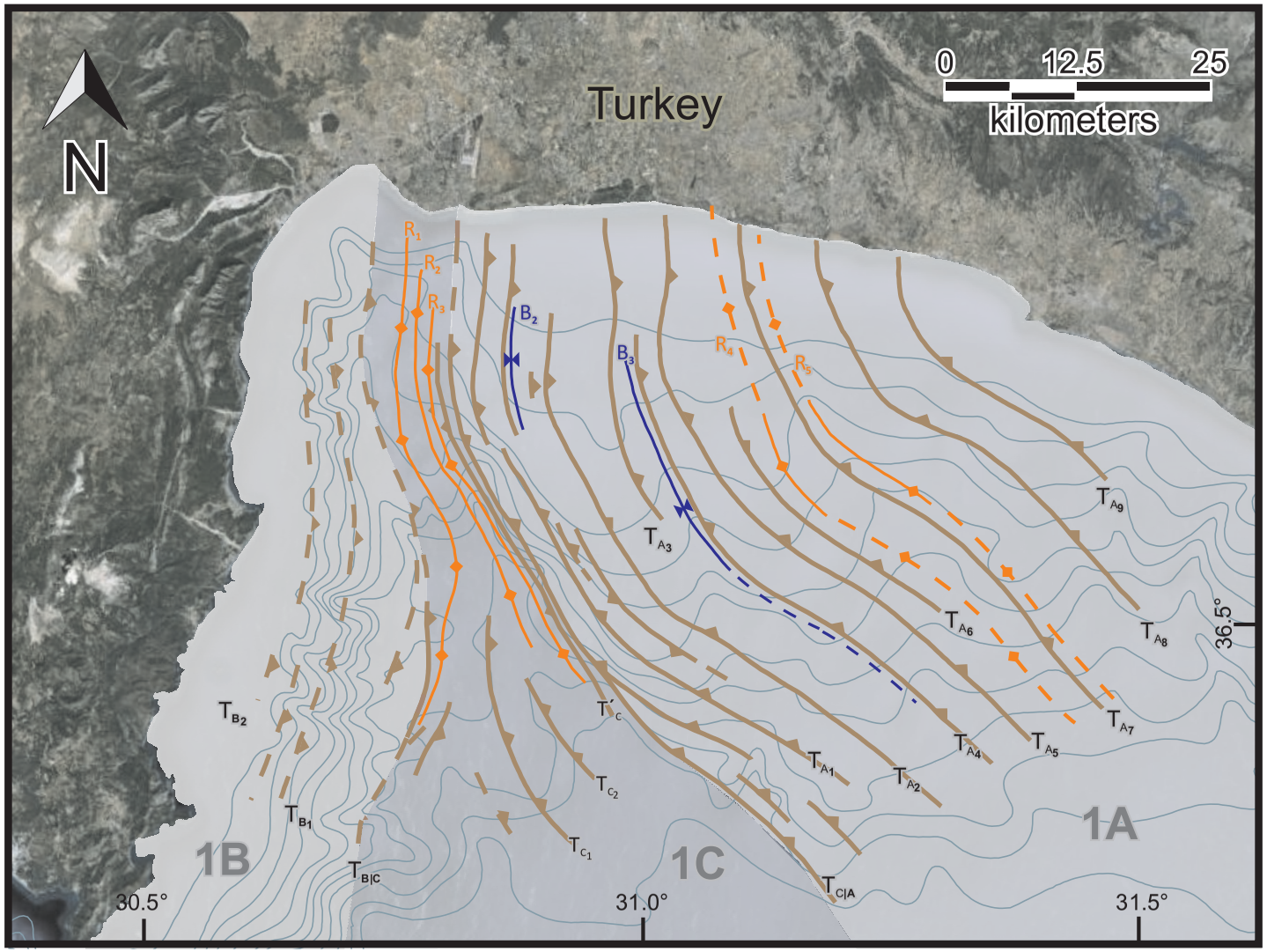

Figure 6.1: Structural map of the western Antalya Basin during the Miocene showing major structures including: thrust faults, shown with filled triangular ticks; crestal hinge lines of prominent ridges, shown with diamond ticks; and trough lines of major piggy-back basins developed on the backlimbs of major thrusts, shown with bow-tie ticks. Structural domains 1A, 1B, 1C are highlighted.

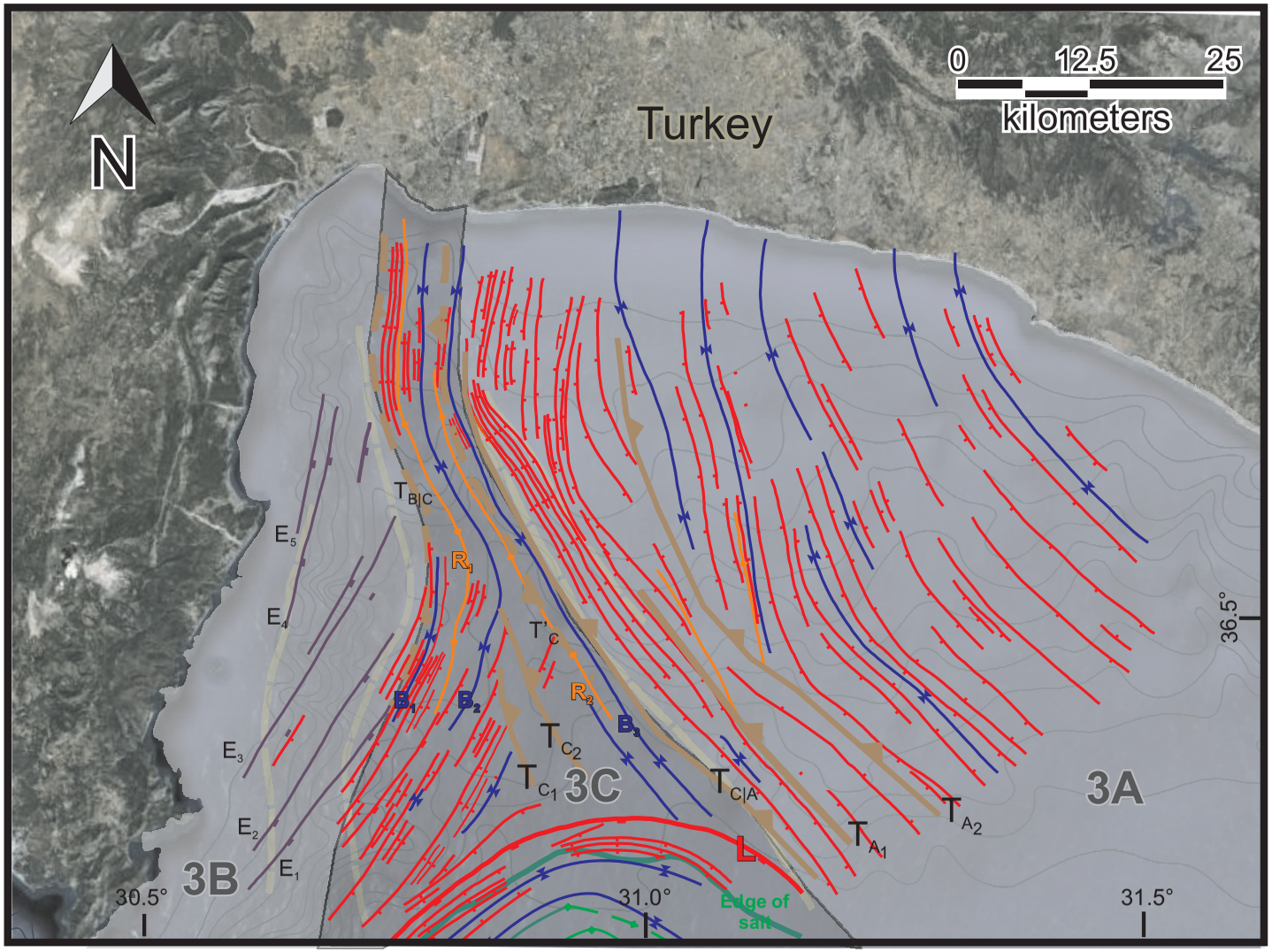

Figure 6.2: Structural map of the western Antalya Basin showing the spatial partitioning of strain that characterizes the structural architecture of the region during the Pliocene-Quaternary. Major structures include: normal faults, shown with filled rectangular ticks on the hanging walls; thrust faults, shown with filled triangular ticks on the hanging walls; the crestal hinge lines of prominent ridges, shown with diamond ticks; and trough lines of major basins, shown in bow-tie ticks. Structural domains 3A, 3B, and 3C are highlighted.

So what is the significance of these structural domains? What are these structures telling us, not only about the evolution of the western Antalya Basin, but of the evolution of the greater Isparta Angle? Of the eastern Mediterranean Sea? In the following discussion, the structures and stratigraphic relationships described in Chapters 4 and 5 are examined to place them in a local and regional context in an attempt to answer some of these questions and add yet another piece to the eastern Mediterranean jigsaw puzzle. A tectonostratigraphic chart is shown in Figure 6.3 which summarizes the key findings from this study as well as key findings from studies in the surrounding area (e.g., Dumont, 1976; Özgül, 1984; Monod, 1977; Waldron, 1984; Robertson and Woodcock, 1986; Dilek and Rowland, 1993; Poisson et a., 2003a,b) to show how the region has evolved since the late Cretaceous following the onset of E-W compression which initiated the formation of the Isparta Angle.

6.1 Morphotectonic elements of the Miocene fold-thrust belt

The seismic stratigraphy and structural analysis of the seismic reflection profiles described in Chapters 4 and 5 reveals that two prominent crustal-scale imbricate fold-thrust belts are developed in the western Antalya Basin during the Miocene. The thrusts associated with the eastern belt display broadly arcuate map traces which trend NW-SE in the central region, but progressively assume a NNW-SSE trend toward the present-day shoreline. The thrusts associated with the western belt exhibit straighter map traces and have broadly NNE-SSW orientations. These two systems converge in west-central Antalya Basin to delineate an inverted V-shaped structure with an axis in a broadly N-S orientation (Fig. 6.1). These diverging thrust belts

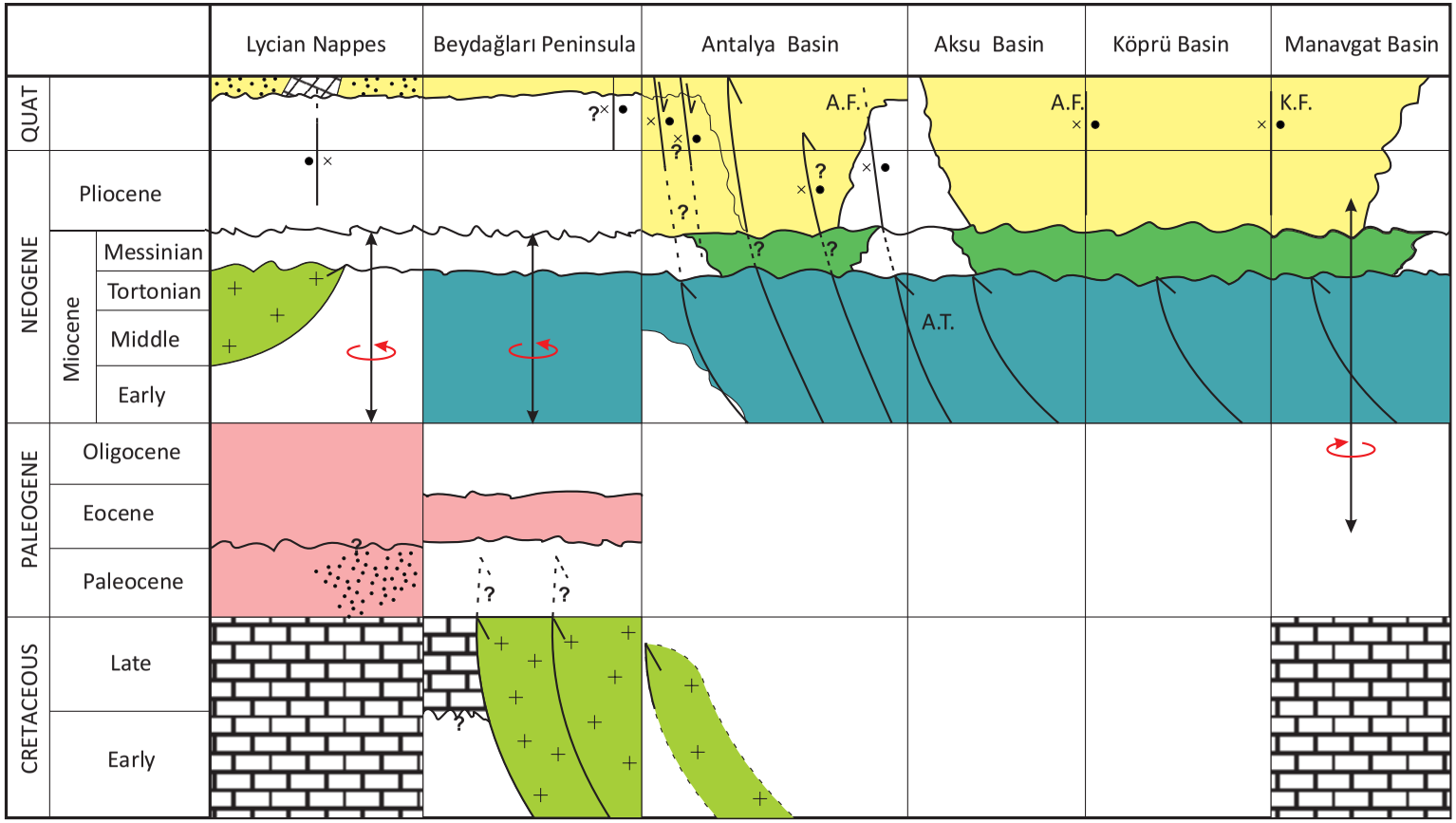

Figure 6.3: Tectonostratigraphic chart summarizing the evolution of the greater Isparta Angle. Note that the Burdur-Fethiye Fault zone, which transects the Lycian Nappes, is characterized by sinistral strike-slip faults with a considerable normal dip-slip component (Şaroğlu et al., 1987; Price and Scott, 1994; Barka et al., 1997). During the Miocene, the western limb of the Isparta Angle, including the Beydağları massif experienced a 30° counterclockwise rotation (Kissel and Poisson, 1987; Morris and Robertson, 1993), whereas the eastern limb experienced a 40° clockwise rotation since the Eocene (Kissel et al., 1990). Color/texture legend: yellow- Pliocene-Quaternary siliciclastics; green (plain)- Messinian evaporites; blue - Miocene siliciclastics and carbonates; green with plus signs - ophiolites; pink - siliciclastics and carbonates; black/white brick - platform carbonates.

are believed to be related, forming the elements of a larger, broadly E-W trending fold-thrust belt, discussed in detail below.

The northernmost seismic reflection profile where the NNW-SSE trending thrusts are observed in the marine data is only 5 km south of the present-day shoreline, allowing an immediate correlation of the marine structures with the similarly-trending and similarly-verging structures mapped onland. The structures mapped in this study clearly show that both the eastern and western fold-thrust belts extend toward the north, and that the apex of the inverted V-shaped Miocene fold-thrust belt is situated in the onland Antalya Basin (Fig. 6.1). Here, it is important to note that the N-S orientation of the axis of the V-shaped structure formed by the convergence of the eastern and western fold-thrust belts appears to align with the axis of the Isparta Angle (Robertson, 2004; Poisson et al., 2003a,b). However, while the trends of the eastern and western fold-thrust belts in the western Antalya Basin appear to match the trends of the eastern and western limbs, respectively, of the Isparta Angle, the broadly WSW-vergence of the thrusts mapped across the Antalya Basin aligns only with the eastern limb of the Isparta Angle. In fact, this broadly WSW-vergence is consistent with the structures mapped onland across the eastern limb of the Isparta Angle (e.g. Waldron, 1984; Poisson et al., 2001, 2003) as well as the thrusts mapped onland in the Beydağları region. This strongly suggests that the SW- and W- verging thrust systems mapped in the eastern and western Antalya Basin, respectively, are actually divergent elements of the fold-thrust belt which tightened the eastern limb of the Isparta Angle during the Oligocene and Miocene. Seismic reflection profiles and borehole data further document that the Tortonian and older successions are involved in the fold-thrust panels, suggesting that the Isparta Angle continued to evolve at least into the latest Miocene. Within the 9-12 thrust panels characterizing the structural architecture of the easternmost portion of the splaying fold-thrust belt (i.e. Domain

1A), 2-3 panels emerge as very prominent structures. One of the prominent panels (i.e. thrusts T_{A_2} - T_{A_5} (Fig. 6.1) is correlated to the thrusts mapped by Işler et al. (2005) and interpreted to be the offshore continuation of the Aksu Thrust mapped onland (e.g. Poisson et al., 2003a,b; further discussed below).

During the Middle-Late Miocene, the greater Isparta Angle (including the marine Antalya Basin as well as the present-day onland Aksu, Köprü and Manavgat Basins) was situated between the evolving Tauride culminations in the north and the subduction zone at the southern edge of the Neotethys Ocean. The Late Miocene (mainly Serravallian to Tortonian) successions of the Karpuzçay and Aksu Formations (see Chapter 4) and their correlative successions imaged in seismic stratigraphic Unit 3 were deposited within a large, elongated, broadly E-W trending foredeep extending from the Bitlis Ocean in the east (e.g. Şengör et al., 1985), across the present-day Iskenderun, Adana and Cilicia basins (Aksu et al., 2005a,b; Burton-Ferguson et al., 2005), and the Kyrenia Range (Calon et al., 2005 a,b) into the Antalya Basin in the west. The final collision of the Arabian Microplate with the eastern portion of the Aegean-Anatolian Microplate in the Late Miocene not only created the Bitlis-Zagros suture zone, but also modified the broadly E-W trending foredeep to create the mainly arcuate deformation fronts observed across the eastern Mediterranean today (Şengör et al., 1985; Dewey et al., 1986). In the eastern section of the deformation front, Middle-to-Late Miocene regional compression led to the development of a broadly NE-SW oriented arcuate fold thrust belt, including the Misis-Kyrenia fold-thrust belt, the Amanos-Larnaka fold-thrust belt and the zone linking the Tartus Ridge with the Cyprus Arc (Robertson, 1998a; Vidal et al., 2000; Hall et al., 2005a,b). In the western portion of the deformation front, this Late Miocene contraction led to the development of a broadly arcuate, but NW-SE oriented structures such as the Aksu-Kyrenia fold-thrust belt (Işler et al., 2005). The structures associated with this Late

Miocene compression are clearly seen within the western Antalya Basin (see Chapter 5). Similar structures were also documented in the eastern portion of the Antalya Basin where large imbricate thrust sheets and their associated ramp anticlines and piggyback basins showed protracted contractional deformation during at the least the deposition of the upper portion of the Miocene Unit 3 (Işler et al., 2005). The current study as well as Işler et al., (2005) show that the Antalya Basin remained as a foredeep during this phase of contraction, allowing the deposition of a thick succession of Unit 3 (see Chapters 4 and 5). This style of Late Miocene tectonic and sedimentary evolution within a foredeep in front of the evolving Tauride culminations is very similar to that described in the Cilicia and Iskenderun Basins (Aksu et al., 2005 a,b), in the Kyrenia Range (Calon et al., 2005 a.b), as well as in the Latakia Basin (Hall et al., 2005).

Progressive northward movement of the Arabian Microplate resulted in its subsequent suturing with the Aegean-Anatolian Microplate in the Late Miocene (Şengör et al., 1985). During this time, the eastern connection of the Neotethys Ocean with the Indo-Pacific Ocean was closed by the evolving Bitlis-Zagros fold-thrust felt. Towards the end of the Tortonian, the progressive NE-directed motion of the African Plate relative to the Eurasian Plate resulted in the narrowing and eventual closure of the connection between the Neotethys Ocean (i.e. Mediterranean Sea) and the Atlantic Ocean to the west. At the end of the Tortonian, the Mediterranean Sea was situated at approximately the same subtropical latitude as today and was completely isolated from both the Atlantic and Indian Oceans. This configuration led to the Messinian Salinity Crisis (Hsü et al., 1978).

During the Messinian, the Mediterranean Sea became desiccated (i.e. the Mediterranean Salinity Crisis, Hsü et al., 1978), and the ensuing lowering of the base level and subsequent subaerial exposure led to profound erosion of all the Mediterranean basins. This erosional event is represented by the N-reflector where Messinian

evaporites are present and by the M-reflector where they are absent. The observed thicknesses of the Messinian evaporite successions range from 3000 m in the Herodotus Basin to 2500 m in the vicinity of the Florence Rise (Biji-Duval et al., 1978), and to 1000 m in the Cilicia and Latakia Basins (Aksu et al., 2004a; Hall et al., 2004). Işler et al. (2005) showed that the present-day volume of Mediterranean Sea can only produce 40 m - thick evaporite deposits if completely desiccated. Thus, they argued that approximately 70 times the current volume of the Mediterranean Sea would be needed to produce the 2500-3000 m - -thick evaporite deposits in the deeper basins. The final phase of desiccation of the Mediterranean Sea at the end of the Messinian (Hsü et al., 1978) and the associated subaerial exposure of the sea floor resulted in the development of the well-known unconformity represented in the seismic reflection profiles as the M-reflector. The truncation of the folded Unit 3 strata (e.g. Domain 1A in Chapter 5) implies that the initial thicknesses of the Miocene sedimentary fill in the piggy-back basins were greater than what is now observed in the seismic reflection profiles. Furthermore, preferential erosion of the crestal regions of the ramp anticlines suggests that at the onset of evaporite deposition during the Messinian, considerable paleotopographic relief may have existed across the contractional domain and the lower portion of the evaporite succession may, therefore, have been deposited in restricted depressions. The progression of contractional deformation during the early Messinian is difficult to establish because the architecture of the evaporite sequences was changed considerably by both contractional deformation and halokinesis that took place after the early Pliocene.

6.2 Morpho-tectonic elements of the Pliocene-Quaternary

A major kinematic change occurred during the transition from the Miocene to the Pliocene, when the regional strain was partitioned into three spatially localized tectonic domains: (1) an extensional/transtensional domain occupying the continental shelf and slope in the westernmost Antalya Basin (i.e. Domain 3B); (2) a domain of reactivated Miocene contractional structures in the southern and central portion of the study area (i.e. Domain 3C); and (3) a predominantly extensional domain, temporally confined to the Pliocene-Quaternary Unit 1, occupying the northeastern potion of the study area (i.e. Domain 3A).

6.2.1 Extensional/transtensional zone in the western Antalya Basin (Domain 3B)

One of the most remarkable aspects of the structural evolution of the western Antalya Basin during the Pliocene-Quaternary is the development of a broad NE-SW trending zone of invariably SE-dipping extensional structures (Fig. 6.2). These steeply-dipping faults cut the Pliocene-Quaternary successions and become deeply rooted in the Miocene successions. This largely N-S trending fault system appears to control the morphology of the present-day continental margin in the westernmost Antalya Basin. Indeed, there are several prominent scarps along the shoreline where the strike of the scarp face is nearly identical to the strike of the individual faults in this system. The fact that these faults are steeply and deeply cutting the Miocene (or older) successions, and that they delineate a series of sharp escarpments both onland and across the shelf break suggests that they form part of a large crustal-scale structure

which shapes the present-day morpho-tectonic framework of the westernmost Antalya Basin. Recent mapping of the onland Beydağları and Antalya Complex (often referred to as the Kemer Peninsula) also delineated numerous Quaternary and younger faults which appear to have developed over the similarly trending Miocene and older thrust surfaces (Fig.6.3). These faults display NNE-SSW trends and extend along the entire Kemer Peninsula (C. Yaltırak, personal communication, June 2012). This fault system appears to link with a major N-S trending strike-slip fault zone that extends 200 km from the towns of Kırka to Afyon, and then to Isparta (Savaşçın et al., 1995). Onland, this strike-slip fault zone is associated with a prominent N-S trending potassic alkaline volcanic belt situation between the Menderes and Kırşehir Massifs. Savaşçın et al. (1995) used radiometric ages and geochemical data on the volcanic successions to show that the volcanism occurred along this N-S zone paralleling the apex of the Isparta Angle. They showed that the age of the volcanic rocks becomes progressively younger from the north (i.e. the region of Kırka and Afyon date at 21-17 Ma) toward the south (i.e. Isparta at 4 Ma and Antalya at 3-1.5 Ma; Bassang et al., 1977; Sunder, 1982; Lefevre et al., 1983). They further argue the motion along the fault zone is dextral.

To the south, the zone extends with a broadly NNE-SSW trend toward the Anaximander Mountains (Fig. 6.4, *sensu lato*). A companion study south of the study area for this thesis (Çınar, in progress) mapped a similar trending fault zone that links northward with the extensional/transtensional NNE-SSW trending faults mapped in this study. The author strongly suggests that the westernmost Antalya Basin is marked by a prominent fault zone that extends 300-400 km from the onland Isparta Angle across the westernmost Antalya Basin into the Anaximander Mountains (*sensu lato*). The considerable length of the structure combined with the Late-Miocene to Pliocene-Quaternary volcanism observed in the onland portion as well as the deeply

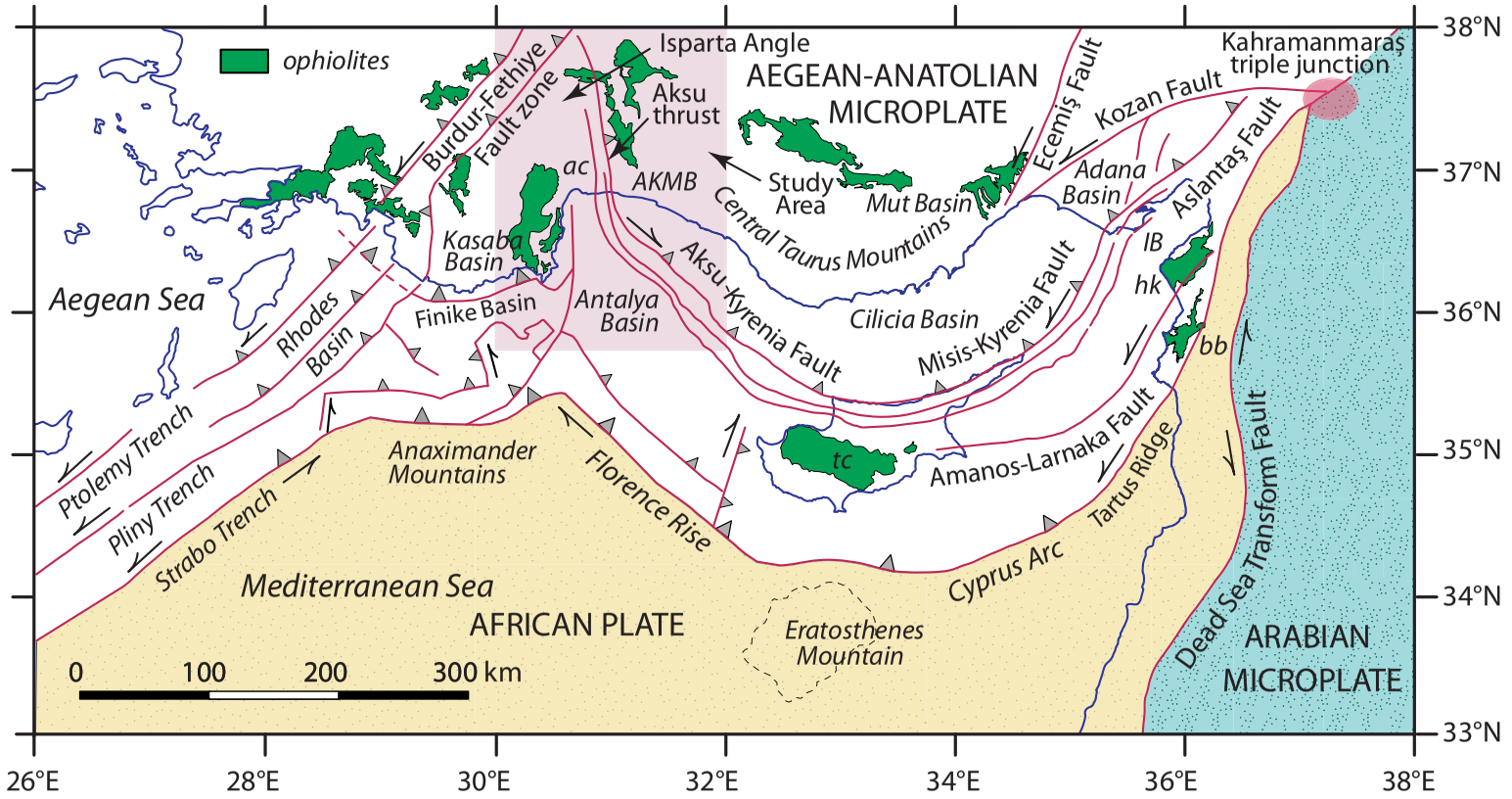

Figure 6.4: Simplified plate tectonic map of the eastern Mediterranean Sea and surrounding regions, showing major plate/microplate boundaries, ophiolites and associated rocks (green fill: ac= Antalya complex, bb= Baér-Bassit complex, hk= Hatay and Kizildag complexes, tc= Troodos complex) and major tectonic elements. AKMB= Aksu, Köprüçay, Manavgat Basins, IB= Iskenderun Basin. Half arrows indicate transform/strike-slip faults.

extending faults in the marine portion of the region collectively support the notion that this is indeed a crustal-scale strike-slip zone in the eastern Mediterranean. Although the marine seismic reflection profile data described in this thesis are mute regarding the sense of horizontal slip, Savaşçin et al. (1995) argue the radiometric ages on the onland volcanics clearly show dextral slip. A major strike-slip zone in this region is also speculated by Aksu et al. (2009), where a sinistral strike-slip fault is proposed for the Sırrı Erinç Plateau between the Anaximander Mountain (*sensu stricto*) and the Anaxagoras and Anaximenes Mountains in the east and south, respectively. The speculated strike-slip zone extended from the Sırrı Erinç Plateau toward the apex of the Isparta Angle, marking the westernmost continental margin of the Antalya Basin. Solely based on the slip directions of the major strike-slip systems in the region, Aksu et al. (2009) proposed that this strike-slip zone must also be sinistral: and this agrees with the first motions of an earthquake occurring at the southern tip of the Kemer Peninsula (Hall et al., 2009). However, based on the volcanic evidence (i.e. Savaşçın et al., 1995), it is suggested here that strike-slip along the western margin of the Antalya Basin is dextral. Note that the sense of slip may have changed with time.

6.2.2 Reactivated contractional structures (Domain 3C)

A distinctly spatially localized contractional zone is situated in the eastern and central portion of the western Antalya Basin. Here, the prominent pre-existing Miocene thrusts are reactivated in the Pliocene-Quaternary, as indicated by the growth strata architecture that developed in the associated piggy-back basins (see Chapter 5). This belt mimics the map traces of the Miocene thrusts and defines an arcuate, predominantly NW-SE trending zone consisting of 4-6 large thrust panels. The belt is traced toward the northeast to within <10 km of the present-day shoreline and links with the large thrust panels mapped onland associated with the Aksu

phase of compression (i.e. Aksu Thrust, Poisson et al., 2003a,b, 2011). These onland thrusts are developed over the pre-existing Miocene thrusts, similar to the architecture observed and described in the offshore Antalya Basin. Poisson et al. (2003a) documented that the compressional deformation continued into the lower-middle Pliocene in the onland Aksu, Köprü, Manavgat basins. The seismic reflection data described in Chapters 4 and 5 showed a similar timing for the thrust activity in the northern portion of the offshore Antalya Basin, where growth strata were developed within the lower and middle portion of the Pliocene-Quaternary sediments. However, the offshore data also showed that the thrust activity continued into the upper Pliocene-Quaternary, particularly in the southern and southeastern portion of the study area. The general slowing of thrusting activity toward the north has important implications (discussed below).

The correlation of the offshore thrust panels with those mapped onland suggests that the fold-thrust belt associated with the Aksu phase of thrusting formed an (at least) 200 km long and 30 - 50 km wide deformation front. Toward the southeast, the large thrust panels can be linked with the thrusts mapped in the eastern Antalya Basin (e.g. Işler, 2004; Işler et al., 2005). Işler et al. (2005) suggested that these thrusts can be readily traced toward the southeast, where they link with the thrust panels that define the core of the Kyrenia Mountains of northern Cyprus (Işler et al., 2005, their figures 9, 10). They further suggested that these thrusts can be readily correlated with the Orga, Kythrea and Ovgos thrusts mapped onland in Cyprus, respectively. These onland thrusts exhibited a very similar timing and structural and stratigraphic architecture to those mapped offshore (e.g. Calon et al., 2005a,b). Therefore, this crustal-scale zone of deformation extends from the eastern thrust panels of the Isparta Angle across the Antalya Basin and onto the thrust panels mapped in the Kyrenia Range of northern Cyprus, making this deformation zone at least 300 km long. Fur-

thermore, Aksu et al. (2005) clearly documented that the fold-thrust panels mapped in the Kyrenia Range extend to the east with a NE-SW trend to link with the fold-thrust panels mapped in the Misis Mountains of southern Turkey and then further north-eastward toward the Kahramanmaraş triple junction in southeastern Turkey. Thus, this is, in fact, a 750 - km long south-convex deformation front extending from the Isparta Angle all the way to the Kahramanmaraş triple junction (Fig. 6.4). In the literature, this deformation front is referred to as the Misis-Kyrenia-Aksu Fault Zone (c.f. Aksu et al., 2005; Calon et al., 2005a,b; Işler et al., 2005). It developed during the Pliocene-Quaternary in response to the large-scale rearrangement of microplates and continental fragments following the pervasive collision between the Arabian Microplate and the Eurasian Plate which resulted in the continuing westward escape of the Aegean-Anatolian Microplate. Domain 3C is only a small piece of the puzzle in the tectonic evolution of the eastern Mediterranean region.

The individual faults of the northwestern limb of this arcuate deformation front (i.e. the Aksu Fault and Kırkkavak Fault) exhibit notable dextral Pliocene-Quaternary strike-slip displacement (e.g. Yağmurlu et al., 1997; Marker and Reilinger, 1997; Çiner et al., 2008, Meijers et al., 2011), whereas the individual faults of the northeastern limb of the deformation front (i.e. the Misis-Kyrenia Fault zone, the Misis Thrust, the Kyrenia Thrust and the Aslantaş Thrust) are all known to have sinistral strike-slip movements (e.g. Kelling et al., 1987; Kozlu, 1987; Gökçen et al., 1988). The fact that the northwestern and northeastern limbs of this arcuate deformation front exhibit oppositely-directed slip directions suggests that the southernmost apex of the deformation front must be a zone of intense contractional deformation. The protracted Pliocene-Quaternary thrusting along the Kyrenia Range supports this contention.

6.2.3 Pliocene-Quaternary extensional fault zone (Domain 3A)

Immediately northeast of the Aksu-Kyrenia portion of the deformation zone (i.e. the reactivated contractional structures of Domain 3C), there is a similarly trending zone that is dominated by faults with notable extensional stratigraphic separation (also recognized by Işler, 2004 and Işler et al., 2005). Işler et al., 2005 showed exquisite examples of extensional faults where the thickness of the Pliocene-Quaternary strata above a marker reflector in the footwall of the fault was significantly thicker than observed in the hanging wall. They argued that under normal sedimentary conditions where faulting is syn-sedimentary, strata on the hanging wall must be thicker than that in the footwall. Therefore, they argued, these faults with extensional separations must also accommodate considerable strike-slip displacement. Small amounts of growth strata observed in the hanging walls of these faults in the lower portion of the Pliocene-Quaternary successions suggest that the faulting may have initiated during the early Pliocene.

The presence of a zone dominated by extension and transtension (Domain 3A) immediately adjacent to a zone dominated by transpression (Domain 3C) is enigmatic. Işler et al. (2005) interpreted this zone as an important transtensional lineament that developed to accommodate the partitioning of displacements created by the ensuing westward escape of the Aegean-Anatolian Microplate in the north (i.e. Dewey et al., 1986) and the ongoing destruction of the Neotethys Ocean and ocean-forearc collision in the south. They further proposed that the westward escape of the eastern segment of the Aegean-Anatolian Microplate is accommodated at its southern boundary by an arcuate splay of the East Anatolian Transform Fault, which is represented by a major fault zone extending from the Misis Mountains of southern Turkey to the Kyre-

nia Range of northern Cyprus and further west to the northwestern segment of the Antalya Basin. They used GPS data to show that the motion of the eastern segment of the Aegean-Anatolian Microplate relative to a fixed Eurasian Plate is invariably west directed east of 30° longitude with no evidence of rotation or fragmentation (e.g. McClusky et al., 2003). Based on this observation, they suggested that the sense of movement along this arcuate extensional fault zone must be sinistral (with respect to the African Plate).

It is very difficult to determine the sense of slip unless a piercing point is identified both in the footwall and the hanging wall of a fault. Unfortunately, no such structure has been readily identified in the study area, thus rendering the present study mute regarding the sense of oblique slip that may be present across the normal faults mapped in this area. However, significant information exists in the onland geology north of the study area. The evaluation of the kinematics of the region within the context of the extensive work in the onland Aksu, Köprú and Manavgat Basins where dextral strike-slip has been identified specifically in large reactivated thrusts (Yağmurlu et al., 1997; Barka and Reilinger, 1007; Poisson et al., 2003a,b, 2001; Çiner et al., 2008; Meijers et al., 2011) strongly suggest that the offshore continuations of these re-activated thrusts must also have a dextral sense of slip. It is, therefore, proposed that the extensional fault zone immediately northwest of these reactivated contractional structures must also have dextral strike-slip motion.

6.3 Regional synthesis

The above discussion placed the study area into a regional context, linking major structural elements with their marine and land counterparts (Fig. 6.4). In this section, the area under investigation is further zoomed out to include the Hellenic and

Cyprus Arcs and their internal elements such as the Pliny-Strabo Trenches, Anaximander Mountains (*sensu lato*) and the Florence Rise so that the plate-tectonic scale ramification of the tectonic history can be discussed.

Today, the zone of convergence between the African Plate and the Aegean-Anatolian Microplates is delineated by two prominent north-concave arcs in the eastern Mediterranean Sea: the Hellenic Arc in the west and the Cyprus Arc in the east (Fig. 6.4). The Pliny and Strabo Trenches form the NE-SW trending broad zone which links these two arcs. Recent studies showed that the subduction is ceased along the Cyprus Arc, but continues along the Hellenic Arc (Kempler and Ben-Avraham, 1987; Robertson, 1998b). In this region, the relative motion between the African Plate and the Aegean-Anatolian Microplate has essentially halted. Subduction of the northern fringes of the African Plate beneath the Hellenic Arc is accompanied by slab roll-back (e.g. Govers and Wortel, 2005). The overriding plate shows back-arc extension in response to the movement of the trench, such as the N-S extension seen in the western segment of the Aegean-Anatolian Microplate. Another consequence of the subduction along the Hellenic Arc and the cessation of subduction along the Cyprus Arc is the tearing of the lithosphere along transform-parallel zones. The tearing transform segment along the present-day Pliny-Strabo Trenches is referred to as the STEP fault system (Govers and Wortel, 2005). These transform zones have sinistral strike-slip and the blocks between them experience counterclockwise rotation.

During the Early-Middle Miocene, the convergence vector between the African Plate and the Anatolian segment of the then-Eurasian Plate was nearly orthogonal to the current-day trend (e.g. Wdowinski et al., 2006) and the entire region was situated within a predominantly compressional tectonic regime. Aksu et al. (2009) showed that in the Late Miocene, the northwestern Florence Rise and the Anaxagoras Mountain likely experienced a small clockwise rotation to assume its NW-SE

trend. They further suggested that this rotation was probably associated with the Aksu Phase of deformation that also shaped the eastern margin of the Isparta Angle (e.g. Poisson et al., 2003a). This NW-SE trend is also documented in the Antalya Basin (Işler et al., 2005). Aksu et al. (2009) further suggested that the clockwise rotation of the Florence Rise and the Anaxagoras Mountain was complemented by a counterclockwise rotation in the western portion of the Anaximander Mountains. During the Pliocene-Quaternary, the counterclockwise rotation of the Anaximander and Anaximenes Mountain in the west and the clockwise rotation of the Anaxagoras Mountain in the east created an arrow-shaped structure across the Anaximander Mountains (*sensu lato*)with limbs displaying NE-SW and NW-SE trends in the west and east, respectively (Fig. 6.4).

It is speculated that a protracted contraction and thrusting occurred in the Late Miocene with its peak activity possibly during the Tortonian (Işler et al., 2005). This episode of pre-Messinian compression is responsible for the large open folds observed along the northern slopes of the Anaximander Mountain, as well as within the core of the Sırrı Erinç Plateau. The lack of both progressive unconformities that merge with the M-reflector toward the ridge crests and syn-tectonic growth strata within the pre-Messinian evaporite successions of Unit 2 in the southwestern Antalya Basin collectively suggest that thrusting may have been relatively inactive during Late Messinian erosion. Note, however, that we might not see growth strata within the Messinian unit since these evaporite sequences have migrated and deformed post-deposition.

Within this backdrop, the importance of the Antalya Basin becomes evident. This study documents that the Miocene successions in the marine Antalya Basin constitute the southern extension of the greater Isparta Angle. The above discussion illustrates that deformation associated with the evolution of the eastern limb of the

Isparta Angle is not solely restricted to the Eocene (Kissel et al., 1990), but continued well into the Late Miocene (i.e. Tortonian) as indicated by the prominent fold-thrust structures that developed within Unit 3. The reactivation of the fold-thrust belt in the Pliocene-Quaternary as a strike-slip zone is well documented in this study and confirms the presence of a very large arcuate south-convex deformation zone linking the splays of the East Anatolian Fault Zone across the Misis Mountains to the Kyrenia Range, and then to the Aksu Thrust. These findings support previous work by Işler et al. (2005) in the central and eastern Antalya Basin.

Along the western margin of the Antalya Basin and the eastern fringes of the western limb of the Isparta Angle, a major strike-slip system developed during the Pliocene-Quaternary. Recent mapping along the onland Kemer Peninsula documented that this dextral strike-slip system extends west into the Beydağları region. It is speculated that this strike-slip system provides a probable link between the Isparta Angle and the Anaximander Mountains (*sensu lato*) and is likely related to the STEP fault zone generated by the slab roll-back at the junction of the Hellenic and Cyprus Arcs (Govers and Wortel, 2005).

How can the strike-slip across the western Antalya Basin and adjacent Beydağları be related? Figure 6.5 shows a simplified version of GPS motion vectors from McClusky et al. (2000) relative to a fixed Aegean-Anatolian Microplate. The Aegean Sea is generalized by vectors showing strong southerly motion. Vectors from stations MATR and HELW show that the African Plate is moving northward about a rotation pole near the eastern edge of the map. Convergence at the Florence Rise increases westward. Vectors from stations ANTG, KASO and SIRA show that the triangular block between the Burdur-Fethiye Fault zone and the Aksu-Kyrenia Fault zone is moving northward at a slower rate than the the African Plate. This is indicative of contraction across at least the western region the Florence Rise. The northward mo-

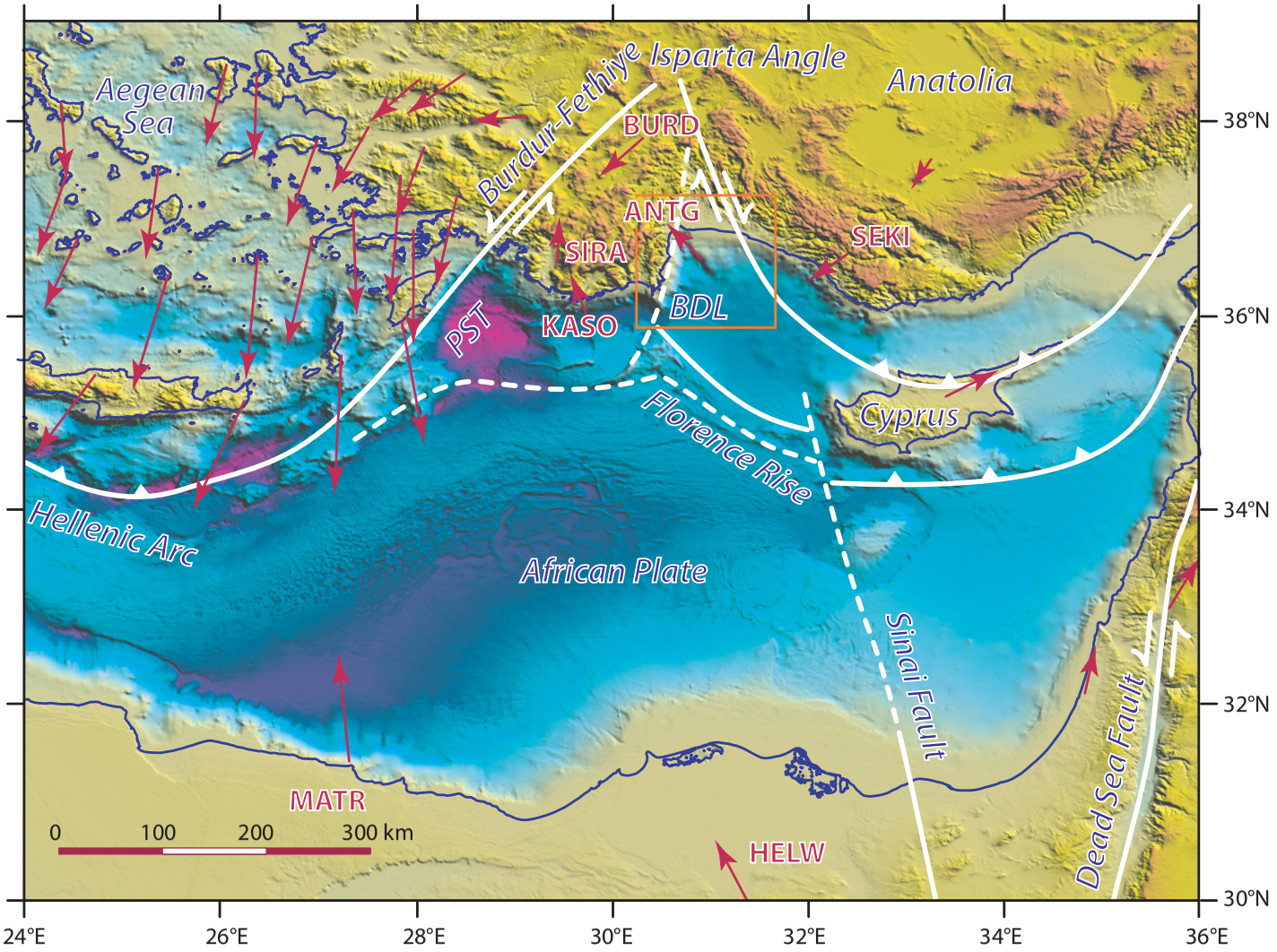

Figure 6.5: Physiography of the eastern Mediterranean Sea showing a selection of GPS vectors, relative to a fixed Anatolia, redrawn from McClusky et al. (2000). The topography and bathymetry are compiled from GeoMapApp (Ryan et al., 2009), the coastline and the selected isobaths contours are from the International Oceanographic Commission (1981). Major structural lineaments are drawn in white; coastlines in black; GPS vectors and site names are shown in red with white outline. Study area of the western Antalya basin is shown as orange rectangle. PST= Pliny-Strabo Trenches, BDL= Beydağları Lineament. GPS vectors are shown in red. Strike-slip motions across major lineaments indicated by GPS vectors are shown in white.

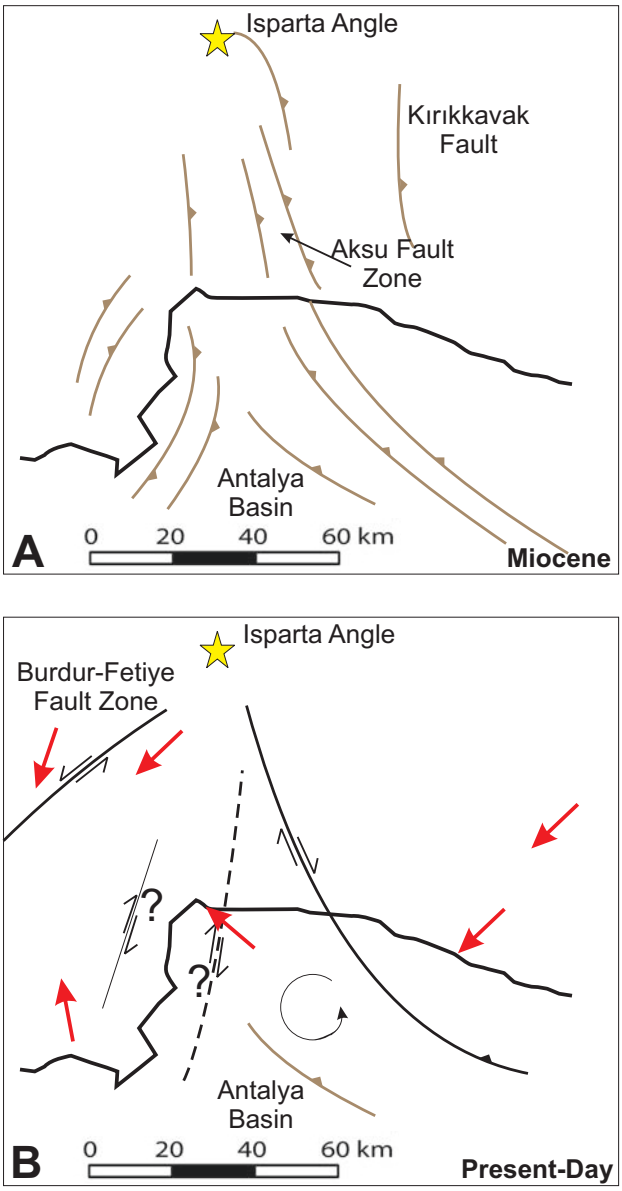

Figure 6.6: Line diagram illustrating the evolution of the Antalya microblock. (A) Pre-Messinian Miocene simplified tectonic map showing contraction dominated this interval. Onland thrusts compiled from Blumenthal, 1963. (B) Present-day simplified tectonic map with GPS vectors (RED) show distinct change from contractional to (mainly) extensional features with strike-slip components. Interpretation of dextral slip both onland and offshore on the western margin of Antalya Basin suggests the microblock is rotating counterclockwise. GPS vectors suggest a northward migration of this microblock relative to the surrounding blocks. Antalya coastline in thick black. GPS vectors relative to a fixed Anatolia in RED (redrawn from McClusky et al., 2000). Thrusts shown with filled triangular ticks on hanging walls; oblique faults shown with half arrows indicating sense of slip.

tion of the triangular block contrasts with the southerly motion of the Aegean segment of the Aegean-Anatolian Microplate, confirming the sense of sinistral strike-slip across the Burdur-Fethiye Fault zone. The southwesterly vector at BURD contrasts with the northerly vector at SIRA, suggesting that sinistral transpression extends some distance into the triangular block from the Burdur Fethiye Fault Zone. Northeast of the Aksu-Kyrenia Fault Zone, the vector at SEKI indicates continuing contraction across the thrust zone, but also dextral strike-slip relative to vectors at ANTG, KASO and SIRA. Such dextral strike slip might extend farther into the triangular zone, confirming oblique slip across many of the steep extensional faults at the edge of the continental shelf in the western Antalya basin. The Beydağları Lineament (BDL, Fig. 6.5) could mark the boundary of the dextral strike slip fault zone from the sinistral strike-slip faulting which characterizes the Burdur-Fethiye Fault zone. No clear evidence exists from the GPS vectors regarding present-day extension in the triangular zone. The continued northward motion of the African Plate, which increases in rate to the west, appears to have resulted in contraction across the Florence Rise, but that its northward motion is partly transmitted to the triangular block, resulting in sinistral strike slip towards its western margin and dextral strike slip towards its eastern margin.

It is speculated that the strike-slip zones on the eastern and western flanks of the study area (i.e. the Aksu-Kyrenia Fault and the Beydağları faults) are facilitating the western Antalya Basin sandwiched between them to behave as a separate microblock (Fig. 6.6). This observation is further evidenced by the present-day thrusting in the region (e.g. Chapter 5). This study clearly shows that there is still compression-related activity in the offshore Antalya Basin. The fact that reactivated Miocene thrusts in the study area have generally increasing activity toward the south (i.e. greater M-reflector offset, more growth in the Pliocene-Quaternary basins, larger in-

flections on the seabed) is suggestive of the possible microplate rotation in this region. The complex deformation documented in the more northern region of the study area (e.g. the possible inversion structure described in Domain 3C) might be related to this block rotation. The dextral strike slip along the Aksu-Kyrenia Fault suggests the Antalya micro block might be rotating counter-clockwise. This observation would be accommodated by dextral strike slip along the Beydağları region (Fig. 6.6). GPS vectors indicate the microblock is also migrating northward relative to the surrounding blocks (e.g. Figs. 6.5 and 6.6).

It is possible that the complex deformation occurring in the proposed Antalya microblock during the Pliocene-Quaternary initiated the displacement of the Messinian evaporites contained in the large, deep basin described in Domain 3C of Chapter 5. Hints of strike slip motion along the listric fault which bounds this deeper basin could be explained, at least in part, by a rotation micro block immediately north of it. It is likely that transtension in this region is also related to the structures further south (i.e. STEP fault zone at the junction of the Hellenic and Cyprus Arcs) which link with the transtensional structures described in the western Antalya Basin. The fact that the subduction is halted along the Florence Rise, but is continuing along the Hellenic Arc is creating a crustal-scale tear along the Pliny-Strabo Trenches (Govers and Wortel, 2005). The cessation of subduction along the Cyprus Arc strongly suggests that the ocean floor south of the Florence Rise is likely not typical oceanic crust as seen south of the Hellenic Arc, but is either thickened oceanic crust or, possibly, the northern fringes of the attenuated continental margin of the African Plate. The new refraction studies south of Cyprus (Hall, Memorial University of Newfoundland, personal communication, May 2012) will undoubtedly shed important light on the nature and thickness of the crust in this region.

The eastern Mediterranean remains as one of the most extensively studied, yet poorly understood, regions of the most recent orogen. Collision in the eastern Mediterranean is embryonic and gives us a glimpse of the Himalayas or the Appalachian Mountains in their infancy. The Antalya Basin is one of several places that hold important clues in the delineation of the tectonic and sedimentary evolution of the eastern Mediterranean jig-saw puzzle. Knowledge gained in such places is incremental and pivotal in the understanding of the initiation and kinematic evolution of continent-continent collision.

Chapter 7

Conclusions

Detailed interpretation of high-resolution multichannel seismic reflection profiles together with industry seismic profiles and well chronologies reveal the following salient conclusions:

- The Miocene to Recent tectonic evolution of the western Anatlya Basin occurred in three distinct intervals: the pre-Messinian Miocene, the Messinian, and the Pliocene-Quaternary.

- The pre-Messinian Miocene is characterized by a prominent fold-thrust belt which shows arcuate NW-SE striking, SW-verging thrust panels in the east and broadly N-S striking, W-verging thrust panels in the west. These two seemingly separate thrust systems form an inverted V-shaped structure within the marine western Antalya Basin, developed immediately south of the Isparta Angle onland. The similarities between the strike and vergence of the thrust panels in the eastern and western limbs of the Isparta Angle and those mapped within the marine areas clearly document that the thrusts mapped in the marine areas once defined a broadly E-W striking, S-verging fold-thrust belt and they

assumed their present day configuration associated with the crustal buckling of the Isparta Angle. This thesis documents that the Isparta Angle (*sensu lato*) is a much large structure than mapped onland and extends south into the marine Antalya Basin.

- Various pieces of evidence document that the Messinian interval was tectonically quiet, including: (i) the large folds delineated and mapped in the pre-Messinian Miocene successions are not concordant with the N- and M-reflectors; (ii) the largely homogeneous and/or weakly-reflective Messinian sediments often show folding that does not follow the amplitude and wavelength of the folds developed in the pre-Messinian Miocene sediments; and (iii) the termination of some of the thrusts below the N-reflector.

- The Pliocene-Quaternary interval marks an overall change in tectonic style. This thesis suggests that the strain is partitioned into discrete regional morpho-tectonic domains.

- In the east, the Miocene fold-thrust belt remained largely inactive; however, several prominent thrusts became re-activated during this time. Mapping showed that these thrusts can be readily traced toward the southeast and correlated with the Ovgos, Kythrea and Orga thrusts mapped onland Cyprus. Along the continental slope and shallower shelves, the tectonic framework of the Pliocene-Quaternary succession is delineated by faults that exhibit variable extensional stratigraphic separations. Field observations suggested that these faults also have considerable strike-slip components.

- In the west, the structural framework was dominated by a series of broadly N-S striking, invariably steeply E-dipping extensional faults which form a zone of deformation that is 20-30 km wide. This zone occurs over the very steep

continental slope in western Antalya Basin, and extends west into the Kemer Peninsula and into the Beydaglari region. Onland these broadly N-S and NNE-SSW striking faults are documented to have notable strike-slip components.

- The western Antalya Basin behaves as a counter-clockwise rotating microblock, accommodated by dextral strike-slip motion along the Beydağları region.
- Within the larger plate tectonic framework, the study area is a forearc basin north of the Cyprus Arc. However, this forearc basin evolved since the Oligo-Miocene as part of the Isparta Angle.

References

Akay, E. and Uysal, S., 1985. Orta Toroslarin batisindaki (Antalya) Neojen çökellerinin stratigrafisi, sedimantolojisi ve yapisal jeolojisi. Mineral Research Exploration Institute (MTA), unpublished report, 276 pp.

Akay, E., Uysal, S., Poisson, A, Craveue, J., Muller, C., 1985. Antalya Neojen havzasinin stratigrafisi (the stratigraphy of the Neogene Antalya Basin), in Turkish. Bulletin of the Geological Society of Turkey, 28:105-1 19.

Aksu, A.E., Calon, T.J., Piper, D.J.W, Turgut, S, Izdar, E.K., 1992a. Architecture of late orogenic basins in the eastern Mediterranean Sea. Tectonophysics, 210: 191213.

Aksu, A.E., Calon, T.J., Hall, J., Mansfield, S. and Yasar, D., 2005a. The Cilicia - Adana Basin complex, Eastern Mediterranean: Neogene evolution of an active fore-arc basin in an obliquely convergent margin. Marine Geology 221: 121-159.

Aksu, A.E., Calon, T.J., Hall, J., and Yaşar, D., 2005b. Origin and evolution of the Neogene Iskenderun Basin, northeastern Mediterranean Sea. Marine Geology 221: 161-187.

Aksu, A.E., Hall, J. and Yaltırak, C., 2005c. Editorial - Miocene to Recent tectonic evolution of the eastern Mediterranean: new pieces of the old Mediterranean puzzle. Marine Geology, 221: 1-13.

Aksu A.E., J. Hall, and Yaltırak, C., 2009. Neogene evolution of the Anaximander Mountains and Finike Basin at the Junction of Hellenic and Cyprus Arcs, Eastern Mediterranean. Marine Geology, 258: 24-47.

Aksu, A.E., Calon, T.J., Hall, J., Mansfield, S., and Yasar, D., 2005b. The CiliciaAdana Basin complex, Eastern Mediterranean: Neogene evolution of an active fore arc basin in an obliquely convergent margin. Marine Geology, 221: 121159.

Aksu A.E., J. Hall, and Yaltirak, C., 2009. Neogene evolution of the Anaximander Mountains and Finike Basin at the Junction of Hellenic and Cyprus Arcs, Eastern Mediterranean. Marine Geology, 258: 24-47.

Anastasakis, G., Kelling, G., 1991. Tectonic connection of the Hellenic and Cyprus arcs and related geotectonic elements. Marine Geology, 97: 261277.

Barka A., Relinger, R., Şaroğlu, F. and Şengör, A.M.C., 1997. The Isparta Angle: its important in the neotectonics of the eastern Mediterranean region. International Earth Sciences Colloquium on the Aegean Region (IESCA-1995), Proceeding 1: 3-17.

Bassant, P., Van Buchem, F.S.P., Strasser, A. and Görür, N., 2005. The stratigraphic architecture and evolution of the Burdigalian carbonatesiliciclastic sedimentary systems of the Mut Basin, Turkey. Sedimentary Geology, 173, 187-232.

Biju-Duval, B, and L Montadert, comps. Structural History of the Mediterranean Basin. Paris: Editions Technips, 1977. Barka A. and Relinger, R., 1997. Active tectonics of the eastern Mediterranean region: deduced from GPS, neotectonic and seismicity data. Annali di Geofisica, 40: 587-610.

Blumenthal, M.M., 1963. Le système structural du Taurus Anatolies. Bulletin de la Société Géologique de France. In: Livre à Mémoire de Professor P. Fallot. Mémoires de la Société Géologique de France 1(2): 611-662.

Blumenthal, M., 1963b, (Compiler). Geological Map of Turkey, Konya-sheet, 1:500,000, Institute of Mineral Resources and Exploration (MTA), Ankara, Turkey.

Bridge, C., Calon, T.J., Hall, J., Aksu, A.E., 2005. Salt tectonics in two convergent margin basins of the Cyprus Arc, Eastern Mediterranean. Marine Geology, 221: 223-259.

Burton-Ferguson, R., Aksu, A.E., Calon, T.J., and Hall, J., 2005. Seismic stratigraphy and structural evolution of the Adana Basin, Eastern Mediterranean. Marine Geology, 221: 189-222.

Çinar, E., (in progress). The Miocene to Recent tectonic evolution of an active transform fault at the junction of Hellenic and Cyprus Arcs, eastern Mediterranean: The linkage between the western Antalya Basin, Finike Basin, and Anaximander Mountains. In progress MSc thesis, Memorial University of Newfoundland.

Çiner, A., Karabıyıkoğlu, M., Monod, O., Deynoux, M. and Tuzcu, S., 2008. Late Cenozoic sedimentary evolution of the Antalya Basin, southern Turkey. Turkish Journal of Earth Sciences, 17: 1-41.

Calon, T.J., Hall, J. and Aksu, A.E., 2005a. The Oligocene-Recent evolution of the Mesaoria Basin (Cyprus) and its western marine extension, Eastern Mediterranean. Marine Geology 221: 95-120.

Calon, T.J., Aksu, A.E. and Hall, J., 2005b. The Neogene evolution of the Outer Latakia Basin and its extension into the Eastern Mesaoria Basin (Cyprus), Eastern Mediterranean. Marine Geology 221: 61-94.

Cipollari, P., Cosentino, D., Radeff, G., Schildgen, T.F., Faranda, C., Grossi, F., Gliozzi, E., Smedile, A., Gennari, R., Darbas, G., Dudas, F.Ö., Gúrbúz, K., Nazik, A., and Echtler, H., 2013. Easternmost Mediterranean evidence of Zanclean flooding event and subsequent surface uplift: Adana Basin, south-

ern Turkey. Geological Society, London, Special Publications, 372: 473-494, doi:10.1144/SP372.5.

Cleintaur, M.R., Knox, G.J., Ealey, P.J., 1977. The geology of Cyprus and its place in the eastern Mediterranean framework. Geol. Mijnb. 56 (1): 66 82.

Chorowicz, J., P. Luxey, N. Lyberis, J. Carvalho, J. F. Parrot, T. Yürür, and N. Gndogdu (1994). The Maras triple junction (southern Turkey) based on digital elevation model and satellite imaginary interpretation, J. Geophys. Res. 99, 20,22520,242.

Cranshaw, J., 2010. Miocene to Recent tectonic and sedimentary evolution of the Anaximander Seamounts; eastern Mediterranean Sea. Unpublished MSc thesis, Memorial University of Newfoundland, 256 pp.

Cosentino, D. Buschwaldt, R., Sampalmieri, G., Iadanza, A., Cipppolari, P., Schildgen, T., Hinnov, L.A., Ramezani, J., and Bowering, S.A., 2013. Refining the Mediterranean "Messinian gap" with high-precision U-Pb zircon geochronology, central and northern Italy. Geology, 41: 323-326.

Cosentino, D., Radeff, G., Darbas, G., Dudas, F., Gürbüz, K., and Schildgen, T., 2010, Late Miocene geohistory of the Mut and Adana Basins (southern Turkey): Insight for the uplift of the southern margin of the Central Anatolia Plateau, in Tectonic Crossroads: Evolving Orogens of Eurasia-Africa-Arabia: GSA Global Meeting, Ankara, Turkey, 24 October 2010: Boulder, Colorado, Geological Society of America, abstract number 122, p. 3435.

Dercourt, J., Zonenshain, L.P., Ricou, L.E., Le Pichon, X., Knipper, A.L., Grandjaquet, C., Sbortshikov, I.M., Geussant, J., Lepvrier, C., Pechersku, D.H., Boulin, J., Bazhenov, M.L., Lauer, J.P., Biju-Dival, B., 1986. Geological evolution of the Tethys belt from the Atlantic to the Pamirs since the Lias. Tectonophysics 123: 241-315.

Dewey, F.J. and Şengör, A.M.C., 1979. Aegean and surrounding regions: complex multiplate and continuum tectonics in a convergent zone. Bulleton of the Geological Society of America, 90: 8492.

Dewey, F.J., Hempton, M.R., Kidd, W.S.F., Şaroğlu, F. and Şengör, A.M.C., 1986. Shortening of continental lithosphere: the neotectonics of eastern Anatolia - a young collision zone. In: M.P. Coward and A.C. Ries (Eds.), Collision Tectonics. Geological Society Special Publication, 19: 3-36.

Deynoux, M., Çiner, A., Monod, O., Karabıyıkoğlu, M., Manatschal, G. and Tuzcu, S., 2005. Facies architecture and depositional evolution of alluvial fan to fan-delta complexes in the tectonically active Miocene Kpr[U+FFFD] Basin, Isparta Angle, Turkey. Sedimentary Geology, 173, 315-343.

Dilek, Y. and Rowland, J.C., 1993. Evolution of a conjugate passiva margin pair in mesozoic southern Turkey. Tectonics, 12(4): 954-970.

Droz, L., R. Kergoat, P. Cochonat, and S. Berne, 2001. Recent Sedimentary Events in the Western Gulf of Lions (Western Mediterranean). Marine Geology 176: 23-37.

Einsele, G., 1993. Sedimentary Basins: Evolution, Facies and Sediment Budget. Springer-Verlag, Berlin, New York. 628 pp.

Elboth, T., Reif, B.A.P. and Andeassen, [U+FFFD], 2009. Flow and swell noise in marine seismic data. Geophysics, 74: Q17-Q25. doi: 10.1190/?1.3078403

Eriş, K.K., Bassant, P. and Ülgen, U.B., 2005 Tectono-stratigraphic evolution of an Early Miocene incised valley-fill (Derin[U+FFFD] Formation) in the Mut Basin, Southern Turkey. Sedimentary Geology, 173: 151-185.

Garfunkel, Z., 2004. Origin of the Eastern Mediterranean Basin: a reevaluation. Tectonophysics, 391: 11-34.

Glover, C. and Robertson, A., 1998. Neotectonic intersection of the Aegean and Cyprus tectonic arcs: extensional and stike-slip faulting in the Isparta Angle, SW Turkey. Tectonophysics, 298(1-3): 103-132.

Gogacz, A., (in progress). Miocene to Recent sedimentary and structural evolution of the western Antalya Basin, Eastern Mediterranean Sea. In progress MSc thesis, Memorial University of Newfoundland.

Gökçen, S.L., Kelling, G., Gökçen, N. and Floyd, P.A., 1988. Sedimentology of a late Cenozoic collisional sequence: the Misis Complex, Adana, southern Turkey. Sedimentary Geology, 59: 205-235.

Govers, R. and Wortel, M.J.R., 2005. Lithosphere tearing at STEP faults: Response to edges of subduction zones. Earth and Planetary Science Letters 236: 505 523.

Hall, J., Aksu, A.E., Calon, T.J. and Yaşar, D., 2005a. Varying tectonic control on basin development at an active microplate margin: the Iskenderun - Latakia Basin complex, Eastern Mediterranean. Marine Geology, 221: 15-60.

Hall, J., Calon, T.J., Aksu, A.E., and Meade, S.R., 2005b. Structural evolution of the Latakia Ridge and Cyprus Basin at the front of the Cyprus Arc, Eastern Mediterranean Sea. Marine Geology, 221: 261-297.

Hall, J., Aksu, A.E., Yaltırak, C., Winsor, J.D., 2009. Structural architecture of the Rhodes Basin: a deep depocentre that evolved since the Pliocene at the junction of Hellenic and Cyprus Arcs, eastern Mediterranean. Marine Geology, 258: 1-23.

Haq, B.U., J. Hardenbol, and P.R. Vail, 1987, Chronology of fluctuating sea levels since the Triassic: Science, v. 235, p. 1156-1167.

Harding, T. P. 1985. Seismic characteristics and identification of negative flower structures, positive flower structures, and positive structural inversion. Bulletin of the American Association of Petroleum Geologists 69(4), 582-600.

Hayward, A. B., 1984. Sedimentation and basin formation related to ophiolite nappe emplacement; Miocene, SW Turkey. Sedimentary Geology,.40:105-129.

Hiscott, R.N. and Aksu, A.E., 1994. Submarine debris flows and continental slope evolution in front of Quaternary ice sheets, Baffin Bay, Canadian Arctic. American Association of Petroleum Geologists, 78 (3): 445-460.

Hsü, K.J., Cita, M.B. and Ryan, W.B.F., 1973. The origin of the Mediterranean evaporites. In: W.B.F. Ryan, K. Hsü, et al., Initial Reports of the Deep Sea Drilling Project, XIII, Part I, 1203-1231. U.S. Government Printing Office, Washington.

Hsü, K.J. Montadert, L., Bernoulli, D., Cita, M.B., Erickson, A., Garrison, R.E., Kidd, R.B., Mélières, F., Müller, C. and Wright, R., 1978. History of the Mediterranean salinity crisis. In: K. Hsü, L. Montadert et al., Initial Reports of the Deep Sea Drilling Project, XLII, Part I, 1053-1078. U.S. Government Printing Office, Washington.

Hudec, Michael R, et al. The Salt Mine : a Digital Atlas of Salt Tectonics. Austin, Tex.: Bureau of Economic Geology, Jackson School of Geosciences, University of Texas at Austin , 2011.

Intergovernmental Oceanographic Commission (IOC), 1981. International Bathymetric Chart of the Mediterranean. Published by the Head Department of Navigation and Oceanography, Russia, under the authority of IOC,.

Işler, F.I., 2004. Miocene to Recent stratigraphy, structural architecture and tectonic evolution of the Antalya Basin, eastern Mediterranean Sea. Unpublished MSc

thesis, Department of Earth Sciences, Memorial University of Newfoundland, 248 pp.

Işler, F.I., Aksu, A.E., Hall, J., Calon, T.J. and Yaşar, D., 2005. Neogene development of the Antalya Basin, Eastern Mediterranean: an active fore-arc basin adjacent to an arc junction. Marine Geology, 221: 299-330.

Ilgar, A. and Nemec, W., 2005. Early Miocene lacustrine deposits and sequence stratigraphy of the Ermenek Basin, Central Taurides, Turkey. Sedimentary Geology, 173, 233-275.

Jaffey, N. and Robertson, A.H.F., 2001. New sedimentological and structural data from the Ecemis Fault Zone, southern Turkey: implications for its timing and offset and the Cenozoic tectonic escape of Anatolia. Journal of the Geological Society, 158, 367378.

Karabıyikoğlu, M., Çiner, A., Monod, O., Deynoux, M., Tuzcu, S. and [U+FFFD][U+FFFD], S., 2000. Tectonosedimentary evolution of the Miocene Manavgat Basin, western Taurides, Turkey. Geological Society, London, Special Publications, 173: 271-294. doi: 10 .1144/GSL.SP.2000.173.01.14

Karabıyikoğlu, M., Tuzcu, S., Çiner, A., Deynoux, M., Örçen, S. and Hakyemez, A., 2005. Facies and environmental setting of the Miocene coral reefs in the late-orogenic fill of the Antalya Basin, western Taurides, Turkey: implications for tectonic control and sea-level changes. Sedimentary Geology, 173, 345-371.

Karig, D.E. and Kozlu, H., 1990. Late Paleogene - Neogene evolution of the triple junction region near Mara?, south-central Turkey. Journal of the Geological Society, London, 147: 1023-1034.

Kelling, G., Gökçen, S.L., Floyd, P.A., Gökçen, N., 1987. Neogene tectonics and plate convergence in the eastern Mediterranean: new data from southern Turkey. Geology, 15: 425-429.

Kempler, D., and Ben-Avraham, Z., 1987. The tectonic evolution of the Cyprean Arc. Ann. Tecton., 1, 58-71.

Kempler, D. and Garfunkel, Z., 1994. Structure and kinematics in the northeastern Mediterranean: a study of irregular plate boundary. Tectonophysics, 234: 19-32.

Kennedy, S., (2012). Miocene to Recent structural evolution of the Inner Cilicia Basin with special emphasis on the Pliocene-Quaternary sedimentary relationship of the Göksu River and the Cilicia Basin: a quantitative study of volumetrics, subsidence in the Cilicia Basin and concomitant uplift in the Mut basin, Taurus Mountains. Unpublished MSc thesis, Memorial University of Newfoundland.

Kissel, C. and Poisson, A., 1986. Étude paleomagnetique préliminaire des formations Cenozoique des Bey Dağlari (Taurides occidentales - Turquie). C.R. Acad. Sci. Paris 302 Ser. 11(8): 343-348.

Kissel, C., Averbush, O., Frizon de Lamotte, D., Manod, O., and Allerton, S., 1990. First paleomagnetic evidence for a post-Eocene clockwise rotation of the western Taurus thrust belt, east of the Isparta reentrant (southwestern Turkey). Earth and Planetary Science Letters, 117: 1-14.

Kozlu, H., 1987. Structural development and stratigraphy of MisisAndirin region. Proceedings of the 7th Petroleum Congress of Turkey. Turkish Association of Petroleum Geologists, pp. 104 116.

Kurtboğan, B., 2013. Structural and sedimentary evolution of the central Cilicia Basin, eastern Mediterranean Sea. M.Sc. thesis, Memorial University of Newfoundland.

Lastras, G., M. Canals, J.E. Hughes-Clarke, A. Moreno, M. De Batist, D.G. Masson, and P. Cochonat, 2002. Seafl oor imagery from the BIG95 debris flow, western Mediterranean. Geology, 30: 871-874.

Le Pichon, X., Angelier, J., 1979. The Hellenic Arc and trench system: a key to the neotectonic evolution of the eastern Mediterranean area. Tectonophysics 60: 1-42.

Le Pichon, X., Bergerat, F., Roulet, M.J., 1988. Plate kinematics and tectonics leading to the Alpine belt formation. A new analysis. In: Clark, S.P., Burchfiel, B.C., Suppe, J. (Eds.), Processes in Continental Lithospheric Deformation. Special Paper, Geological Society of America 218, pp. 111-131.

McClusky, S., Balassanian, S., Barka, A., C. Demir, S. Ergintav, I. Georgiev, O. Gürkan, M. Hamburger, K. Hurst, H.-G. Hans-Gert, K. Karstens, G. Kekelidze, R. King, V. Kotzev, O. Lenk, S. Mahmoud, A. Mishin, M. Nadariya, A. Ouzounis, D. Paradissis, Y. Peter, M. Prilepin, R. Relinger, I. Sanli, H. Seeger, A. Tealeb, M.N. Toksöz, G. Veis, 2000. Global positioning system constraints on plate kinematics and dynamics in the eastern Mediterranean and Caucasus. Journal of Geophysical Research, 105: 5695-5719.

McKenzie, D. and Yılmaz, Y., 1991. Deformation and volcanism in western Turkey and the Aegean, Bulletin of the Istanbul Technical University, pp. 345-373.

Meijers, J.M., Hinsbergen, D.J.J., Dekkers, M.J., Atlıner, D., Kaymarkı, N., Langeris, C.G., 2011. Pervasive Palaeogene remagnetization of the central Taurides fold- and thrust belt (southern Turkey) and imiplications for rotations in the Isparta Angle. Geophysical Journal International, 184: 1090-1112.

Mitchum, M. R., Jr., Vail, P. R. and Sangree, J. B., 1977a. Seismic stratigraphy and global changes of sea level, Part 6: Stratigraphic interpretation of seismic reflection patterns in depositional sequences. In: C. E. Payton (Editor), Seismic Stratigraphy Applications to Hydrocarbon Exploration. Memoir of the American Association of Petroleum Geologists, 26: 117-135.

Mitchum, R.A.Jr., Vail, P.R.and Thompson III, S., 1977b. Seismic stratigraphy and global change of sea level.Part 2: The depositional sequence as a basic unit for stratigraphic analysis.In:C.E.Payton (Editor), Seismic Stratigraphy Applications to Hydrocarbon Exploration.American Associationof PetroleumGeologists. Memoir, 25: 5362.

Monod, O., 1977. Recherces géologiques dans le Taurus occidentales au sud de Beyşehir (Turquie). Thèse de Doctorat dÉtat ès Sciences, Université de Paris-Sud, Orsay, France. 442 pp.

Monod, O., Kuzucuoğlu, C. and Okay, A.I. 2006. A Miocene paleovalley network in the western Taurus (Turkey). Turkish Journal of Earth Sciences, 15, 123.

Moores, E.M. and Twiss, R.J., 1995. Tectonics. W.H. Freeman and Company, New York, 415 pp.

Mulder, C.J., 1973. Tectonic framework and distribution of Miocene evaporites in the Mediterranean. In: Drooger, C.W. (Ed.), Messinian Events in the Mediterranean. Koninklijke Nederlandse Akademic von Weterschappen, North-Holland Publishing Company, Amsterdam, 44-59 pp.

Ocakoğlu, F., 2002. Palaeoenvironmental analysis of a Miocene basin in the high Taurus Mountains (southern Turkey) and its palaeogeographical and structural significance. Geological Magazine, 139: 473487.

Perinçek, D. Günay, Y., and Kozlu, H., 1987. New observations on strike-slip faults in east and southeast Anatolia. In: Proceedings of the 7th Petroleum Congress of Turkey, Turkish Association of Petroleum Geologists, 89-103.

Piercey, T., 2011. A seismic reflection study of the Neogene sedimentary history of the outer Cilicia Basin, eastern Mediterranean. Unpublished MSc thesis, Memorial University of Newfoundland, 183 pp.

Poisson, A., Wernli, R., Sağular, K., and Temiz, H., 2003a. New data concerning the age of the Aksu Thrust in the south of the Aksu valley, Isparta Angle (SW Turkey): consequences for the Antalya Basin and the Eastern Mediterranean. Geological Journal, 38: 311327.

Poisson, A., Yağmurlu, F., Bozcu, M., Şentŭrk, M., 2003b. New insights on the tectonic setting and evolution around the apex of the Isparta Angle (SW Turkey). Geological Journal, 38, 257-282, doi:10.1002/gj.955

Price, S. and Scott, B., 1994. Fault block rotations at the edge of a zone of continental extension, southwest Turkey. Journal of Structural Geology, 16: 381-392.

ProMAX 3D Reference Guide, 1998. A reference guide for ProMAX Geophysical Processing Software, V1 and V2.

Radeff, G., Cosentino, D., Schildgen, T.F., Güldemin Darbaş, G., and Grbz, K., 2011. Differences and similarities in the Late Miocene geohistory of the Mut and Adana basins (southern Turkey): a record of surface uplift of the southeast margin of the Central Anatolian plateau. Geophysical Research Abstracts, Vol. 13, EGU2011-1691, 2011, EGU General Assembly 2011.

Robertson A.H.F. 1998a. MesozoicTertiary tectonic evolution of the Easternmost Mediterranean area: integration of marine and land-based evidence. In Proceedings of the Ocean Drilling Program, Scientific Results, Robertson AHF, Emeis K-C, Richter C, Camerlenghi A (eds), 160: 723782.

Robertson, A.H.F. 1998b. Tectonic significance of the Eratosthenes Seamount: a continental fragment in the process of collision with a subduction zone in the eastern Mediterranean (Ocean Drilling Porgram Leg 160). Tectonophysics, 298, 63-82.

Robertson, A. and Comas, M., 1998. Collision-related tectonic processes in the Mediterranean region - introduction. Tectonophysics, 298: 1-4.

Robertson, A.H.F. and Dixon, J.E., 1984. Introduction: aspects of the geological evolution of the Eastern Mediterranean. Geological Society, London, Special Publications, 17: 1-74. doi: 10.1144/GSL.SP.1984.017.01.02

Robertson, A.H.F. and Mountkrakis, D., 2006. Tectonic development of the Eastern Mediterranean Region. Geological Society. London, Special Publications, 260: 1-9.

Robertson, A.H.F. and Woodcock, N.H., 1986. The role of Kyrenia Range lineament, Cyprus, in the geological evolution of the eastern Mediterranean area. Royal Society of London Philosophical Transactions, Series A, V. 317: 141-177.

Robertson, A.H.F., Poisson, A., Akinci, Ö., 2003. Developments in research concerning Mesozoic-Tertiary Tethys and neotectonics in the Isparta Angle, SW Turkey. Geological Journal, 38: 195-234.

Ryan, W.B.F., 1969. The floor of the Mediterranean Sea. PhD Thesis, Columbia University, New York, 236 pp.

Ryan, W.B.F. et al., 2009. Global Multi-Resolution Topography synthesis. Geophys. Geosyst., 10, Q03010.

Şafak, [U+FFFD] Kelling, G. Gökçen, N.S., and Gürbüz, K., 2005. The mid-Cenozoic succession and evolution of the Mut basin, southern Turkey, and its regional significance. Sedimentary Geology, 173: 121150.

Şaroğlu, F., Boray, A. and Emre, O., 1987. Active faults of Turkey. Mineral Research Exploration Institute (MTA), Turkey, unpublished report 8643, 394 pp.

Satur, N., Kelling, G., Cronin, B.T., Hurst, A. and Gürbüz, K., 2005. Sedimentary architecture of a canyon-style fairway feeding a deep-water clastic system, the Miocene Cinöz Formation, southern Turkey: significance for reservoir characterisation and modelling. Sedimentary Geology, 173, 91-119.

Savaşçin, M.Y., Francalanci, L., Innocenti, T., Manetti, P., Birsoy, R., Dağ, N., 1995. MiocenePliocene potassicultrapotassic volcanism of the AfyonIsparta region (centralwestern Anatolia, Turkey). Petrogenesis and geodynamic implications: International Earth Sciences Colloquium on the Aegean Region (IESCA-1995), Proceedings, V-II,pp. 487502.

Şengór, A.M.C., Yılmaz, Y., 1981. Tethyan evolution of Turkey: a plate tectonic approach. Tectonophysics 75: 181241.

Şengór, A.M.C., Yilmaz, Y., and Ketin, I, 1980. Remnants of a pre-Late Jurassic ocean in northern Turkey: fragments of Permian-Triassic paleo-Tethys? Bulletin of the Geological Society of America, 91: 599-608.

Şengör, A.M.C., Görür, N. and Şaroğlu, F., 1985. Strike-slip faulting and related basin formation in zones of tectonic escape: Turkey as a case study. Society of Economic Paleontologists and Mineralogists, Special Publication 37: 227-264.

Şengör, A.M.C., Tüysüz, O., Imren, C., Sakinç, M., Eyidogan, H., Görür, N., Le Pichon, X., and Rangin, C., 2005, The North Anatolian fault: A new look: Annual Review of Earth and Planetary Sciences, 33: 37112

Sclater, J. G., and P. A. F. Christie, 1980. Continental stretching: an explanation of the post-mid-Cretaceous subsidence of the central North Sea basin: Journal of Geophysical Research, 85: 3711-3739.

Sheriff, R.E. and Geldart, L.P., 1995. Exploration Seismology. Cambridge University Press, Ed. 2, 592 pp.

ten Veen, J.H.,Woodside, M., Zitter, T.A.C., Dumont, J.F., Mascle, J., Volkonskaia, A., 2004. Neotectonic evolution of the Anaximander Mountains at the junction of the Hellenic and Cyprus Arcs. Tectonophysics 391: 3565.

Toker, E. and Yağmurlu, F., 2010. Tectono-sedimentary evolution of the Eocene transgressive deposits in the Acigöl, Burder and Isparta Areas (SW Turkey). AGD Landscape Environment 4(2): 58-70.

Twiss, R. J. Moores, E. M. 1992. Structural geology. W.H. Freeman Company, New York.

Uffenorde, H., Lund, J.J., Georgi, K.H., 1990. Biostratigraphy of the Neogene in the Iskenderun Basin. Turkish Association of Petroleum Geologists. Proceedings of the 8th Petroleum Congress of Turkey, pp. 363370.

Vail, P.R., R.M. Mitchum, and S. Thompson, 1977, Seismic stratigraphy and global changes of sea level, part 3: Relative changes of sea level from coastal onlap, in C.E. Clayton, ed., Seismic stratigraphy - applications to hydrocarbon exploration: Tulsa, Oklahoma, American Association of Petroleum Geologists Memoir 26, p. 63-81.

Vail, P.R., J. Hardenbol, and R.G. Todd, 1984, Jurassic unconformities, chronostratigraphy, and sea-level changes from seismic stratigraphy and biostratigraphy, in J.S. Schlee, ed., Interregional unconformities and hydrocarbon accumulation: Tulsa, Oklahoma, American Association of Petroleum Geologists Memoir 36, p. 129-144.

van Hinsbergen, D.J.J., Krijgsman, W., Langereis, C.G., Cornée, J.-J., Duermeijer, V.E., van Vugt, N., 2007. Discrete Plio-Pleistocene phases of tilting and counterclockwise rotation of the southeastern Aegean Arc (Rhodos, Greece): early Pliocene formation of the south Aegean left-lateral strike-slip system. Journal of Geological Society London, 164: 1133-1144.

van Wagoner, J.C., H.W. Posamentier, R.M. Mitchum, P.R. Vail, J.F. Sarg, T.S. Loutit, and J. Hardenbol, 1988, An overview of the fundamentals of sequence stratigraphy and key definitions. In: C.K. Wilgus, B.S. Hastings, C.G.St.C.

Kendall, H.W. Posamentier, C.A. Ross, J.C. Van Wagoner, eds., Sea-level changes: an integrated approach. Society of Economic Paleontologists and Mineralogists Special Publication No. 42, p. 39-45.

Walsh, S., 2012. Miocene to Recent structural evolution of the Inner Cilicia Basin with special emphasis on the Pliocene-Quaternary sedimentary relationship of the Gksu River and the Cilicia Basin: a quantitative study of volumetrics, subsidence in the Cilicia Basin and concomitant uplift in the Mut basin, Taurus Mountains. Unpublished MSc thesis, Memorial University of Newfoundland, 256 pp.

Waldron, J.W.F., 1984. Structural history of the Antalya Complex in the 'Isparta Angle', southwest Turkey. In: The Geological Evolution of the Eastern Mediterranean, J.E. Dixon and A.H.F. Robertson (Eds), Geological Society Special Publication 17: 273-286.

Wdowinski, S., Z. Ben-Avraham, R. Arvidsson, and G. Ekstrom (2006). Seismotectonics of the Cyprian Arc, Geophys. J. Int., 164, 176-181, 10.1111/j.1365-246X.2005.02737.x.

Williams, G.D., Ünlügenç, U.C., Kelling, G. and Demirkol, C., 1995. Tectonic controls on stratigraphic evolution of the Adana Basin, Turkey. Journal of Geological Society of London, 152: 873-882.

Woodcock, N. H. 1986. The role of strike-slip fault systems at plate boundaries. Philosophical Transactions of the Royal Society of London A317, 13-29.

Woodcock, N.H. Fischer, M, 1986. Strike slip duplexes. Journal of Geology 8(7), 725-735.

Woodside, J.M., 1977. Tectonic elements and crust of the eastern Mediterranean Sea. Marine Geophysical Research, 3: 317-354.

Woodside, J., Mascle, J., Zitter, T., Limonov, A., Ergn, M., Volkonskaia, A., 2002. The Florence Rise, the Western Bend of the Cyprus Arc. Marine Geology 185, 175194.

Yağmurlu, F., Savaşçın, Y. and Ergün, M., 1997. Relation of alkaline volcanism and active tectonism within the evolution of the Isparta Angle, SW Turkey. The Journal of Geology, 105: 717-728.

Yetiş, C., Kelling, G., Gökçen, S.I., Baroz, F., 1995. A revised stratigraphic framework for Late Cenozoic sequences in the northeastern Mediterranean region. Geol. Rundsch. 84: 794812.

Yılmaz, Ö., 2001. Seismic Data Analysis: Processing, Inversion and Interpretation of Seismic Data (2 Volumes). Investigations in Geophysics No: 10. Society of Exploration Geophysicists.

Yılmaz, Y., 1993. New evidence and model on the evolution of the southeast Anatolian orogen. Geological Society of America Bulletin, 105: 251-271.

Zitter, T., Woodside, J., Mascle, J., 2003. The Anaximander Mountains: a clue to the tectonics of southwest Anatolia. Geological Journal, 38, 375-394.